Department of Naval Architecture, Ocean and Marine Engineering

University of Strathclyde

Dynamic Analysis of a Spar-type Offshore Floating Wind Turbine and its Mooring System

Xue XU

A thesis presented in fulfilment of the requirements for the degree of Doctor of Philosophy

January 2020

I would like to dedicate this thesis to my loving parents and grandparents.

Declaration

I hereby declare that this thesis and all material contained herein is a record of work carried out in the Department of Naval Architecture, Ocean and Marine Engineering of Engineering Faculty, University of Strathclyde during the period from October 2013 to January 2020. This thesis is the result of the author's original research except where otherwise indicated. It has been composed by the author and has not been previously submitted for examination, which has led to the award of a degree.

Signed: Date:

Acknowledgements

First of all, I would like to express my deepest gratitude to my supervisor Prof Sandy Day for his kind support, inspirations and giving me his expert advice on completing my PhD thesis. I would like to thank Dr Narakorn Srinil for help me on the scholarship application which enables me to start my research journey.

I would like to thank Mr David Clelland for his kind help on using Matlab and all the other helpful comments. I would also like to thank Mr Charles Keay, Mr Edward Nixon, Mr Grant Dunning, Mr Bill McGuffie and Mr Bill Wright for their kind support for my experiment at KHL. I would like to thank Ms Susan Pawson, Ms Thelma Will and Mr Ross Gilmour for their kind support on all the administrative details and IT problems during my PhD.

I would like to give my appreciation to Dr Jason Jonkman for his time and patience for answering my endless questions about FAST and FASTlink. I would like to thank the support team from OrcaFlex who have helped me solve a lot of puzzles. I would also like to thank Dr Yiqing Xia, for her kind help on the start of my PhD on using FAST codes.

I would like to specially thank Dr Wendi Liu, for his encouragement and accompany during these years.

Finally, I would like to sincerely thank my parents and my grandparents, for their endless love and support on my education and life.

Abstract

The demand for developing sustainable and renewable energy is increasing due to the greenhouse gas effect and the reducing availability of fossil fuels. Wind energy is one of the cleanest and most sustainable renewable resources. People mainly use two types of wind turbines – onshore and offshore, to harvest the wind energy. Compared with onshore wind, offshore wind resources allow more reliable generation of electricity. In shallow water, bottom-fixed turbines may be used. However, as water depths increase it becomes increasingly difficult to build suitable fixed foundations, and floating offshore wind turbines become attractive.

The OC3-Hywind is an offshore floating wind turbine (OFWT) supported by a spar platform and held in place with three mooring lines. It is important to study the dynamic responses of the floating platform and the mooring system behaviour so that the OFWT can be designed and constructed safely and economically and generate electricity with reliability. However, there are not many studies which have validated the numerical simulation results for floating offshore wind turbines with physical experiments while published studies rarely show the details of the mooring line motion behaviour for OFWTs.

This thesis investigates the dynamic behaviour of a spar-type OFWT including its mooring systems, analysed under various environmental loads both by using state-of-the-art numerical software and conducting an experiment campaign at the Kelvin Hydrodynamics Laboratory. The free decay test has been carried out first to get the spar platform's motions natural frequencies and damping characteristics. A range of

regular and irregular waves has been applied to the platform (both with and without realistic mooring lines) to obtain the platform motion RAO (response amplitude operator) – which can be used to predict the platform dynamic responses under other wave conditions – and to examine the reliability of the numerical predictions under realistic sea conditions.

For the mooring line tensions and motion, the software shows its limitations in the calculation. A non-linear snatching phenomenon has been observed at the tank for some wave frequencies, which has rarely been discussed in published research. It is very important to study this non-linear behaviour as it is shown that snatching leads to the high instantaneous mooring line loads and platform accelerations, which could cause the failure of the mooring lines in the real structure.

Nomenclature

Roman symbols

A	=	amplitude of the fitted function (m)
A_d	=	drag area (m^2)
a	=	area (m^2)
a_r	=	fluid acceleration relative to the body (m/s^2)
a_w	=	fluid acceleration relative to earth (m/s^2)
B	=	offset value
c	=	wave celerity (m/s)
C_a	=	added-mass coefficient
Cd	=	drag coefficient
D	=	length of the hanging wire (m)
D_{KC}	=	characteristic length of the object (m)
D_s	=	diameter of spar (m)
d	=	water depth (m)
E	=	Young's modulus (N/m^2)
f	=	wave frequency (s)
$F(t)$	=	fit function
$F_e(t)$	=	difference between experimental value and fit function value
F_r	=	Froude number
F_w	=	fluid force (N)
g	=	gravitational acceleration (m/s^2)
h	=	distance between the two hanging wires (m)

H_s = significant wave height (m)

H_ω = wave height (m)

I = platform pitch/roll inertia ($kg \cdot m^2$)

L = wave length (m)

l = characteristic length (m)

M = mass of the body (kg)

p = measured mean period of one harmonic motion of the structure (s)

Re = Reynolds number

t = time history (s)

T = wave period (s)

T_{KC} = oscillation period (s)

T_p = wave spectrum peak period (s)

U = oscillating amplitude of the flow velocity or the object's velocity (m)

V = volume of the platform submerged below sea water line (m^3)

Vr = fluid velocity relative to the body (m/s)

$X(t)$ = experimental value

X_{rms} = the root-mean-square value

Greek symbols

Δ = mass of fluid displaced by the body (kg)

ζ = damping ratio

λ = scaling factor

ρ = fluid density (kg/m^3)

φ	=	phase angle (rad)
ω_d	=	damped natural frequency (rad/s)
ω_n	=	undamped natural frequency (rad/s)

Abbreviations

AMP	Motion Amplitude
BEM	Blade Element Momentum
CM	Centre of Mass
COB	Centre of Buoyancy
COG	Centre of Gravity
DOF	Degree of Freedom
GRG	Generalized Reduced Gradient
JONSWAP	Joint North Sea Wave Period
KC	Keulegan-Carpenter number
KHL	Kelvin Hydrodynamics Laboratory
LVDT	Linear Variable Displacement Transformer
MAX	Maximum Value
MEAN	Average Value
MIN	Minimum Value
NREL	National Renewable Energy Laboratory
OFWT	Offshore Floating Wind Turbine
PDF	Probability Density Function
RAO	Response Amplitude Operator

RMS	Root Mean Square
SB	Spar Buoy
SDB	Shallow Drafted Barge
STD	Standard Deviation
SWL	Sea Water Level
TLB	Tension Leg Buoy
TLP	Tension Leg Platform
VIM	Vortex Induced Motion
VIV	Vortex Induced Vibration

Contents

List of Figures

List of Tables

Chapter 1 Introduction

1.1 Introduction

With the burning of fossil fuel such as coal, natural gas and oil, a huge amount of greenhouse gas has been emitted to the environment and has caused severe pollution problems. Also, the fossil fuel is not sustainable. Thus, developing clean and renewable energy is becoming an urgent priority; one of the potential resources for large-scale renewables is wind energy.

Wind energy is a kind of very sufficient resources and can be extracted nearly everywhere. People have been used wind resources for at least 3000 years, although the use of wind as renewable energy for generating electricity only started at the late nineteenth century -- a 12 kW wind turbine generator was constructed in the USA by Charles Brush. However, the interest in commercial wind energy was relatively low until the oil price increased dramatically in the 1980s, and this lead to a number of government funded research, development and demonstration projects (Burton et al., 2011). At the end of 2016, the technology for both onshore and offshore wind turbines construction has reached a relatively mature level with a steadily increasing rate since 2011; the total installed wind energy capacity reached 539,581MW by the end of 2017, as presented in Figure 1. 1.

With the development of wind turbine technology, wind turbines have been constructed and installed in many countries. Figure 1. 2 shows the top 10 countries for total installed wind energy capacity till December of 2017. The main regions for wind turbines installation are China, USA and Europe. By the end of 2016, 5% of the

world's electricity is provided by wind resources. In UK, about more than 15% of electricity generation was contributed by wind power in 2017.

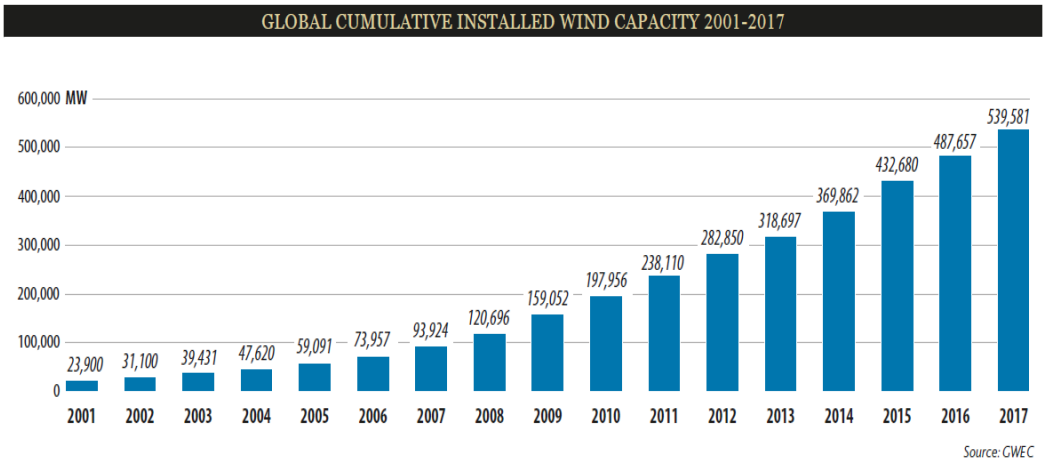

Figure 1. 1 Total Installed Capacity 2011-2017 [MW] (Global Wind Energy Council, 2018)

However, the disadvantages of onshore wind turbine farms are that they occupy a large area on land, making noise and affecting people living nearby; also the wind speed over land is rather lower and much more turbulent than the wind over the ocean surface, as shown in Figure 1. 3. Consequently, developing offshore wind farms would be a better choice.

The UK became the world leader of offshore wind power generation in 2008 and the world largest offshore wind farm has begun construction which is located 74.5 miles off the coast of Yorkshire, where 174 of 7.0 MW turbines will be installed and it can generate 4.1 TWh of electricity per year. In addition, it is estimated that UK has over a third of Europe's total offshore wind resource and this means three times the electricity needs of the nation at current electricity consumption rates (Oswald et al. 2008). Figure 1. 4 present the worldwide offshore wind farm capacity, and we can see a rapid increase in the last decades.

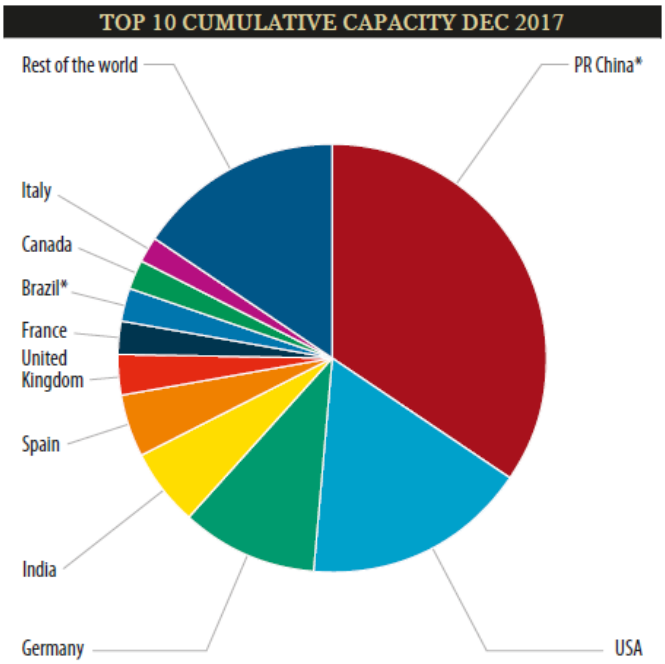

Country	MW	% Share
PR China*	188,232	35
USA	89,077	17
Germany	56,132	10
India	32,848	6
Spain	23,170	4
United Kingdom	18,872	3
France	13,759	3
Brazil*	12,763	2
Canada	12,239	2
Italy	9,479	2
Rest of the world	83,008	15
Total TOP 10	**456,572**	**85**
World Total	**539,581**	**100**

Source: GWEC

Figure 1. 2 Top 10 Cumulative Capacity Dec 2017 (Global Wind Energy Council, 2018)

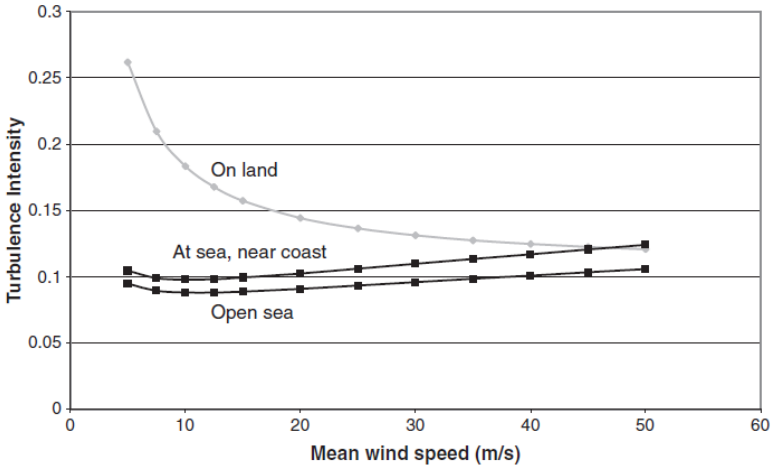

Figure 1. 3 Variation of turbulence intensity with wind speed – onshore and offshore (Burton et al., 2011)

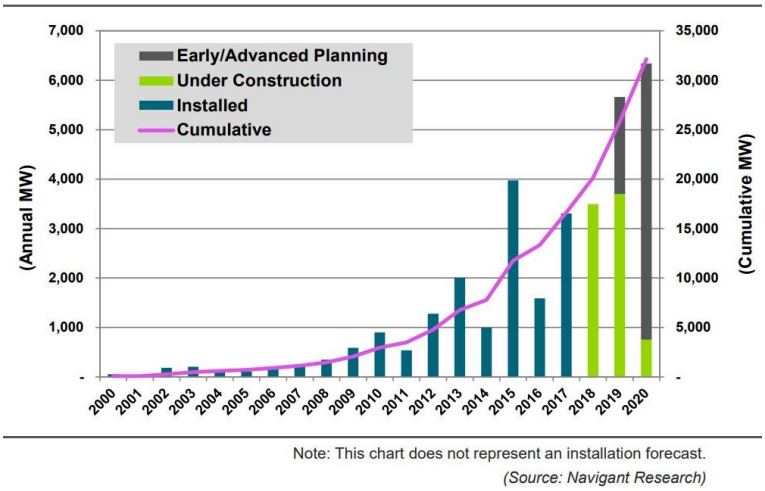

Figure 1. 4 Offshore wind farm capacity worldwide (2000–2020) (Hill, 2018)

According to the water depth of the offshore environment, two types of foundation systems for offshore wind turbines have been proposed -- fixed foundations and floating platforms with mooring systems. For sites near the UK coast, the water depth is usually between 20 to 50 m, and fixed foundations would be the preferred choice due to the lesser cost. However, while the water depth can be up to hundreds of metres on sites further away from the coast and where the wind resources are greater than near shore, floating systems should be used in this condition.

Fixed Foundation

In general, there are four kinds of fixed bottom foundation for offshore wind turbines -- Monopile, Tripod Foundation, Jacket Foundation and Gravity Foundation, as shown in Figure 1. 5. Monopile is one of the favourite choices due to its long history of usage, simplicity in design and suited in shallow water depth. Up to 2015, there are 84 offshore wind farms (including sites under construction) in Europe. In these wind farms, 80% of installed substructures are Monopiles, 9.1% are gravity foundations,

5.4% are jackets foundations and tripods account for 3.6% (EWEA report, 2016). New concepts and designs are being proposed and constructed as the requirement arises, such as full-truss structure and suction bucket.

In March 2016, an offshore wind farm – with eleven 8.4 MW wind turbines, was under construction in Scotland, which is known as the Aberdeen Offshore Wind Farm. The installed total capacity is 93.2 MW. The foundation uses the Suction Bucket (three legged jacket with suction anchor foundations). The water depth range of this site is 20 m to 30 m. The distance from shore is about 2.4 km. With the £300 million investment, this wind farm has start its operation in summer 2018 and can produce 309 GWh annually. In addition, this have reduced CO_2 emission by 132,977 tonnes per year. The project is the Scotland's largest offshore wind farm, and it is a remarkable test and demonstration facility, which can help the industry to reduce the cost of offshore wind production in future product generation (EOWDC, 2018).

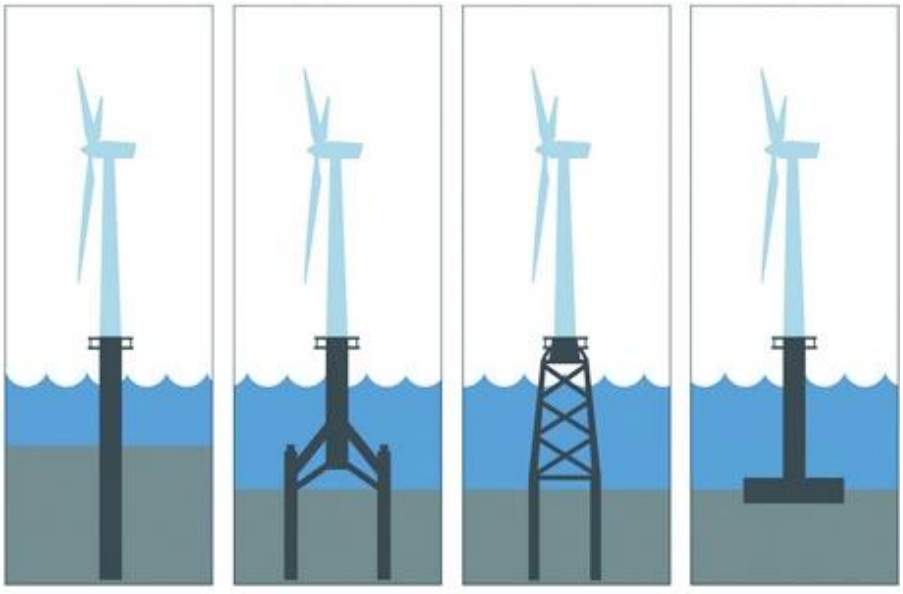

Figure 1. 5 Fixed foundation for offshore wind turbines (from left to right):Monopile, Tripod, Jacket and Gravity Foundation (Czyzewski, 2012)

However, with the development of wind turbine technology, turbine rotors are getting larger to capture more wind energy. For example, the turbine rotor diameter can be up to 130 m for a 5 MW wind turbine. This will cause visual pollution for coastlines. Thus, people are trying to move the offshore wind turbines as far from the land as possible, which means deeper water depth and better wind resource. In this case, the offshore floating wind turbine would be an economic choice.

Floating Platform and its Mooring System

According to the experience from offshore oil and gas industry, there are basically three main categories of floating systems, according to how the concepts achieve basic static stability in pitch and roll for offshore floating wind turbines (OFWT): Mooring Line Stabilised, Buoyancy Stabilised and Ballast Stabilised. Figure 1. 6 shows three representative examples of the floating systems – Spar type floating platform, Tension Leg Platform (TLP) and Barge.

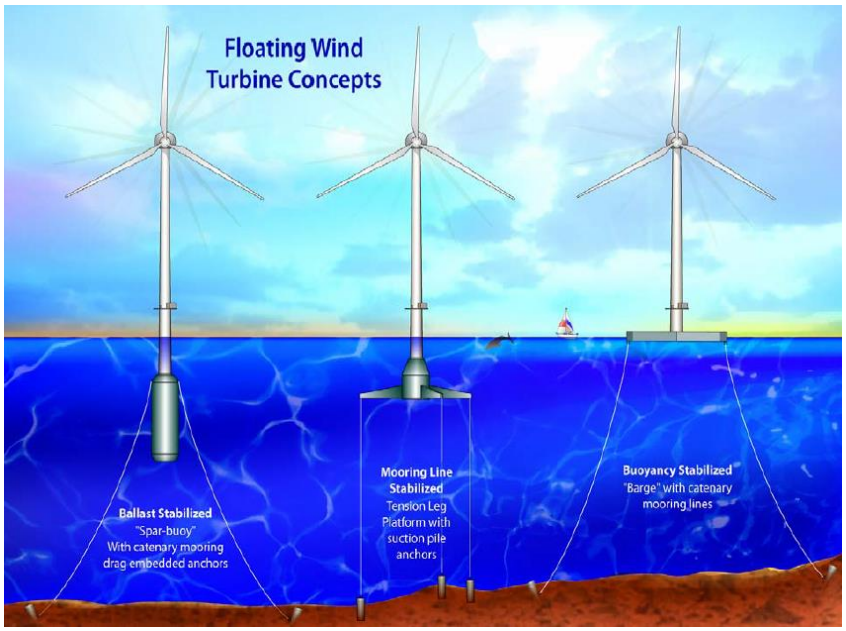

Figure 1. 6 From left to right: Spar, TLP and Barge platform for offshore floating wind turbines (Jonkman et al., 2007)

Normally, a TLP consists of a buoyant platform and taut mooring lines with suction pile anchors. A MIT/NREL (Massachusetts Institute of Technology and National Renewable Energy Laboratory) TLP model was presented by Matha in 2009, for supporting a 5 MW NREL wind turbines. The pitch restoring is mainly provided by its mooring system (Matha, 2009). The TLP, due to its taut mooring systems, is very stiff in pitch and experiences less pitch motion compared to catenary moored systems (such as the spar platform). The TLP is especially suitable for moderately deep water. However, this type of platform will require high sophistication for the mooring and anchoring systems which makes TLP a potentially expensive option.

The barge platform, usually has a simple floating structure with a large water-plane area which can provide sufficient buoyancy for the whole system; it can be anchored to the seabed with catenary moorings or taut vertical mooring lines. The ITI Barge concept was developed by W. Vijfhuizen, supervised by Professor N. Barltrop of the Department of Naval Architecture, Ocean and Marine Engineering at the Universities of Glasgow and Strathclyde, in 2006 (Vijfhuize, 2006). When the platform is displaced in heave, pitch and roll, the barge platform can provide great restoring moments. At the end of April 2018, a 2 MW OFWT with barge type platform has been installed at the coast which is 20 km off the town of Le Croisic, France. This project is known as the Floatgen Project and developed by the Ideol and other 6 partners (Ideol, 2018). Figure 1. 7 shows the image of the barge wind turbine model. The semi-submersible platform works in the similar principal with the barge and an example is shown in Figure 1. 8, which is known as the DeepCwind.

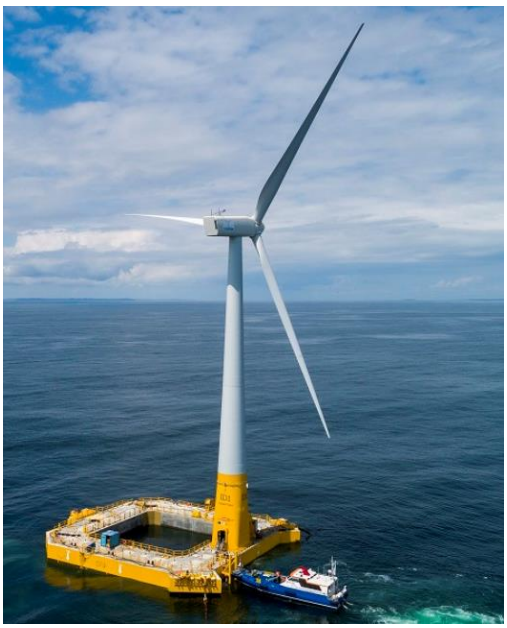

Figure 1. 7 Floatgen Project (Ideol, 2018)

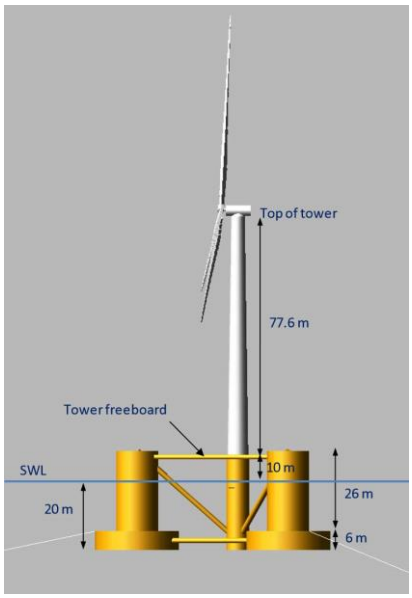

Figure 1. 8 The DeepCwind floating wind turbines (Robertson et al., 2012)

The spar platform is a ballast stabilized substructure for offshore floating wind turbines. It normally consists of a spar buoy and catenary mooring lines. The long cylindrical spar platform achieves stability by using ballast to lower the centre of mass

far below the centre of buoyancy, which creates righting moment and high inertial resistance in pitch (Proskovics, 2015).

In 2009, the world's first large-scale offshore floating wind turbine, which is known as the Statoil Hywind, was installed 10 km off the western coast of Norway. It consists of a 2.3 MW wind turbine with a ballasted steel cylinder which is attached to the seabed with 3 catenary mooring lines. The water depth is about 200 m and the draft of the spar platform is about 100 m. After 8 years of operating, the Statoil Hywind is still working in good condition and survived from 11 m waves in 2010. Consequently, Statoil started to build the world first floating wind farm in 2015, located 29 km off Peterhead, Scotland, and it is operating since October 2017. This project is known as the Hywind Scotland Pilot Park. The total capacity of this floating wind farm is 30 MW, consists of five 6 MW floating wind turbines and can produce power for 85 GW annually.

Based on the Statoil Hywind model, Jason Jonkman from NREL proposed the OC3-Hywind spar floating system to support the NREL 5 MW baseline wind turbine. The draft of the OC3-Hywind spar platform is 120 m. It consists of a 6.5 m diameter cylinder and a 9.4 m cylinder – the two cylinders are connected by a linearly tapered conical region (Jonkman, 2010 a). Figure 1. 9 shows a sketch of the OC3-Hywind model. The detailed parameters of the OC3-Hywind will be presented in Chapter 2. The present research study utilizes the OC3-Hywind model, and will use both numerical and experimental methods to study the properties of the whole floating systems – including the platform and its mooring systems.

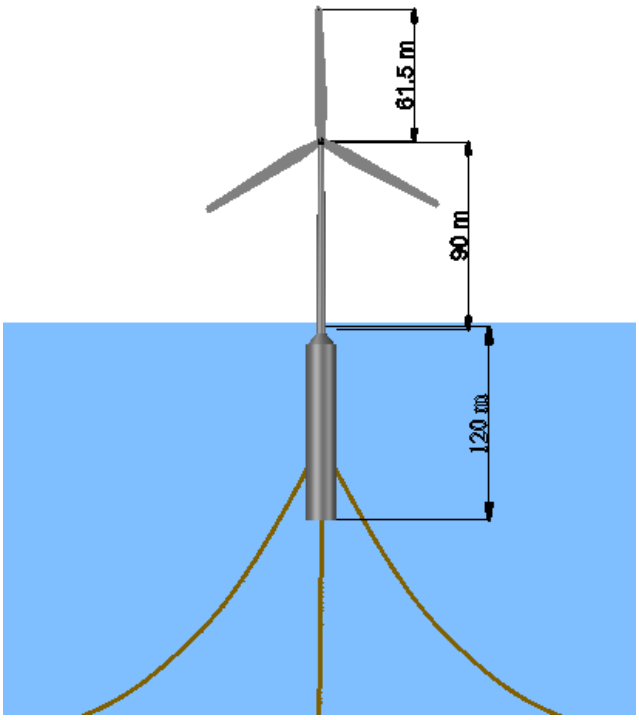

Figure 1. 9 The OC3-Hywind spar-type wind turbine (Xu and Srinil, 2015)

1.2 Objectives of Thesis

Over the last three decades, the technology of wind turbines has been developed tremendously, due to the abundant potential of wind to produce clean energy. The rated power has increased from 50 kW in the 1980s (Myhr et al, 2011) and up to now a prototype of 12 MW wind turbine is supposed to be developed by 2020 (Ambrose, 2018). Nowadays, to make use of the steadier and stronger wind resources at deep water areas compared with onshore resources, engineers have developed and researched offshore floating wind turbines (OFWT). Spar platforms are one favored solution for deep water sites because of their simplicity in design, suitability in modeling and commercialization (Shin, 2011).

However, the interactions between the rotating wind turbine and the support foundation have not yet been completely understood, and the developments of theories and data validations are necessary to advance this knowledge (Koo, et al 2014).

The main aim of this thesis is to reveal the dynamic behavior of the spar type offshore floating wind turbines and, in particular, its mooring systems under various environmental loads by using both experimental and numerical methods. The NREL OC3-Hywind model was chosen and been modified with the tank test conditions.
The specific objectives of this study are:

- Quantify the spar platform (without mooring lines) dynamic responses under various wave loads in both numerical and experimental tests;
- Investigate the spar platform with a certain mooring configuration dynamic behavior under various wave loads in both numerical and experimental tests;
- By using both software and tank tests recordings, predict one of the mooring lines motion under various wave loads;
- Compare the three mooring line tensions measured in the tests with the numerical simulations, and hence explore the ability of the simulation software to correctly predict the mooring line behavior;

A number of case studies will be provided in the following chapters.

1.3 Thesis Structure

This thesis is split into seven chapters. Chapter 1 examines the development of wind energy resources utilisation and the importance and benefit of using offshore floating wind turbines. Chapter 2 presents the technical backgrounds mainly focused on the fluid mechanics and reviews the literature regarding research of offshore floating wind turbines, especially about spar type floating platforms and its mooring systems. The software used in this thesis are being introduced in Chapter 3, with the verification of numerical codes and software used in this study with published data. Chapter 4 presents the physical experiment design and calibration in detail. Chapter 5 shows the tank test results for spar platform only and the comparison with the numerical simulations. Chapter 6 presents the spar platform with realistic mooring lines responses under various wave loads. The platform responses, mooring tensions and one of the mooring line motions recorded in the tank tests are compared with results from the numerical codes. Chapter 7 is the summary of the whole thesis and some suggestions for future research have been pointed out.

Chapter 2 Technical Background and Literature Review

This chapter presents the technical theories relative with this study and an overview of past-published research studies, which are relevant to the present research. The purpose of this chapter is to have a good understanding of technical background, the fluid properties and its effect when passing through a spar type floating platform. The wind turbine and its control systems will be presented first, as the turbine will affect the performance of the floating systems. Then, the technical background will be presented. As introduced in Chapter 1, the main research focus is on spar type floating systems. Then, the review of past research about spar platform will be presented. The mooring system models and their properties are then being reviewed.

2.1 NREL 5 MW Baseline Wind Turbine

As the key component of the whole OFWT systems, the wind turbine extracts the kinetic energy from the wind. The wind passes through the turbine blades and drives the rotor to generate electricity. As the main research focus of this study is the floating system, the NREL 5 MW OC3-Hywind benchmark wind turbine have been chosen as the wind turbine model for the spar type floating systems in the whole study.

Components

Generally, a wind turbine consists of blades, hub and nacelle, drivetrain, control system and the tower as a connection with the platform. Table 2. 1 shows the NREL 5 MW baseline wind turbine's properties and Figure 2. 1 presents the major component

parts of a wind turbine. As can be seen from the table below, this wind turbine is a horizontal upwind turbine with three blades and the rated wind speed is 11.4 m/s.

Table 2. 1 Properties of NREL 5 MW Baseline Wind Turbine (Jonkman et al., 2009)

Parameters	Values/Type	Units
Rating	5	*MW*
Control	Variable speed, Collective Pitch	
Drivetrain	High Speed, Multiple-Stage Gearbox	
Rotor configuration	Upwind, 3 Blades	
Rotor diameter	126.0	*m*
Hub height, diameter	90.0, 3.0	*m*
Cut-in, rated, cut-out wind speed	3.0, 11.4, 25.0	*m/s*
Cut-in, rated rotor speed	6.9, 12.1	*rpm*
Rated tip speed	80.0	*m/s*
Rotor, nacelle, tower mass	110.0, 240.0, 347.5	*tonnes*
Coordinate of overall mass centre	(-0.2 , 0.0, 64.0)	*m*

The control system for this NREL 5 MW wind turbine is a conventional variable-speed, variable blade-pitch-to-feather configuration. When the wind speed is below rated, it controls the power production by using a generator-torque controller to acquire maximize wind energy; when the wind speed is above 11.4 m/s, the power-production will rely on a full-span rotor-collective blade-pitch controller to regulate the generator speed (Jonkman, et al., 2009). When the wind speed is above 25 m/s – the cut-out wind speed, the blade will pitch to feather and park.

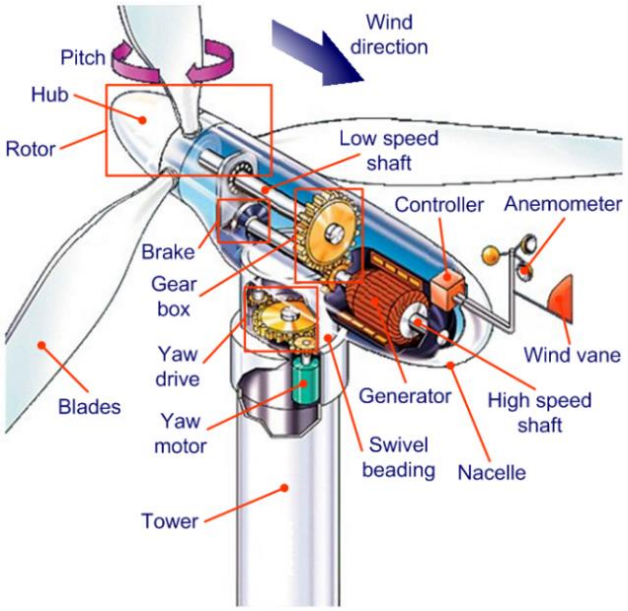

Figure 2. 1 A typical horizontal-axis, three-bladed upwind turbine (Molina et al., 2011)

The Lanchester-Betz Limit

The maximum achievable value of power coefficient is known as the Lanchester-Betz limit, which was published in 1919 by the German physicist Albert Betz. It indicates that no turbine can extract more than 59.3% of the kinetic energy in wind (Burton et al., 2011). This limit is based on an idealized “actuator disk” -- that captures energy from the wind stream, and derived from the principles of conservation of mass and momentum. In practice, some wind turbine models can achieve at peak 75% to 80% of the Lanchester-Betz limit.

2.2 Technical Background

In this study, the main research object is a spar platform – which is essentially a simple cylindrical structure. The flow around a cylinder is a classical topic within hydrodynamics. This section will address the flow pattern around the spar platform

and the influence of the flow on the floating structure and its moorings. The influence of the boundary layer, flow separation, Froude number, Reynolds number, vortex shedding, drag and lift, the Keulegan-Carpenter number and Morison's equation will be discussed. In addition, the scaling issues and influence will be addressed.

Boundary Layer

The boundary layer is the narrow region of fluid next to the surface of the body. Within the boundary layer, there are, basically, two types of flow – laminar flow, in which the flow is in "layers" and each layer slips past the others and turbulent in which the layers of flow "mix" and energy and momentum are interchanged between fluid layers). Although the boundary layer characteristics depend on the incident flow (whether it is laminar or turbulent), there is a short region where the boundary layer flow must be laminar due to the strong viscous effects (where low values of the Reynolds number are found).

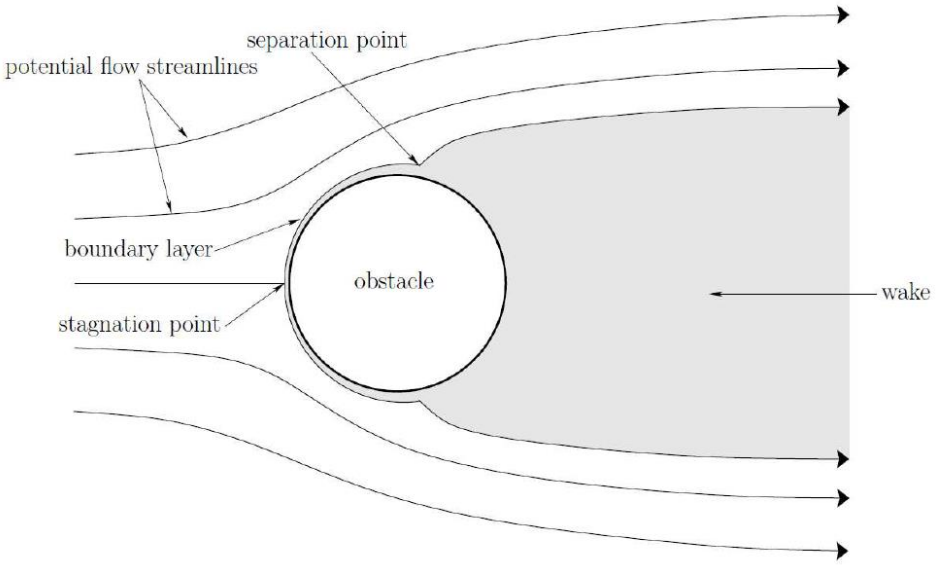

Figure 2. 2 Flow passing through a cylinder (Fitzpatrick, 2012)

Flow Separation

As shown in Figure 2. 2, flow separation happens when the flow speed at the body surface is zero relative to the structure. The separation point is defined as the point between the forward and backward flow, where the shear stress is zero. The overall boundary layer initially thickens suddenly at the separation point and is then forced off the surface by the reversed flow at its bottom. The flow separation will generally result in the increase of drag.

Froude Number

Froude number is a dimensionless number which describes the relationship between inertial and gravitational forces. It forms the basis of a scaling method for physical experiments in water waves in which viscous forces are of lesser importance, as maintaining Froude similarity (i.e. keeping the correct model scale Froude number) will scale the waves and the dynamic behaviour of structures correctly. Thus, Froude scaling is used to conduct the experiment campaign in this study.

It is important to scale the model and environmental conditions as reliably as possible, such that the result is meaningful and helpful for real design and further research. Both Reynolds number and Froude number are important non-dimensional scaling parameters for fluids. However, Reynolds number is normally used to scale flows around models in unbounded fluids dominated by viscous effects, which is not the case in the present experiment. The Froude number, which relates the effect of inertial and gravity forces acting on a fluid, is generally used to maintain similitude for wave basin

tests. By using the Froude number similitude, the governing parameters in wave mechanics and the dynamics of floating structures are well scaled (Chakrabarti, 1994). For this reason, the Froude scaling method will be used for the experiment (detail model parameters can be find in Chapter 4.3), the Froude number (F_r) for a free surface wave is:

$$F_{r_{wave}} = \frac{c}{\sqrt{gl}} \quad (1)$$

Or can be expressed as

$$F_r^2 = \frac{Inertial\ Forces}{Gravitational\ forces} \quad (2)$$

where *c* is wave celerity, *g* is the local gravitational acceleration and *l* is a characteristic length.

Consequently, for a scaling factor - λ, to satisfy both the geometric similarity and the Froude similarity, the scaling relationship between a full scale and a model scale will be:

- Geometric similarity, e.g., length:

$$l_{full\ scale} = \lambda * l_{model} \quad (3)$$

- Froude similarity:

$$F_{r_{full\ scale}} = F_{r_{model}} \quad (4)$$

According to the above discussion, an established scaling factor table for OFWT model test has been generated, as shown in Table 2. 2.

Table 2. 2 Established Scaling Factors for OFWT model test (Rolo, 2014)

Parameter	Unit	Scale Factor
Length (e.g. displacement, wave height and length)	L	λ
Area	L^2	λ^2
Volume	L^3	λ^3
Density	M/L^3	l
Mass	M	λ^3
Time (e.g. wave period)	T	$\lambda^{0.5}$
Frequency (e.g. rotor rotational speed)	T^{-1}	$\lambda^{-0.5}$
Velocity (e.g. wind speed)	LT^{-1}	$\lambda^{0.5}$
Acceleration	LT^{-2}	l
Force	MLT^{-2}	λ^3
Moment (e.g. rotor torque)	ML^2T^{-2}	λ^4
Power	ML^2T^{-3}	$\lambda^{3.5}$
Stress	$ML^{-1}T^{-2}$	λ
Mass moment of inertia	ML^2	λ^5
Area moment of inertia	L^4	λ^4

Reynolds Number

Reynolds number (*Re*) is a dimensionless quantity, which is the ratio of inertial force to viscous force. The Reynolds number can be calculated by the equation shown below:

$$Re = \frac{uX}{v} \qquad (5)$$

where u is the flow speed with respect to the body, X is the characteristic dimension of the body, v is the kinematic viscosity of the fluid.

For fluid dynamics problems in which viscous forces are dominant, and gravitational forces are less important, such as aerodynamic studies, keeping the Reynolds Number constant will ensure that viscous forces are scaled correctly. However, when Froude similarity is adopted, it is not possible to achieve the correct Reynolds Number at model scale, and hence viscous forces will not scale correctly. Ideally the Reynolds number will still take a value at model scale in which viscous drag coefficients are in broadly the correct regime (see Figure 2.3). During the tank tests of this study, the water temperature is around 14 °C, so the kinematic viscosity of fresh water will be $1.169*10^{-6}$ (IAPWS, 2008); hence the *Re* would be more than $3.5*10^{6}$ for the spar platform model, while the full-scale *Re* will be more than $6.*10^{7}$. It can thus be seen that the viscous drag coefficient of the model scale spar will be broadly similar to that of the full-scale platform. However, the diameter of the mooring lines, is very small compared to the spar (0.09 m in full scale and 0.0012 m in test scale) and therefore the Reynolds number would typically be small. As a result, the flow around the mooring lines is a regime in which drag coefficient is sensitive to Reynolds Number. The drag coefficient for the mooring lines will be larger than that for the spar platform, as shown in Figure 2. 3, and since the model scale Reynolds Number of flow past the mooring lines will be small compared to the full-scale case, hence the drag coefficient at model scale is likely to be rather high compared to the full-scale case, leading to higher drag forces on the lines than would be ideal.

Vortex Shedding, Drag and Lift

When the flow passes a cylinder, it will generate a force on it, due to the combination of normal (pressure) and shear (friction) stresses. One is the in-line drag force and the other one is the lift force in transverse direction. For the symmetrical cylinder (such as the spar platform), the lift force would be zero if the flow is also symmetrical.

When $Re > 10^4$, friction drag will contribute less than 2 – 3 % to the total drag force, so it will be ignored in this study, and only the form drag will be considered. The detailed drag coefficient selection is shown in Chapter 3.3.

As shown in Figure 2. 4, at some ranges of Reynolds Number, the wake may become unstable and vortex shedding may start to occur. The forces associated with these vortices dominate the transverse force and could result in the spar platform VIM (vortex induced motion) and the mooring line VIV (vortex induced vibration). However, these phenomena were not observed during the tank tests.

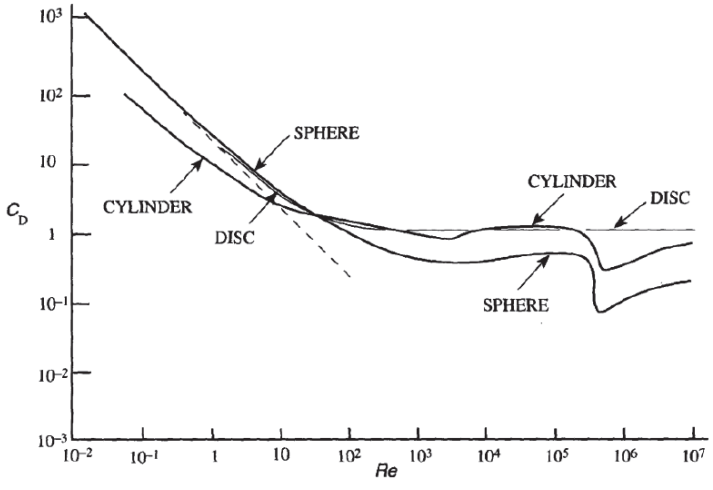

Figure 2. 3 Logarithmic plot of the drag coefficient Cd as a function of Reynolds number Re for cylinders (Caballero et al., 2014)

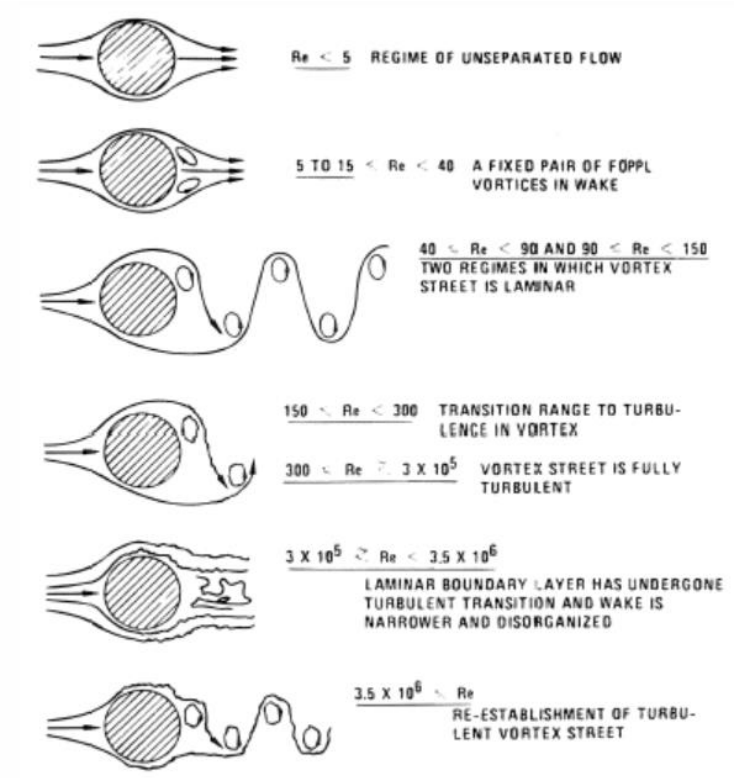

Figure 2. 4 Flow Regimes around a smooth cylinder (Blevins, 1990)

Keulegan-Carpenter number

The Keulegan-Carpenter (KC) number indicates the relative importance between the drag and the inertia forces on floating bodies in oscillating flows. The KC number is defined as:

$$KC = \frac{U * T_{KC}}{D_{KC}} \qquad (6)$$

where U is the amplitude of the oscillating flow velocity (or the amplitude of the oscillating object's velocity), T_{KC} is the oscillation period and D_{KC} is the characteristic length of the object. When the flows are oscillating in a sinusoidal manner, for spar platform, this reduces to

$$KC = \frac{\pi H_\omega}{D_s} \qquad (7)$$

where D_s is the spar diameter and H_ω is the wave height. When $KC > 2$, flow separation is likely to occur which will typically lead to increased drag.

the KC number for OC3-Hywind spar model along its depth in different sea states have been presented by Jonkman, (2010 a), as shown in Figure 2. 5. The Sea State 5 to Sea State 8 in the figure refers to the sea states numbered from 1 to 4 in this study (details can be found in Table 4. 8). It shows that for Sea State 2 to Sea State 4 in this study, the flow separation happens at the free surface, while in the smaller waves the flow is expected to remain attached. It may be concluded that in the small regular waves and Sea State 1 in the present study, it is the inertia force dominate for spar platform while in the larger irregular waves the drag forces will show more effect, and the response will be expected to be more non-linear. It can also be seen from the figure that the KC number reduces significantly over the depth of the platform, which is due to the wave particle motions reducing with the water depth.

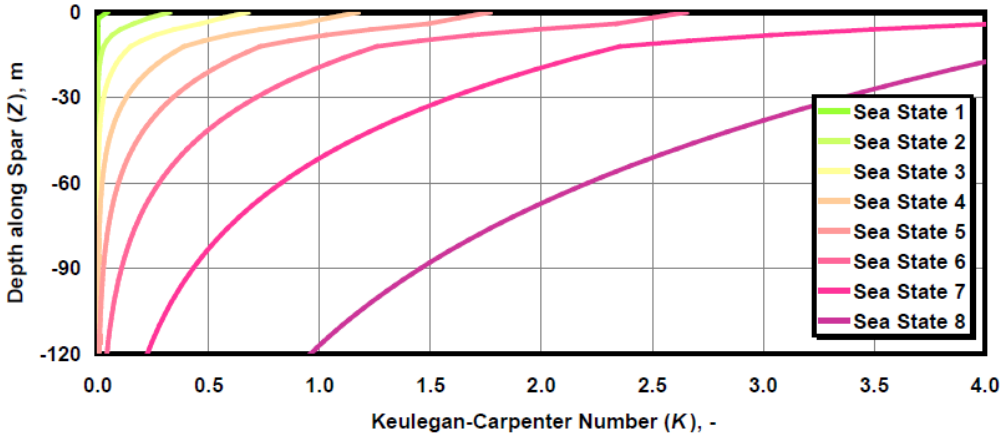

Figure 2. 5 KC number for OC3-Hywind (Jonkman, 2010 a)

Morison's Equation

Morison's equation is often used to calculate the hydrodynamic forces on a floating structure (both platforms and mooring lines) when the dimension of the structure (length or diameter) is much less than the wave length. It turns out to be very accurate when the ratio between the platform diameter and wave length is less than 0.2, when forces due to diffraction are negligible. Figure 2. 6 shows this ratio of OC3-Hywind model under the 4 sea states covered in this study – Sea State 5 to Sea State 8 in the figure, and other moderate sea states, which show that Morison's equation is applicable to most of the cases. It can be seen that for all the sea states in this study, the body diameter to wavelength are smaller than 0.2 and hence the diffraction forces can be ignored in this study.

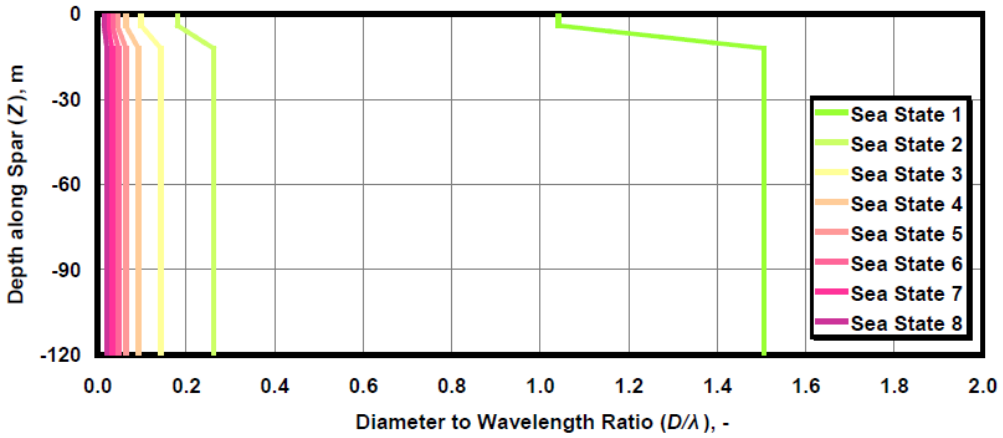

Figure 2. 6 Diameter to wavelength ratio for OC3-Hywind (Jonkman, 2010 a)

The Morison's equation can be used to calculate the forces due to flow passing a slender body, as shown below:

$$F_w = (\Delta * a_w + C_a * \Delta * a_r) + \frac{1}{2}\rho * Cd * A_d * V_r * |V_r| \qquad (8)$$

where F_w is the fluid force, Δ is the mass of fluid displaced by the body, a_w is the fluid acceleration relative to earth, C_a is the added-mass coefficient for the body, a_r is the fluid acceleration relative to the body, ρ is the density of fluid, Cd is the drag coefficient for the body, A_d is the drag area and V_r is the fluid velocity relative to the body. The selection of the value for $C_a$and Cd will be discussed in detail in Chapter 3.3.

As shown in the equation above, the Morison's equation is composed of two parts – the inertia force and the drag force. In this study, the movement of the platform (and mooring lines) and its interactions with waves should be considered. Therefore, the inertia force will be consisting of two parts, one proportional to fluid acceleration relative to earth, i.e. which is known as the Froude-Krylov component, and one proportional to fluid acceleration relative to the body, i.e. the added mass component. As discussed in the KC number part, in most moderate sea states, the inertia term will dominate and for the extreme sea states the drag term will dominate. It should be noted that, Morison's equation uses a constant drag coefficient in the calculation, so it can predict the mean drag value, but cannot capture some unsteady effects, such as those due to vortex shedding. Nonetheless, Morison's equation is known to predict good results in many cases for fluid loading in uni-directional waves, which are used in this study. As shown in detail in Chapter 3.2, the software used in this study, using versions of the Morison's equation, should in principle be appropriate for predicting the platform performance.

Scaling Issues and Influence

During tank tests, the scaled model should be designed to match the full scale model in terms of global properties, such as the mass, COG, and the inertia, etc., (Ruzzo, 2018). In this thesis, the global properties of the tank test model (both spar and mooring lines) have been scaled using the Froude number and the mass and inertia properties are matching well with the full scale model used in numerical simulations (as shown in detail in Chapter 4.3). However, as discussed before, the mooring line drag properties are likely to be affected by the model-scale Reynolds number. Therefore, the mooring line drag characteristics cannot be modelled correctly under the Froude scaling.

2.3 Review of Research on Dynamic Behavior OFWT

Spar platforms are favoured in deep water because of their simplicity in design, modelling and propinquity to commercialization (Xu and Srinil 2015). In order to accelerate the commercialization of the spar type OFWT, researchers and engineers have carried out many investigations and achieved many breakthroughs on it in the past decades.

The world's first full-scale OFWT is the Hywind Demo, with a capacity of 2.3 MW, which is a spar type OFWT developed by Statoil. This design was idealised by the NREL as the OC3-Hywind. It has been installed and commissioned in Norway in 2009, located 10-km west of the island of Karmøy off the Norwegian west coast, where the water depth is 220 m. This project proved the suitability of the spar type platform for conventional multi-megawatt turbines (Driscoll et al, 2016).

The investigation of spar type floating offshore wind turbine can be classified into two categories in the literature, which are experimental test and numerical modelling. Both of them have been adopted for the present study. In the following sections. Past studies have been reviewed and gaps have been identified on both the experimental and numerical investigations of the OFWT, respectively.

Experimental Study on the OFWT

The earliest tank test of a 5 MW spar type OFWT (the Hywind model) was conducted by Skaare et al, in 2007 at a linear scale of 1:47 using Froude scaling. Both the irregular wave and wave load were investigated, but the focus was on the comparison with a numerical soft code (SIMO/REFLEX) and platform dynamic characteristic was not presented (Nielsen et al, 2006). This, however, still provides a reference scaling ratio model tests on the Hywind model.

Utsunomiya et al. (2009) have conducted an experiment for a spar-type floating platform with 60 m draft and a 2MW wind turbine under both regular/ irregular waves and steady wind load (scale factor 1:22.5). The experimental results were compared with their numerical simulations to verify the numerical codes (mainly based on Morison's Equation). Reasonable agreement was achieved but the damping force evaluations needed further improvement. They then developed a 2 MW wind turbine with 70 m draft spar platform and a 1:10 model has been made, to conduct at-sea experiment, where the wind speed/ direction, tidal height, wave height, motion of the spar platform, mooring tension and strains in the tower/spar platform have been measured. Their platform is designed as a hybrid structure, where the upper part is

constructed of steel and the lower part is pre-stressed concrete. This provides a good preliminary concept model for further design of offshore wind turbines (Utsunomiya et al., 2013 a). This hybrid-spar had also survived during the Typhoon Sanba, where the average wind speed at the hub height was 48.3 m/s, which verifies the safety of the structure (Ishida et al., 2013). The author also developed numerical tools to compare the simulation results with the at-sea measurement. Their dynamic mass-spring model for mooring lines show better agreement with the experimental measured values than the quasi-static catenary mooring model. The standard deviations of yaw responses were overestimated by the numerical tools in standard deviations but the mean values agreed well (Utsunomiya et al., 2013 b). In the at-sea experiment, Utsunomiya group used a 100 kW wind turbine on top of the hybrid-spar, and the platform responses were investigated when the turbine was operating, where they found the mean pitch responses was insignificant with the effect of turbulence intensities, but the standard deviation of the roll/pitch responses was significant (Utsunomiya et al., 2014). In 2015, they published the design methodology for hybrid spar which includes the environmental design conditions, design load cases, dynamic and fatigue analysis; the installation procedure was also presented, where they consider the spar as a simple one-dimensional structure. However, they also pointed out that further studies are needed to reduce the cost for commercial application (Utsunomiya et al., 2015).

The most recent open-sea experiments on spar type OFWT is conducted by Ruzzo et al. (2018), and they used a 1:30 scale model of the OC3-Hywind. The experiments site is located in the sea front of Reggio Calabria (Italy). The intermediate-scale, open-sea experiment can help to overcome some limitations of small scale models, such as the

limitation of experiment durations and the scale effects. However, the open-sea wave frequencies may not able to cover the complete frequency range of the platform motions, but, in their studies, the roll/heave/pitch motions can be captured.

The research group in University of Ulsan have also done experiment studies on the OC3-Hywind model, with scaling factor 1:128. In 2011, Shin conducted a model tests to investigate the OC3-Hywind platform motion characteristics (Shin, 2011). They then developed three new spar platforms with the same mass and volume of the OC3-Hywind but different body shapes (as shown in Figure 2. 7), and carried out the model tests still with the scale 1:128. Both the wave and wind (with operating turbine) were tested, and the platform motion RAOs and maximum motion were presented. By adding the ring cylinders on the spar platform, they found that the added mass and damping has increased which resulted in the motion period increase and decrease in platform motion amplitude. They pointed out that the M3 model (as shown in Figure 2. 7) could be good to survive in extreme weather (Shin et al., 2013). However, their rotor was scaled with the Froude method, which means the aerodynamic characteristics may not be captured accurately and thus the platform responses presented may not be precisely represented. The 1:128 OC3-Hywind tank test model has also been used to validate their in-house code and a numerical software – FAST v8. The platform six DOFs/ mooring tensions (only mooring line 3 results were presented) under both regular and irregular wave with wind load are been tested. They suggested that for a coupled wind and wave tank test for floating wind turbines, when Froude scaling method were used, the blade geometry should be designed for a low Reynolds number environment. In sea state 7 (Tp=13.6, Hs=9.14), a strong nonlinearity in surge have

been noticed in experiment (Ahn et al., 2017). The tank tests of Shin's group had inspired this study, and most of the wave profile in their papers have been included in this thesis.

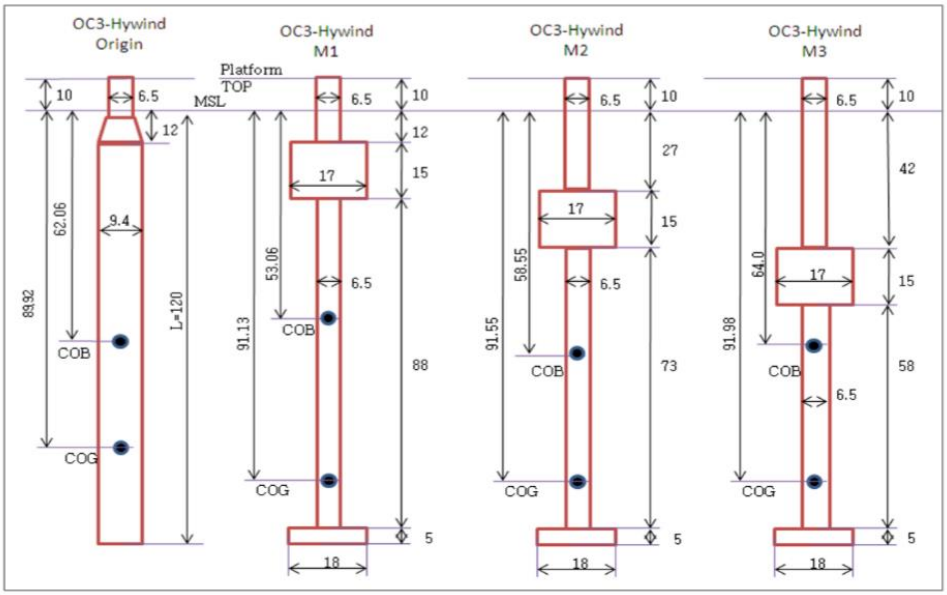

Figure 2. 7 Three new platforms in comparison with Oc3-Hywind spar (Shin et al., 2013)

Apart from the investigations of the platform six DOFs characteristics, some other tank tests have also been carried out to study different platform design or with different mooring systems. Such as, Seebai et al. (2009) have installed a squared plate under the bottom of the spar platform and conducted tank tests (scale factor 1:100) to investigate the effect of taut and catenary mooring, under both regular and irregular waves. The results show that both the horizontal and vertical acceleration RAO are greater with the catenary mooring than the taut mooring model. The heave shows reduced response due to the increased damping caused by the plate under the spar platform bottom. Myhr et al. (2011) have compared the Tension-Leg-Buoy (TLB) with the OC3-Hywind Spar-Buoy (SB) properties by conducting the experiment (scale factor 1:100) and compared

with numerical simulations (3Dfloat and ANSYS). They found that the TLB shows smaller motions and higher anchor load than the SB in both experiment and software, which is due to the taut mooring taking the loads directly to its anchors and restricting motions. Goupee et al. (2012) have also conducted tank tests to compare the TLP, spar and semi-submersible properties with the NREL 5 MW baseline wind turbine (scale factor 1:50). The floating systems are under both regular and irregular sea states, with static or dynamics winds in both operational and extreme conditions. The experiment data can be used to develop the analysis tools for the floater and wind turbine coupled response and also can validate the FAST code. They found that the surge response for spar-buoy based systems are not affected in any significant way by the presence of an operating wind turbine subjected to winds. However, for the spar-buoy, the pitch motion can create larger bending moments than a TLP, which means that the pitch motion is quite critical for spar type OFWT. Also, when in the low energy sea states, it is the significant energy at the platform pitch natural frequencies of the systems affect the bending moment response, while the dynamics of the three platforms will be controlled by the wave energy frequency response for larger sea state. Ramachandran et al. (2013) have compared the RAOs for OFWT by using WAMIT (a linear frequency-domain potential flow hydrodynamics solver) with FAST, based on white noise wave with 2 m significant wave height. The RAOs were checked with no wind load with rigid floating wind turbine, operational and flexible wind turbine with below-rated, rated and above rated wind conditions. The purpose is to understand the effects of structural flexibility, aerodynamic damping, control actions and waves on the system responses. It is found that the aerodynamic damping can decrease the platform surge and pitch responses and the gyroscopic excitation can increase the yaw response.

However, in their study, the platform viscous drag coefficient is neglected. Another experiment has conducted by Sethuraman et al. (2013) (scale factor 1:100) to investigate the hydrodynamic responses of a floating spar (with four mooring lines) wind turbine under regular/irregular waves, and the results have been compared with the OrcaFlex. The four-point mooring lines system is found can reduce the surge motion significantly and can keep the yaw motion at acceptable levels.

The research group in Shanghai Jiaotong University - Duan et al. (2015) have investigated the isolated wind/wave effects and the integrated wave-wind effects on the OC3-Hywind floating systems by conducting the model test (scale factor 1:50). They then (Duan et al. 2016 a) have conducted a model test on the OC3-Hywind spar-type floating platform, by using two different rotor systems under both wind and wave load conditions to investigate the floating system response behaviours. The gyroscopic effects from the rotor rotation resulted in yaw decays and strong coupling effect between surge and pitch, and the heave motions were quite independent. In addition, they found that the wind load can restrain the platform decay motions at natural frequencies. The mooring tensions were also being checked which is found mainly to be affected by the environmental loads.

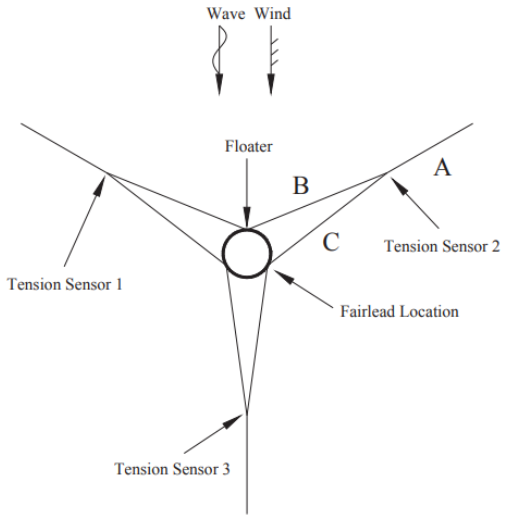

Figure 2. 8 Test model by Duan et al (2016 b)

Duan et al. (2016 b) have conducted another model test for the OC3-Hywind model to check the floating system dynamic responses, as shown in Figure 2. 8. The calibration tests included the characterized stiffness of the delta type mooring system and free decay responses. It is found that the wind loads have obvious influence on surge, heave and pitch motions of the spar type floating wind turbine. Similarly, to their previous study, the mooring tensions measured from the experiment were found to be affected by either the wave or wind-wave excited surge/pitch and heave coupling and it was found that the wind loads can have a clear influence on the dynamic responses of the mooring system. It is also found that the aerodynamic loads can somewhat reduce the floating system peak response amplitudes, which could be beneficial for extending the fatigue life of the mooring system.

Tomasicchio et al. (2018) have also used a Froude scaled model to conduct tank tests of an OFWT. They presented a very detailed literature review about the experiment on

OFWT, and they have pointed out the major difficulties on conducting wave-basin experiments of OFWTs. They had also investigated the hydrodynamic and dynamic behaviour of the platform and the interactions with the mooring system.

To summarise, many experiments have been conducted by researchers in the past decades to investigate the characteristics of OC3-Hywind and other spar type platforms; the scaling factor ranged from 1:128 up to 1:10, and the minimum scale factor for the OC3-Hywind model is 1:30. It is seen that most of the studies are focused on the platform motions or the mooring tensions, but there has been little or no research on the detailed mooring line motion. The mooring line motion, is coupled with platform motion, and thus can also show the coupling effect with the operating turbines, so it is very important to study the mooring line motion behaviours. Consequently, in this study, the one of the mooring line motions will be investigated in the tank tests, and then compared with the validated numerical codes.

Numerical Study on the OFWT

Numerical simulation has several advantages compared with experimental tests, especially for complicated systems such as floating wind turbines. There are several codes, either open-source or commercial, for the simulation of floating offshore wind turbines. These include FAST (Fatigue, Aerodynamics, Structures, and Turbulence), an open-source code developed by NREL, which is one of the most advanced codes specialized in floating/fixed horizontal-axis wind turbines. FAST is widely used by both academic and industrial researchers to investigate the properties or evaluate the

design of floating wind turbines. Many past publications have confirmed the successful use of FAST in their research on floating wind turbines.

Wayman et al. (2006) have used FAST to investigate the interactions between the wind turbine and the floating system (a Shallow Drafted Barge, i.e. SDB, and TLP), including the gyroscopic loads of the wind turbine, the aerodynamic damping caused by the rotor, and hydrodynamic damping introduced by wave-body interactions and the wave excited hydrodynamic forces. Then, Jonkman et al. (2010 b) compared the OC3-Hywind model responses in different computer codes, including FAST, to understand offshore floating wind turbine dynamics and modelling techniques better. Yu et al. (2015) have also used the FAST code in the time domain and FFT method for the frequency analysis to investigate the hydrodynamic properties and mooring loads of the OC3-Hywind system under various sea states with both wind and wave loads. The gyroscopic effect caused by the rotor was found to induce a strong nonlinearity for the system and resulted large yaw motion. The surge and pitch coupling effect were observed and the mooring line loads mainly affected by the surge displacement, while the surge motion is mainly varied with the wind load. They also found that the surge and pitch responses can be influenced more with low-frequency excitation loads, especially around their natural frequencies, while only small responses were found with the wave frequencies. Their results also indicate that the large displacement in surge direction can cause the risk of failure on the mooring line align with the surge motion direction.

The results of FAST code have also been compared with the results of tank tests, as mentioned in the literature review about the experiments, and most of the dynamic responses of the platform predicted in FAST show comparable results with tank test data. Many challenges are found in the modelling of mooring systems for OFWTs, including the stability of light-weight minimalistic platforms and shallow water depths, etc. The extreme tension in mooring lines of a light displacement platform in shallow-water is dominated by snap loads, which is due to the light pre-tension requirements in the line may be insufficient to prevent the mooring lines from being exposed to wave motion-induced slack and shock events. There is a need to capture and investigate this phenomenon using numerical tools. The built-in mooring line model in FAST, like other floating wind turbine simulation codes, is a quasi-static approximation. This mooring line model is straight-forward on coding and does not need large computational resources on predicting the mooring motion, but it neglects mooring line inertia and hydrodynamics which will tend to under predict the mooring tensions and the effect of slow varying motions. Many researchers have tried to enhance the accuracy of the mooring line model in FAST in different ways.

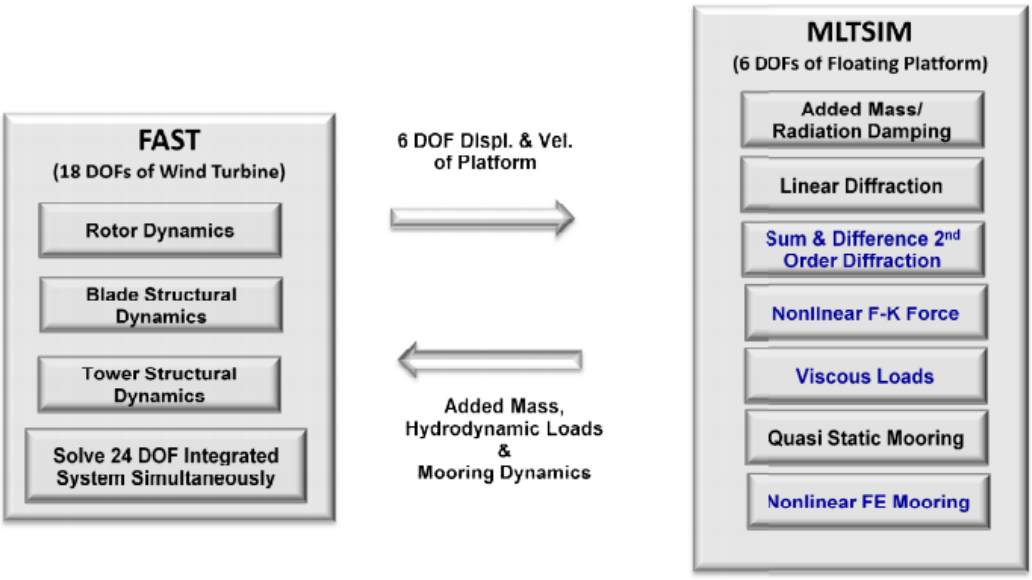

Figure 2. 9 MILTSIM-FAST flow chart by Koo et al. (2014)

Hall et al. (2011) have modified the FAST code with the use of an alternative, fully dynamic mooring model based on the hydrodynamics simulator ProteusDS and compared with the FAST built-in quasi-static mooring model. The OC3-Hywind model has been implemented in this study. The overall platform damping in translations DOFs during platform decay tests in still water has been observed significantly in the dynamic mooring model. Among all the tests, it is shown that only when the platform motions and wave velocities are not synchronized that the damping from the dynamic mooring model makes a large difference. However, the irregular wave tests were missed in their research. Karimirad (2013) have conducted numerical modelling with a catenary moored spar type OFWT by using different hydrodynamic models based on the Morison formula, Pressure integration method and Panel method considering the mean drift, first and second-order forces. It is found that the damping and inertia forces of the mooring lines have important effect on the tension responses.

Also, the mooring line damping can help to damp out the high-frequency elastic-deformations of the mooring system, while the platform motions are not affected obviously by this mooring line damping effects. However, the heave responses have been affected more by the drift and second-order forces, while the motion and tensions do not show such effects. Koo et al. (2014) have found that the quasi-static mooring analysis tends to under predict the mooring tensions and slow varying motions of the DeepCwind semi-submersible wind turbine, so they have conducted the experiment to validate their numerical code – MILTSIM-FAST, as shown in Figure 2. 9. Their research shows that platform and mooring coupling can be observed quite obviously in the tank tests and matched well with the numerical code. Also, their code can capture both low frequency and wave frequency of the catenary mooring line dynamics behaviour correctly.

Peng et al. (2014) have developed a code named COUPLE and integrated with FAST to conduct the coupled numerical analysis of an OFWT – the OC3-Hywind. Different wave/wind directions (the wind and wave come towards the same direction) and wind speeds have been applied to the spar model in this numerical code. Their results show that the surge motion and mooring line tensions are related to the wave/wind directions. When the wind/wave direction is coming towards one of the mooring lines, the surge motion amplitude is the smallest while the mooring line reaches the highest tension, and feature might be important for the design of mooring systems. In addition, when the wind speed is at the turbine's rated wind speed, the platform shows the largest responses, which is due to the blade-pitch-control of the wind turbine. They have also

found that the blade pitch under higher wind speeds can reduce the wind forces on the OFWT and result in lower platform motions.

Apart from the researchers who developed in-house codes, there is an alternative way to replace the built-in quasi-static mooring model in FAST, which is to use an existing commercial code to couple with FAST. Masciola et al. (2013) studied the influence of the dynamic mooring line on the response of a coupled model of an offshore floating wind turbine (semi-submersible) compared with an equivalent uncoupled model (with quasi-static mooring model). FAST and OrcaFlex have been used to carry out the study. In OrcaFlex, the mooring line is represented as a lumped-mass cable system to capture the mooring line dynamics, as opposed to the quasi-static mooring model in FAST. It is concluded that the uncoupled model using the quasi-static mooring approximation can underestimate peak mooring line loads compared to a coupled model using a dynamic mooring line. They also showed that the surge and heave for a semi-submersible are not influenced too much by the mooring line dynamics, but that the tension could be significant when under extreme sea-states. The snap loads occur in the coupled and uncoupled models can result in different platform responses. A snap load results in a large force being applied to the platform due to rapid cable re-tensioning, which explains the large differences between the coupled and uncoupled models in regions near snap loads.

Hsu et al. (2015) used the OrcaFlex and FAST (i.e. FASTlink) to examine the hydrodynamic behaviour of both the platform (semi-submersible) and mooring system and the results are compared with tank test data. The snap loads which have been

observed from both numerical simulations and tank tests are one of the main factors to cause mooring failure. The snap load frequency and magnitude have been analyzed with a probabilistic approach. Both the test data and FASTlink show snap loads occurring with wave period in the range of 7.5 to 10.5 seconds; while FASTLink prediction also showed snap loads for periods between 10 and 10.5 seconds which were not seen in the experiment results. This snap load is quite similar to the nonlinear mooring line behaviour discovered in this study, which will be presented in detail in Chapter 6.

Apart from the numerical studies based on the FAST code, some other software, such as SESAM have been used to investigate the platform and mooring systems dynamic performance. Zhao et al. (2012) have introduced a numerical model to simulate the dynamic behaviour of a new semi-submersible type offshore floating wind turbine system in the frequency domain. It is important to capture correct performance of motion and mooring system dynamics for the design of a cost-effective and durable floating platform. The hydrodynamics of the platform and mooring system dynamics were calculated by SESAM and the results show that SESAM could be used as an effective tool for the analysis of offshore floating wind turbines, but the aerodynamic coupling may not be as good as FAST. Brommundt et al. (2012) have developed a tool for the optimization analysis of catenary mooring system for offshore floating wind turbines with a semi-submersible support structure. The linear response of the platform was calculated from the frequency domain. The model has been analyzed at two sites in the North Sea, with different water depths and distinct directionality of environmental loads, and they pointed out that the spectral wind loads should be taken

into consideration when designing mooring systems for offshore floating wind turbines. Utsunomiya et al. (2019) have compared their in-house code with their hybrid-spar model at-sea experiment, where the turbine is considered in operating condition, but only power generation performance and platform pitch responses has been presented and no mooring research been given.

Since it can theoretically give a more accurate prediction of the tension/motion of the mooring system and does not required intensive code development/maintenance, the coupling of the OrcaFlex and FAST (i.e. FASTlink) shows a great potential on the investigation and design of the floating offshore wind turbine in both academic and industrial filed. There is a need to validate this coupling code to confirm its accuracy. Masciola et al. (2011) have compared the OC3-Hywind model behaviour in FAST with the FASTlink. Their results show the FASTlink predicted higher tensions (about 5%) than FAST, and this difference is expected due to the different models in the two software packages. Also, they show that the FASTlink can predict reasonable results for the combination of aerodynamic and hydrodynamic analysis and it can be used to build a high-fidelity offshore wind turbine model. However, their results had not been validated with experiment.

It can be seen that most of the numerical studies used FAST itself or FAST with OrcaFlex only (or some in-house code) to investigate the platform dynamic behaviours, but there has been no study, on the OC3-Hywind model, so far, which had validated the FASTlink (FAST+OrcaFlex) results with experiment data. Hence, in this study, the capability of the FASTlink software will be investigated. In addition, as

FASTlink can output the mooring line motions, this will also be validated with experiment results.

2.4 Summary

In this chapter, the technical theories and published literatures related to the spar type offshore floating wind turbines and its mooring systems have been presented. To this end, the following gaps on the investigation of the spar type offshore floating wind turbine is identified:

1. Many researchers investigated the platform and/or turbine part of the floating turbine system either by numerical simulation or by experiment, but there is not any experimental study focused on the mooring line motions of the system, especially for the long draft spar-type platform.

2. The state-of-the-art of the offshore floating wind turbine modelling tool, FASTlink, need to be verified by experimental results to check its usability and accuracy.

Therefore, this thesis is aimed to bridge the above gaps for the spar type offshore floating wind turbine. An experiment has been carried out on the mooring line motions and tensions of the offshore floating wind turbine and reported in the following chapters. The FASTlink simulation results have also compared with the experimental data as a usability and accuracy check. The outcomes and conclusions of this thesis will also act as a guidance on the OFWT design, especially on the mooring line design and maintenance for the industrial field.

Chapter 3 Numerical Methodology and Code Verification

3.1 Introduction

The numerical software used in this study will be introduced in this part. To demonstrate that the numerical code can generate results comparable with other research, the verification process will also be presented in this part. The model used is the NREL OC3-Hywind spar model. The data generated from the FASTlink and FAST software used in this study will be compared with NREL published data using FAST simulations. A free decay tests will be checked first to ensure the natural frequencies and the damping matrix are consistent. Then, since this study focusses on the analysis of mooring lines, a one-dimensional load-displacement verification for the mooring systems will be presented.

3.2 FAST and FASTlink

Two numerical software packages have mainly been used in this study, FAST and FASTlink (FAST + OrcaFlex). The detailed information about the two numerical codes will be given below.

FAST

FAST is a comprehensive time domain aero-hydro-servo-elastic tool for modelling and analyzing of land-based and offshore wind turbines. The maximum simulation running time is up to 9999 seconds –about 2 hours and 40 mins. It is recommended by the ITTC (Stansberg et al., 2002) to form up a full storm in offshore engineering tests. Although the software running time is a bit of less than the 3 hours, but it will be

running the same time duration with the scaled tank tests, so the results should still be acceptable and comparable. FAST has being kept updated and for this study, the most up to date Version 8 has been used. The program structure is show in Figure 3. 1, see e.g. Barahona et al. (2015).

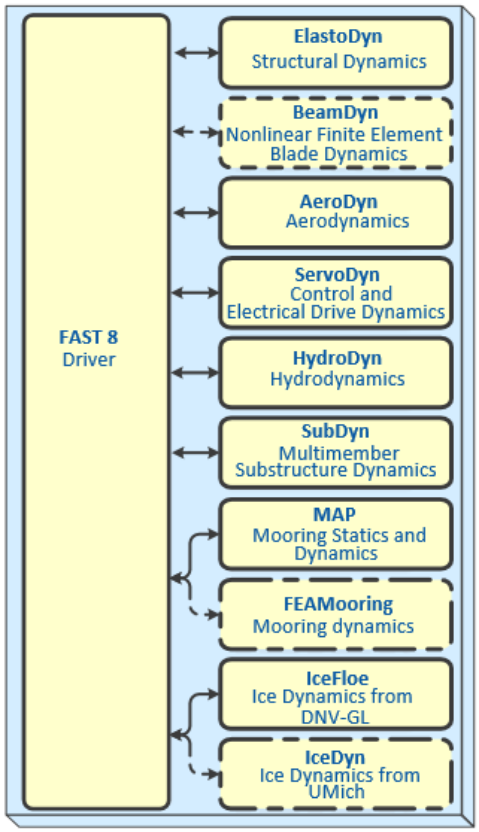

Figure 3. 1 FAST Version 8 modularization framework (Barahona et al, 2015)

Normally, to run the aero-hydro-servo-elastic simulation for an OFWT, the ElastoDyn, AeroDyn, BeamDyn, ServoDyn, HydroDyn and MAP modules will be employed, and if the ice load been considered, the IceDyn and IceFloe should also be used. In this study, the aerodynamic and ice loads are not being considered, so only the setup of ElastoDyn, HydroDyn and MAP will be discussed in detail. The AeroDyn and

ServoDyn will still be used to setup the OFWT model structure, but the turbine will not operate in the simulations and there will be no wind load.

AeroDyn

In AeroDyn, the user will need to input the name list of the airfoils data file, where appropriate, to define the blade geometry and aerodynamic properties. The air density/kinematic viscosity should also be input here. An additional InflowWind file will be needed to define the pass by wind load (the wind file can either be uniform or turbulent). To calculate the aerodynamics of the wind turbine, BEM theory and Momentum theory are used. The Blade Element theory assumed that the blades can be calculated by dividing each blade into small elements, which act independently and operate as two-dimensional aerofoils. Then the total forces are summed along the span of the blade and moments exerted on the turbine. In the Momentum theory, the induced velocities from the momentum lost in the wind flow in the axial and tangential directions can be calculated.

As there is no wind load been studied in this thesis, the AeroDyn relevant data files are only used to represent the geometry and mass properties of the wind turbine.

ServoDyn

The ServoDyn is to define the wind turbine's control system. It provides choices includes Pitch Control, Generator and Torque Control and Simple Variable-Speed Control, etc. There is also an option for "user-defined" control system. As the turbine

is not operating in this study, so the default NREL control system has been used in this thesis.

ElastroDyn

In the ElastroDyn module, the 16 DOFs of the whole system is defined to be "open" (True) or "close" (False), such as the 6 DOFs of the platform are defined as "True" so that the dynamic properties of the platform can be simulated; the Generator DOF is turned off, as there is no wind load and the rotor is considered as parked condition in this study. The Initial Conditions need to be set up before running each simulation. For example, as shown in Chapter 3.4, for the surge free decay simulations, an initial displacement of surge will be given, and then the damped curve of surge motion time history can be obtained from the Output file. In this module, the Turbine Configuration is also need to be set up, such as the number of the blades, the turbine diameter, the tower height, etc. The Mass and Inertia should then be set up, such as the hub mass/inertia, nacelle mass/inertia, platform mass/inertia, etc. The blades data/tower file (where the blade/tower parameters and properties are defined) and the nodes used for analysis are also linked and setup here. The Drivetrain properties - when the simulation needs to consider working turbine condition, is also set up in this module, defining parameters such as the gearbox efficiency, etc. Also, the Output channel should be defined before finishing this part's set up, such as each DOF of the platform motion, etc.

HydroDyn

In HydroDyn, the hydrodynamic forces for OFWT (and also fixed platform) are calculated. It mainly uses the potential flow theory or the strip theory to get the solutions, and these two theories can also be combined. The linear wave (linear Stokes wave) theory has been employed in the HydroDyn to simulate the waves.

The fluid density, water depth, the wave profile, current (which is not been considered in this study), the floating platform potential-flow model (in this study, the spar platform hydrodynamic properties is calculated by WAMIT) and the drag forces are calculated by using the Morison's equation. The platform geometry/hydrodynamic coefficients/displaced volume, each DOF force flags (to define which DOFs of force are included in the calculations), and any additional stiffness/damping on the platform are all set up in this part. Also, the output channel can be defined, such as the wave elevation, etc. Figure 3. 2 shows the calculation procedure of HydroDyn.

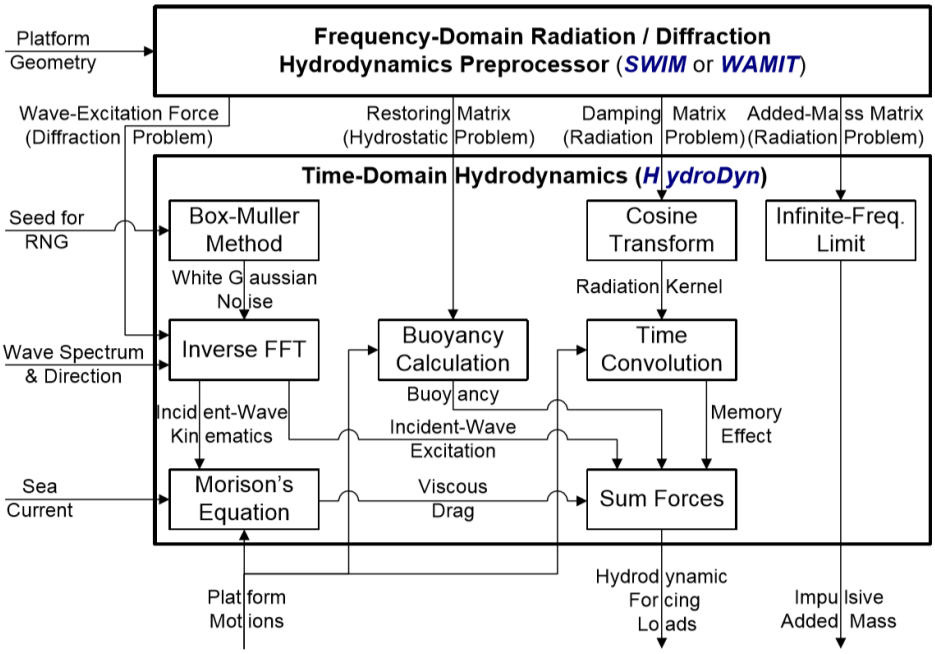

Figure 3. 2 Summary of the HydroDyn calculation procedure (Jonkman, 2007)

Hydrodyn, accounts for the linear hydrostatic restoring; nonlinear viscous drag from incident-wave kinematics, sea currents, and platform motion; added-mass and damping contributions from linear wave radiation, including free surface memory effects and incident-wave excitation from linear diffraction in regular or irregular seas. However, FAST only includes the first order inviscid hydrodynamics, which is the incident wave induced loads and motions, and excludes the second order hydrodynamic loads such as the slowly varying drift loads and sum frequency loads (Jonkman, 2007). Hence, although the second order wave effect inevitably happen in the tank tests, they are neglected in all numerical simulations. This is because, as can be seen in Chapter 5 and Chapter 6, in the tank tests, the platform motion is mainly dominated by the first order wave loads, so it is felt to be reasonable to ignore the second order wave in this study.

MAP

In this module, the mooring line properties are defined, such as the line type, its length/diameter/mass in air (or water), and the anchor position and connection points (fairlead position) with the platform. A quasi-static continuous cable theory is being used to emulate mooring line behaviour when modelling the catenary mooring lines for OC3-Hywind, which means that the mooring tension is calculated at each time step's platform position, but it ignores the inertia and hydrodynamic damping of the mooring cables. Since the mooring lines weight and diameter is very small compared to the platform's mass and geometry, so it is assumed to be acceptable to ignore the inertia and drag effects of the mooring lines. In addition, the vortex shedding effects would be also very small on the mooring lines when compared with the platform.

For the OC3-Hywind, in the real design, there will be a delta connection between the floating platform and the main mooring lines to increase the mooring's yaw stiffness, as shown in Figure 3. 3. In the NREL FAST code (for all versions), the delta connection is eliminated and a yaw spring stiffness 98,340,000 Nm/rad will be used to achieve the proper overall yaw stiffness.

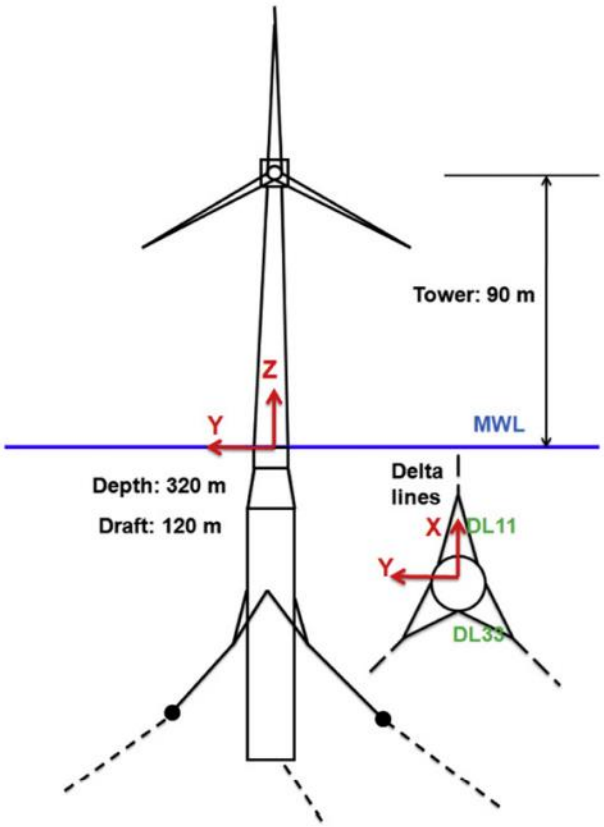

Figure 3. 3 OC3-Hywind delta line connection plot (Karimirad, 2013)

FASTlink

FASTlink is a new software by coupling the FAST with another software - OrcaFlex.

OrcaFlex is a commercial time-domain, finite element software which has been used to model the response of cables or to couple behaviour between a surface vessel and

its moorings. It is commonly used in the offshore industry as a means to predict the mooring line snap loads, rapid re-tensioning and transient motions.

When calculating the forces on the spar, it still uses a potential flow solution, here calculated from WAMIT + Morison's equation. For the mooring cables, it will only use Morison's equation. The mooring cables in OrcaFlex can be idealized as a system of mass nodes (which separates the mooring line into many segments) connected to viscous-elastic elements. For example, in this study, there are 26 nodes for each mooring line (each mooring line length is 263.07 m in full scale). To some extent, the greater the number of segments set up on the mooring line, the more accurate the result would be, but the running time should also be considered. Generally, the 10-m segment would be enough to capture the mooring line behaviours. The inherent mass, stiffness and damping properties of the mooring ensure it responses to varying end forces and displacements, which can hardly be achieved in the quasi-static mooring model in FAST.

OrcaFlex also employs the Morison's equation for the calculation of wave loads on floating structures and the mooring line drag forces. However, as stated before, the mooring drag and its damping properties have not been included in the FAST code, which could be acceptable for static analysis but inaccurate for dynamic simulations. A detailed discussion about the effect of the mooring drag term will be given in Chapter 6.2. In addition, OrcaFlex can calculate the second order wave effect, but it has been excluded in this study to maintain the consistency with FAST simulations.

In summary, in FASTlink, the wind turbine part, i.e., the wind turbine configuration /geometry /mass properties, etc., aerodynamic loads, control system, tower and the platform mass and inertia properties are still modelled in FAST, while the HydroDyn and MAP will be replaced by OrcaFlex. This means the subsea components, such as the mooring lines and the platform motions (the potential-flow model is also calculated in WAMIT first and then import into OrcaFlex) will then be modelled and calculated in OrcaFlex.

In FASTlink, the platform position and velocity vectors will be calculated first in FAST and then passed to OrcaFlex; the mooring line tensions and platform hydrodynamic added mass and damping matrices etc. will then be calculated by OrcaFlex. The added mass and damping matrices and total force and moment on the platform will then be passed back to FAST and then the resulting platform motion is solved in FAST. Figure 3. 4 shows the working principal of the FASTlink.

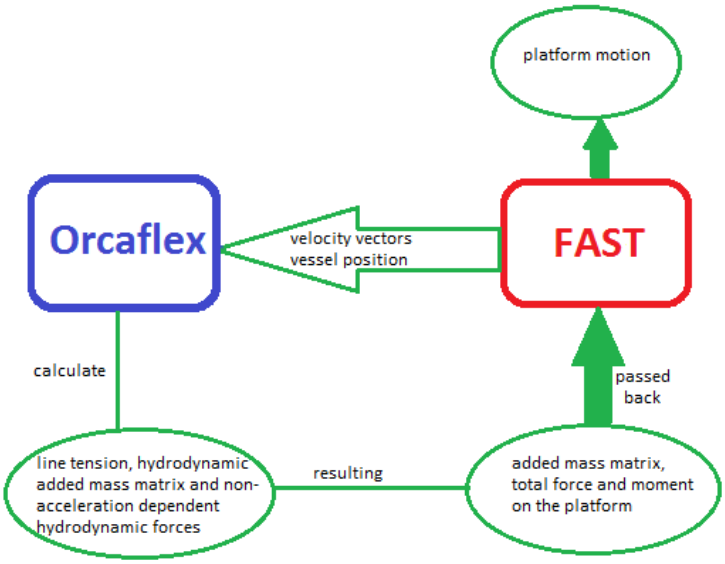

Figure 3. 4 FASTlink flow chart

3.3 OC3-Hywind Model Description

The NREL 5MW baseline wind turbine properties are shown in Table 2. 1. Table 3.1 presents the parameters for the OC3-Hywind floating system. These data will be used to set up the model in both FASTlink and FAST to run the simulations and then compared with available published results for the verification purpose. The full scale OC3-Hywind model has been shown in Figure 1. 9.

Table 3. 1 Parameters for the OC3-Hywind floating system (Jonkman, 2010 a)

Parameters	Values/Type	Units
Depth to platform base below SWL (total draft)	120	*m*
Water displaced volume	8,029	m^3
Elevation to platform top (tower base) above SWL	10	*m*
Depth to top of taper below SWL	4	*m*
Depth to bottom of taper below SWL	12	*m*
Platform diameter above taper	6.5	*m*
Platform diameter below taper	9.4	*m*
Platform mass, including ballast	7,466.33	*tonnes*
CM location below SWL along platform centreline	89.92	*m*
Platform roll inertia about CM	4,229,230	$ton \cdot m^2$
Platform pitch inertia about CM	4,229,230	$ton \cdot m^2$
Platform yaw inertia about platform centreline	164,230	$ton \cdot m^2$
Number of mooring lines	3	
Angle between adjacent lines	120	*deg*
Depth to anchors below SWL (water depth)	320	*m*
Depth to fairleads below SWL	70	*m*
Radius to anchors from platform centreline	853.87	*m*
Radius to fairleads from platform centreline	5.2	*m*

Unstretched mooring line length	902.2	*m*
Mooring line diameter	0.09	*m*
Equivalent mooring line mass density	77.71	*kg/m*
Equivalent mooring line weight in water	698.1	*N/m*

Before running the simulations, to obtain suitable hydrodynamic damping for the OC3-Hywind platform, the drag coefficient – Cd, should be applied to the hydrodynamic calculations in the Morison's equation. "*This augmentation to linear potential-flow theory is needed to obtain suitable hydrodynamic damping in severe sea conditions, which in the OC3-Hywind spar is dominated by (nonlinear) flow separation.*" (Jonkman, 2010 a).

For the platform drag coefficient – Cd, it is not a constant, instead, it depends on the flow speed, flow direction, structure position and size, fluid density and fluid viscosity and these characteristics are incorporated with the Reynolds number. Thus, for certain body shapes, the drag coefficient only depends on the Reynolds number and the direction of the flow in incompressible flow (which in the scope of this study). Therefore, the drag coefficient can often be treated as a constant (Clancy, 1975).

As stated in the NREL technical report (Jonkman, 2010 a), "*the OC3-Hywind spar experiences oscillatory Reynolds numbers exceeding 10^5 in most conditions of importance—that is, in moderate to severe sea conditions, is taken to be 0.6 (which is the typical coefficient for a cylinder at high oscillatory Reynolds numbers)*", so the Cd = 0.6 will be applied in all numerical simulations throughout this thesis.

In addition, in the NREL technical report (Jonkman, 2010 a), it also pointed out that "*The linear radiation damping (from potential-flow theory, which is small) and the nonlinear viscous-drag (from the relative form of Morison's formulation), when summed, do not capture all of the hydrodynamic damping for the motions of the real Hywind platform. As such, Statoil recommended that the hydrodynamics models for the OC3-Hywind system be augmented with additional linear damping. Additional linear damping of 100,000 N/(m/s) was needed for surge and sway motions, 130,000 N/(m/s) was needed for heave motions, and 13,000,000 Nm/(rad/s) was needed for yaw motions to match the free-decay responses supplied by Statoil*". The additional linear damping matrix in the NREL technical report (Jonkman, 2010 a) is shown in Figure 3. 5, which will be input for the simulations in this chapter and will be adjusted for the tank test model (details will be shown in Chapter 5 and Chapter 6).

$$B_{ij}^{Linear} = \begin{bmatrix} 100{,}000\ N/(m/s) & 0 & 0 & 0 & 0 & 0 \\ 0 & 100{,}000\ N/(m/s) & 0 & 0 & 0 & 0 \\ 0 & 0 & 130{,}000\ N/(m/s) & 0 & 0 & 0 \\ 0 & 0 & 0 & 0 & 0 & 0 \\ 0 & 0 & 0 & 0 & 0 & 0 \\ 0 & 0 & 0 & 0 & 0 & 13{,}000{,}000\ Nm/(rad/s) \end{bmatrix}$$

Figure 3. 5 Additional linear damping matrix for OC3-Hywind (Jonkman, 2010 a)

As discussed in Chapter 2.2, the added-mass coefficient – Ca also needs to be selected to define the equivalent added-mass in surge of the floating platform. On the assumption that Ca is independent of depth and the motion of platform is of low-frequency, Jonkman (2010 a) found the added mass coefficient for the OC3-Hywind model to be 0.970, and this value is used in the present study.

3.4 Code Verification

In this part, the output generated by the FASTlink and FAST code will be compared with data from NREL, to ensure that the code implementation used in this study is correct.

Free decay tests compare with NREL-47534

Figure 3. 7, Figure 3. 9, Figure 3. 11 and Figure 3. 13 show the surge, heave, pitch and yaw free decay motions for the OC3-Hywind model published by NREL. In their study, an initial position at 20 m (away from the equilibrium centre) has been set along the positive X-axis, to conduct the surge free decay test; an initial position at 5 m has been set along the positive Z-axis for the heave free decay test; an angle of 10° has been set for the pitch and -5° for the yaw free decay. Thus, in the present study these starting positions will be used in FASTlink and FAST runs to check if the results are comparable with the NREL published results. The blue solid line shown in Figure 3. 7 to Figure 3. 13 represents the NREL FAST results.

Figure 3. 6, Figure 3. 8, Figure 3. 10 and Figure 3. 12 show the surge, heave, pitch and yaw free decay motion curves calculated by the FASTlink and FAST code, which shows a perfect match with the NREL paper. There are some tiny differences between FASTlink and FAST in heave and pitch, but these are regarded as acceptable and small enough to be negligible.

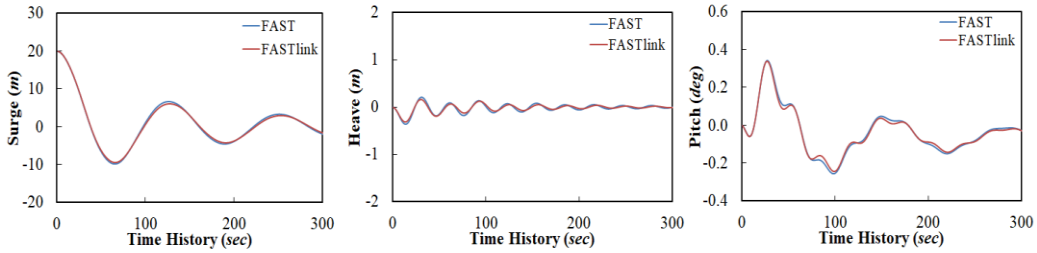

Figure 3. 6 Surge free decay tests, FASTlink and FAST

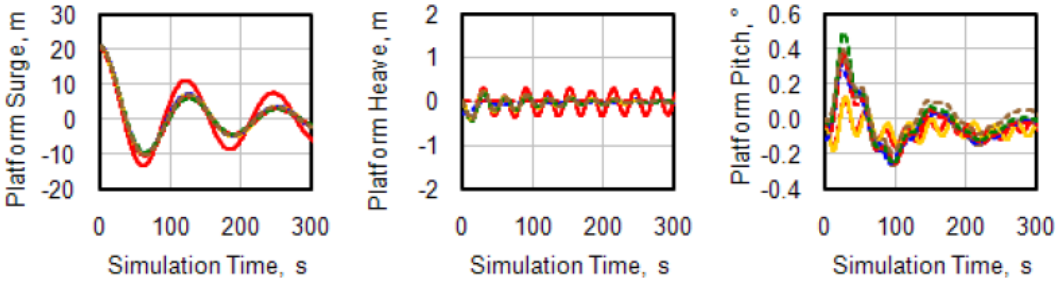

Figure 3. 7 Surge free decay tests, NREL-47534

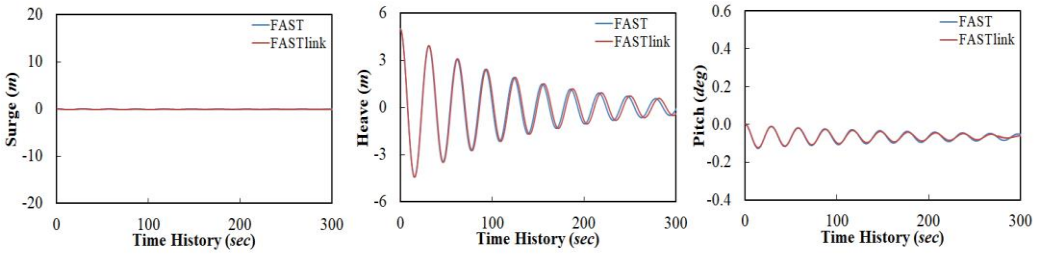

Figure 3. 8 Heave free decay tests, FASTlink and FAST

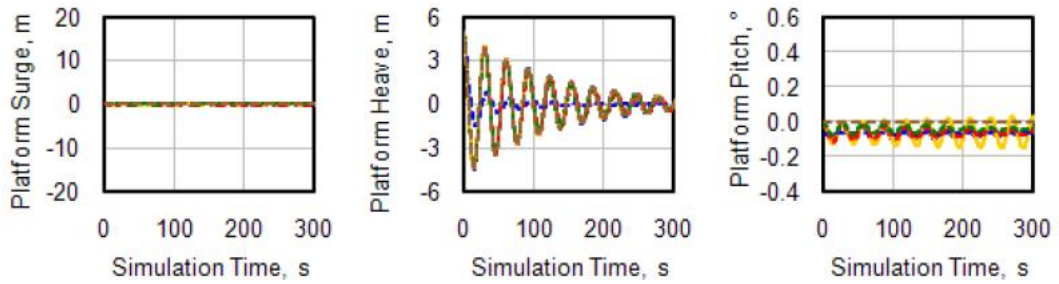

Figure 3. 9 Heave free decay tests, NREL-47534

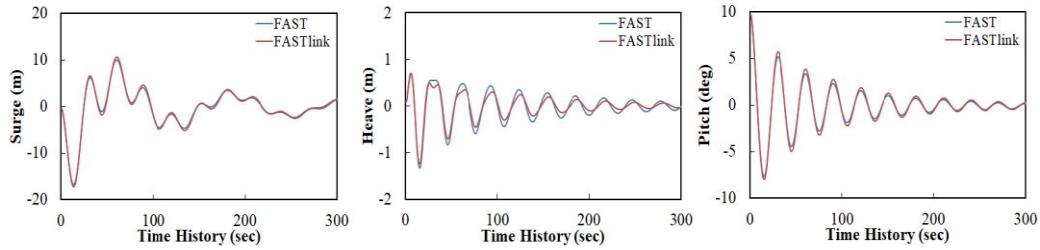

Figure 3. 10 Pitch free decay tests, FASTlink and FAST

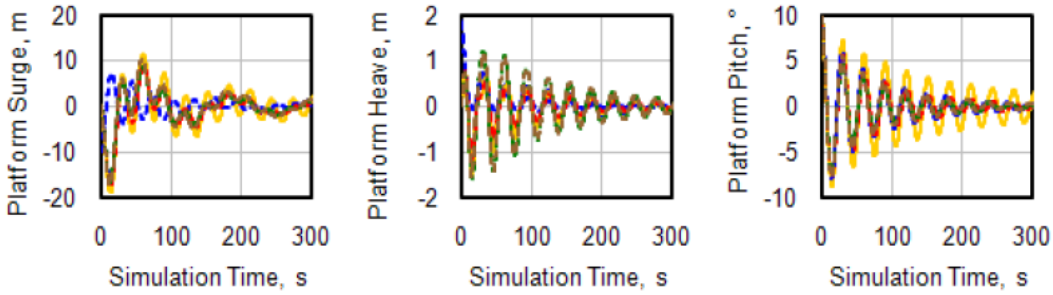

Figure 3. 11 Pitch free decay tests, NREL-47534

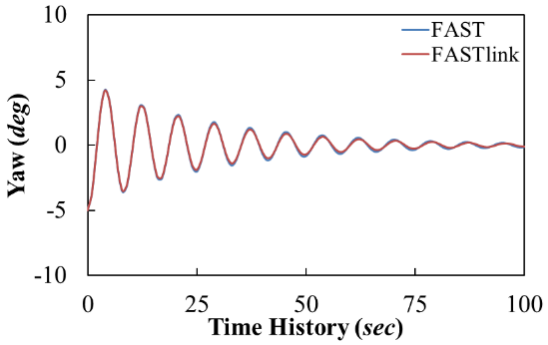

Figure 3. 12 Yaw free decay tests, FASTlink and FAST

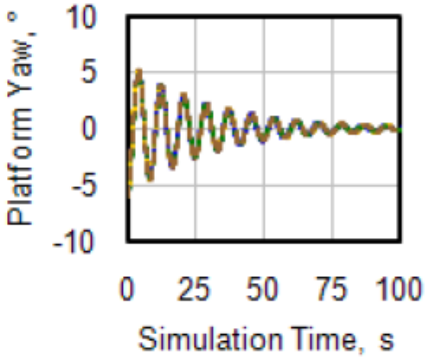

Figure 3. 13 Yaw free decay tests, NREL-47534

Static load-displacement compare with NREL-47535 (Jonkman, 2010 a)

The Figure 3. 14 to Figure 3. 31 show the linearization analysis performed by the NREL FAST code, and FAST and FASTlink code used in this study, for the OC3-Hywind mooring system.

The indices 1 to 6 represents the platform 6 DOFs: 1 = surge, 2 = sway, 3 = heave, 4 =roll, 5 = pitch and 6 = yaw. In the NREL study, the load-displacement relationships were being calculated from FAST code by giving the platform a discrete combination of the displacements. The surge and sway were varied from -36 m to 36 m in steps of 6m; heave was varied from -12 m to 12 m in steps of 4m; the roll and pitch were varied from -10° to 10° in steps of 2° and the yaw displacement was varied from -20° to 20° in steps of 4°. When calculated for one specific DOF, the other 5 DOFs were turned off (Jonkman, 2010 a).

To validate the FASTlink and FAST code used in this study, the same procedures as the NREL study was conducted. In the NREL report, they put the force and moments in one figure. To make the results more clear, the force and moments will be put into separate figures in this study, as shown from Figure 3. 15 to Figure 3. 31. It shows that the FASTlink results can match perfectly with the FAST code for each mooring lines, and the two codes been used in this study are matching perfect with the NREL figure. For the yaw motion, as the FAST/FASTlink code been used in this study has set a limitation between -15° to 15°, thus only -12° to 12° were been calculated and the curves tendency looks matching perfectly with the NREL study. Thus, it shows that

the two numerical codes used in this study can predict the expected results and the author has the ability to use the codes correctly.

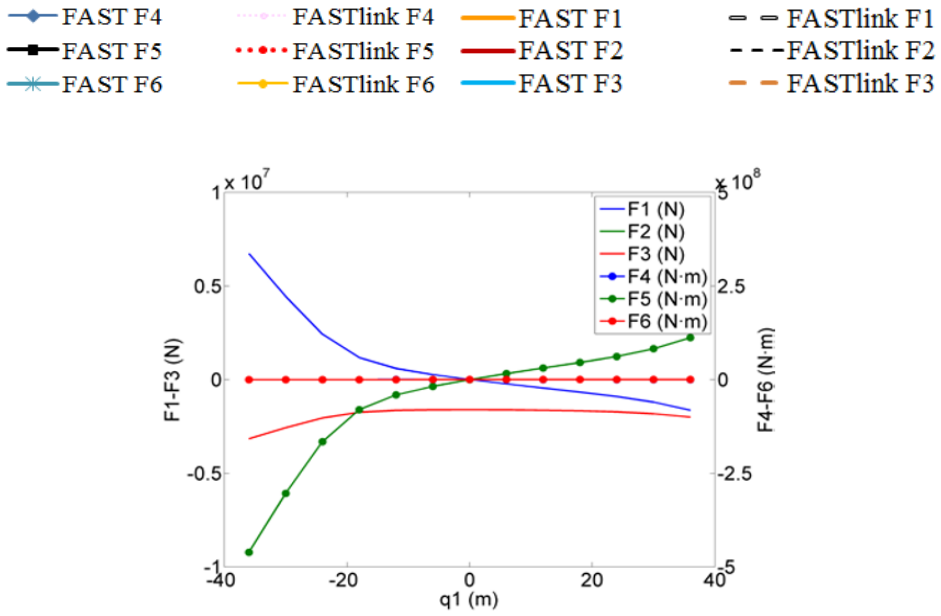

Figure 3. 14 Load-displacement (force and moment) relationships in Surge, NREL-47535

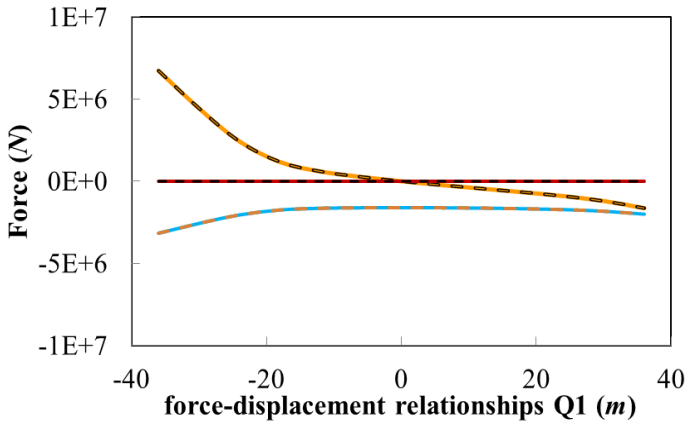

Figure 3. 15 Force-displacement relationships in Surge, FASTlink and FAST

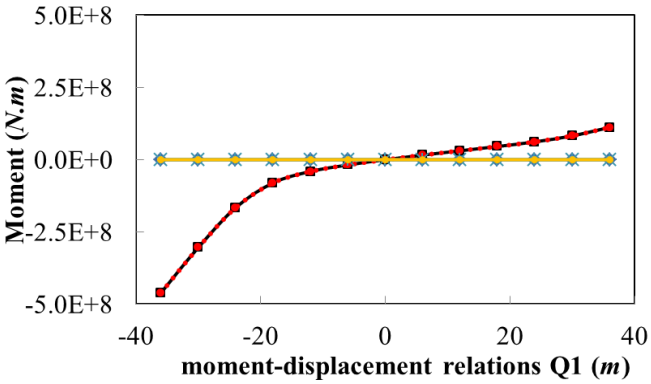

Figure 3. 16 Moment-displacement relationships in Surge, FASTlink and FAST

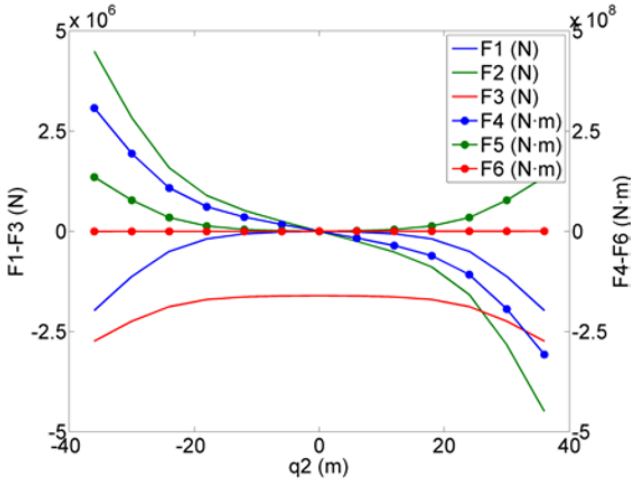

Figure 3. 17 Load-displacement (force and moment) relationships in Sway, NREL-47535

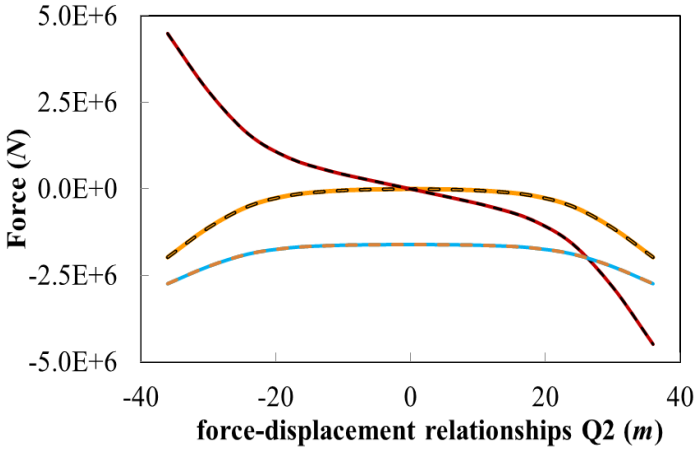

Figure 3. 18 Force-displacement relationships in Sway, FASTlink and FAST

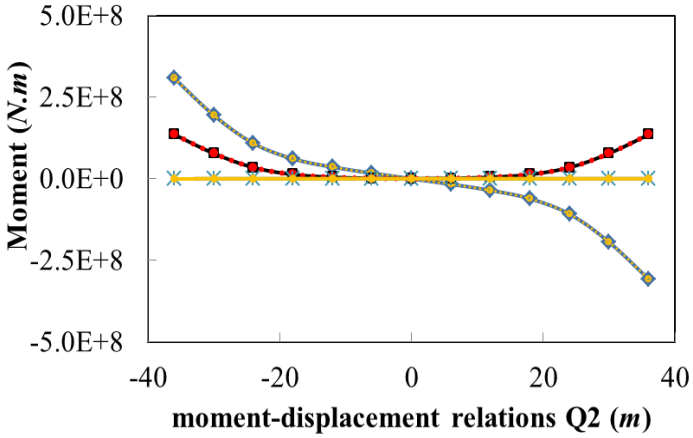

Figure 3. 19 Moment-displacement relationships in Sway, FASTlink and FAST

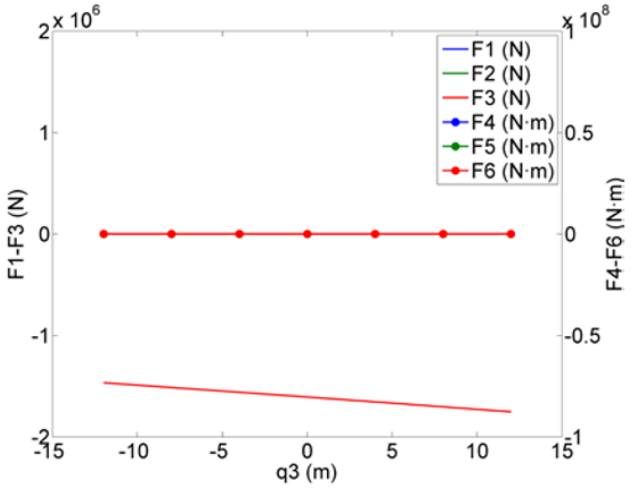

Figure 3. 20 Load-displacement (force and moment) relationships in Heave, NREL-47535

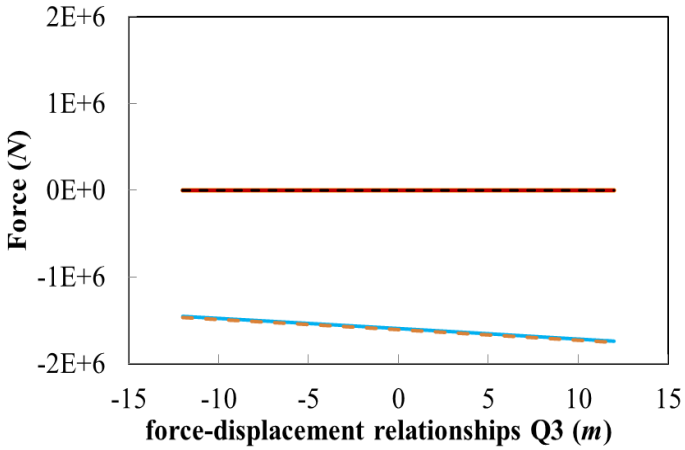

Figure 3. 21 Force-displacement relationships in Heave, FASTlink and FAST

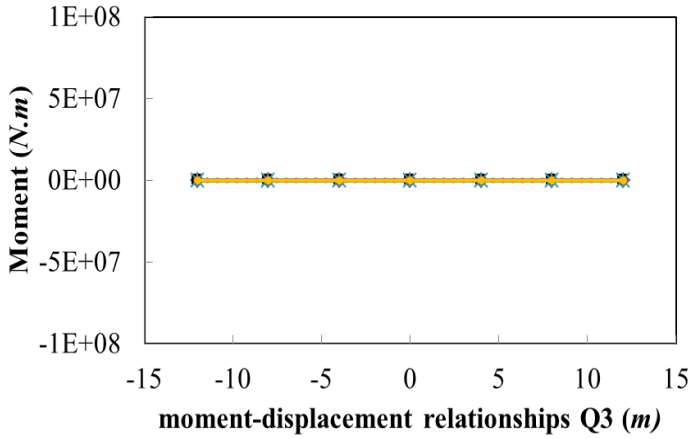

Figure 3. 22 Moment-displacement relationships in Heave, FASTlink and FAST

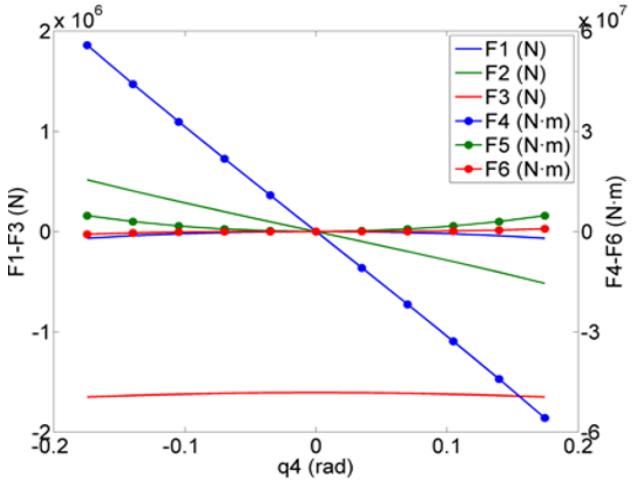

Figure 3. 23 Load-displacement (force and moment) relationships in Roll, NREL-47535

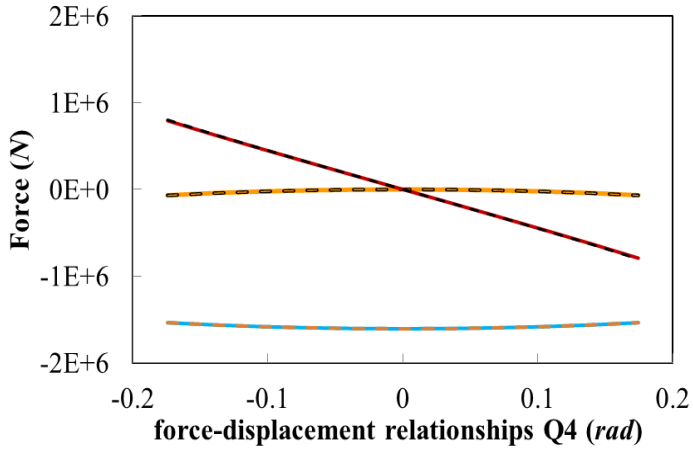

Figure 3. 24 Force-displacement relationships in Roll, FASTlink and FAST

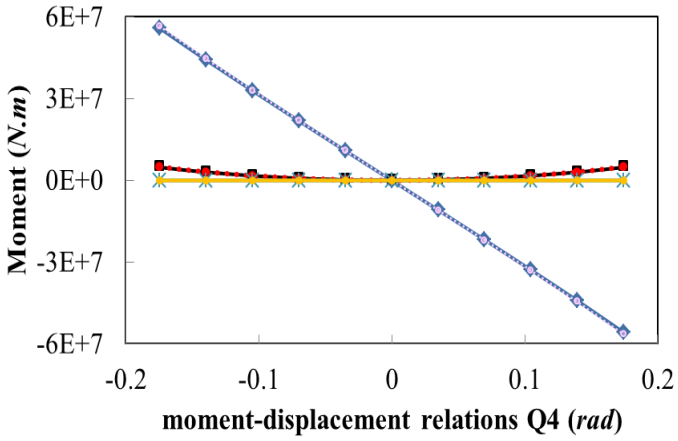

Figure 3. 25 Moment-displacement relationships in Roll, FASTlink and FAST

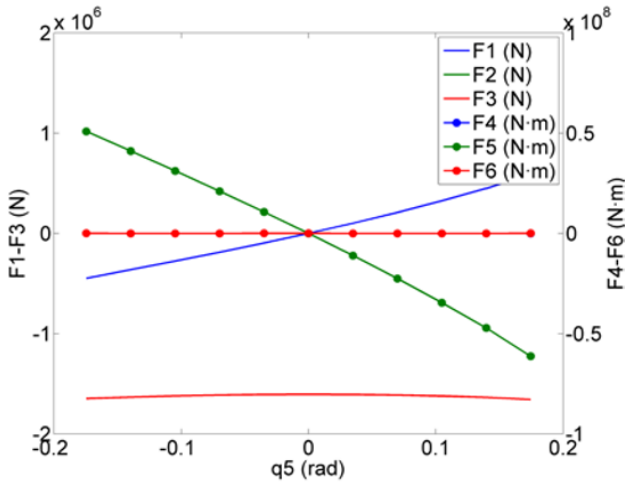

Figure 3. 26 Load-displacement (force and moment) relationships in Pitch, NREL-47535

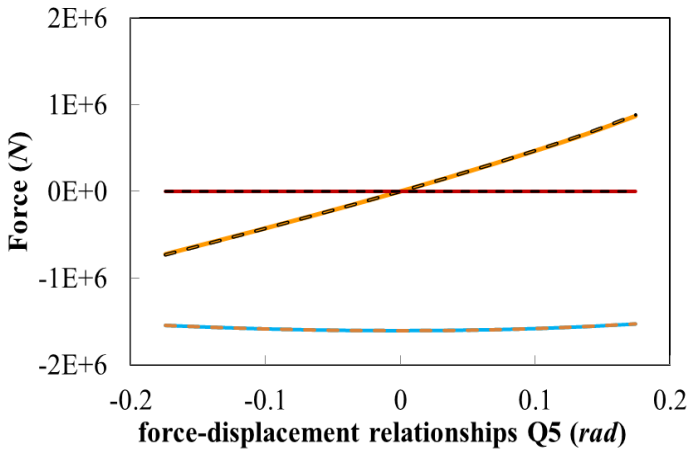

Figure 3. 27 Force-displacement relationships in Pitch, FASTlink and FAST

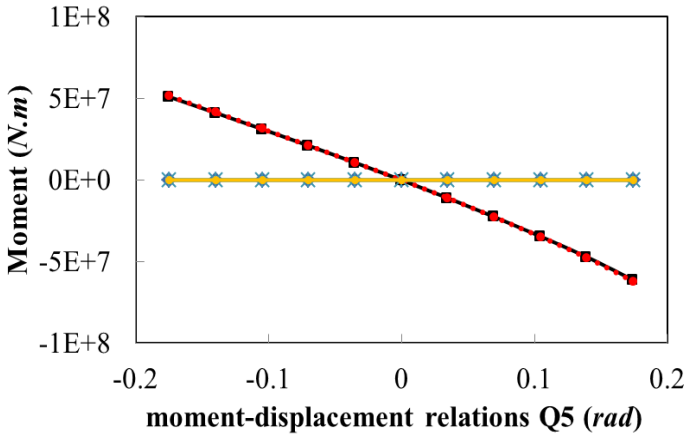

Figure 3. 28 Moment-displacement relationships in Pitch, FASTlink and FAST

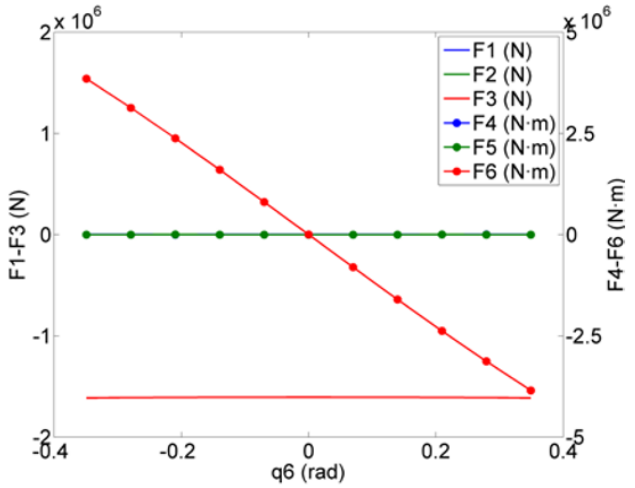

Figure 3. 29 Load-displacement (force and moment) relationships in Yaw, NREL-47535

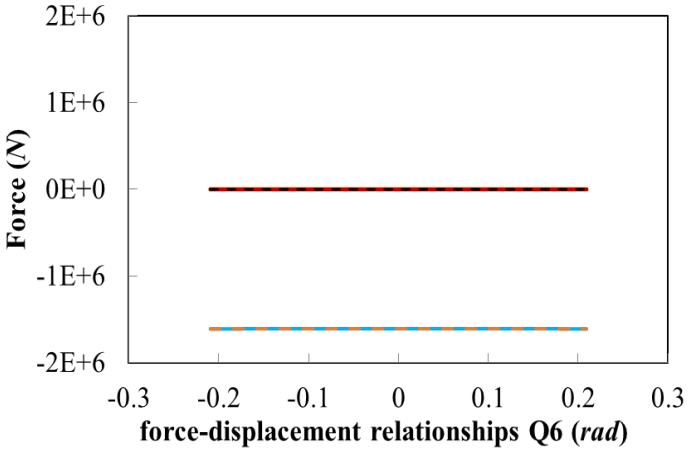

Figure 3. 30 Force-displacement relationships in Yaw, FASTlink and FAST

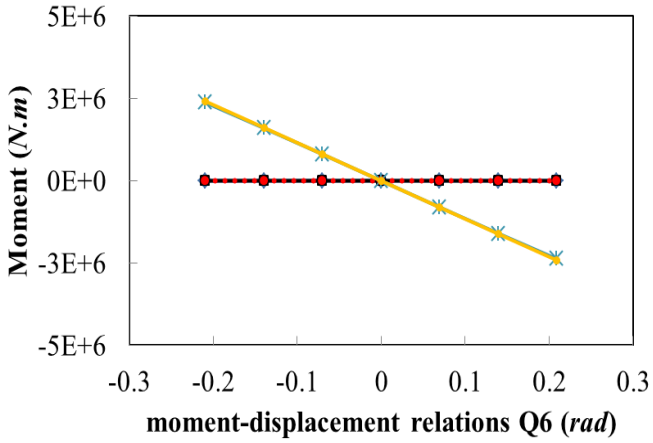

Figure 3. 31 Force-displacement relationships in Yaw, FASTlink and FAST

3.5 Summary

In this chapter, the FAST and FASTlink have been introduced in detail and the software limitation have been discussed. The OC3-Hywind floating structure properties are given. The FASTlink and FAST code are then been validated with the NREL published results – the platform free decay motions and the load displacement relationships of the mooring system. Both of these case studies show that the data from the code used in this study are matching perfectly with the NREL data, and thus that results generated in the following chapters are credible. In addition, for the static load-displacement, the FASTlink and FAST data are matching quite well, while for the free decay, some tiny differences can be seen in heave and pitch motion, presumably due to the different mooring models used in the two codes; FASTlink using the dynamic mooring model while FAST using the quasi-static mooring model for the calculations. This shows the fidelity of the numerical simulations in this study.

Chapter 4 Experimental Modelling of a Spar OFWT

4.1 Introduction

To investigate the OFWT spar platform and its mooring systems hydrodynamics behaviour thoroughly, it is necessary to carry out experimental measurements. This chapter will give the details in the preparation stage of the experiment been carried out at the Kelvin Hydrodynamics Laboratory (KHL). A brief introduction of the KHL facilities will be given first. The design and limitations of the experiment will be discussed. The parameters scaling, such as the scaling methodology and the scaled model dimensions will be given. The set-up of the instrument been used in the experiment and also the relevant data analysis software will be presented in detail. Calibrations, which is the most important procedure before the start of the tank test will be presented.

Kelvin Hydrodynamics Laboratory

The Kelvin Hydrodynamics Laboratory (KHL), at the University of Strathclyde, is one of the largest hydrodynamic test tanks in the UK. The tank can do a wide range of marine hydrodynamics tests for measuring the performance of surface ships and a wide variety of floating and underwater structures. Its dimensions are 76 m*4.6 m*2.5 m. It is equipped with a variable-water-depth computer-controlled four-flap absorbing wave maker, which can generating both regular and irregular waves over 0.5 m height (subject to the water depth), as shown in Figure 4. 1. At the back of the tank, there has a high quality variable-water-depth sloping beach, with reflection coefficient typically less than 5% over frequency range of interest. A state-of-the-art, real-time, non-contact

infrared camera system has been installed in the tank to measure the motions of floating vessels and structures. Up to 25 wave probes are available at the tank to determine water surface elevation.

Figure 4. 1 Four Flap Wave Maker at KHL

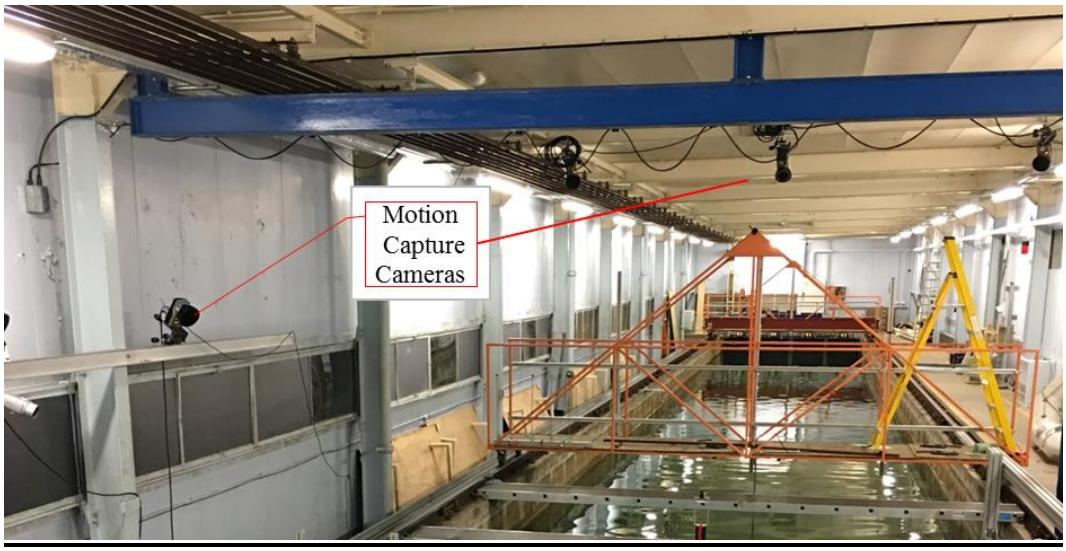

Figure 4. 2 Structure Motion Capture Cameras at KHL

For this experiment, five motion capture cameras have been installed above the tank. Two at the left side and the other three are above the tank, as shown in Figure 4. 2. To capture the mooring line motions, three underwater cameras have been installed in the tank. Full details will be given in Chapter 4.4.

4.2 Experiment Design and Brief Model Description

In this part, the detailed factors affecting the design of the experiment will be discussed, including the water depth, the scaling factor, the mooring design, the wave frequencies been tested, tests running time and sampling frequency and the effect of using the 2-D flume assumption.

Water Depth

The water depth in the tank is chosen as 2.0 m, according to the wave conditions during tests, and the wave maker capability. The beach at the back of the tank has been adjusted in height to maximise absorption over the frequency range of interest, as some long duration runs of waves will be generated during the test.

Scaling Factor

Considering the 2.0 m water depth at the KHL, the scaling factor has been chosen as 1:74 (Santos-Herrán, 2016), which gives the spar platform model draft at 1.621 m. As introduced in Chapter 1, the Hywind Scotland Pilot Park, the water depth on site is 105m and the draft of the spar platform is 78 m (“How Hywind works”, 2019). Its ratio

between water depth and platform draft is about 0.743 and 0.810 in this study, which shows the scaling factor -- 1:74 is reasonable.

Mooring Design

Compared with the OC3-Hywind model, the water depth in full scale has decreased from 320 m to 148 m, although the platform draft can work well, the mooring length and anchor position need to be adjusted. This has been done by using the Principle of Similarity based on the geometry, and the static balance has been checked in numerical model before conducting experiment, which shows satisfied balance. For the mooring stiffness, it has been scaled (using the scaling factor) down from the OC3-Hywind mooring system. As the transverse forces on mooring lines are dominated by the viscous effect, ideally it should use the Reynolds scaling method. But this study focus on the platform dynamic responses, which used the Froude scaling so it could not capture all the mooring responses correctly. However, the mooring line length, diameters and its weight distribution has only shown small differences with the target value, so the mooring model is felt to be acceptable in this study. The details of the mooring set up can be found in Chapter 6.2.

In addition, due to the width limitation of the tank, the mooring configuration has been slightly re-designed. For the NREL OC3-Hywind model, the angle between each mooring line is 120°. In this tank test, to make the mooring system as similar as possible to the NREL model, the Mooring Line 1, as shown in Figure 4. 5, is aligned with the wave direction, i.e., positive of X-axis but the angle between the other two

mooring lines is reduced to 60°, which are symmetrical about the centreline of the tank. The mooring property details can be found in Table 4. 3.

Since the Froude scaling method is used in this study (detail discussion can be found in Chapter 4.3), the fluid viscous effect on the mooring lines cannot be calculated accurately. However, for validation purposes this difference can be ignored if the numerical model is calculated with the same mooring model properties.

Wave Frequencies

The wave frequencies are being tested in the range from 0.253 Hz to 1.229 Hz (at tank test scale), which can not only cover the predicted spar platform heave and pitch natural frequencies, but also cover the range over which the wave maker (and the beach absorption) can work efficiently and generate desired wave profile.

Test Running Time and Sampling Rate

For free decay tests, depending on the degree of freedom, the test duration can have big differences, since for example the heave motion can damp much more slowly than the yaw motion. In most cases at least 10 to 15 motion cycles have been recorded and usually 10 motion cycles will be used for the natural frequency and damping ratio calculations (only about 5 cycles for yaw motion).

For regular wave tests, the recorded running time is about 120 s at tank test scale, which is enough for the platform to respond for at least 10 stable periodic motion

cycles. The data used for the analysis is started when the platform motion becomes stable, as it can take about 10 s for the generated wave to reach the model. In addition, when the wave has just reached the model, it can cause some transient splash effects and the first few cycles of platform motion do not show correct response under regular waves.

For irregular wave tests, the recorded running time is about 1200 s at tank test scale, (including the time when the wave approaching the model position), which is about 2 hr 40 mins (9600 s) in full scale. According to the ITTC report (Stansberg et al., 2002), in offshore engineering tests, it normally takes 3 hours to modelling a full storm. Thus, and the 2 hr 40 mins time period is reasonable to be applied to cover most extreme sea states encountered in real sea site.

The sampling frequency is set at 137 Hz during the tank tests, which means the highest recorded frequency which can be identified without aliasing is 68.5 Hz (the Nyquist frequency). This value is chosen based on prior experience in the laboratory. The choice of a prime number reduces the risk of harmonics, while the value chosen is large enough, as shown before, to cover all the possible wave frequencies, as well as any A further consideration is possible noise from the AC mains electricity with frequency 50 Hz in UK. Thus, if the mains noise (could from the data recording and transferring equipment) appears during the data recording process, it can be identified from the spectrum analysis and can be eliminated from the predicted response spectrum of the floating systems. In this study, the mains frequency has not been found through all the tank tests.

However, as will be presented in Chapter 6, a non-linear snatching behaviour has been discovered in the floating systems. In this phenomenon, the mooring line becomes very tight and then slack in a short time period. The time histories of the mooring tension data have been checked, as shown in Figure 4. 3. There are about 160 points recorded in the 10 seconds during the period in which the snatching is happening. If we look at the curve peak, there are still about 5 points, which shows that it is quite unlikely some higher points can be missed and it makes sure that all the featured changes in the floating system have been recorded. Thus, it can be seen that the sampling frequency at 137 Hz is a reasonable recording frequency.

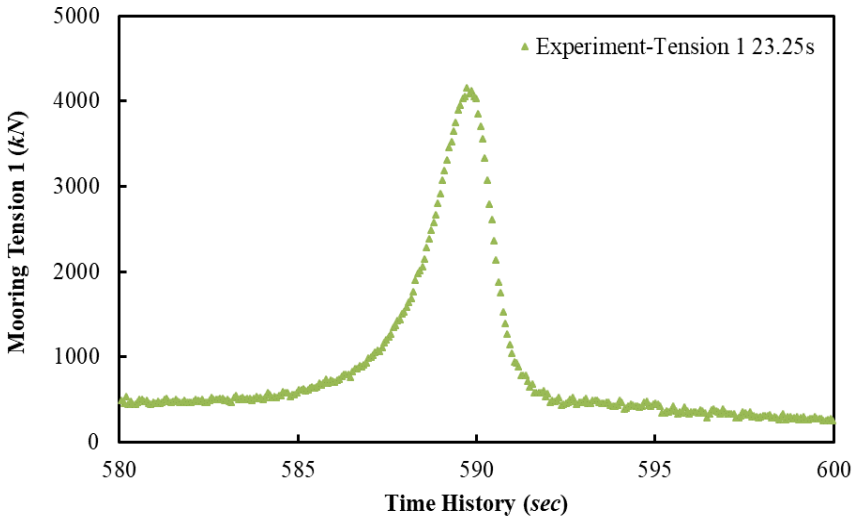

Figure 4. 3 Recorded time steps of mooring tension in experiment

2-D Flume

The wave generated at KHL is considered as a 2-D flume, which means that there are no directional waves as in real open seas. However, compared with the platform motion in real sea site, the motion can be larger in the tank tests than would be the case

in the real sea, as the wave energy are all in one direction, instead of spreading to other directions. However, the result is still acceptable, as it is being used to compare with the numerical simulations, where the 2-D flume assumption is also being employed.

Blockage and Wall Effects

When conducting the tank tests*, "the model should be small enough to avoid noticeable effects of restricted water in the towing tank" (*Zürcher, 2016). Thus, the blockage and wall effects of the tank should be considered, such as the radiated and diffracted waves. The blockage means the effects of finite width due to tank walls on the flow around a body and also the wall effect on reflected waves. In this study, the blockage ratio, i.e. the ratio between the model's cross sectional area and the cross-section area of the tank is 2.24%, which is very small.

In addition, as shown in the heave free decay test figures (Figure 5. 4 and Figure 6. 10), no motions due to the reflections of radiated waves have been observed, which also reinforces the view that wall effects are very small in this study. Thus, the blockage and wall effects are neglected in this tank test campaign.

Brief Model and Test Description

A spar-only model and a spar with three scaled realistic mooring lines will both be tested in free decay, a range of regular waves and four sea states. A simplified tower has been installed upon the spar platform in order to allow correct ballasting. The tank tests will involve no wind flow. The spar model is placed at the middle of the tank both

longitudinally and transversely and a wave probe has been placed centrally between the spar model and the wave maker, as shown in Figure 4. 4 and Figure 4. 5.

For spar-only tests, four very soft elastic moorings were applied to the platform to keep it in station. These are chosen so that they do not affect the first order (wave-frequency) motions of the platform as shown in Figure 4. 4.

For the test of the spar with scaled realistic mooring lines, a frame will be used at the bottom of the tank to attach the load cell and the mooring lines, as shown in Figure 4. 5. Through all the tests, the spar platform natural frequencies and RAOs will be checked. For tests of the spar with scaled realistic mooring lines, the mooring line tensions and the motions of Mooring Line 1 (which is the mooring line downstream of the wave maker aligned with the X-axis) will be recorded as well. Figure 4. 6 shows the soft moorings and their connection for the spar-only test. Figure 4. 7 presents the spar with scaled realistic mooring lines and its fairlead connections.

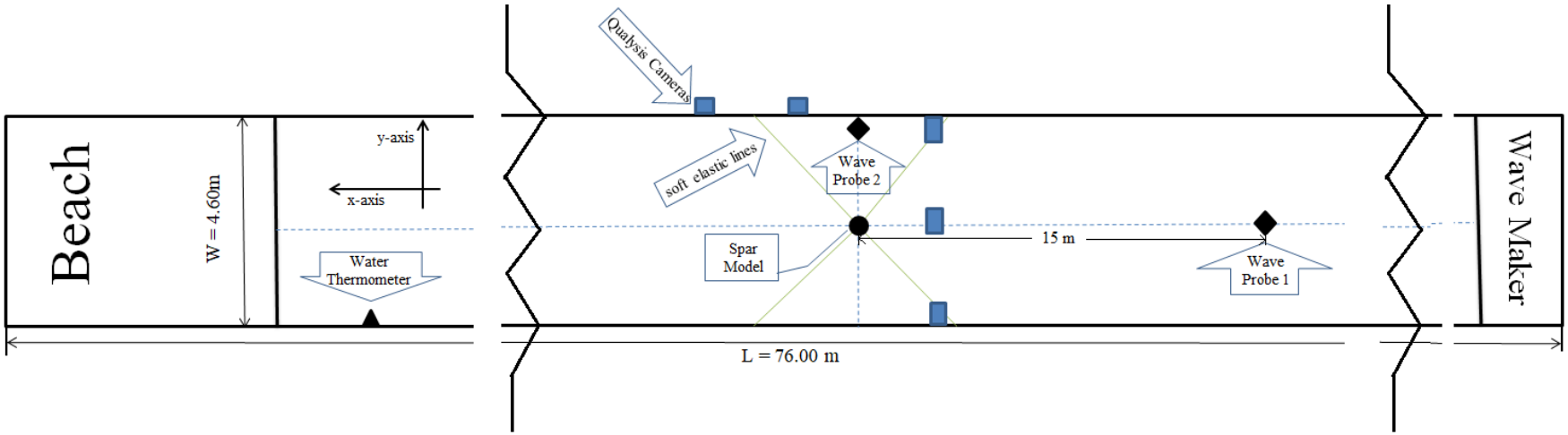

Figure 4. 4 Spar-only test

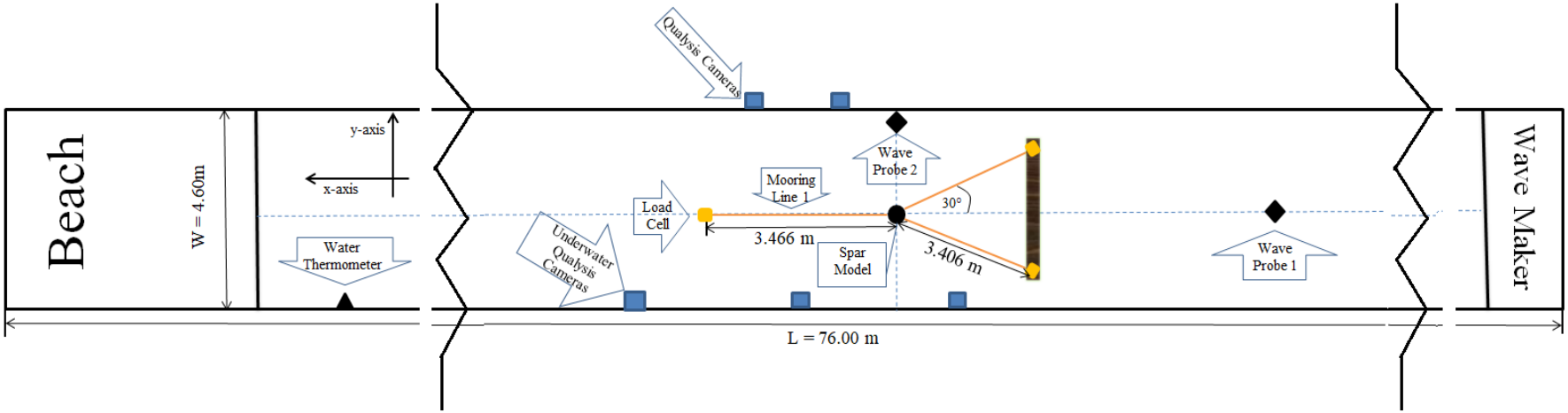

Figure 4. 5 Spar with realistic mooring test

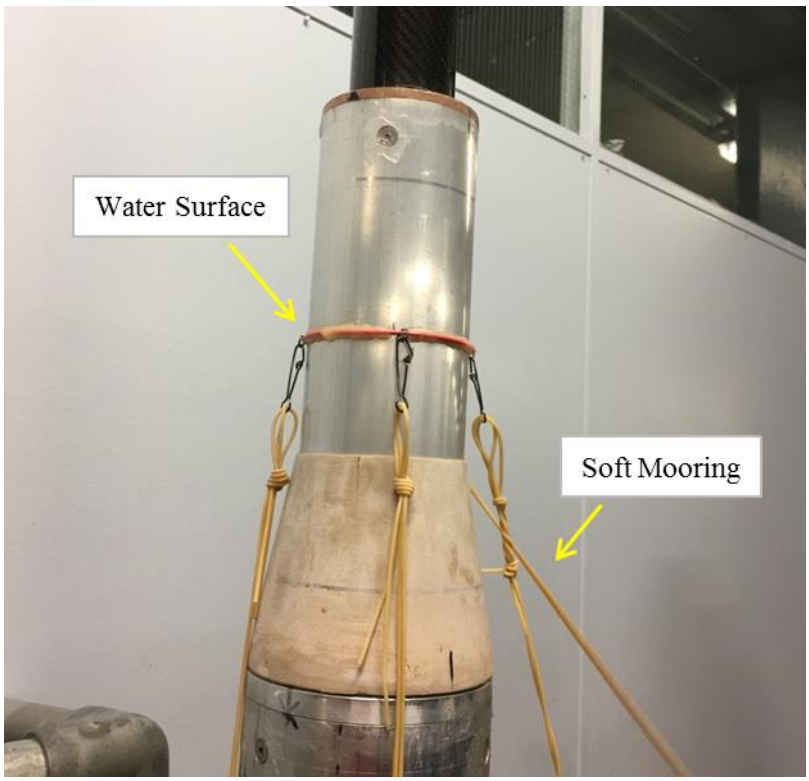

Figure 4. 6 Soft lines for spar-only tank test

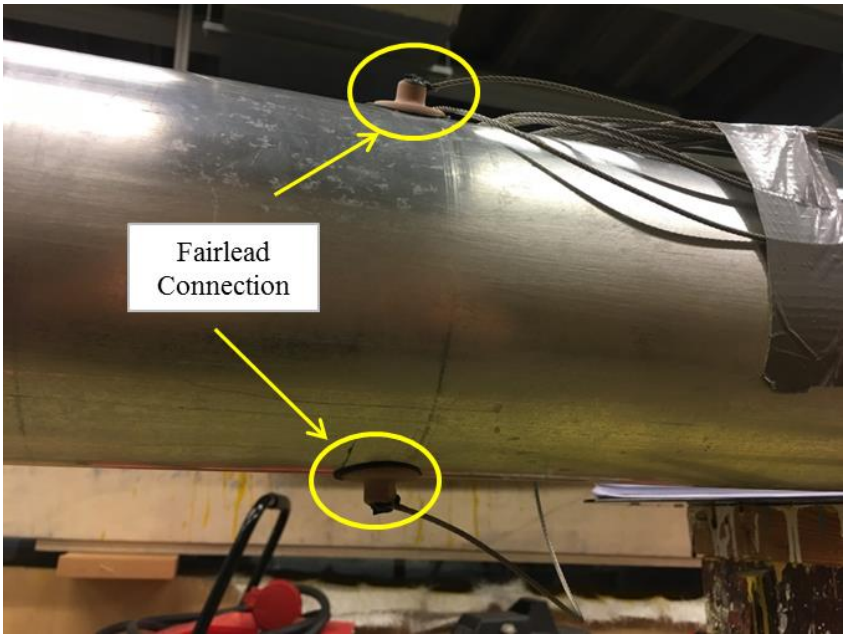

Figure 4. 7 Fairlead connections for mooring lines

4.3 Model Scaling Methodology and Tank Test Model Parameters

As discussed in Chapter 2.2 and according to the scaling factors for OFWT model test as shown in Table 2. 2, the detailed model parameters are shown in tables below.

Table 4. 1 NREL Full Scale/Target Scaled Tower Properties

Tower Properties		
	NREL Full Scale OC3-Hywind Model	Target Scaled Model
Hub Height (*m*)	90	1.216
Rotor Mass (*kg*)	110,000	0.271
Nacelle Mass (*kg*)	240,000	0.592
Tower Mass (*kg*)	249,718	0.616
CM Location of Tower Above SWL Along Tower Centreline (*m*)	43.400	0.586

Table 4. 2 NREL Full Scale/Target Scaled Platform Parameters

Platform Parameters		
	NREL Full Scale OC3-Hywind Model	Target Scaled Model
Depth to Platform Base Below SWL (Total Draft) (*m*)	120	1.622
Water Depth (*m*)	320	2
Depth to Top of Taper Below SWL (*m*)	4	0.054
Depth to Bottom of Taper Below SWL (*m*)	12	0.162
Platform Diameter Above Taper (*m*)	6.5	0.088
Platform Diameter Below Taper (*m*)	9.4	0.127
Platform Mass, Including Ballast (*kg*)	7,466,330	18.425
CM Location Below SWL Along Platform Centreline (*m*)	79.9	1.080
Platform Roll/Pitch Inertia of Whole Structure about CM (*kg*m^2*)	19,710,783,420	8.883

Table 4. 3 NREL Full Scale/Target Scaled Mooring Properties

Mooring Properties		
	NREL Full Scale OC3-Hywind Model	Target Scaled Model
Number of Mooring Lines	3	3
Angle Between Adjacent Lines (*deg*)	120	0,150,210
Depth to Fairleads Below SWL (*m*)	70	0.946
Radius to Anchors from Platform Centreline (*m*)	853.87	11.539
Radius to Fairleads from Platform Centreline (*m*)	5.2	0.070
Unstretched Mooring Line Length (*m*)	902.2	12.192
Mooring Line Diameter (*m*)	0.09	0.001
Equivalent Mooring Line Mass Density (*kg/m*)	77.707	0.014
Equivalent Mooring Line Weight in Water (*N/m*)	698.094	0.127
Equivalent Mooring Line Extensional Stiffness (*N/m*)	384,243,000	70,168.554

Table 4. 1 to Table 4. 3, show the original NREL OC3-Hywind model's parameters and the target model dimensions after scaling, including the tower, spar platform and mooring line properties. The tank test model is designed as far as possible according to these three tables.

As the aerodynamic load is not one of the concerns in this experiment, the tower in the tank test will be simplified as a cylinder with no turbine on it; however, the mass and inertial properties of the whole structure (platform + tower) are designed to be the same as the NREL 5 MW OC3-Hywind OFWT. Figure 4. 8 shows whole structure of the tank test model; the black cylinder is the tower part.

Figure 4. 8 Tank test model, tower and spar platform

Since the spar platform is a perfect axis-symmetric cylinder, the pitch and roll inertia will be the same. In addition to the changes in the mooring geometry, the flow fluid properties have also changed. The water density for the NREL model is the seawater density, which is 1025 kg/m^3, while in the tank test the water density should be fresh water density, which is 1000 kg/m^3. Thus, the whole structure mass should be reduced to ensure the same total draft and underwater volume. According to the Archimedes principle:

$$M_1 * g = \rho_{seawater} * g * V_1 \quad (9)$$

M_1 is the NREL full scale platform mass; g is the gravitational acceleration, $\rho_{seawater}$ stands for the sea water density, V_1 is the volume of the platform submerged below sea water line. For the NREL model: M_1 = 7466330 kg, g = 9.806 kg/N, $\rho_{seawater}$ = 1025 kg/m^3, then the V_1 = 7284.22439 m^3.

To have the same draft, i.e., the same volume of the platform submerged underwater (V_1), the platform mass – M_2 will be

$$M_2 * g = \rho_{freshwater} * g * V_1 \quad (10)$$

where, $M_2 = 7284224.39\ kg$. Thus, in the tank test model, the platform mass will be 17.98 kg in fresh water.

The whole model mass is measured by putting it on a scale. Then the COG is measured by placing the model on a knife-edge, adjusting its position until the model reached a balance position and then measuring the distance from the platform base to that point, as shown in Figure 4. 9. Then, the whole system pitch/roll (due to the symmetrical configuration of the model) inertia about its COG is measured by conducting the Bifilar Suspension test (by hanging the model with two wires and then conduct a free decay test of the model). The COG of the whole structure is located at the middle position of the two hanging wires, as shown in Figure 4. 10 and Figure 4. 11. The equation to calculate the pitch/roll inertia for this spar is:

$$I = \frac{M * g * D^2 * p^2}{16 * \pi^2 * h} \quad (11)$$

I stands for the pitch/roll inertia; *M* is the whole structure mass; g is the gravitational acceleration; *D* is the length of the hanging wire; *p* is the measured mean period of one harmonic motion of the structure; π is the circumference ratio; *h* represents for the distance between the two hanging wires.

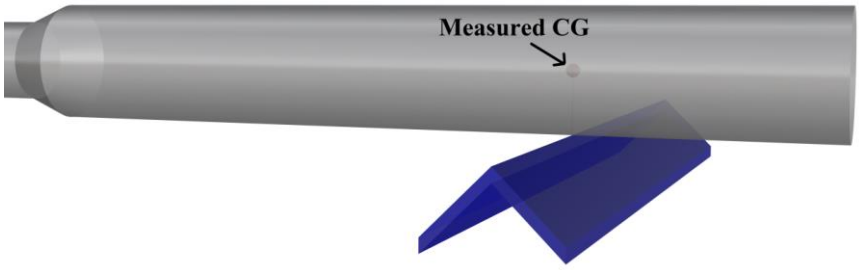

Figure 4. 9 Measure the CG of the whole model

Table 4. 4 shows the final measured tank test model properties and the re-designed full scale model, which parameters will be input into FASTlink and FAST to run numerical simulations and then compared with the tank test results. From Table 4. 4, it is clear that the geometric parameters of platform are ideally matched with the designed model.

Table 4. 4 Real tank test model properties and parameters (which will be input into numerical simulations)

Final Model Properties	Tank Test Model	Full scale Model	NREL full scale model
Water Depth (*m*)	2.000	148.000	320.000
Depth to Platform Base Below SWL (Total Draft) (*m*)	1.622	120.028	120.000
Depth to Top of Taper Below SWL (*m*)	0.054	4.000	4.000
Depth to Bottom of Taper Below SWL (*m*)	0.162	12.000	12.000
Platform Diameter Above Taper (*m*)	0.088	6.500	6.500
Platform Diameter Below Taper (*m*)	0.127	9.400	9.400
Platform Mass, Including Ballast (*kg*)	18.500	7.497E+06	7.466E+06
CM Location of the Whole Structure Below SWL Along Platform Centreline (*m*)	1.090	80.660	79.900

Pitch/Roll Inertia of the Whole Structure about CG (*kg*m^2*)	9.303	2.064E+10	1.971E+10
Number of Mooring Lines	3	3	3
Angle Between Adjacent Lines (*deg*)	0,150,210	0,150,210	120
Depth to Fairleads Below SWL (*m*)	0.947	70.078	70.000
Unstretched Mooring Line Length (*m*)	3.555	263.070	902.200
Mooring Line Diameter (*m*)	0.002	0.133	0.090
Equivalent Mooring Line Mass Density (*kg/m*)	0.013	71.188	77.707
Equivalent Mooring Line Extensional Stiffness (*N/m*)	163,268	8.94E+08	384,243,000
Radius to Anchors from Platform Centreline (*m*)	3.466, 3.406	256.45, 252.064	853.870
Anchor Depth (*m*)	1.89, 1.828	139.86,135.272	316.67
Radius to Fairleads from Platform Centreline (*m*)	0.074	5.476	5.200
Tower Height (*m*)	1.210	89.540	90.000
Tower Total Mass (*kg*)	1.290	522,738.960	599,000

Figure 4. 10 The Bifilar Suspension test to check the whole structure pitch/roll inertia

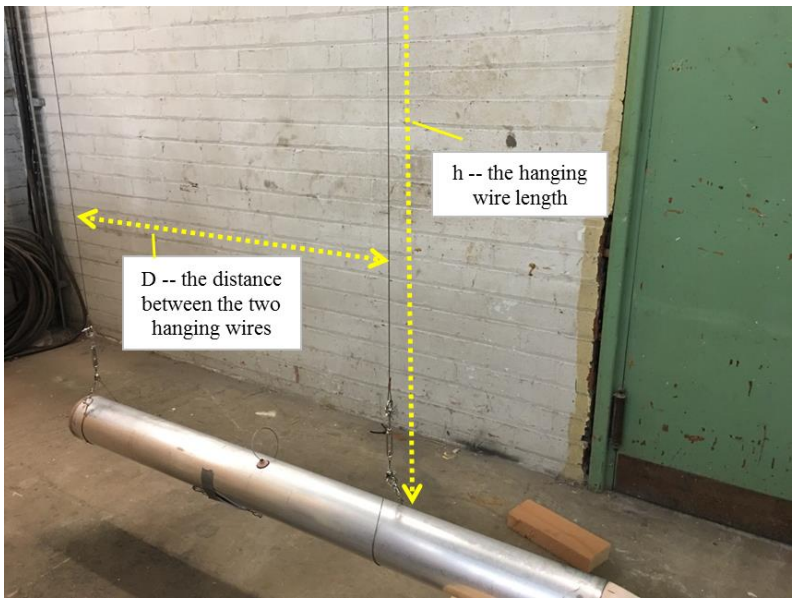

Figure 4. 11 The data needed in the Bifilar Suspension equation

In this test, the measured D = 0.960 m and h = 4.816 m. Three 10 cycles of the harmonic motion are measured as t_1 = 63.030s, t_2 = 62.670s and t_3 = 62.990s. Thus the pitch/roll inertia of the whole structure will be I = 9.303 kgm^2. The pitch/roll inertia of the NREL model after scaling is I_{NREL} = 8.883 kgm^2.

Thus, the difference between the NREL model and the designed tank test model of the whole structure pitch/roll inertia is less than 5%, which means the ballast arrangement of the tank test model is very good. Consequently, the model is acceptable for the experiment. Figure 4. 12 shows the geometry scope of the tank test model.

For the mooring line been used in this experiment, the details of calculating its Equivalent Mooring Line Extensional Stiffness will be given in the Appendix 1**.**

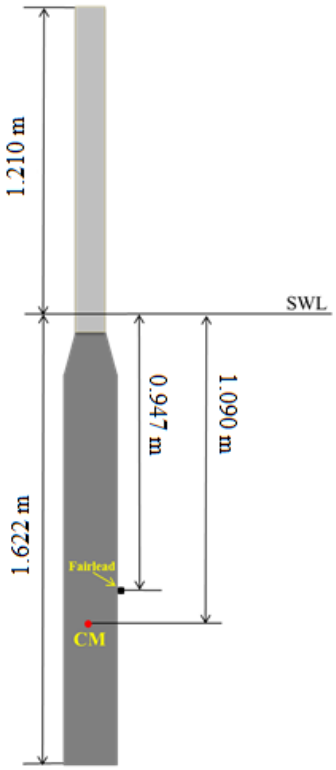

Figure 4. 12 Final design tank scale model

4.4 Experimental Instrumentation and Model Set-up

To capture the 6 degree of freedom (DOF) of the spar platform motions, the mooring line tension loads and also the mooring line motions, the following equipment would be needed to be installed in the tank: Qualysis system including the cameras – five above the tank and three underwater, two wave probes, Spike data acquisition software, three underwater load cells and the frame to support them, and the Accelerometer is mounted on top of the model tower.

Qualysis System and the Cameras

The platform 6 DOF motions – surge, sway, heave, roll, pitch and yaw, and the underwater mooring line motions (X, Y and Z) will be recorded by the Qualysis

system. As shown in Figure 4. 2, there are five optical cameras above the tank to capture the platform motions, and three underwater cameras are shown in Figure 4. 13.

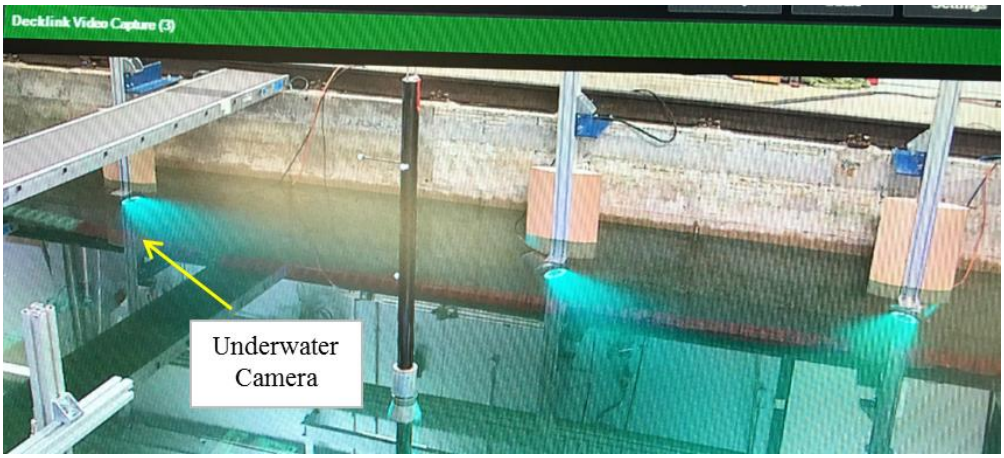

Figure 4. 13 Underwater cameras in the tank

These cameras detect the model's motion by tracking the movement of the reflective targets, which have been installed on the model. To make sure all 6 DOF motions of the platform can be captured; four reflection balls have been installed on the tower part of the model. The weight of these balls has been counted in the tower model already. Figure 4. 14 presents the arrangement of these reflection balls on the tower.

For the underwater mooring line motion capturing, there are seven reflection balls been used. The density of each ball is 991.260 kg/m^3 (detail is shown in Appendix 2), which is very near the fresh water density, so these balls are considered neutrally buoyant and the flow effect been generated by these balls are ignored in this research.

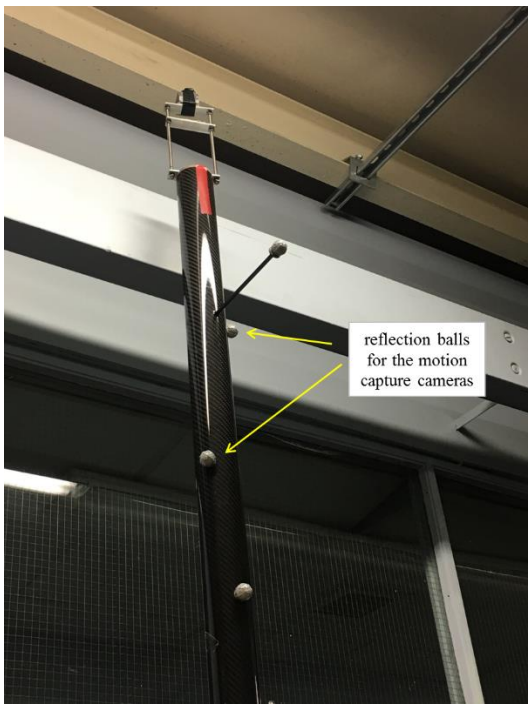

Figure 4. 14 Qualysis reflection balls arrangement on the tower model

The first reflection ball – named as Rear in the Qualysis software, has been installed on the load cell for Mooring Line 1. This rear reflection ball is being used as a reference point, since it is “anchored” and should not move during all the tests, which can help in generating a reference point for the Qualysis system.

Figure 4. 15 shows a load cell with the attached reflection ball. Another reflection ball has been attached on the spar platform at the fairlead position of Mooring Line 1 – named as Spar in Qualysis system, this reflection ball’s motion will be compared with the platform’s motion (measured from the above-water system) to double check if the underwater camera system working well. The other five reflection balls are being attached along the Mooring Line 1. Details of these reflection balls position are presented in Table 4. 5 and Figure 4. 16. These reflection balls are being arranged on

the Mooring Line 1 unevenly, as this can help to reduce the possibility of mis-identification of the balls by the Qualysis system.

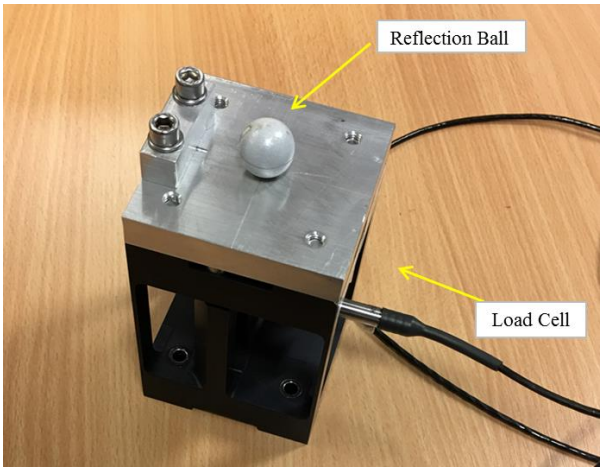

Figure 4. 15 Load cell 1 with the underwater reflection ball

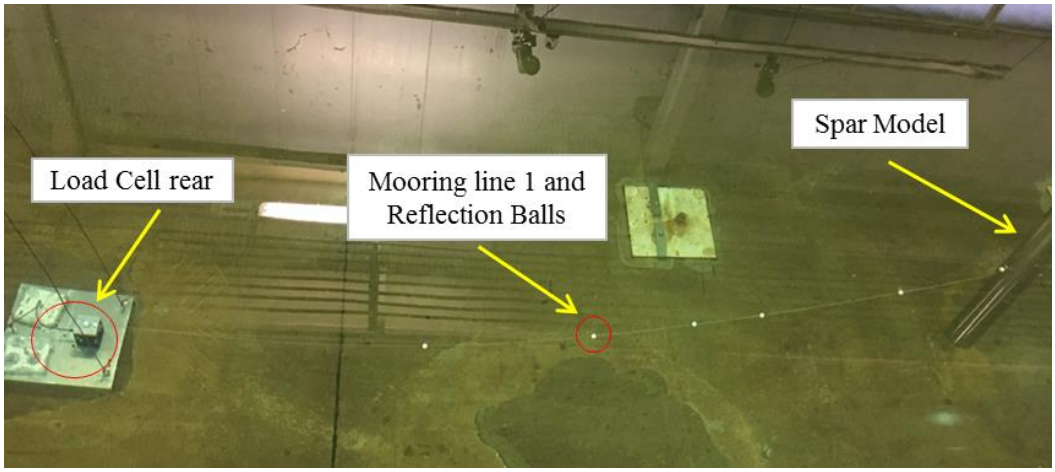

Figure 4. 16 Mooring line with underwater reflection balls in the tank

Table 4. 5 Reflection balls position on the Mooring Line 1

Arc Length	Model Scale	Full Scale
Reflection Ball Number	(*mm*)	(*m*)
1	2321.150	172.007
2	1638.460	121.417
3	1228.850	91.063
4	955.770	70.827
5	409.620	30.354
Spar (at fairlead)	0	0

Underwater Load Cells and the Frame

Three under water load cells are been used to record the three mooring line tensions. The load cells check for loads from 0 to 100 N very accurately, which lies in the range of the expected measured mooring tensions. The calibration part – Chapter 4.5 gives more detail on the proof of its accuracy and the error is less than 1%. One of the load cells with the reflection ball on its top will be used to record the tension of Mooring Line 1, as shown in Figure 4. 15. The other two load cells were installed on a long frame to make sure that they are on the line which is parallel with the width edge of the tank and they are been used to record the mooring tension of Mooring Line 2 and 3, respectively. Figure 4. 17 presents the frame.

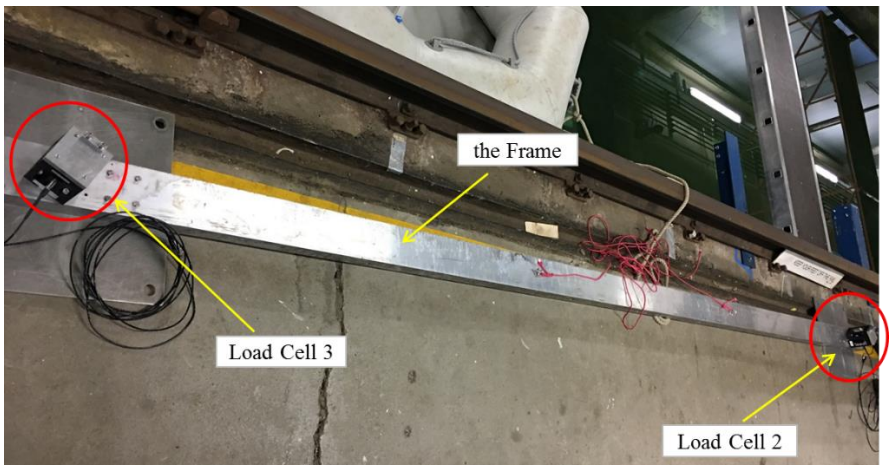

Figure 4. 17 Frame for Load Cell 2& 3

The height of this frame and the load cells should be considered as this will affect the mooring line anchorage height and position. The height of the load cell and the frame are shown in Figure 4. 18. The total height of the frame and the load cell was 172 mm. Thus, for the full scale, the anchor height for Mooring Line 2 & 3 will be 12.728 m above the bottom of the sea bed, and 135.272 m below water surface. For load cell at the rear, i.e., for Mooring Line 1, a flat plate has been placed under the load cell and the height is 10 mm, i.e., the total height with the load cell will be 110 mm, which means that in full scale the anchor position will be 8.14 m above the sea bed and 139.86 m below water surface. The details of the measured pre-tensions will be shown in Chapter 6.2.

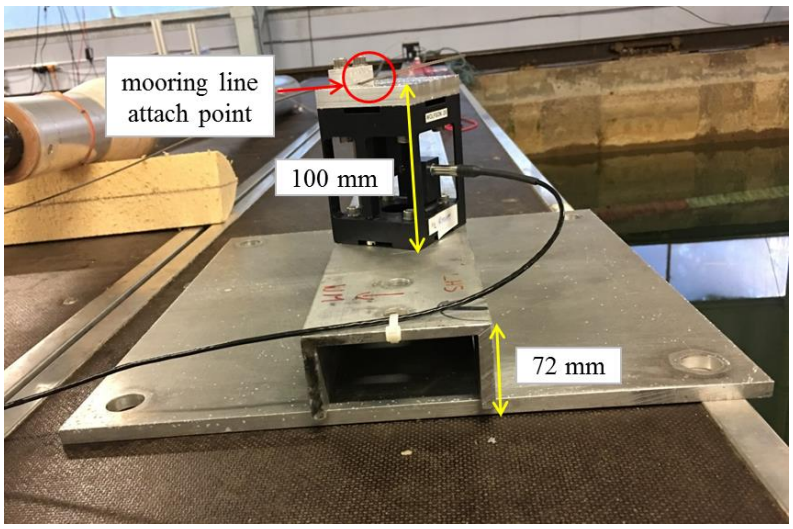

Figure 4. 18 Load cell and its frame dimensions

Accelerometer, Wave Probe and the Spike software

A three-axis (X, Y and Z) wireless accelerometer has been put on top of the tower (the weight of the accelerometer has been counted in the tower total weight already), to measure the acceleration of the tower top during the tank tests. Figure 4. 19 shows the accelerometer on top of the tower and Figure 4. 20 (a) and (b) shows the accelerometer and the base station which are been used in this experiment. The signal from this wireless accelerometer will be received by its wireless base station, and the Spike software can then record the detected signal. In principle, it is possible to obtain accelerations by double differentiation of the Qualisys position data; however previous experience has shown that this introduces unacceptable levels of noise.

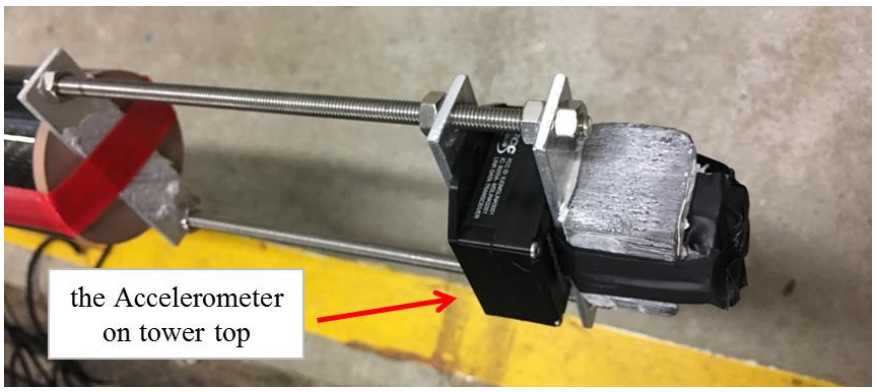

Figure 4. 19 Accelerometer on top of the tower

(a) (b)

Figure 4. 20 (a) the wireless accelerometer; (b) the wireless base station

Two wave probes are being applied in the tank to measure the wave passing the model. One resistance-type probe was installed upstream of the model, and another one is next to the model and on the edge of the tank – which is an ultrasonic wave probe. The detail position of these two wave probes can be found in Figure 4. 4 and Figure 4. 21 shows the Wave Probe 1 -- in front of the spar for a certain distance, so that it can measure the (regular) wave height passing through the model without the diffraction effect. For the irregular wave, the wave profile will be measured at exact the model position (before the experiment start and without model in the tank). Figure 4. 22 shows the two wave probes position in the tank.

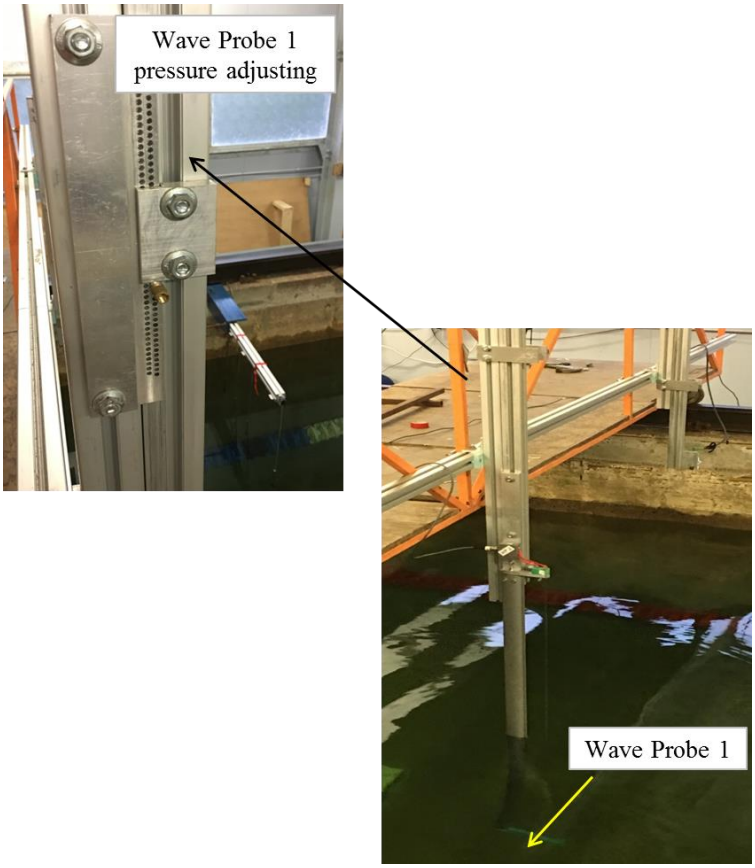

Figure 4. 21 Wave Probe 1

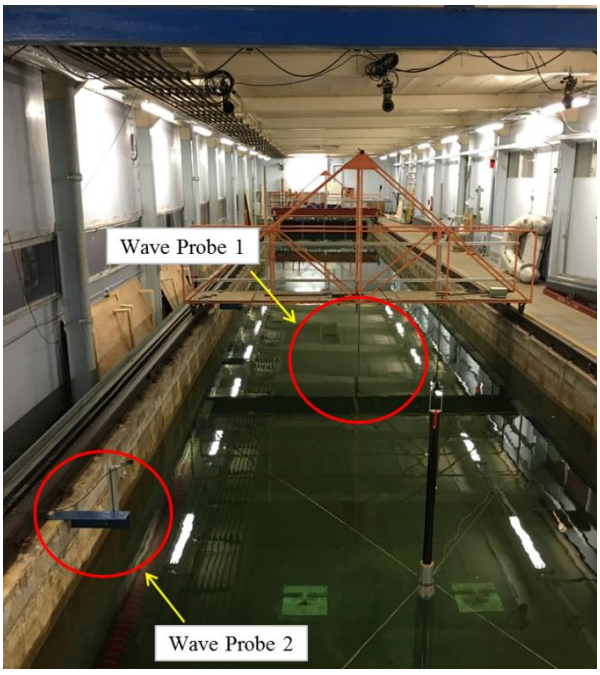

Figure 4. 22 Wave Probe 1 & 2 position in the tank

Spike is a data acquisition software. The platform 6 DOF, the accelerometer signals, Mooring Line 1 motions and the three mooring tensions measured by the load cell, and the wave passing through the model are all will be collected by Spike. These signals are being transferred into Spike. Figure 4. 23 shows the analogue-digital converter and Figure 4. 24 shows the display window of Spike.

Figure 4. 23 Analogue-digital converter

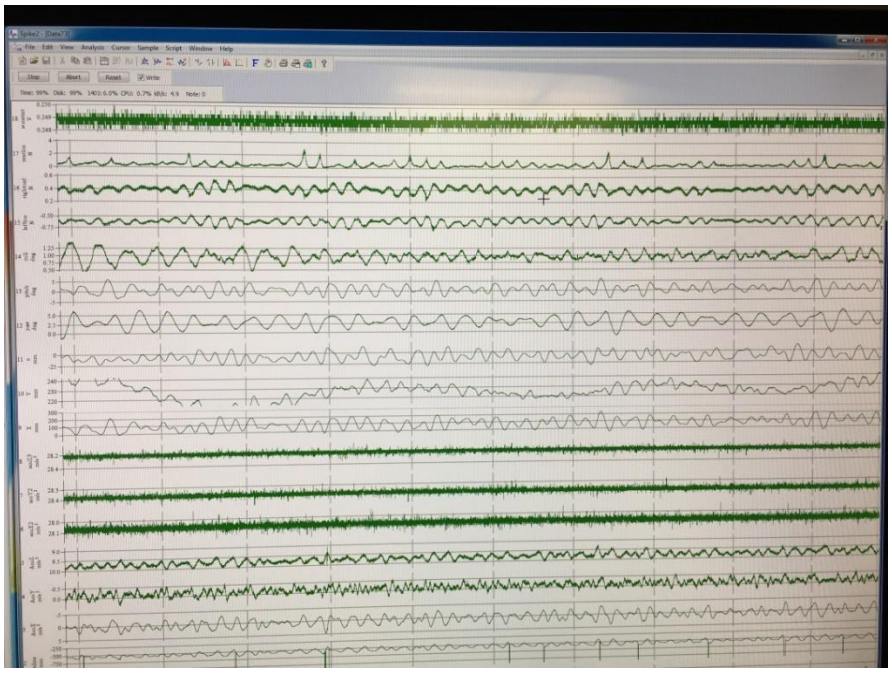

Figure 4. 24 Spike window when recording data

4.5 Calibration – Instrument Calibration, Wave Calibration

Before starting all the tests, it is very important to calibrate all the equipment that will be used through the experiment to ensure that the measured data are reliable. In this experiment, the accelerometer, Qualysis motion capture system (including the underwater cameras), Wave Probe 1, the three load cells are all been calibrated before the start of the tank test. Once the wave probes are calibrated, the four sea state waves will also be calibrated to ensure that the measured wave statistics reflect the target values.

Calibration of Accelerometer

The accelerometers – on top of the tower, were calibrated by accurately rotating it through known angles to apply a known variation in the component of gravity. The output voltage from the accelerometer is input into the A/D converter and Spike software and plotted against the known acceleration. Table 4. 6 presents the applied angle and the resulted applied acceleration. Figure 4. 25 shows the voltage signal relationship with the applied acceleration. To verify if the calibration coefficients are correct in Spike, the applied acceleration will be re-calculated to check if the value will match with the measured one.

Table 4. 6 Calibration of the accelerometer

applied angle (*deg*)	applied acceleration (*g*)	applied acceleration (*m/s^2*)
90	1.000	9.807
60	0.866	8.493
45	0.707	6.934
30	0.500	4.903
0	0.000	0.000
-30	-0.500	-4.903
-45	-0.707	-6.934
-60	-0.866	-8.493
-90	-1.000	-9.807

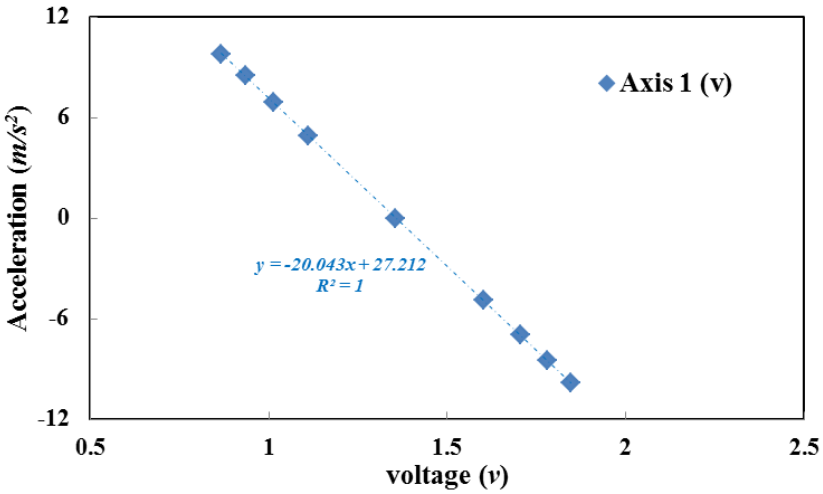

Figure 4. 25 Voltage signal with the applied acceleration

So the coefficient (-20.043, 27.212) will be used to re-calculate the applied acceleration:

$$Calculated\ applied\ acceleration = -20.043 * voltage + 27.212 \qquad (12)$$

Table 4. 7 Calibrated acceleration

applied acceleration (*m/s^2*)	voltage (*v*)	calculated applied acceleration (*m/s^2*)	Error (%)
9.807	0.868	9.810	0.038
8.493	0.935	8.480	0.150
6.934	1.013	6.909	0.362
4.903	1.112	4.924	0.416
0.000	1.355	0.042	0.000
-4.903	1.604	-4.928	0.508
-6.934	1.704	-6.942	0.107
-8.493	1.781	-8.483	0.121
-9.807	1.847	-9.812	0.059

In Table 4. 7, it can be seen that the difference between the calculated applied acceleration in Spike and the measured applied acceleration is below 0.5%, which is quite acceptable.

Qualysis Motion Capture System

To ensure that all the optical cameras can capture the reflection balls movement during the test and reference this correctly to the water surface position, the Qualysis system need to be carefully calibrated by waving a pole with two reflection balls mounted on top separated by a known distance (which is pre-input into the Qualysis system). The system adjusts the calibration to minimise the error between the predicted separation of the balls and the known value averaged over the measurement volume. The underwater Qualysis cameras are calibrated using a similar process. This ensures that the Qualysis cameras can capture all the motions and can output the correct movement

distance. Figure 4. 26 presents a visualisation of the underwater Qualysis cameras and the reflections balls along Mooring Line 1.

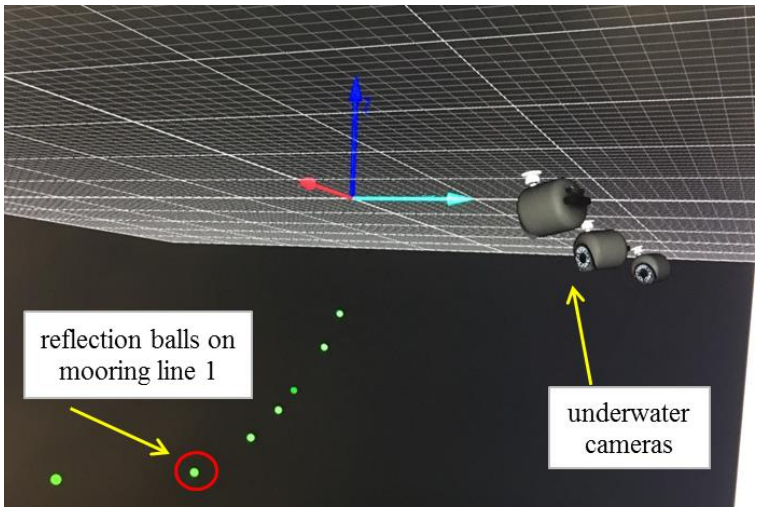

Figure 4. 26 Underwater cameras and the reflections balls on Mooring Line

Wave Probe Calibration

The Wave Probe 1 at the upstream position of the model should be calibrated before putting the model in the tank, and it will be used for recording the wave height during the tank tests. When calibrating this wave probe, the height of the wave probe underwater part will be changed and the output in voltage signal will be input into the data acquisition system. For the sonic wave probe – Wave Probe 2, it does not need to be calibrated in this experiment, as the sonic wave probe calibration factors does not really change and its data might be affected by the model reflected waves. However, it is still worth to use this in line wave probe as a phase reference purpose, so that the wave at certain point can be checked if there are some unexpected platform motion happening. Thus, only the wave data been collected in front of the model will be used

for the regular/irregular wave analysis and the sonic wave probe data will be used mainly for a reference purpose. By changing the vertical displacement of the wave probe underwater part, the different voltage signals will be input into the A/D converter and Spike software. As shown in Figure 4. 21, each hole of the upper beam is 2 mm apart. In this calibration, the wave probe will be adjusted from -60 mm to +60 mm. The calibration result is shown in Figure 4. 27 (a), which shows that the calculated voltage can match perfect with the measured data. The calibration residuals are then been checked, as shown in Figure 4. 27 (b). It can be seen that the residuals are larger when the displacement is at ±60 mm suggesting some non-linearity in the wave probe; however, the residuals are still within the 95% uncertainty confidence level, which is acceptable as recommended by the ITTC report (ITTC, 2014). The calculation details can be found in Appendix 3.

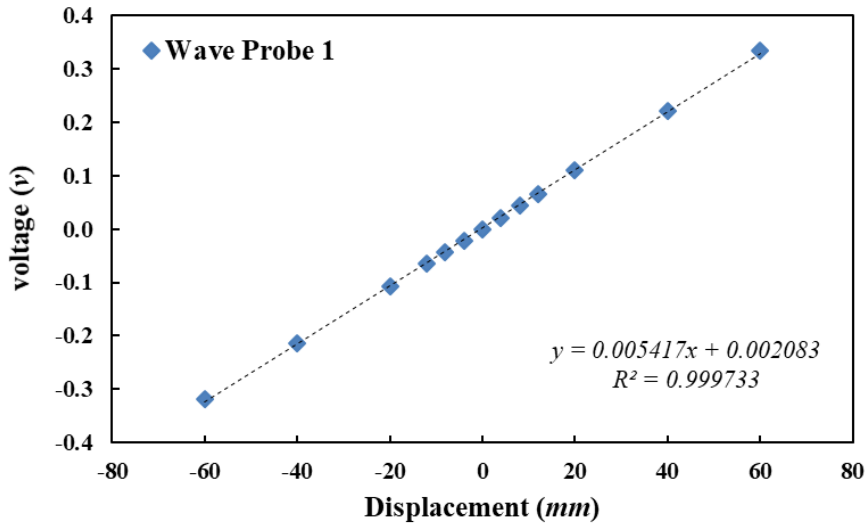

(a) Calibration result

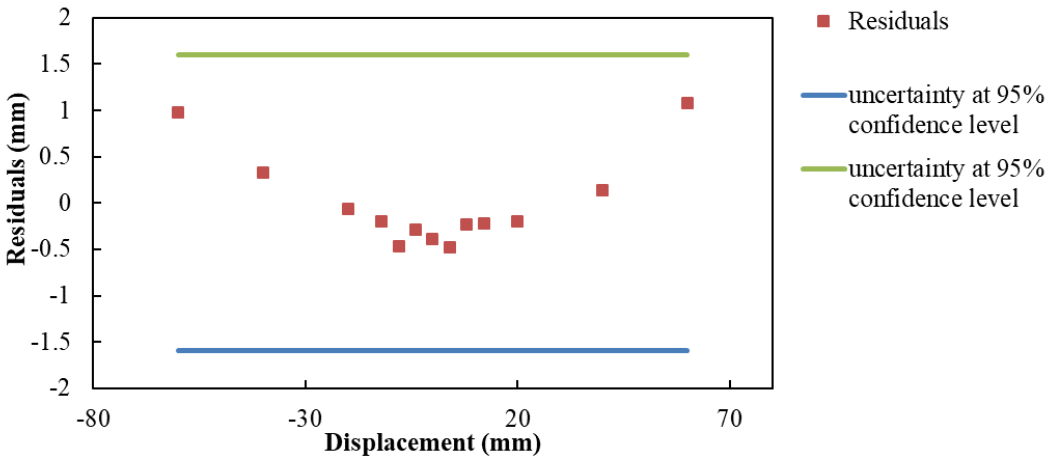

(b) Calibration residuals

Figure 4. 27 (a) Calibration result and (b) Calibration residuals for Wave Probe 1

Load Cells Calibration

This part will introduce the calibration of the three underwater load cells (or the so called transducer). As shown in Figure 4. 11, when facing towards the wave maker, the underwater load cell at the rear of the tank is named as Load Cell 1; at the left of the tank is named as Load Cell 2; at the right of the tank is named as Load Cell 3. Each of the load cells will holding a range of weights from 0 to 2 kg and the interval is 0.1 kg. Figure 4. 28 shows the process used to calibrate each load cell. The load cells use LVDTs (linear variable displacement transformers) rather than strain gauges to measure displacement which is then converted to load.

With the weight on and the tension been generated on the mooring line, the load cell will then generate some voltage. The voltage signal will then be enlarged by the amplifier and input into the A/D converter and Spike software, as shown in Figure 4. 29. A series of mass (from 0 kg to 2 kg with increment of 0.1 kg) will be put on the

load cells and the resulted voltage will be recorded. Figure 4. 30shows the calibrated results.

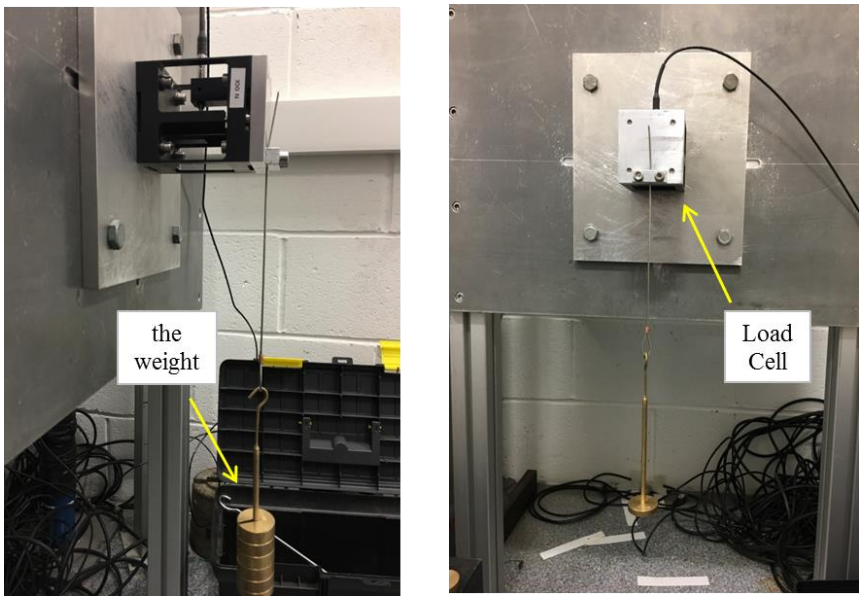

Figure 4. 28 Calibrating the load cell

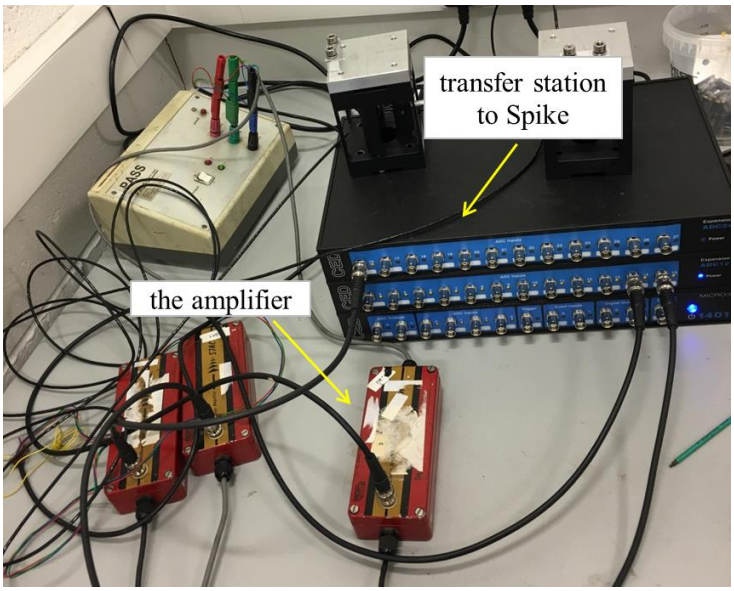

Figure 4. 29 Signal transfer station

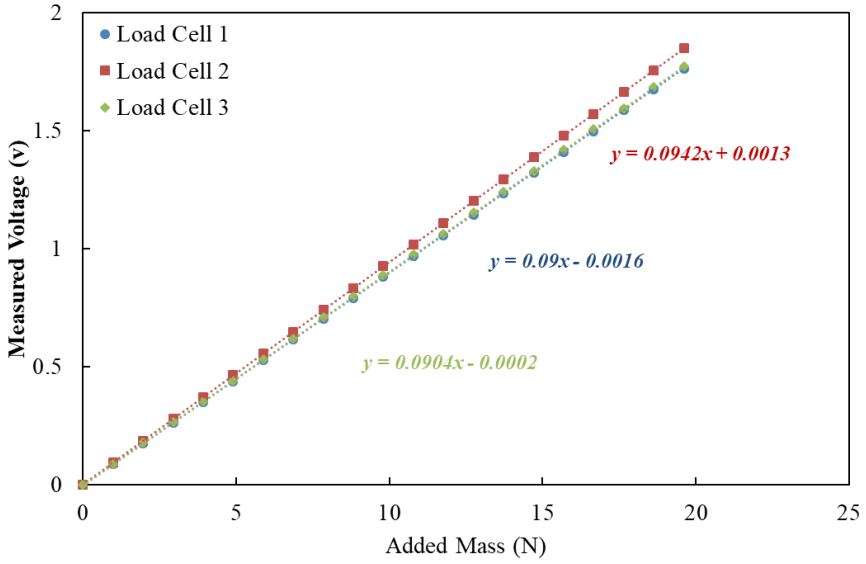

Figure 4. 30 Load cell calibration results

Then, by using the three calibration factors gained from Figure 4. 30, these mass will be put on the load cells again to conduct a re-measurement of the reading weight and check about the errors. The details are shown in Appendix 4 which shows that the error is all less than 1%.

Sea State Calibration

Before the start of the experiment, the final step would be to calibrate the irregular waves (the wave data is from Shin, 2011) passing through the model. This wave calibration is conducted by putting the upstream wave probe (Wave Probe 1) at the exact position where the model will be situated through the tests, so that the wave can be captured exactly of what the model is interacted with. The running time of the irregular wave calibration for each sea state will be the same when put the model in. The four sea states in this experiment are shown in Table 4. 8. Then the wave probe will measure the waves generated by the wave maker in the absence of the model. The

intention is that the discrepancy between measured and target significant wave height is less than 2% of the target value. If the measured significant wave height is beyond the expected value, then a gain factor will be applied to the wave maker setup data and this procedure will keep repeating until the difference between the measured value and the target value is less than 2%.

Figure 4. 31 shows the wave amplitude distributions from Sea State 1, the fitted curve can show that it is generally fits the Rayleigh distribution, although there are some unexpected points at the peak. In addition, the measured significant wave heights are matching quite well with the target significant wave heights in each sea state, as shown in Table 4. 8, which shows the satisfactory of the wave maker's work. The results for other three sea states (includes the wave spectrum) are shown in Appendix 5, which all show the similar satisfactory results presented here. The wave spectrum from Sea State 1 is shown in Figure 4. 32, where it shows perfect match between the measured wave from Wave Probe 1 and the calculated target wave spectrum. The target wave spectrum is calculated by using the JONSWAP equation and the detail is shown in Appendix 14.

Table 4. 8 Wave parameters for the four sea states

	Target Full Scale		Target Tank Scale		Measured Tank Scale	
Case No.	Tp (*s*)	Hs (*m*)	Tp (*s*)	Hs (*m*)	Tp (*s*)	Hs (*m*)
1	9.700	3.660	1.128	0.050	1.093	0.050
2	11.300	5.490	1.314	0.074	1.302	0.075
3	13.600	9.140	1.581	0.124	1.569	0.124
4	17.000	15.240	1.976	0.206	1.883	0.205

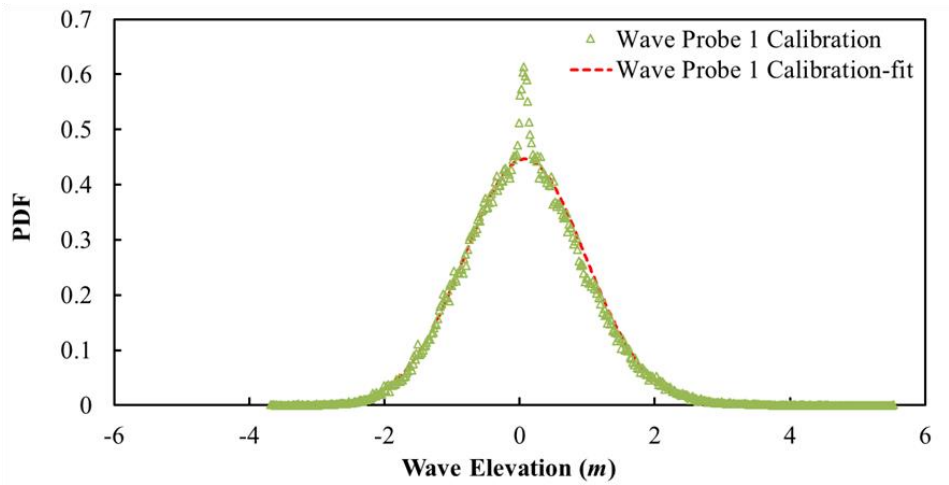

Figure 4. 31 Wave amplitude distribution, measured by Wave Probe 1 for Sea State 1 (full scale)

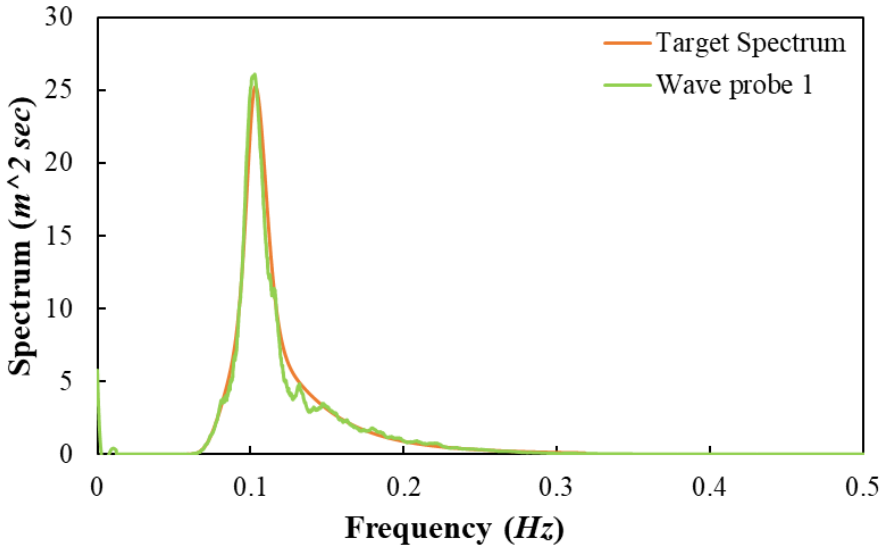

Figure 4. 32 Wave spectrum, measured by Wave Probe 1 compared with the target wave spectrum, for Sea State 1 (full scale)

4.6 Daily Check and After Experiment

To make sure that the tank tests results are as much accurate as possible, there are some necessary daily checks need to be conducted before the start of each experiment day, such as the water depth - as this will affect the wave properties generated by the wave

maker, and the model position need to be checked daily to ensure the leaking does not happen.

In addition, after the experiment been done completely, the whole model dimensions, mass, COG, pitch inertia, mooring line length and the underwater Qualysis balls positions are all need to be measured again to double check that there has no leaking and the model has not changed so that the experiment results can be relied upon.

4.7 Summary

This chapter gives the idea about how the model been designed and constructed, what equipment are being used through the experiment and how does them been calibrated. These essential procedures show the fidelity of the acquired experimental results.

Chapter 5 Spar-Only Tank Test

5.1 Introduction

This chapter will give the details of the tank test data and the analysis of the experimental results for the spar-only test campaign. The free decay tests for the spar platform will be conducted first. The natural frequencies and the damping ratios from the tests will be given. For the regular wave tests, the wave with one chosen wave height and a range of different frequencies will be generated by the wave maker and passing through the model, allowing the platform RAOs to be analyzed. Then the four irregular wave sea states will be applied on the model to check the survival condition of the model. All of the tank tests data will be compared with the numerical results. For both the tank tests and the numerical results, the platform motion is defined at the reference point of the model on water surface.

5.2 Free Decay Test

As a main parameter which can affect the platform's dynamic behaviour, the natural frequencies can be obtained by analysis of the free decay test.

The free decay tank test was conducted by using a pole to give the model an initial displacement in each mode of motion and then let it freely oscillate until it is still. As the spar model is a perfect symmetrical cylinder, the pitch and roll, and the surge and sway will be the same. In addition, although there has no realistic scaled mooring line for the spar-only test, four elastic mooring lines have been used to prevent the model drifting away, which are sufficiently soft to make sure that the motion response for the

heave and pitch won't be affected by the presence of the lines. The sway will be ignored as the wave propagates only in one direction – along the X-axis. Therefore, only the surge, heave, pitch and yaw data will be recorded through the data acquisition system. Figure 5. 1 shows how did the free decay tests been conducted.

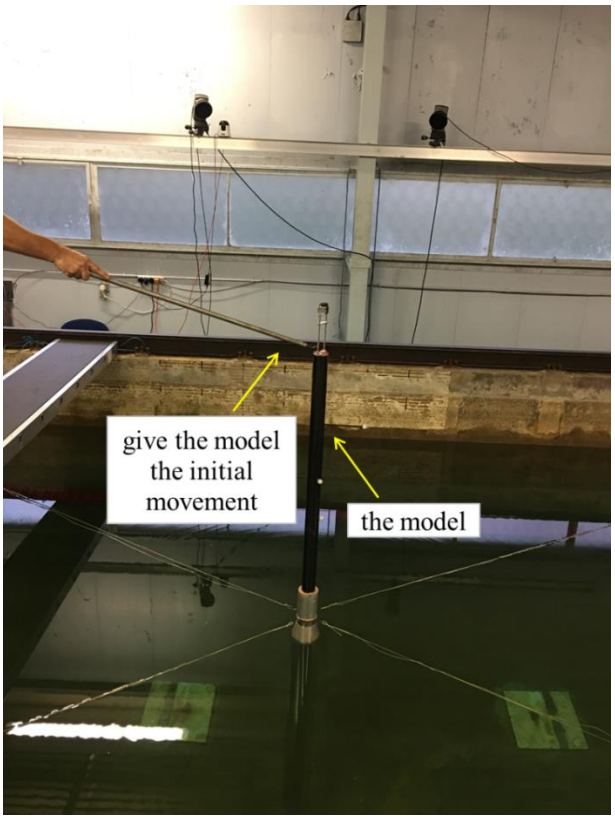

Figure 5. 1 Conducting a free decay test

It has been noticed that in the tank test, the damping ratio is more variable than the natural frequencies among each mode of the free decay test, so the free decay tests were repeated 10 times for surge, heave and pitch, and 5 times for yaw. The data recorded by Spike - each mode of motion in each free decay test, will then be selected for 5-10 cycles and a fit function will be applied to get the natural frequencies and the damping ratios.

Fit Function

To get the natural frequencies and the damping ratio from each mode of the free decay, a linearized model of free decay function has been used. This function is calculated in Microsoft Excel and fitted to the experiment data using the Excel Solver function. The equation of this linearized function is:

$$F(t) = A * e^{-\zeta * \omega_n * t} * cos\left(\sqrt{1-\zeta^2} * \omega_n * t - \varphi\right) + B \qquad (13)$$

where *F(t)* is fitted value after calculation – ideally this should be the same as the experimental data; *t* is the time history; *A* is the amplitude of the fitted function; ζ is the damping ratio; ω_n is the undamped natural frequency; φ is the phase angle and *B* is the offset.

The difference between the experimental value – *X(t)*, and the fitted value is represented by $F_e(t)$, thus

$$F_e(t) = X(t) - F(t) \qquad (14)$$

In reality, all the mode of motion will damp during the tank tests. The damped natural frequency is represented by ω_d and the relationship between the undamped and damped frequency is:

$$\omega_d = \sqrt{1-\zeta^2 * \omega_n} \qquad (15)$$

The sum of the squared error, $F_e\ (t)^2$ is calculated through the selected part of the time history and the Solver in the Excel will be used to minimise this value by adjusting the value of *A*, *B*, ζ, φ and ω_n. This is an iterative process; the solving method chosen is called the GRG Nonlinear. The GRG represents for the Generalized Reduced Gradient.

In solving nonlinear programming problems, the GRG is a reliable and precise method (Lee et al., 2004). The fitting examples for each mode of motion are given below.

For free decay in surge, since the soft moorings lead to a very low natural frequency, the surge decays in a small number of cycles; hence only two cycles were selected. Figure 5. 2 shows an example of the surge free decay and its fit curve. The fit curve function can calculate out the natural frequencies and the damping ratio. In the surge free decay test, as shown in Figure 5. 2, the small variations is from the coupling effect from the pitch motions. Also, it can be seen that the surge natural frequencies are away from both heave and pitch natural frequencies, which shows that the four station-keeping lines will not affect the heave/pitch natural frequencies.

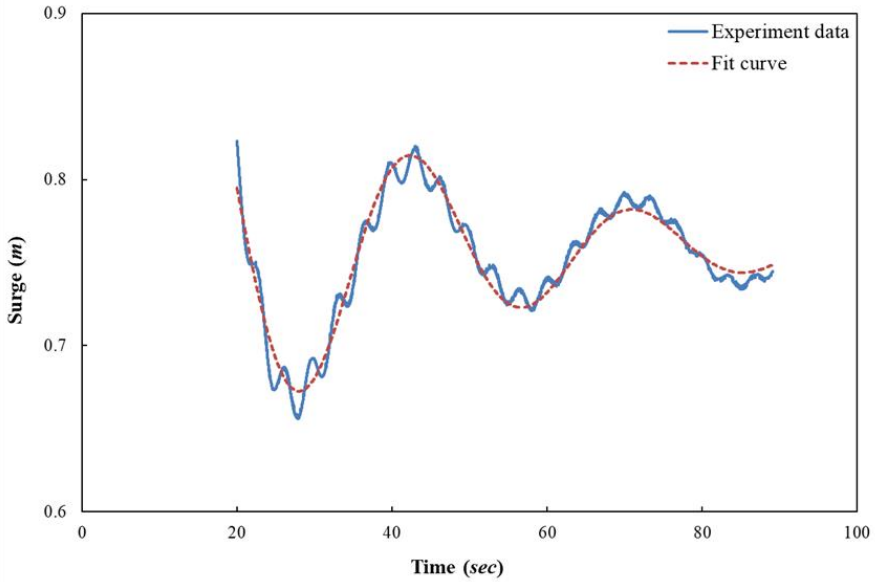

Figure 5. 2 Surge free decay in experiment, spar-only (tank test scale)

Figure 5. 3 presents one of the yaw free decay tank test with its fit curve, which shows that the fit curve matches very well with the tank test data and the yaw damps very

quickly. Figure 5. 4 and Figure 5. 5 shows the heave and pitch free decay with the fitting curves, respectively, which can give us their natural frequencies and damping ratios.

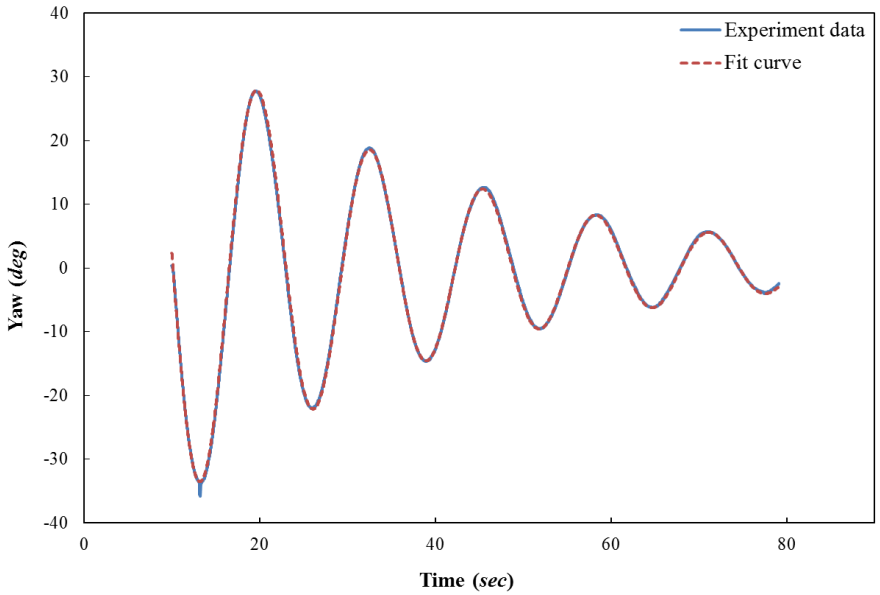

Figure 5. 3 Yaw free decay in experiment, spar-only (tank test scale)

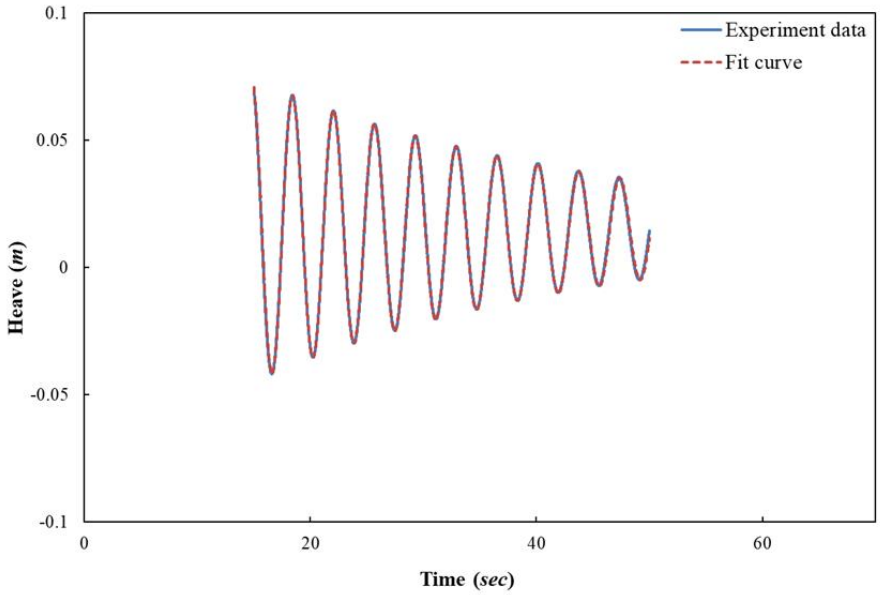

Figure 5. 4 Heave free decay in experiment, spar-only (tank test scale)

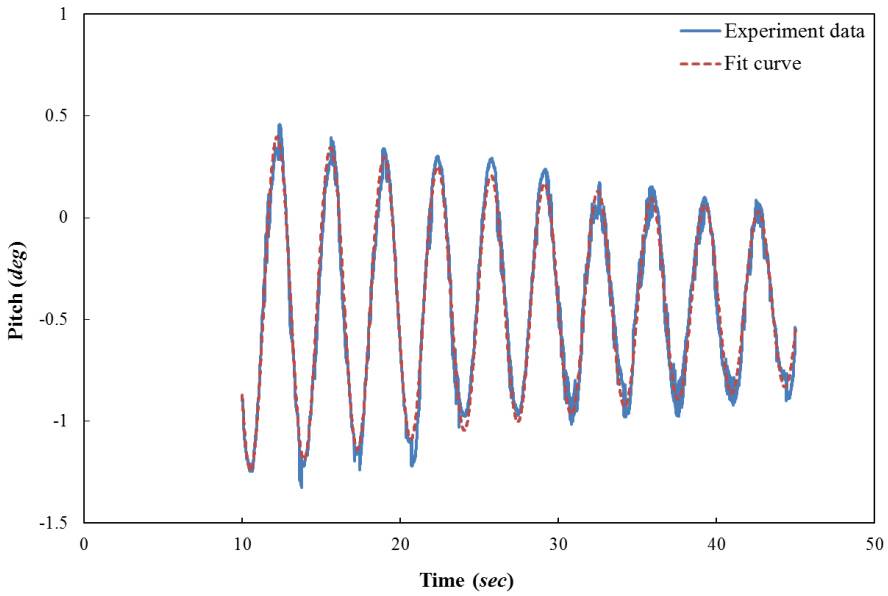

Figure 5. 5 Pitch free decay in experiment, spar-only (tank test scale)

Natural Frequencies

According to the GRG method introduced above, both the damping ratio and natural frequency for each mode of motion can be acquired. Table 5. 1 presents the mean value of measured natural frequencies of the spar platform and the NREL OC3-Hywind spar platform's, with its realistic mooring systems, natural frequencies. The pitch natural frequency is 0.0344 Hz and the heave natural frequency is 0.032 Hz. The surge and yaw natural frequency is acquired with soft moorings rather than realistic mooring lines. It can be seen that for the tank test in this thesis, the spar model's heave and pitch motion's natural frequencies are matching quite well with the NREL model. The big differences for the surge and yaw motion's natural frequencies are due to the effect of mooring systems.

Table 5. 1 Natural frequencies for spar-only acquired from the experiment compared with the NREL OC3-Hywind spar platform natural frequencies, with mooring lines (Ramachandran et al., 2013)

	Experiment Measured Value	Full Scale	NREL
Pitch Frequency (*Hz*)	0.292	0.034	0.034
Heave Frequency (*Hz*)	0.275	0.032	0.032
Yaw Frequency (*Hz*)	0.077	0.009	0.121
Surge Frequency (*Hz*)	0.034	0.004	0.008

Damping Ratio

Table 5. 2 presents the mean value and the standard deviation (STD) of the damping ratio for each mode of motion from the free decay tests. The mean value and the STD are calculated by the GRG method. For heave and pitch, the difference between each of the tests are below 2%. The small value of the STD shows that the damping although may change from each test but it is till stable.

Table 5. 2 Mean value and STD of damping ratio, for spar platform only acquired from the experiment

	Mean Damping Ratio	STD
Heave	0.014	0.004
Pitch	0.023	0.013

To make the numerical model as much as possible to match with the real tank model, a linear damping matrix has been added into the numerical simulations (i.e., in both FAST and FASTlink). This is a necessary procedure to make the numerical model hydrodynamic properties can be comparable with the tank test results. The damping

matrix are calculated by making the damping ratio from the numerical simulations matching with the experimental measured results. In this case, only the additional damping along heave direction is non-zero, which is 46,170.65 N/ (m/s):

$$\text{Damping Matrix for Spar platform only in FAST/FASTlink} = \begin{bmatrix} 0 & 0 & 0 & 0 & 0 & 0 \\ 0 & 0 & 0 & 0 & 0 & 0 \\ 0 & 0 & 46{,}170.65 & 0 & 0 & 0 \\ 0 & 0 & 0 & 0 & 0 & 0 \\ 0 & 0 & 0 & 0 & 0 & 0 \\ 0 & 0 & 0 & 0 & 0 & 0 \end{bmatrix}$$

The resulting total heave and pitch ratio in the numerical model are shown in Table 5. 3, which shows a very good agreement with the experiment model.

Table 5. 3 Damping ratio, for spar platform only in numerical/experiment model

Damping Ratio	FAST v8	FASTlink	Experiment Measurement
Heave	0.0141	0.0142	0.0143
Pitch	0.0233	0.0196	0.0225

5.3 Regular Wave Test

After checking the natural frequencies and the damping ratios of the model, a range of regular wave will be applied to the model to get the platform's heave and pitch Response Amplitude Operators (RAO). In this part, due to the lack of realistic moorings, only heave and pitch RAO will be analyzed. In addition, during the tank test, it is important to quantify the repeatability of the test results, to give an idea of the reliability of the experimental results. Finally, a linearity check for both the heave and pitch will be made. Table 5. 4 and Table 5. 5 present the tank test scale and the full scale wave data, respectively. The full scale wave data will be applied into FAST

and FASTlink for the numerical simulations. For the regular wave tank test, the wave height will not change through all the RAO tests, while the wave frequency will change in each test. The Measured Wave Amplitude data is measured by Wave Probe 1, which is in front of the model. To get the heave RAO, the equation is

$$Heave\ RAO = \frac{Heave\ Motion\ Amplitude\ (m)}{Wave\ Amplitude\ (m)} \tag{16}$$

For pitch RAO, the wave length will be needed, and the equation is shown below

$$Pitch\ RAO = \frac{Pitch\ Motion\ Amplitude\ (deg)}{arctan\frac{2 * \pi * Wave\ Amplitude}{Wave\ Length} * \frac{180}{\pi}\ (deg)} \tag{17}$$

According to the water depth effect on the wave speed, when the water depth (d) is less than half of the wave length (L), it is considered as shallow water, and the deep water is when $d > L/2$. Thus, the wave length will be calculated as:

For shallow water:

$$L = \frac{gT^2}{2\pi} * tanh(\frac{2\pi d}{L}) \tag{18}$$

For deep water:

$$L = \frac{gT^2}{2\pi} \tag{19}$$

Table 5. 4 Regular wave parameters, for spar-only tests (tank test scale)

Wave Frequency (*Hz*)	Wave Period (*s*)	Measured Wave Amplitude (*m*)	Wave Length (*m*)
1.229	0.814	1.187	1.034
0.950	1.053	1.288	1.731
0.717	1.395	1.170	3.037
0.506	1.976	1.230	5.922
0.410	2.441	1.324	8.409
0.358	2.790	1.135	10.230
0.344	2.906	1.254	10.826
0.331	3.022	1.292	11.416
0.319	3.139	1.207	12.003
0.307	3.255	1.229	12.584
0.302	3.311	1.263	12.861
0.297	3.367	1.279	13.138
0.292	3.425	1.248	13.425
0.287	3.487	1.242	13.734
0.282	3.546	1.214	14.019
0.278	3.604	1.169	14.303
0.276	3.627	1.147	14.417
0.275	3.636	1.293	14.463
0.273	3.662	1.141	14.587
0.271	3.690	1.063	14.723
0.269	3.720	1.126	14.870
0.268	3.732	1.120	14.926
0.264	3.787	1.117	15.197
0.261	3.836	1.191	15.433
0.257	3.891	1.336	15.697
0.253	3.952	1.355	15.993

Table 5. 5 Regular wave parameters, for spar-only tests (full scale)

Wave Frequency (*Hz*)	Wave Period (*s*)	Wave Amplitude (*m*)	Wave Length (*m*)
0.143	7.000	1.260	76.478
0.110	9.060	1.260	128.114
0.083	12.000	1.260	224.752
0.059	17.000	1.260	438.294
0.048	21.000	1.260	622.304
0.042	24.000	1.260	757.050
0.040	25.000	1.260	801.144
0.039	26.000	1.260	844.852
0.037	27.000	1.260	888.198
0.036	28.000	1.260	931.207
0.035	28.480	1.260	951.741
0.035	28.960	1.260	972.204
0.034	29.460	1.260	993.451
0.033	30.000	1.260	1016.319
0.033	30.500	1.260	1037.425
0.032	31.000	1.260	1058.468
0.032	31.200	1.260	1066.868
0.032	31.280	1.260	1070.226
0.032	31.500	1.260	1079.451
0.032	31.740	1.260	1089.501
0.031	32.000	1.260	1100.375
0.031	32.100	1.260	1104.553
0.031	32.580	1.260	1124.577
0.030	33.000	1.260	1142.059
0.030	33.470	1.260	1161.578
0.029	34.000	1.260	1183.537

Repeatability Check

To make sure that the tank test results are reliable, it is necessary to repeat a test more than once. In this experiment, a wave frequency (f = 0.2688 Hz, wave amplitude = 0.017m) has been chosen from Table 5. 4. This wave will be applied to the spar platform model three times. In this process, other wave frequencies will be run by the wave maker between each of the repeat test, which can make sure that the results are more accurate. Table 5. 6 presents the results from the repeated tests, which shows a very good agreement among the three tests in the Measured Wave Amplitude, Heave Amplitude and Pitch Amplitude. It can be seen from the table that the experiment results are very stable.

Table 5. 6 Repeatable check test results, spar-only (tank test scale)

	Data20	Data22	Data24	MEAN
Input frequency (*Hz*)	0.269	0.269	0.269	0.269
Measured Wave Amplitude (*mm*)	15.235	15.201	15.427	15.288
Heave Amplitude (*mm*)	107.593	106.202	106.459	106.751
Pitch Amplitude (*deg*)	2.839	2.834	2.854	2.842

Heave and Pitch RAO

Figure 5. 6 and Figure 5. 7 present the heave and pitch RAO of the spar platform, respectively. The experimental data has been compared with the numerical simulation results – the FAST and FASTlink, as shown in the figures. The heave and pitch peak responses from experimental measurement are at 0.032 Hz and 0.035 Hz, which are well matched with the natural frequencies measured from the free decay tests.

In Figure 5. 6, it is observed that the FAST and FASTlink data are matching quite well with the peak response frequency of the experiment, but the amplitude of the RAOs from the numerical simulations are much higher than the experimental results. As discussed in the free decay test, an additional damping has been added to the heave motion in both FAST and FASTlink, which is 46,170.650 N/ (m/s), to make the numerical simulation match with the experiment model damping. The resulted heave damping ratio (with the additional damping) in FAST is 0.0141 and 0.0142 in FASTlink, which are both smaller than the heave experiment damping ratio– 0.0143. Thus, the experimental heave RAO is smaller than the numerical simulations. The drag coefficient for the platform in the numerical simulation is 0.6 (which is the same with the NREL model).

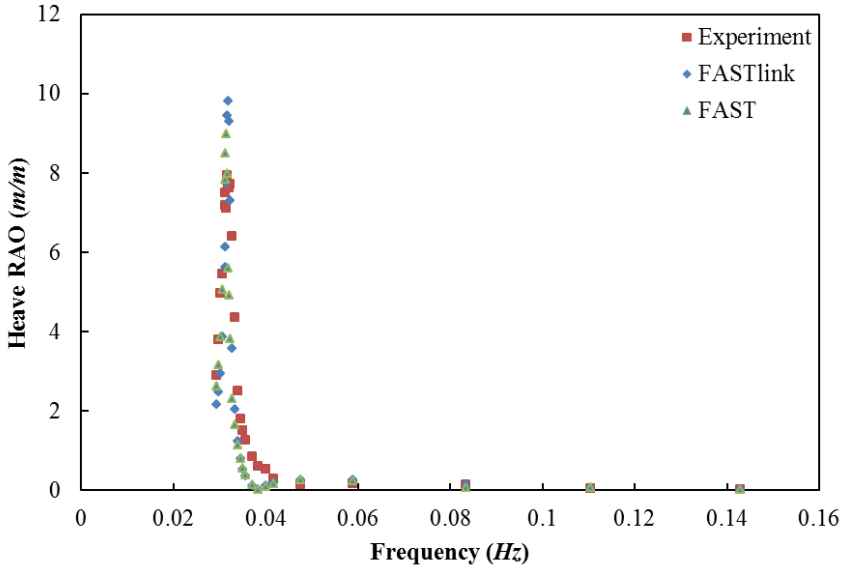

Figure 5. 6 Heave RAO for spar-only (full scale)

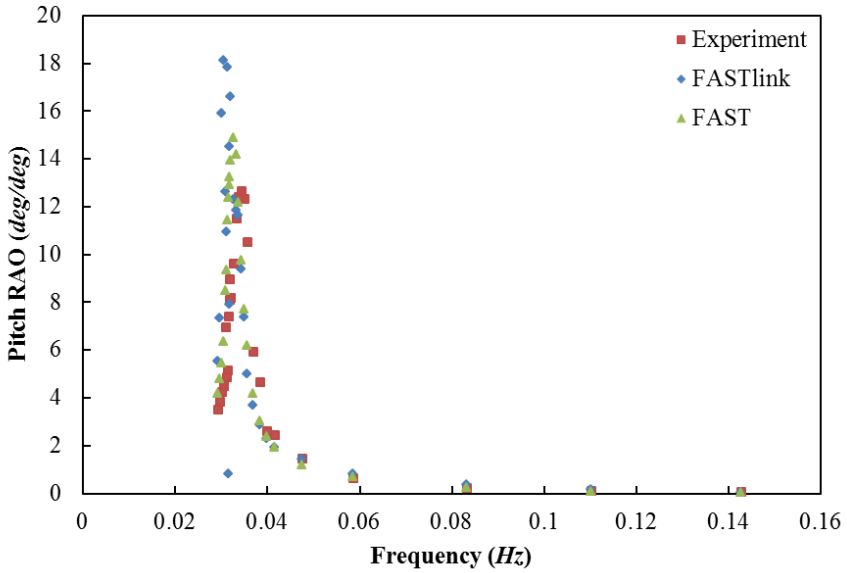

Figure 5. 7 Pitch RAO for spar-only (full scale)

For pitch RAO, as shown in Figure 5. 7, the numerical simulations still overestimate the platform responses amplitude. The pitch damping ratio in FAST is 0.0233 and 0.0196 in FASTlink. A small difference in the peak response frequencies has been noticed – the numerical peak response frequencies are around 0.328 Hz. Such differences have also been found out in other research (Shin, 2011), where the numerical results (FAST) of pitch for both peak RAO and its frequency are higher than experimental measurement.

Compared with the experimental results, FAST tends to predict the spar platform dynamic responses better than FASTlink, as the peak RAO is closer to the experiment results compared with the FASTlink curve.

Heave and Pitch Linearity Tests

Linearity tests have been conducted for both heave and pitch, at their peak RAO frequencies. The purpose of the linearity test is to check how linear is the experimental results. A range of wave amplitude from 0.004 m to 0.018 m has been applied to the spar model. The wave frequencies are at the peak RAO frequency of heave and pitch, respectively. The detailed wave data are shown in Table 5. 7 and Table 5. 8. With the linear increasing of the wave amplitude, at the set wave frequency, the resulted platform RAO is expected to decrease which is due to the increasing of viscous damping. Since the peak RAO pitch frequencies are different between the FAST and FASTlink and experiment, the FAST and FASTlink calculation will use their own peak pitch RAO frequency:

- FAST peak pitch frequency is 0.033 Hz and the wave length is 1037.425 m.
- In FASTlink, the frequency is 0.031 Hz and the wave length is 1104.553 m.

Figure 5. 8 presents the linearity tank test results for heave which shows the heave RAO decreasing with the increasing wave height in both FAST and experiment, which is as expected. While in FASTlink, the Heave RAO increases with increasing wave height. Figure 5. 10 shows the heave amplitude in FAST and FASTlink, which shows that the heave amplitude increases more rapidly with wave height in FASTlink than in FAST. This shows an agreement with the heave RAO in Figure 5. 6 that the FASTlink has higher value than FAST.

Table 5. 7 Heave linearity tank test wave data for spar-only

Tank Test Scale			Full Scale	
Wave Frequency (*Hz*)	Input Wave Amplitude of Wave Maker (*m*)	Measured Wave Amplitude (*m*)	Wave Frequency (*Hz*)	Wave Amplitude (*m*)
0.278	0.004	0.004	0.032	0.296
0.278	0.006	0.006	0.032	0.444
0.278	0.008	0.008	0.032	0.592
0.278	0.010	0.010	0.032	0.740
0.278	0.012	0.012	0.032	0.888
0.278	0.014	0.014	0.032	1.036
0.278	0.016	0.016	0.032	1.184
0.278	0.017	0.017	0.032	1.260
0.278	0.018	0.018	0.032	1.332

Table 5. 8 Pitch linearity tank test wave data for spar-only

Tank Test Scale				Full Scale
Wave Frequency (*Hz*)	Input Wave Amplitude of Wave Maker (*m*)	Measured Wave Amplitude (*m*)	Wave Length (*m*)	Wave Amplitude (*m*)
0.297	0.004	0.004	13.138	0.296
0.297	0.006	0.006	13.138	0.444
0.297	0.008	0.008	13.138	0.592
0.297	0.01	0.010	13.138	0.740
0.297	0.012	0.012	13.138	0.888
0.297	0.014	0.014	13.138	1.036
0.297	0.016	0.016	13.138	1.184
0.297	0.017	0.017	13.138	1.260
0.297	0.018	0.018	13.138	1.332

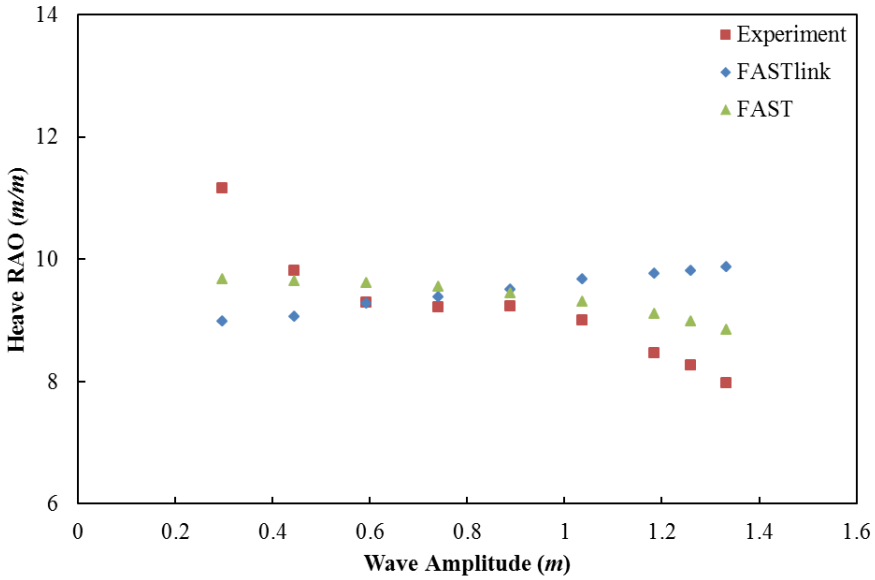

Figure 5. 8 Heave linearity check for spar-only, at the platform heave motion natural frequency (full scale)

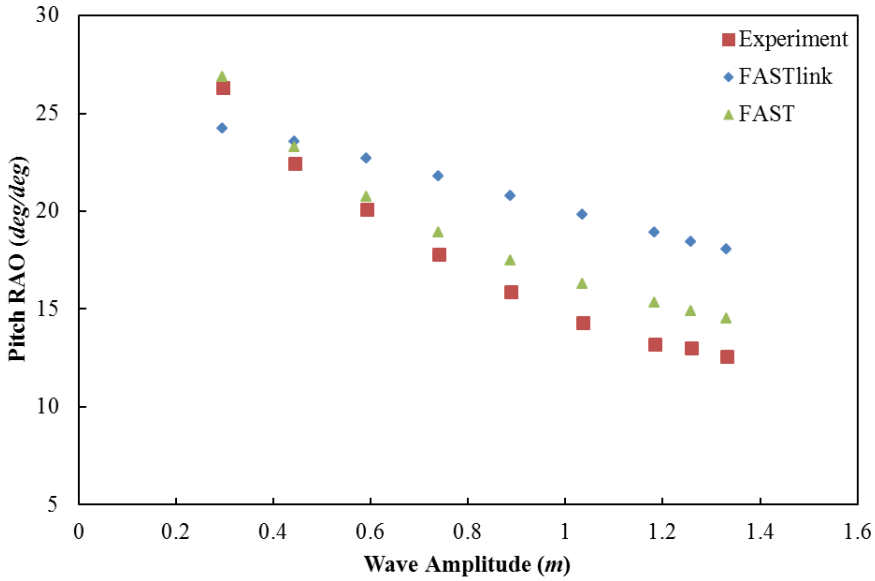

Figure 5. 9 Pitch linearity check for spar-only, at the platform pitch motion natural frequency (full scale)

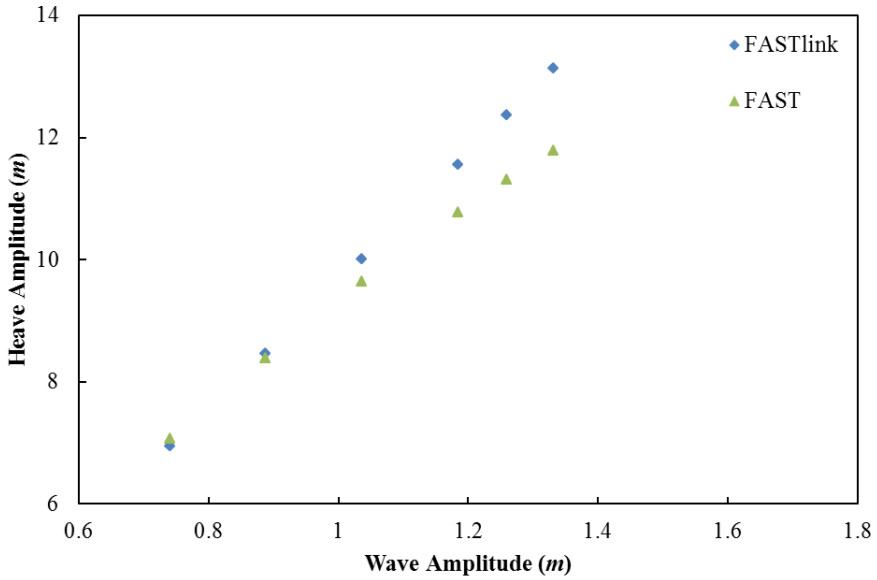

Figure 5. 10 Heave motion amplitude in FAST and FASTlink, spar-only, at the platform heave motion natural frequency (full scale)

In Figure 5. 9, it can be seen that in both numerical and experimental results, the pitch RAOs are decreasing with increasing wave amplitude. The pitch RAO differences between the three methods are increasing with increasing wave amplitude; FASTlink is tends to overestimate the pitch RAO more than FAST.

5.4 Sea States

Four sea states were then applied to the model. Each wave ran for 20 minutes in the tank test and 9999 seconds (due to the limit of the software) in the numerical simulations. A JONSWAP spectral wave model with a peak shape parameter 3.3 is been generated by the wave maker in the tank. The detailed wave data of the four sea states have been shown in Chapter 4, Table 4. 8.

The four sea states generated by the wave maker (measured from Wave Probe 1 at the calibration stage) will be compared with the wave in both FAST and FASTlink, and the detailed plotting will be shown in the Appendix 5. Then the platform's heave and pitch probability density function (PDF) and the response spectrum from Sea State 3 will be presented in this part (the other three sea states results are presented in the Appendix 6).

Wave Spectrum – Sea State 3

Both the PDF and the spectrum are calculated in the MATLAB code. The code detail can be find in the Appendix 13. Figure 5. 11 shows the numerical wave PDF for Sea State 3 which shows that the wave generated in the two numerical software are matching well. The wave amplitude is mostly range within 5 m and can be up to around 9.5 m.

Figure 5. 12 presents the numerical wave spectrum compared with the data measured from the Wave Probe 1 (at the calibration stage), which shows that the three approaches are matching perfectly.

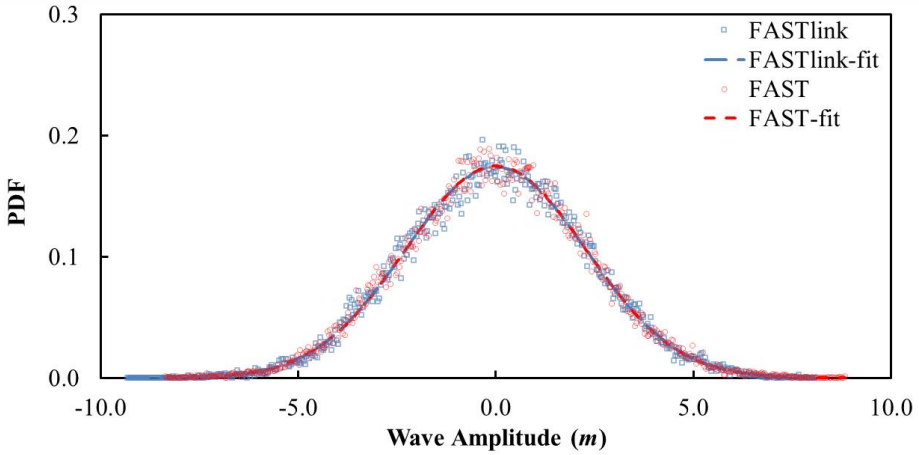

Figure 5. 11 Wave amplitude PDF for Sea State 3, spar-only (full scale)

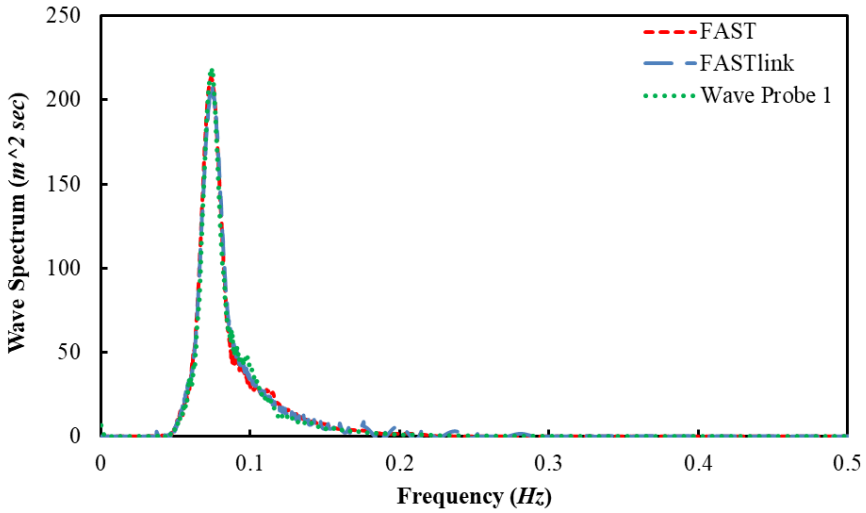

Figure 5. 12 Wave spectrum of both numerical and experimental for Sea State 3, spar-only (full scale)

Heave and Pitch Motion - Sea State 3

Due to the lack of realistic moorings, only the heave and pitch motion's PDF and motion spectrum will be presented at this part. The FAST and FASTlink generated results will then be compared with the experimental measured data (recorded by the Qualysis and Spike). The experimental measured data have been calculated into full

scale before calculating its PDF and spectrum. In Figure 5. 13, it shows that the heave motion in experiment has similar amplitude range (about 1 m) with the numerical results, FAST shows a higher PDF value than FASTlink and experiment.

For experimental heave spectrum, as presented in Figure 5. 14, the first and major peak is happening at its natural frequency and the other peak is at the peak wave frequency – around 0.070 Hz. FAST shows a very small peak at the heave natural frequency while FASTlink and experiment present higher energy than at the peak wave frequency. For the heave natural frequency, although FASTlink shows a much higher peak value than the experiment, but when calculating the area (which represents its energy), it shows that they are nearly the same (the area for FASTlink is around 0.155 and experiment is around 0.154), which shows that the energies are almost the same. Thus, in this sense, FASTlink can be considered to predict the platform responses reasonably well. However, it seems that the energy in FASTlink is concentrated close to the heave natural frequency, suggesting a highly tuned system, while the energy in the tank tests spreads over a wider range of frequencies. This could be due to the viscous effects in the tank tests which cannot be calculated accurately in FASTlink. In fact, as shown in the linearity tests, FASTlink has shown its limitations in heave viscous damping calculations.

The pitch PDFs are matching perfectly between the FAST and the experiment while FASTlink shows a quite wide range of its motion amplitudes, as shown in Figure 5. 15. For the pitch motion spectrum, the major peak for FAST and experiment is at the

peak wave frequency, while FASTlink shows a clear peak spectrum at the pitch natural frequency, while the experiment results just show a very tiny peak.

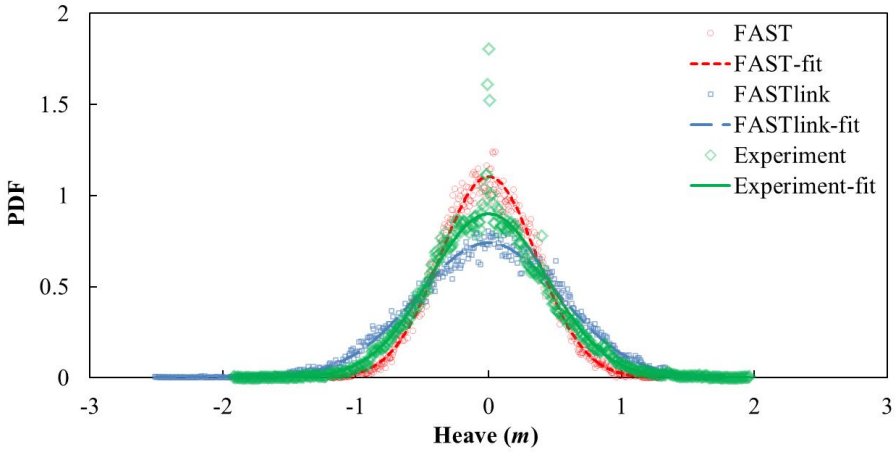

Figure 5. 13 Heave motion amplitude PDF for Sea State 3, spar-only (full scale)

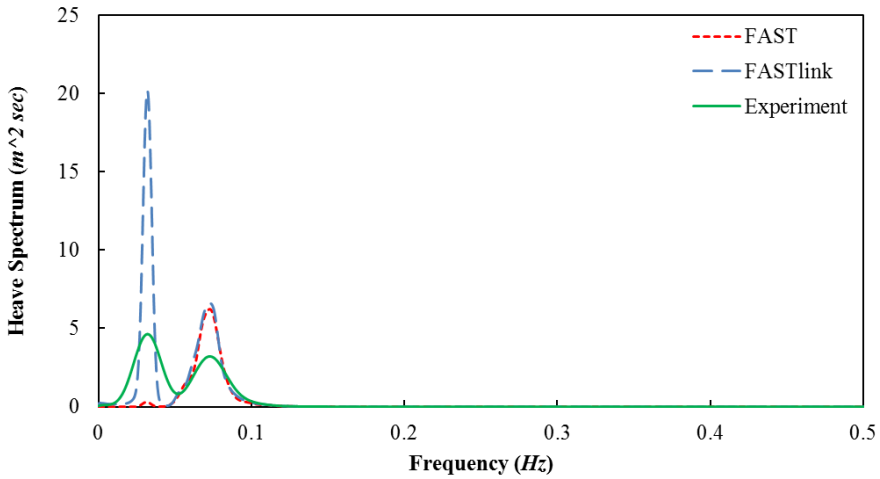

Figure 5. 14 Heave motion spectrum for Sea State 3, spar-only (full scale)

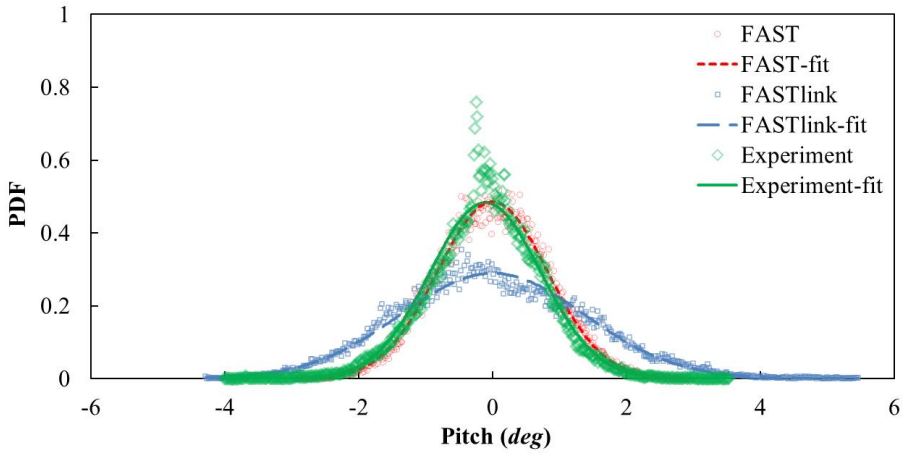

Figure 5. 15 Pitch motion amplitude PDF for Sea State 3, spar-only (full scale)

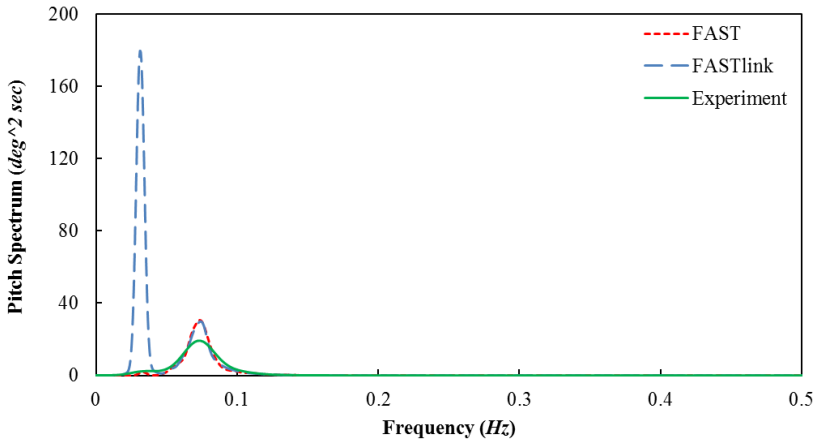

Figure 5. 16 Pitch motion spectrum for Sea State 3, spar-only (full scale)

5.5 Summary

This chapter presented the experimental results along with the numerical results for the OC3-Hywind spar model. Due to the lack of realistic mooring lines, only the heave and pitch motion have been analyzed in this chapter. A free decay test has been conducted first in the tank to get the heave and pitch natural frequencies and the results are matching quite well with the NREL paper. The damping ratios have small differences from each tank test, but the differences are all less than 1% for both the heave and pitch, which is acceptable.

A range of regular waves then has been generated by the wave maker in the tank to check the RAO of the spar platform. One of the waves has been repeated three times at the tank test to make sure that the results from the experiment are reliable. The linearity tests have been conducted for both heave and pitch with the peak RAO frequency, respectively, and a range of wave heights. The results show that with the increasing of the wave heights, the heave and pitch RAO decreasing in the experiment and FAST. But for heave RAO linearity check in FASTlink, it failed, which could be due to the software code calculation problems. The peak RAO frequencies for both heave and pitch are matching well, but the peak RAO amplitude shows that the numerical simulations tend to overestimate the results than experiment. Four sea states, i.e., irregular waves, have been run for the spar platform, and the Sea State 3 results have been presented in this part. The wave spectrums (in full scale) have been checked for both numerical and tank tests. The numerical wave spectrum shows a higher value than the wave generated by the wave maker, which also result a higher platform motion's spectrum in numerical simulations. With the increasing of the wave significant height and its period, the wave spectrum, heave and pitch motion spectrum increase. For both heave and pitch motion's PDF, the ranges of motion are increasing and the major motion's PDF are decreasing. Two peaks have been observed in both heave and pitch motion spectrum, which are caused by its natural frequencies and the peak wave frequency. But the pitch does not show very obvious peak at its natural frequency and disappearing with the increasing of wave spectrum, while the heave motion keeps showing the major peak at its natural frequency.

Chapter 6 Spar with Mooring Line Tank Test

6.1 Introduction

In this chapter, the experimental results for the spar model with three realistic mooring lines will be presented and compared with the numerical simulations. The free decay tank test data will be analyzed first to check the platform's natural frequencies and the damping ratio. In the regular wave tank test, the snatching phenomenon of the floating system has been observed in some wave frequencies and the time history will be discussed for some of these cases. The RMS (root-mean-square) values of platform motions, the tensions of the three mooring lines and the motion of Mooring Line 1 will be discussed. For the mooring line motion, the experimental results will be compared with numerical results obtained from the FASTlink software. For the four sea state tests, platform motions, mooring line motions and tensions will be presented.

6.2 Mooring Set-up

Before the start of all the tank tests for the spar with realistic mooring lines, the anchor positions for the three load cells needed to be adjusted to get pre-tensions which match as well as possible with the numerical simulation predictions. Also, after running all the waves, the pre-tension of the three mooring lines will be measured again to check if the transducer zero drifted and thus make sure that the measured results are correct.

Mooring Line Configuration

The mooring line configuration was shown in Figure 4. 5. The Mooring Line 1 is parallel with the positive X-axis and the other two mooring lines are symmetrically

oriented at 30° to the X-axis. Through all the tests, the waves only propagate in the positive X-axis direction. Thus, only the surge, heave and pitch motion will be analyzed. In both regular and irregular wave tank tests, the motion of Mooring Line 1 will be recorded by the underwater cameras. The three mooring tensions will be measured by the load cells and recorded by Spike.

Pre-tension

Before the tank test start, the three mooring's pre-tension have been measured to check if it matches with the numerical model. Table 6. 1 presents the three mooring line pre-tensions from the experiment and the two numerical models. As shown in the table, the experiment model has larger pre-tensions than the numerical model and the tension on Mooring Line 2 and 3 are slightly different. This is caused by small inaccuracies in locating the model in the tank; it was found to be very hard to adjust the position of the anchor frame extremely precisely, and the transducers are seen to be very sensitive to small movements. Thus, the pre-tension shown in Table 6. 1 were the best results achievable at the tank. Good agreement is seen between Mooring Line 2 and 3 in both numerical models as expected due to symmetry, but the FASTlink calculations show higher tension on each of the mooring lines than in FAST. This is assumed to be due to the different mooring line theory used in the two software packages, as discussed in Chapter 2.

Static Check

When the water surface and the model are still, three masses – 100g, 200g, 300g were added on top of the model tower; the mooring tensions were then recorded during this process to check if the tension changes linearly. As the masses were added, the model draught increased, causing the mooring lines to become more slack; thus the tension should be expected to decrease. To make sure the model anchor position does not change during the tests, this static check was also conducted after all the wave frequencies been run. All values presented are average values measured when the model is still. The figures below show the static check results of the platform position along X-axis and Z-axis. The three mooring tensions at the start and end of the experiment will also be compared with the results from FASTlink (which shows the discrepancies between the numerical results and experimental measurements). The figures in this part are shown at the tank test scale.

Table 6. 1 Pre-tensions of the 3 mooring lines

	Experiment test scale (*N*)	Experiment full scale (*kN*)	FASTlink (*kN*)	FAST (*kN*)
Tension 1	0.938	380.041	298.129	252.542
Tension 2	0.655	265.405	189.129	159.806
Tension 3	0.732	296.567	189.129	159.806

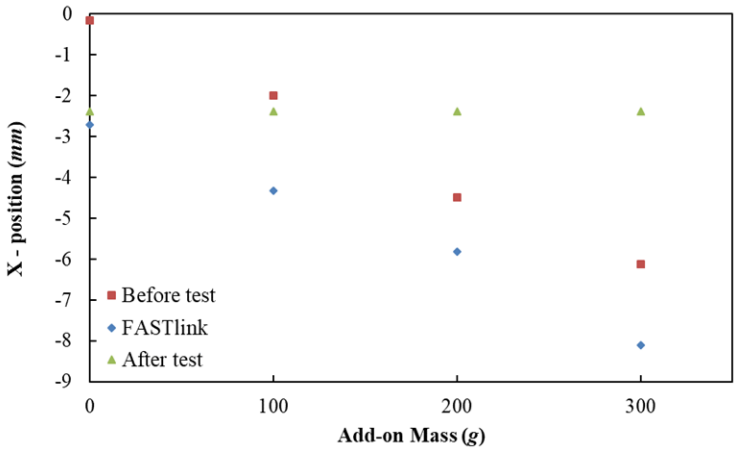

Figure 6. 1 Static check – the platform position along X-axis, before and after all the tank tests, compared with results in FASTlink (tank test scale)

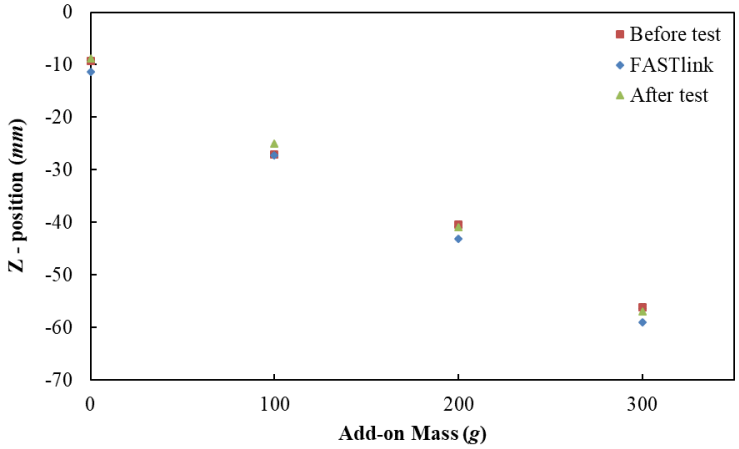

Figure 6. 2 Static check – the platform position along Z-axis, before and after all the tank tests, compared with results in FASTlink (tank test scale)

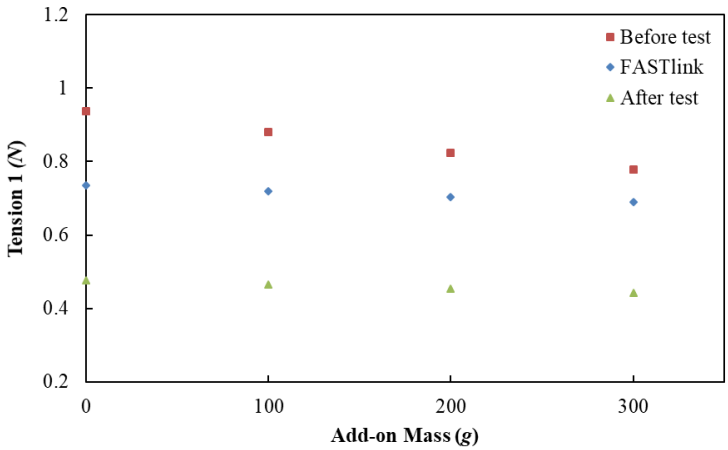

Figure 6. 3 Static check – Mooring Tension 1, before and after all the tank tests, compared with results in FASTlink (tank test scale)

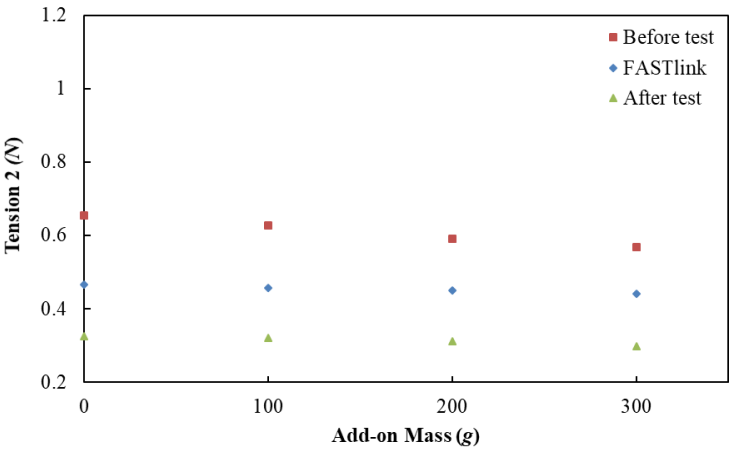

Figure 6. 4 Static check – Mooring Tension 2, before and after all the tank tests, compared with results in FASTlink (tank test scale)

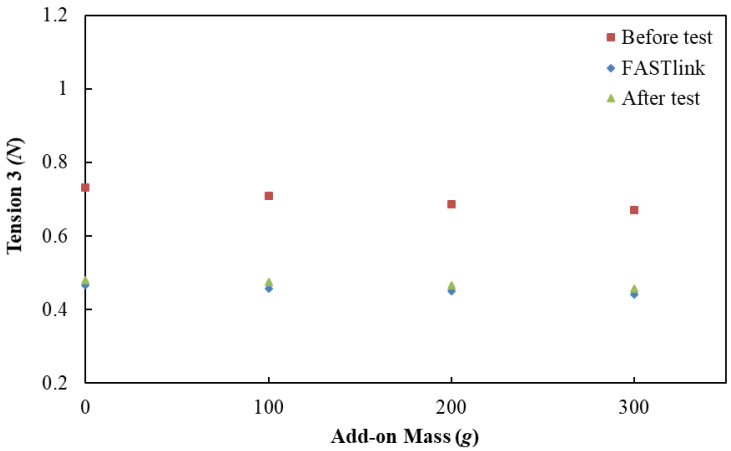

Figure 6. 5 Static check – Mooring Tension 3, before and after all the tank tests, compared with results in FASTlink (tank test scale)

In Figure 6. 1 and Figure 6. 2, it can be seen that the platform position along Z-axis matches quite well between the numerical model and the tank test model. Also, it can be seen that the platform Z position does not change during the tank tests, as the results between the start and the end of experiment do not change. The position along the X-axis at the start of the experiment and the FASTlink also match well. The change of the X-position value results from the mooring model symmetry along the X-axis; the changing of the Z-position, leads initially to an unbalanced tension force in the mooring system which results in a change in the X-position. For the post-test X-position, it seems that the platform position has changed by about 2.4 mm (and 0.178 m in full scale) when no additional mass has been applied, which indicates that the anchor position might have changed during the test. After checking all the tank test data about the anchor position, the results show that the anchor position for Mooring Line 1 has changed by about 50 mm (3.7 m in full scale) in the very last tank test-which is Sea State 4 (the largest sea-state). This means that for all the free decay, regular wave and Sea State 1 to 3, the test results are still reliable and it may be assumed that the anchor position only changed during Sea State 4 due to the loads caused by the larger waves. It should also be noted that in the numerical simulations, the simulation of Sea State 4 failed, which suggests that the wave condition is too large for this anchor position. When looking at Figure 6. 3 to Figure 6. 5, which shows the variation of the three mooring line tensions with increasing mass, there is a difference between the results before and after the tank tests. This is assumed to be due to the amplifier zero value drifting during the tank tests. However, the tension values are seen to reduce linearly with the same gradient before and after the tests. This means that the dynamic changes in mooring tensions in the measured time histories, for example, due

to wave loads or platform motions, are still correct. Thus, the recorded data may be corrected with an offset value representing the estimated drift.

The baseline tension values are taken from the case measured with no added mass before the experiment started, which was recorded just after the load cell / amplifier system had been calibrated and the model been put into the tank, and the mooring anchors adjusted to match the target values as closely as possible. As the amplifiers may be expected to drift slightly during the tank tests, the zero offset values may be variable. However, if the anchors have not moved, and the model draft has not changed, it is reasonable to assume that the tension will not in fact have varied. Thus, before running each test, when the model is still and balanced, the tensions were modified with an offset value to adjust the measured pre-tension in each test match with the values in Table 6. 1. By adopting this process, the modified data will represent the real tensions on each mooring line. The same process was also conducted when dealing with the mooring tensions in irregular waves.

Mooring Drag Coefficient in Numerical Simulation

Another factor which needs to be considered in the comparison between experiment and numerical simulation is the drag coefficient adopted for the mooring lines. In the FAST codes, the hydrodynamic drag for the mooring line is not included in the model. In FASTlink, the default mooring drag coefficient of 1.2 was applied initially in the numerical model. In some cases, such as the regular wave of period 23.25s full-scale, a non-linear response was found in the model tests as shown in Figure 6. 6. FAST was unable to predict this type of behaviour (which will be discussed in detail in Chapter

6.4); as shown in Figure 6. 7, it predicts a sinusoidal variation. A similar result to the experiment was found with FASTlink with the default mooring line drag coefficient but with much smaller responses than in the tank tests.

An investigation was then carried out to determine if FASTLINK could predict these responses. The mass distributions of mooring lines have been checked first, as shown in Table 4. 4– the numerical mooring models are Froude scaled from the measured tank test model, so this property matches correctly. The drag coefficient was then investigated. It was found that the non-linear phenomenon would appear more obvious and closer with the experimental results in the FASTlink (OrcaFlex) data when the mooring line drag coefficient is set to 0 than 1.2, as shown in Figure 6. 8. Comparing Figure 6. 6, Figure 6. 8 and Figure 6. 9 (the mooring tensions), the results from FASTlink with Cd set to 0 show a time history more similar with the experiment.

It was also found that, while changing the Cd does not affect the predicted platform RAO peak frequency, the maximum value of the predicted heave RAO agrees better with test results when using 0 drag coefficient (see Figure 6. 25 and Figure A7. 1, Appendix 7). Since the simulation can still run with zero drag coefficient, the zero value was therefore adopted for subsequent FASTlink simulations in this study, as it can predict similar phenomenon with the experiment.

However, it is clear that the mooring drag coefficient-due to its geometry and the Reynolds number, will not in reality be zero, see e.g. Mustto and Bodstein (2011). This

non-linear behaviour and the factors to affect it are still poorly understood at the present time and need to be investigated with further research.

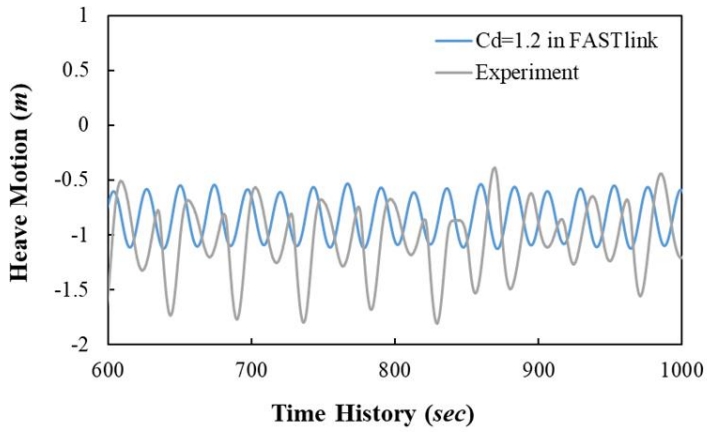

Figure 6. 6 Heave motion predicted in FASTlink (with Cd=1.2) and experiment time history, 23.25s (full scale)

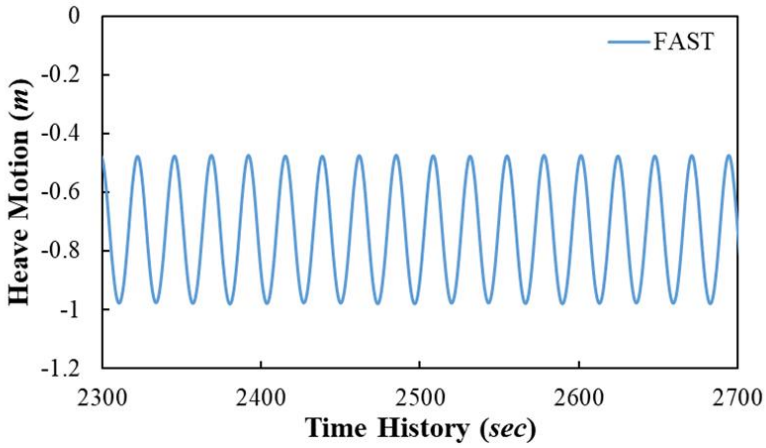

Figure 6. 7 Heave motion predicted in FAST, 23.25s (full scale)

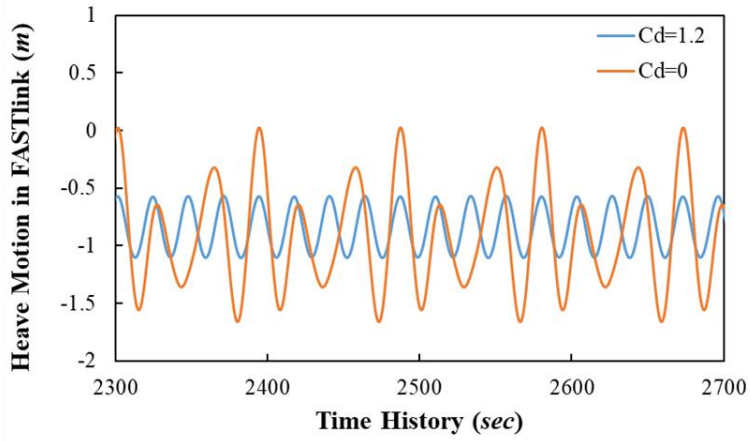

Figure 6. 8 Heave motion in FASTlink with Cd=1.2 and Cd=0, 23.25s (full scale)

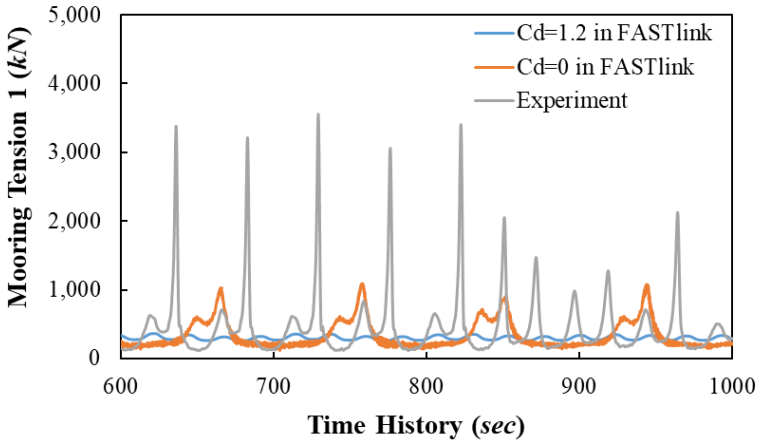

Figure 6. 9 Mooring Tension 1 in FASTlink (with Cd=1.2 and Cd=0) and experiment time history, 23.25s (full scale)

6.3 Free Decay Test

As discussed in Chapter 5, the natural frequency is a key factor which can help to characterise the platform's dynamic behaviour. Thus, when the spar platform is installed with three realistic mooring lines, its natural frequencies were checked first by conducting the free decay tests.

Natural Frequencies and Damping Ratio

The linearized Fit Function, as introduced in Chapter 5.2, was deployed to get the natural frequencies and the damping ratios for the platform with realistic mooring lines through the free decay tests. The free decay test was repeated 10 times for each mode of motion. The examples of the fit curve for each mode of motion are presented from Figure 6. 10 to Figure 6. 15. Figure 6. 10 and Figure 6. 11 show the platform heave free decay test and the fairlead motion (after removing the offset between the two recording points) compared with the platform heave when conducting the heave free decay test. This shows that the two results match perfectly and thus demonstrates that

the underwater Qualysis system data matches the data from the above water system. It was seen all the other four motions, apart from the surge decay, in a linear manner and match quite well with the fitted curves (see Figure 6. 10 - Figure 6. 14). The natural frequencies and the damping ratios can therefore be obtained from the fitted data. For the surge free decay test (see Figure 6. 15), the natural frequency is predicted well by the Fit Function, but the plot shows some non-linear damping behaviour in the surge decays. The rate of decay of the measured data is greater than that for the fitted data, which is typically the case when non-linear viscous damping is affecting the motions. It can thus be concluded that viscous damping has more effect in surge than the other degrees of freedom.

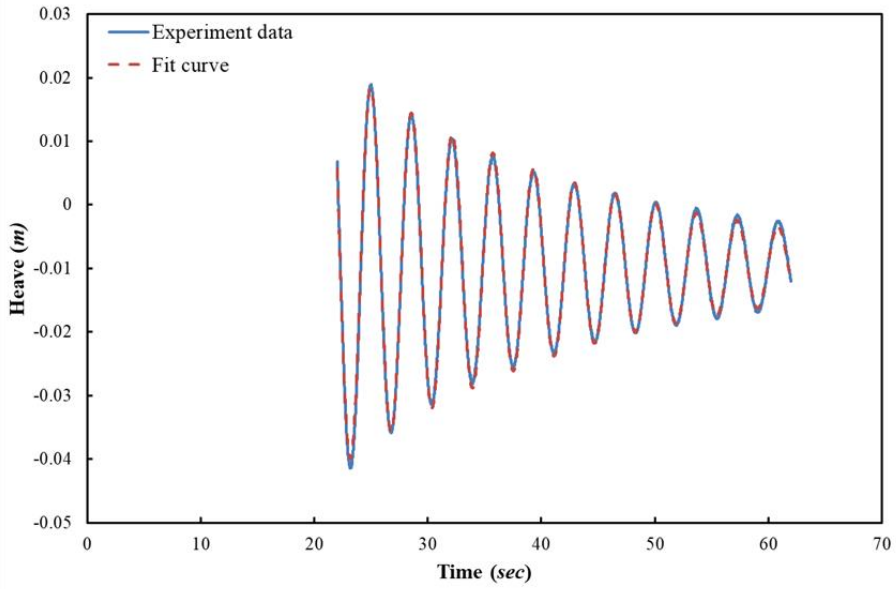

Figure 6. 10 Heave free decay in experiment, spar with realistic mooring lines (tank test scale)

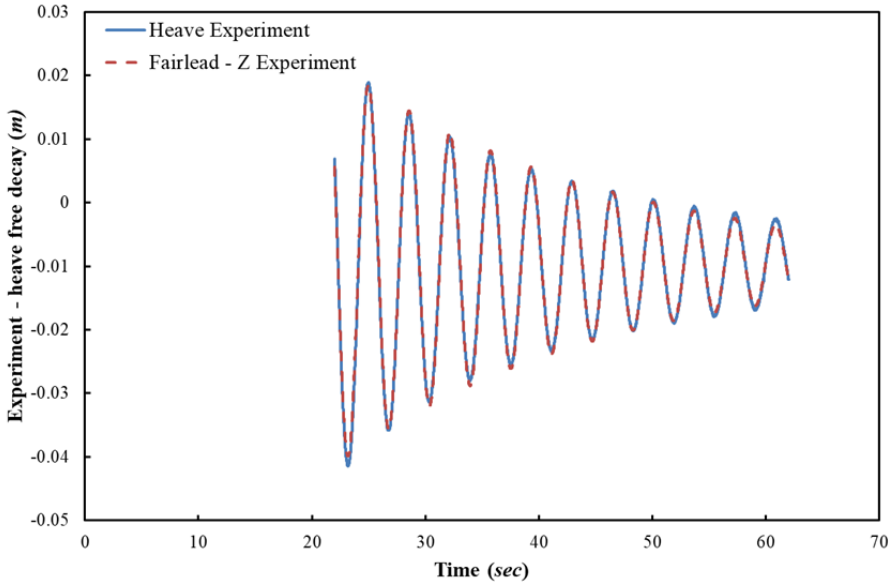

Figure 6. 11 Fairlead-Z and platform Heave free decay motion in experiment, spar with realistic mooring lines (tank test scale)

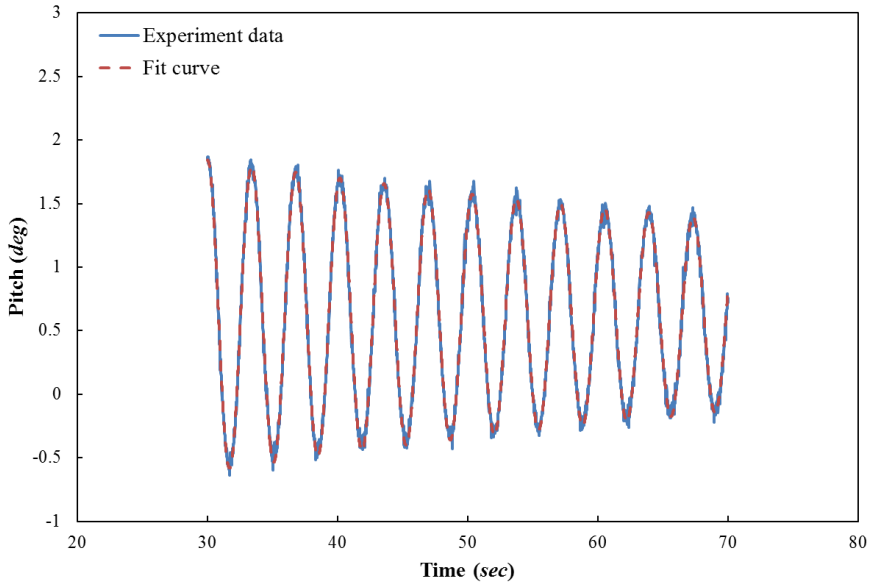

Figure 6. 12 Pitch free decay in experiment, spar with realistic mooring line (tank test scale)

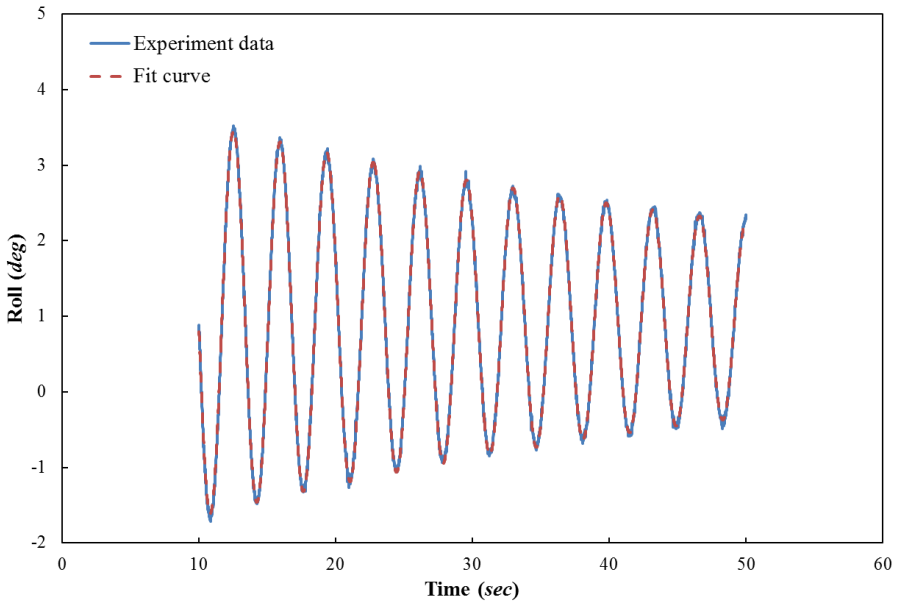

Figure 6. 13 Roll free decay in experiment, spar with realistic mooring lines (tank test scale)

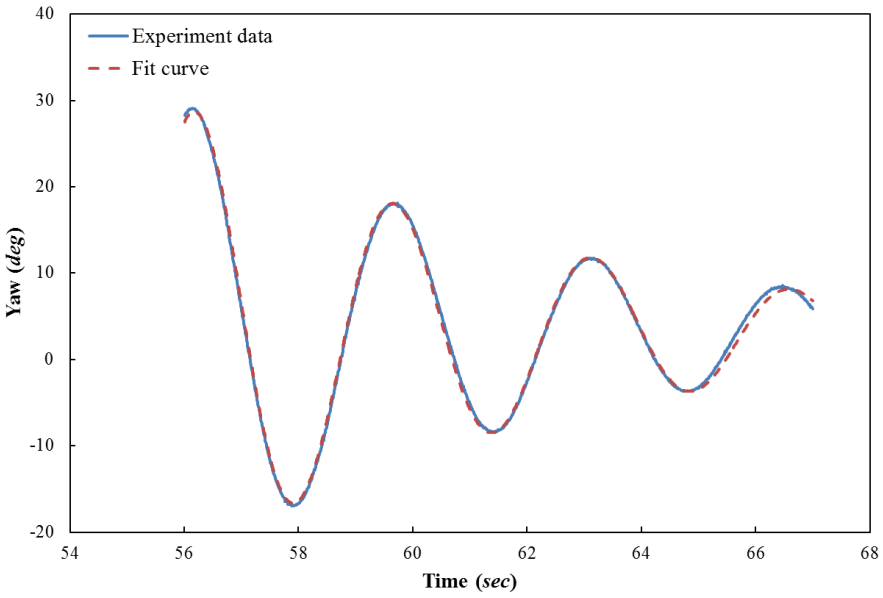

Figure 6. 14 Yaw free decay in experiment, spar with realistic mooring lines (tank test scale)

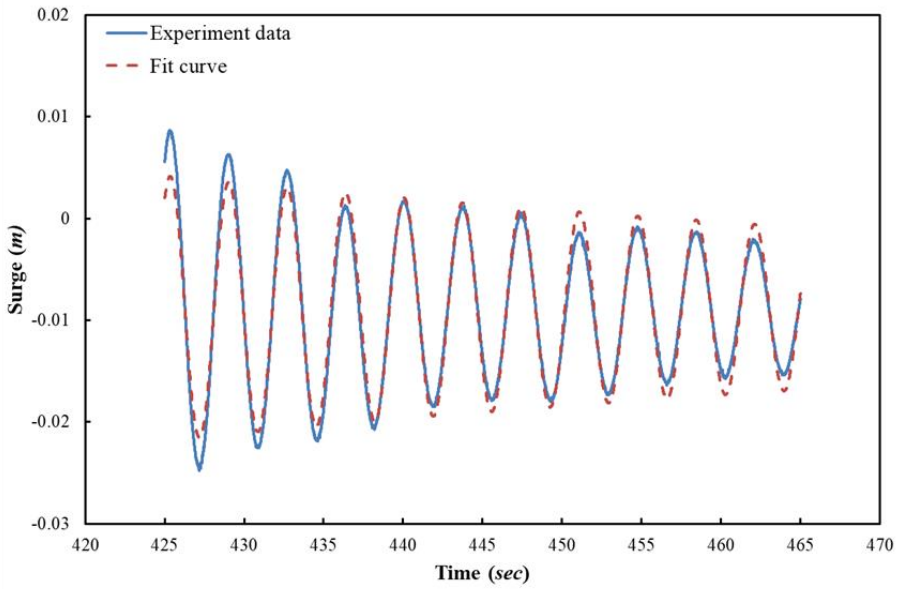

Figure 6. 15 Surge free decay in experiment, spar with realistic mooring lines (tank test scale)

Table 6. 2 shows the mean value over the ten tests of the natural frequencies for each mode of motion of the spar platform with realistic mooring lines compared with the NREL OC3-Hywind model's natural frequencies. It can be seen that only the yaw natural frequency does not match with the NREL model. This is assumed to be due to the slightly different mooring configuration from the NREL results and in particular the lack of the delta connection (which can restrict the yaw motion of the spar platform) (Jonkman, 2010 a) in this experiment. Compared with the spar-only tank tests, the pitch and heave natural frequencies did not change much, but the surge and yaw motion's natural frequencies have increased.

Table 6. 2 Natural frequencies for spar with real mooring lines acquired from the experiment NREL OC3-Hywind spar platform natural frequencies, with mooring lines (Ramachandran et al., 2013) (full scale)

Platform DOFs	Experiment	NREL
Pitch Frequency (*Hz*)	0.034	0.034
Heave Frequency (*Hz*)	0.032	0.032
Yaw Frequency (*Hz*)	0.034	0.121
Surge Frequency (*Hz*)	0.008	0.008
Roll Frequency (*Hz*)	0.034	0.034

Table 6. 3 Mean value and STD of damping ratio for spar with mooring, acquired from the experiment

	Mean Damping Ratio	STD
Heave	0.028	0.004
Pitch	0.007	0.001
Surge	0.017	0.009
Yaw	0.084	0.003
Roll	0.011	0.001

Table 6. 3 shows the damping ratio of the 5 DOFs for the spar with real mooring lines. It can be seen that the standard deviations of the damping ratio are all very small, and the damping behaviour are much more repeatable than the spar-only tests (as compared with Table 5. 3), especially in surge and yaw and thus the tank tests results would be considered acceptable.

As with the simulations presented in Chapter 5, an additional linear damping matrix has been added into both FAST and FASTlink models to make the numerical model

damping ratio match more closely with the experimental model. The damping matrix values are calculated to make the linear damping ratio from the numerical simulations match with the measured experimental results.

Additional damping in heave and yaw were added, with values of $9.352*10^4$ N/ (m/s) in heave and $2.300*10^7$ N/ (rad/s) in yaw. Hence the additional damping matrix is as shown below:

$$\text{Damping Matrix for Spar with mooring in FAST/FASTlink} = \begin{bmatrix} 0 & 0 & 0 & 0 & 0 & 0 \\ 0 & 0 & 0 & 0 & 0 & 0 \\ 0 & 0 & 9.352*10^4 & 0 & 0 & 0 \\ 0 & 0 & 0 & 0 & 0 & 0 \\ 0 & 0 & 0 & 0 & 0 & 0 \\ 0 & 0 & 0 & 0 & 0 & 2.300*10^7 \end{bmatrix}$$

The resulted surge, heave, pitch, roll and yaw damping ratio in the numerical model compared with the experiment model are shown in Table 6. 4. The values for damping ratio match quite well with the experiment results, apart from the pitch motion, for which the numerical prediction shows a value almost four times higher than the experiment result. In Chapter 5, the pitch damping ratio in the experiment without moorings matches well with the numerical model, so the possible reasons for the pitch damping ratio difference could be caused by mooring effects, such as the mooring drag coefficient differences. It should be noted that a comparison of pitch motion RMS (as shown in Figure 6. 26), shows little difference between results from FAST prediction and experiment for the peak amplitude of pitch motion. This might indicate that the actual pitch damping ratio in the experiment does not show significant difference with

the numerical model, and thus the damping matrix is reasonable to be applied in numerical models.

Table 6. 4 Damping ratio for spar with realistic mooring lines in numerical and experiment model

	FAST	FASTlink	Experiment
Heave	0.0281	0.0281	0.0284
Pitch	0.0270	0.0202	0.0069
Surge	0.0172	0.0145	0.0169
Yaw	0.0839	0.0838	0.0842
Roll	0.0127	0.0111	0.0108

6.4 Regular Wave Test

The regular wave tests followed the procedure described for the spar-only tests in Chapter 5. As in the spar-only tests, tests for repeatability of the results and check on linearity of response with the change of wave heights were also conducted. In addition to platform motions, the motion of Mooring Line 1 at the rear (see Figure 4. 5) and the tension on the three moorings were recorded. The wave data from Table 5. 5 was initially used for the tank tests. Due to the mooring lines effect on the behaviour of the spar platform, to get the best results, several additional wave frequencies were later added, as shown in Table 6. 5 and Table 6. 6.

Table 6. 5 Regular wave parameters for spar with realistic mooring lines (tank test scale)

Wave Frequency (*Hz*)	Wave Period (*s*)	Measured Wave Amplitude (*m*)	Wave Length (*m*)
1.229	0.814	1.187	1.033
0.949	1.053	1.288	1.731

0.717	1.395	1.170	3.037
0.506	1.976	1.230	5.922
0.450	2.223	1.242	7.245
0.430	2.325	1.225	7.792
0.420	2.381	1.224	8.089
0.415	2.410	1.231	8.243
0.410	2.441	1.324	8.410
0.370	2.703	1.260	9.780
0.358	2.790	1.135	10.231
0.350	2.857	1.170	10.577
0.344	2.906	1.254	10.826
0.331	3.022	1.292	11.416
0.319	3.139	1.207	12.003
0.314	3.185	1.192	12.236
0.310	3.226	1.217	12.439
0.307	3.255	1.229	12.584
0.302	3.311	1.263	12.861
0.297	3.367	1.279	13.138
0.292	3.425	1.248	13.425
0.287	3.487	1.242	13.734
0.282	3.546	1.214	14.019
0.280	3.571	1.200	14.145
0.277	3.604	1.169	14.304
0.276	3.627	1.147	14.417
0.273	3.662	1.141	14.587
0.271	3.690	1.063	14.723
0.269	3.720	1.126	14.870
0.264	3.787	1.117	15.197

0.261	3.836	1.191	15.433
0.257	3.891	1.336	15.697
0.253	3.952	1.355	15.993

Table 6. 6 Regular wave parameters, for spar with realistic mooring lines (full scale)

Wave Frequency (*Hz*)	Wave Period (*s*)	Wave Amplitude (*m*)	Wave Length (*m*)
0.143	7.000	1.260	76.478
0.110	9.060	1.260	128.114
0.083	12.000	1.260	224.752
0.059	17.000	1.260	438.294
0.052	19.120	1.260	536.112
0.050	20.000	1.260	576.593
0.049	20.480	1.260	598.578
0.048	20.730	1.260	609.997
0.048	21.000	1.260	622.304
0.043	23.250	1.260	723.714
0.042	24.000	1.260	757.050
0.041	24.580	1.260	782.673
0.040	25.000	1.260	801.144
0.038	26.000	1.260	844.852
0.037	27.000	1.260	888.198
0.036	27.400	1.260	905.441
0.036	27.750	1.260	920.485
0.036	28.000	1.260	931.208
0.035	28.480	1.260	951.740
0.035	28.960	1.260	972.204
0.034	29.460	1.260	993.451

0.033	30.000	1.260	1016.319
0.033	30.500	1.260	1037.425
0.033	30.720	1.260	1046.692
0.032	31.000	1.260	1058.468
0.032	31.200	1.260	1066.868
0.032	31.500	1.260	1079.451
0.032	31.740	1.260	1089.501
0.031	32.000	1.260	1100.375
0.031	32.580	1.260	1124.577
0.030	33.000	1.260	1142.059
0.030	33.470	1.260	1161.578
0.029	34.000	1.260	1183.537

When running the series of regular waves (as shown in Table 5. 5), some non-linear phenomena in the floating systems motion were observed for some wave periods. Thus, the RMS values of platform motions will be presented instead of the RAOs due to the lack of the linearity, although some RAOs are shown where the response is sufficiently linear.

Snatching Phenomenon

During the experiment, when monitoring the time history output curves from the Spike, it is interesting to notice at some frequencies a “snatching” like behaviour is seen in which the mooring lines went slack and then suddenly went tight, yielding a substantial effect on platform motions and mooring line tension. Surprisingly, when the wave frequency was near the platform’s heave/pitch natural frequency, the snatching disappeared and the motion reverted back to quite sinusoidal behaviour. As

discussed before, it was found that FASTlink only showed this type of behaviour if the mooring drag coefficient was set as zero, and FAST could not replicate these phenomena at all.

In this section, some examples of the surge motion at 23.25s wave period and heave motion at 31.20s will be presented. Further detailed snatching examples from experiment and FASTlink are shown in Appendix 8.

From Figure 6. 16 and Figure 6. 17, it is observed that the snatching in the mooring lines can lead to its own regular motion. In Figure 6. 18 and Figure 6. 19, it can be seen that the motion reverts to sinusoidal when the wave frequency co-incides with the heave natural frequency. The snatching could result due to a variety of reasons, such as the drag of the mooring lines or the mooring line weight. The detail will be discussed in Chapter 7.

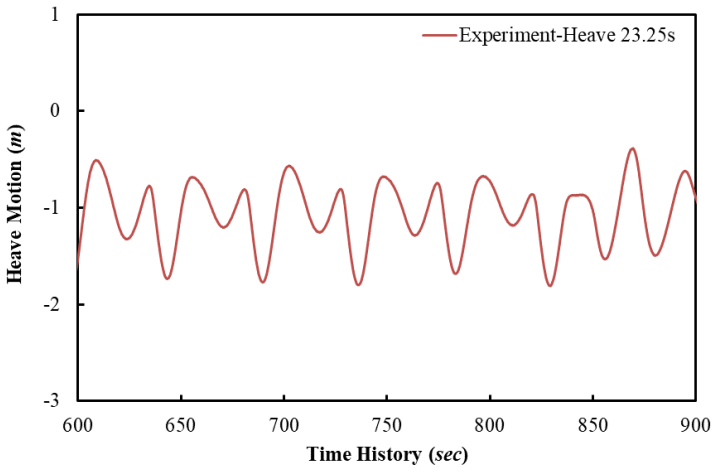

Figure 6. 16 Non-linear heave motion in experiment, 23.25s (full scale)

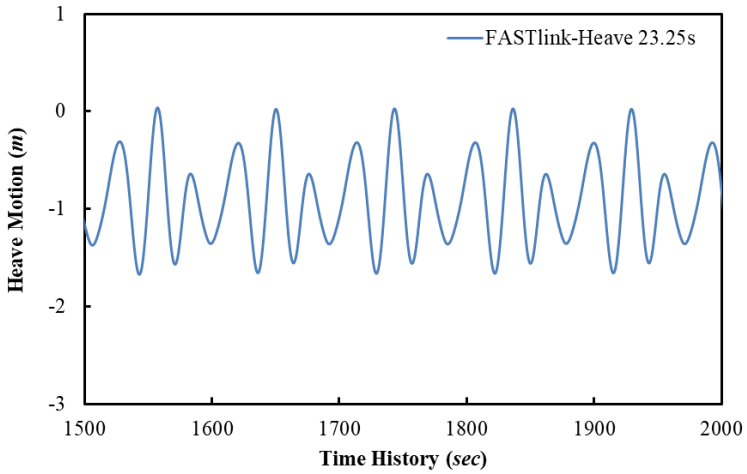

Figure 6. 17 Non-linear heave motion in FASTlink, 23.25s (full scale)

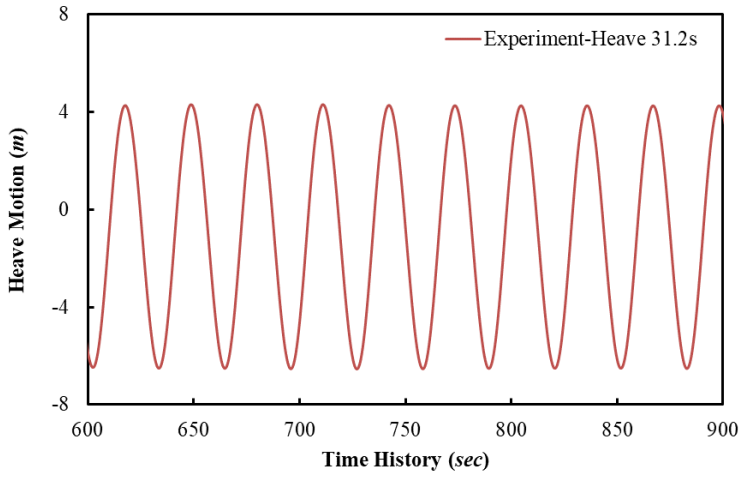

Figure 6. 18 Heave motion in experiment, 31.20s (full scale)

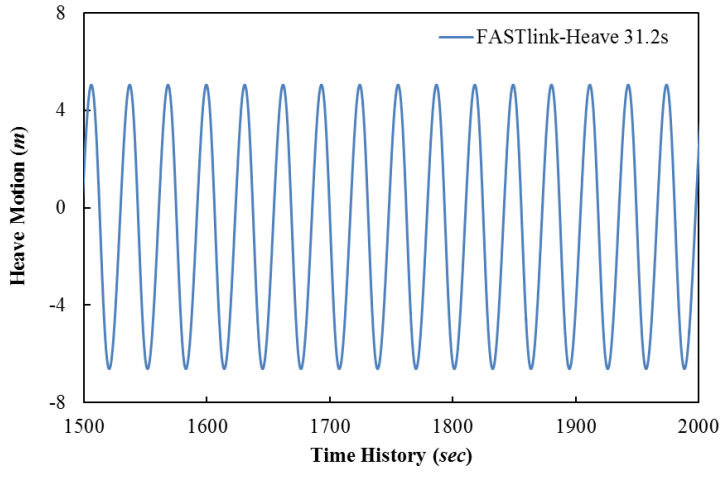

Figure 6. 19 Heave motion in FASTlink, 31.20s (full scale)

This non-linear motion in the platform could potentially be quite harmful for the wind turbine, due to the potential for rapid accelerations on top of the tower along the surge direction. However, there is no suggestion of strongly non-linear behaviour in surge at the tower top, as shown in Figure 6. 20.

Figure 6. 21, shows the tension time history in the Mooring Line 1 when the snatching happens. It can be seen that the mooring tensions can increase dramatically from about 200 kN (the pre-tension) up to more than 4,000 kN, which is very harmful to the mooring lines and could cause the mooring line to fail.

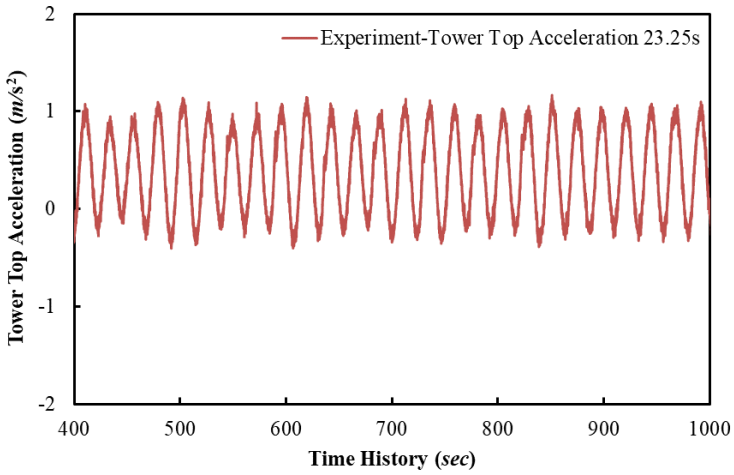

Figure 6. 20 Tower top acceleration in experiment along X-axis, 23.25s (full scale)

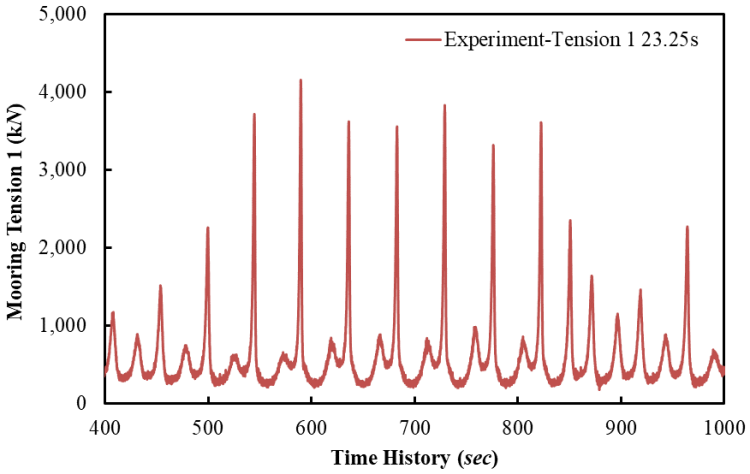

Figure 6. 21 Mooring Tension 1 in experiment, 23.25s (full scale)

Repeatability Check

A wave with frequency – 0.287 Hz (30s wave period in full scale, which is quite near the platform heave/pitch natural frequencies, and the platform motions can show sinusoidal curve) in tank test scale, and amplitude 0.017m, has been chosen to check the repeatability of the tank test result. This wave has been run three times and the duration is about 130s in each tests. The platform motion amplitudes (calculated from the mean position, not the RMS amplitudes here) are getting from the time history when the system is getting stable, around 70s to 120s. Table 6. 7 shows the result. Although there are some small variations, overall it shows a good agreement.

Table 6. 7 Repeatable check test results, spar with realistic mooring lines (tank test scale)

	Data019	Data023	Data025	MEAN
Input frequency (*Hz*)	0.287	0.287	0.287	0.287
Measured Wave Amplitude (*mm*)	16.741	16.745	16.752	16.746
Heave Amplitude (*mm*)	61.176	61.288	61.196	61.220
Pitch Amplitude (*deg*)	4.978	4.964	5.003	4.982
Surge Amplitude (*mm*)	76.510	76.477	77.007	76.665
Yaw Amplitude (*deg*)	1.437	1.410	1.443	1.430

Spar Platform RMS values

Due to the wave only propagating towards the positive X-axis and the lack of wind, no sway and roll will be expected and the yaw would be expected to be very small. Thus, only the surge, heave, and pitch RMS values will be presented in this part, as shown in Figure 6. 22, Figure 6. 24 and Figure 6. 26.

The RMS values are calculated from sections of the data when the platform is showing stable periodic motion curves in both experiment and numerical models. The equation is:

$$X_{rms} = \sqrt{\frac{x_1^2 + x_2^2 + \cdots + x_n^2}{n}} \qquad (20)$$

As shown in Table 6. 2, the surge natural frequency obtained from free decay tests is about 0.008 Hz. This is well outside the capability of the wave maker to generate waves and can happen only very rarely in real ocean environment. However, it is seen in

Figure 6. 22 that the surge RMS (and RAO) has a peak frequency similar to the peak frequency in pitch. This is presumed to be due to a coupling effect between surge and pitch. In the surge RMS, it seems that the FASTlink values are greater than the results from the experiment, as shown in Figure 6. 22. FAST shows a quite smooth curve, since it cannot capture the snatching and FASTlink shows a similar tendency with the experiment results. While if we look at the surge RAO, in Figure 6. 23, FASTlink shows higher peak than the experimental data, as with the RMS. This can also be expected from the damping ratio, as shown in Table 6. 4. The surge damping ratio in both FAST and experiment is about 0.017, which is larger than in FASTlink (about 0.015), so it is to be expected that FASTlink shows higher motion amplitude.

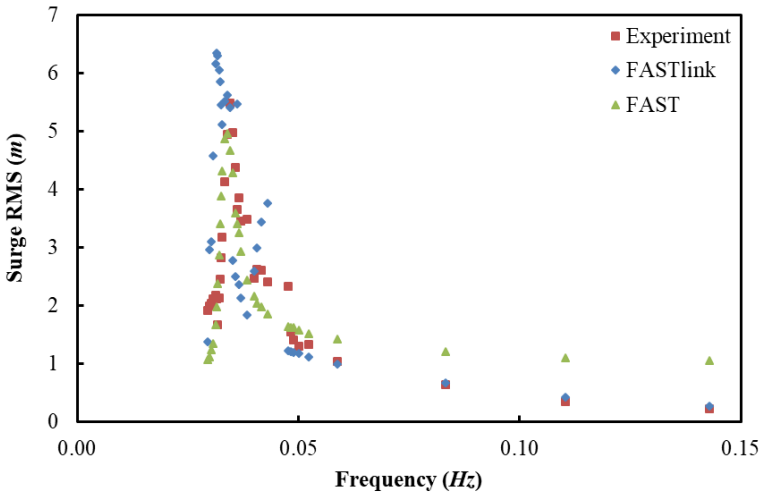

Figure 6. 22 Surge RMS, spar with realistic mooring lines (full scale)

It can be seen in Figure 6. 24 that the peak heave RMS happens at around 0.032 Hz in both experimental and numerical results. FASTlink predicts the curve shape better than FAST when compared with the tank test data, due to the snatching effect in some of the wave frequencies discussed previously. The heave RAO peak value is reduced

compared with the spar-only model, this is presumed to be because of the additional damping introduced by the moorings.

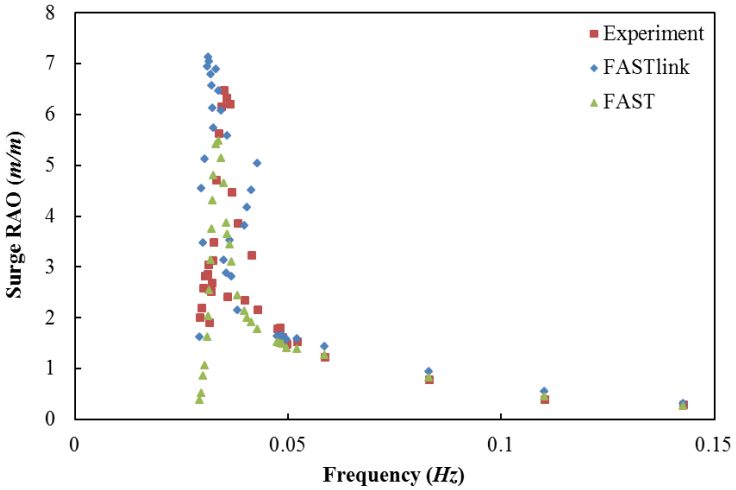

Figure 6. 23 Surge RAO, spar with realistic mooring lines (full scale)

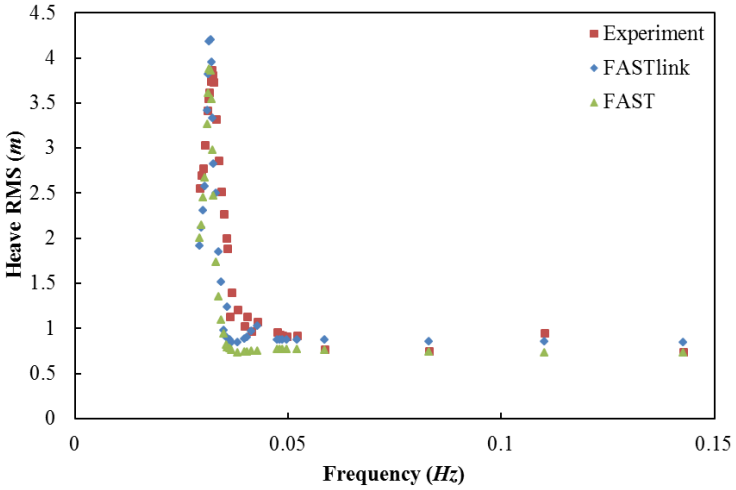

Figure 6. 24 Heave RMS, spar with realistic mooring lines (full scale)

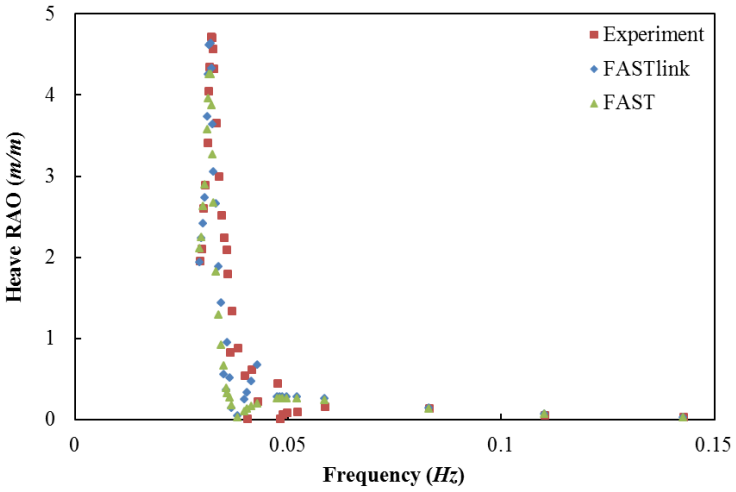

Figure 6. 25 Heave RAO, spar with realistic mooring lines (full scale)

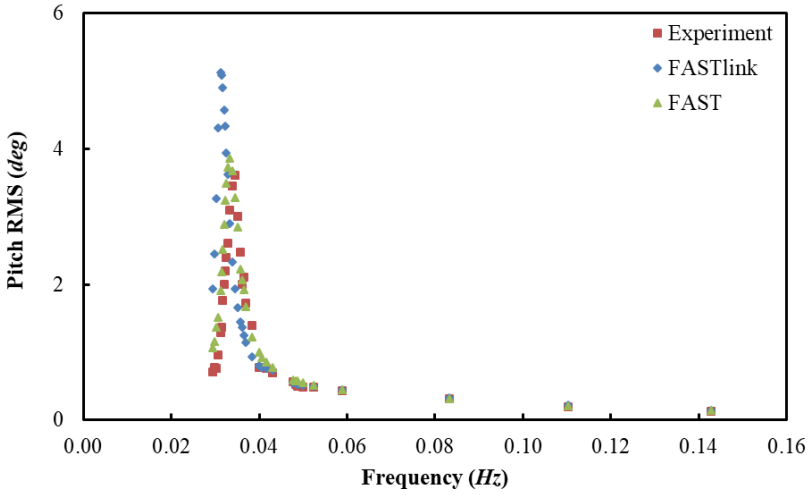

Figure 6. 26 Pitch RMS, spar with realistic mooring lines (full scale)

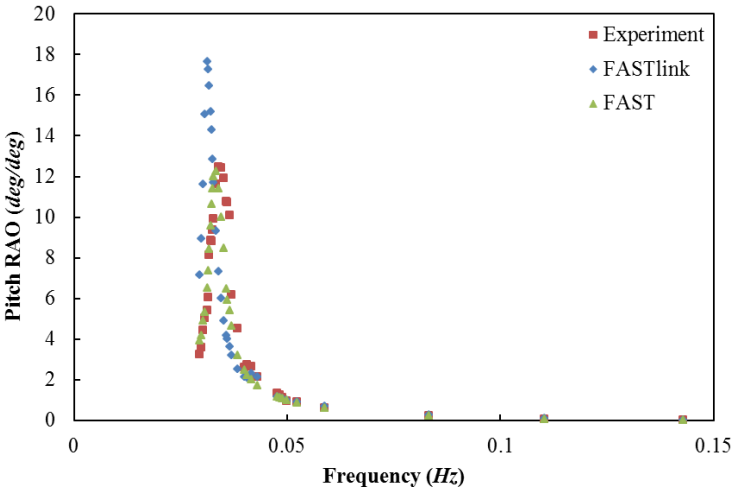

Figure 6. 27 Pitch RAO, spar with realistic mooring lines (full scale)

In pitch, the RAO does not change much when compared with the spar-only tank test, which indicates that the mooring loads do not affect the pitch motion much. It may be assumed that the pitch motion would mainly depend upon the spar platform's pitch inertia, as compared with the pitch motion in Chapter 5, when there is no wind load. The surge/pitch peak RAO, is found at around 0.034 Hz for experiment, 0.033 Hz in the FAST results and around 0.032 Hz in FASTlink, which are all similar to the spar-only tank tests. The pitch damping ratio in FASTlink is smaller than that in FAST, which leads to the higher pitch RMS values in FASTlink compared to FAST/experiment. It is interesting to note that while the damping ratio in pitch is much smaller than the numerical models, the RMS values of pitch from FAST are similar to those from the experiment, as discussed in Chapter 6.3.

Linearity Tests

As discussed previously in Chapter 5, the RAO is expected to decrease with increasing wave heights at the peak frequency of the RAO, which is the natural frequency. It can be seen from the heave and pitch time histories for each wave frequency, that the snatching has disappeared when the wave frequency nears the platform motion natural frequency, as discussed above. Thus, the platform heave/pitch time history show a sinusoidal curve in this part and the RAO can be found in a meaningful manner. The results are quite similar to the spar-only tank tests. In experiment/FAST, both heave and pitch RAO are decreasing with increasing of wave amplitude, while the heave RAO in FASTlink still shows the opposite result, as the heave motion amplitude is increasing more rapidly than the wave height. The details can be found in Appendix 9.

Mooring Motions

The motion of Mooring Line 1 (along with the X-axis) has been recorded by the underwater cameras, as described in Chapter 4. The position of the seven reflective balls on Mooring Line 1 is shown in Table 4. 5. In this section, the Mooring Line 1 RMS motion amplitudes along the X-axis and Z-axis (surge and heave) will be presented. As the wave only propagates towards the positive X-axis, motions in the y-direction will be small. The measured mooring motions will only be compared with FASTlink simulation, since FAST cannot calculate these motions. In this part, only the data for the Points 1, & 4 and the fairlead will be presented; all other data are given in Appendix 10.

Figure 6. 28 to Figure 6. 33, show the motion of two points on Mooring Line 1 and the reference point at the fairlead position in both surge and heave directions. The RMS amplitude is calculated in terms of the motion amplitude of each point relative to its initial static position. The experiment results have been converted into full scale before plotting. It is seen that in most of the cases, the numerical results have larger values than the experiment – which could be due to the zero drag coefficient for mooring lines adopted in the numerical simulations while there exists a certain level of drag force in the experiments, but the curve tendencies are very similar. Along the Z-axis, a peak frequency can be seen which co-incides with the heave natural frequency, while Figure 6. 33 shows that the platform fairlead motion, measured by the underwater Qualisys gives almost the same results as the platform heave RMS, measured by the above-water Qualisys system.

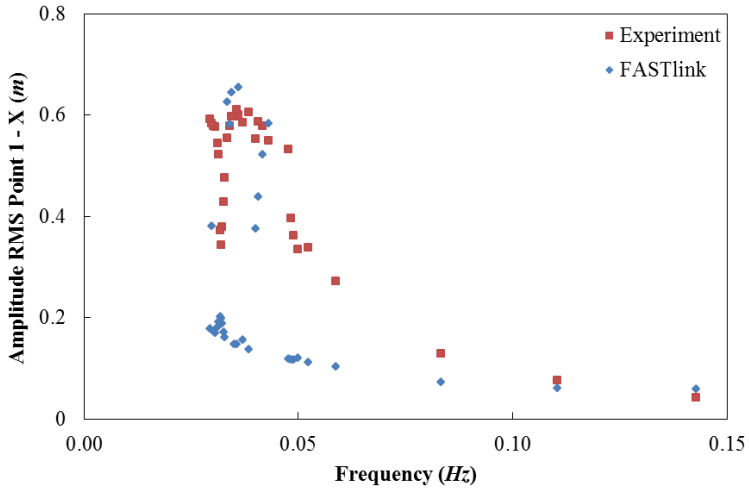

Figure 6. 28 Amplitude RMS for Point-1 along X-axis (full scale)

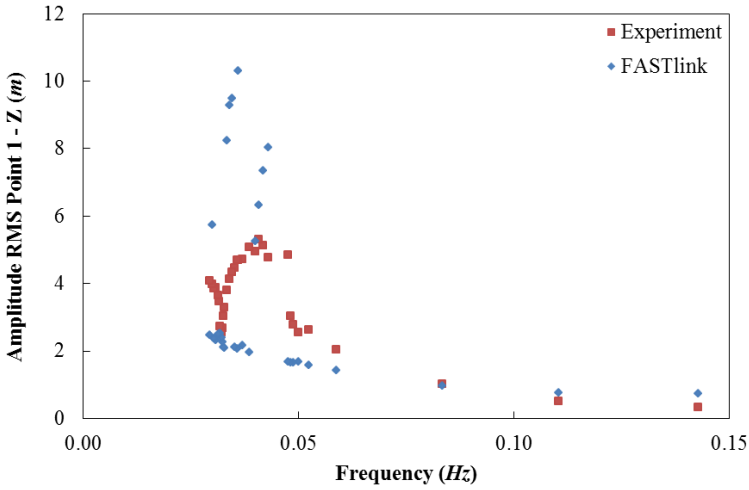

Figure 6. 29 Amplitude RMS for Point-1 along Z-axis (full scale)

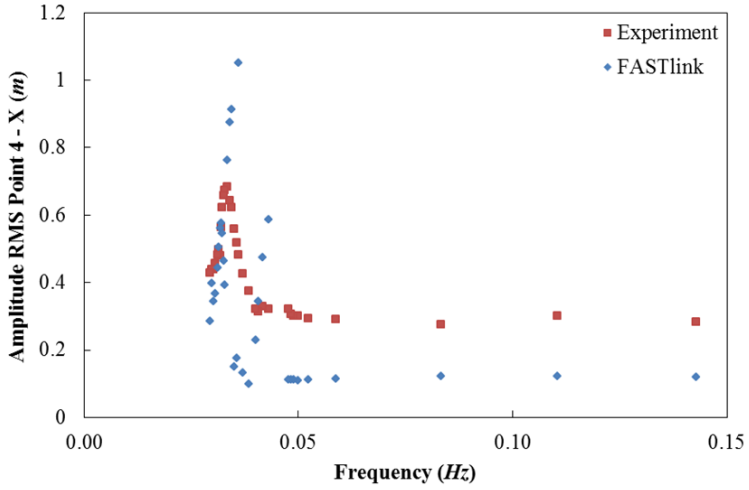

Figure 6. 30 Amplitude RMS for Point-4 along X-axis (full scale)

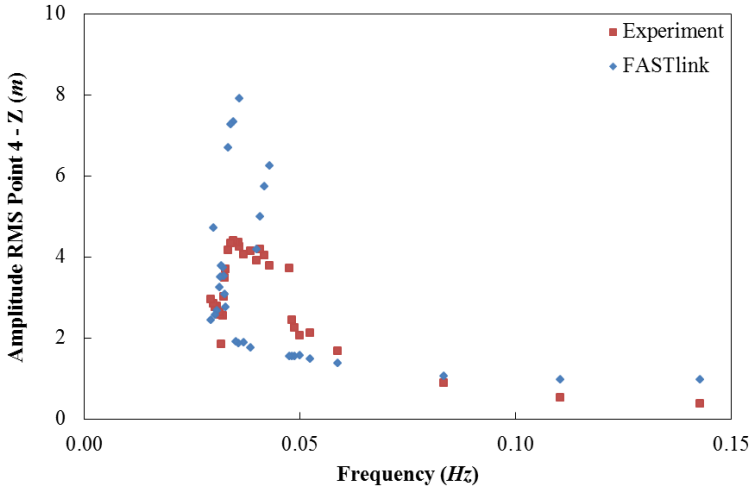

Figure 6. 31 Amplitude RMS for Point-4 along Z-axis (full scale)

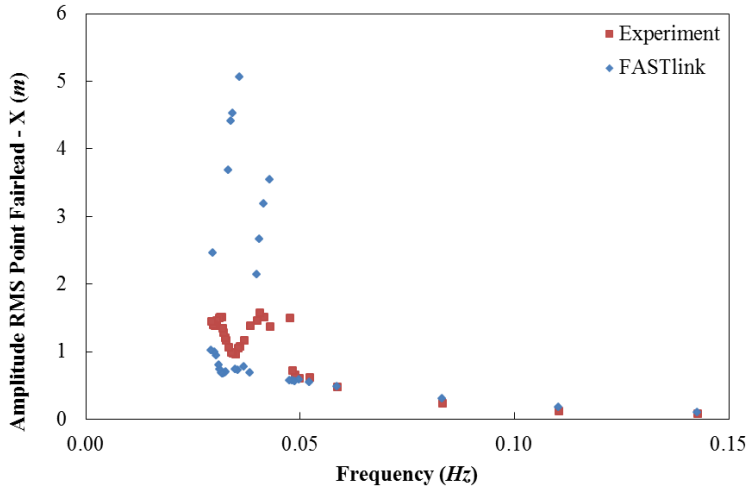

Figure 6. 32 Amplitude RMS for point at the spar Fairlead position along X-axis (full scale)

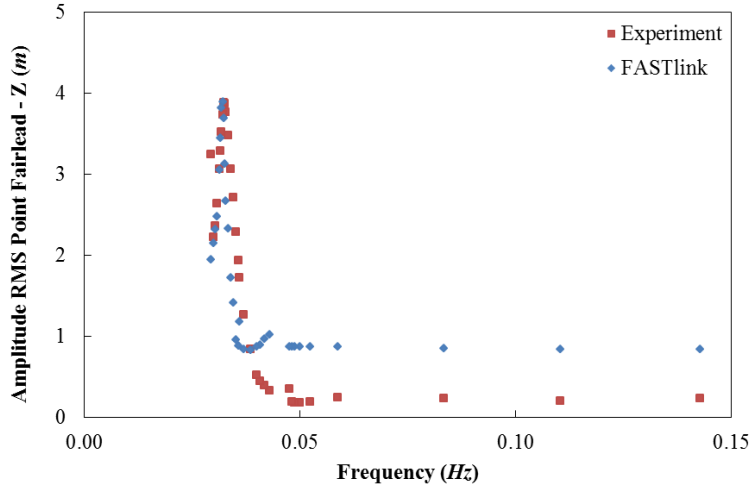

Figure 6. 33 Amplitude RMS for point at the spar Fairlead position along Z-axis (full scale)

Mooring Tensions

As discussed above, when setting up the moorings' anchor positions in the tank, it was very hard to adjust the mooring frame to sit at the exact same position as the scaled numerical model. It is therefore likely that an error of a few millimetres at model scale (or less than 0.5m in full scale) may exist. However, this is small compared with the dimensions of the mooring spread, and was not expected to affect the model results significantly.

As the snatching was seen at some regular wave frequencies, thus, as for the platform motions, it is no longer appropriate to present the results as RAOs. Instead, the RMS mooring tension values, and the maximum and minimum tensions found will be presented.

Figure 6. 34, Figure 6. 35 and Figure 6. 36 present the RMS values of the three mooring line tensions with the various regular wave frequencies. It is observed that FASTlink predicts a curve with a similar tendency to the experiment but with values much smaller than the experiment, while FAST only shows a smooth curve and cannot predict the snatching motion of the floating system. From the RMS values, we can see that the average tension in the experiment could reach up to nearly 1,400 kN on Mooring Line 1 and 1,100 kN on Mooring Line 2 and 3, while FASTlink predicts up to around 600 kN for Mooring Line 1 and about 300 kN for Mooring Line 2 and 3. The big differences between experiment and FASTlink at the peak RMS tension value arise mainly because of the large loads which occur when the lines snatches in the experiment. To illustrate the numerical results more clearly, the tension on Mooring

Line 2 (identical to Mooring Line 3 in numerical) in FAST and FASTlink are shown in Figure 6. 37. This shows a similar curve with the experiment in FASTlink while FAST shows a linear curve peaking at the heave natural frequency.

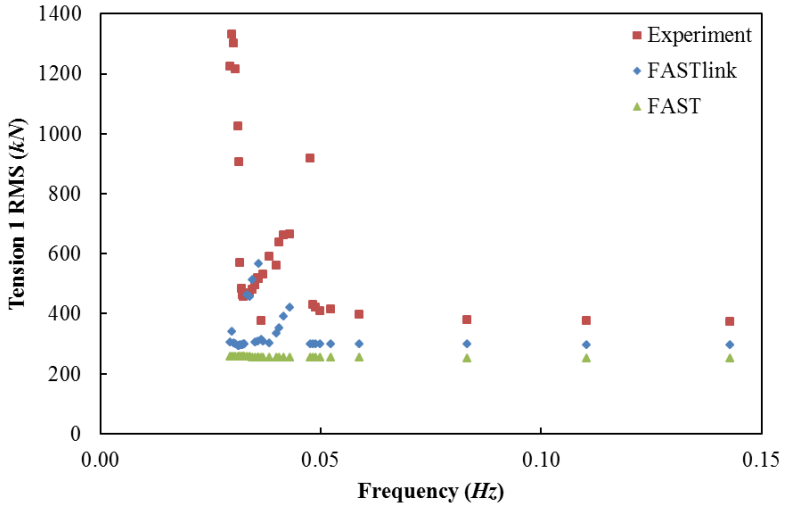

Figure 6. 34 RMS for Mooring Tension 1 (full scale)

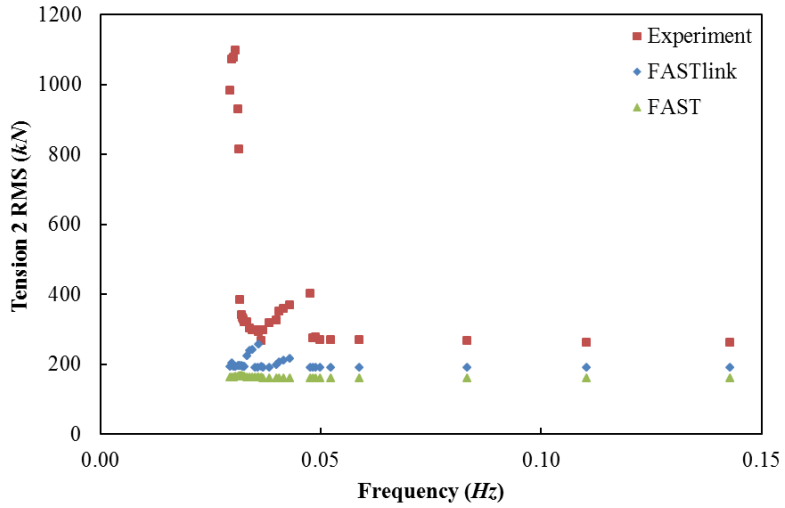

Figure 6. 35 RMS for Mooring Tension 2 (full scale)

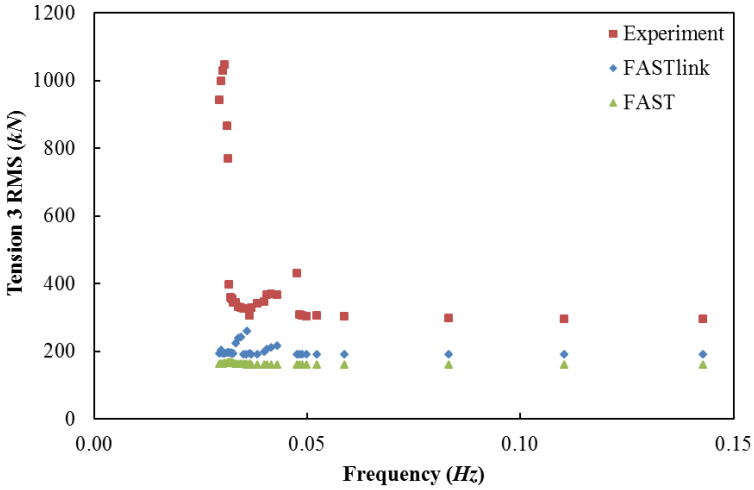

Figure 6. 36 RMS for Mooring Tension 3 (full scale)

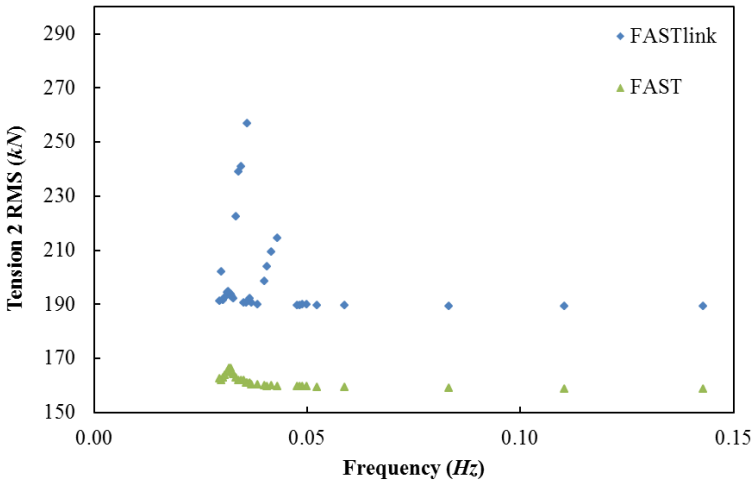

Figure 6. 37 RMS for Mooring Tension 2, FAST and FASTlink (full scale)

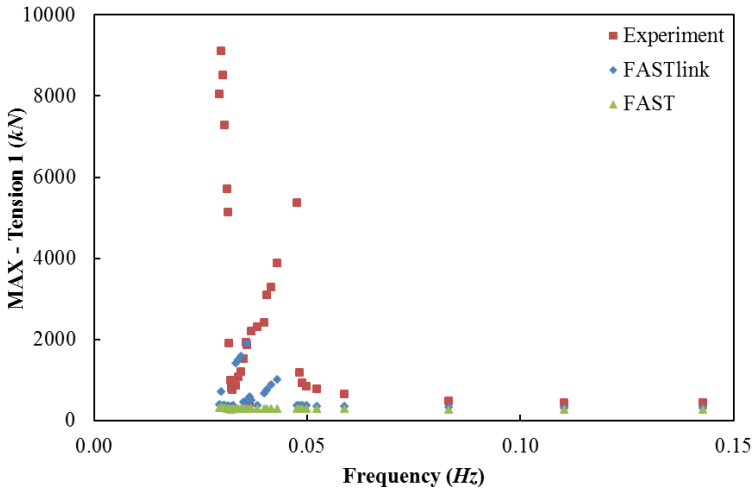

Figure 6. 38 Maximum value for Mooring Tension 1 (full scale)

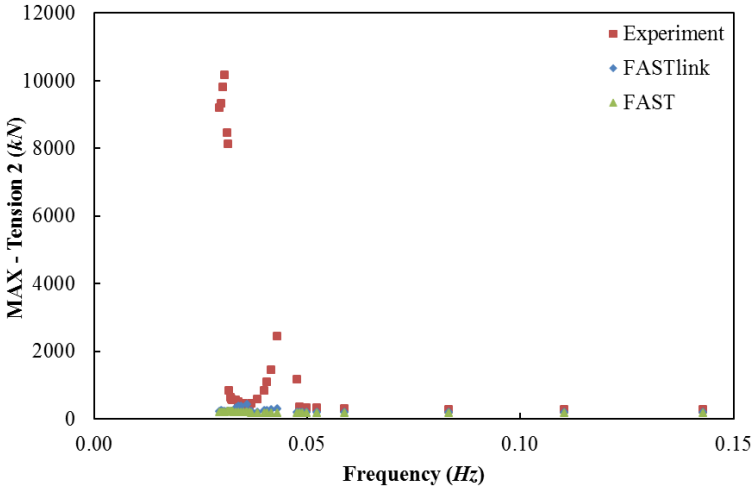

Figure 6. 39 Maximum value for Mooring Tension 2 (full scale)

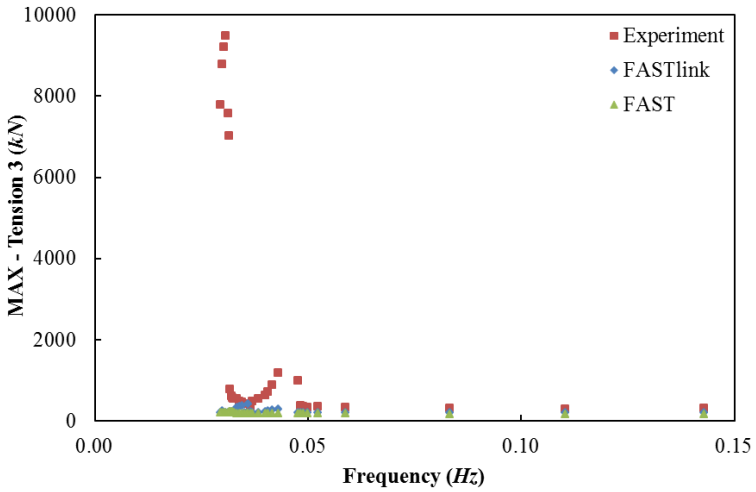

Figure 6. 40 Maximum value for Mooring Tension 3 (full scale)

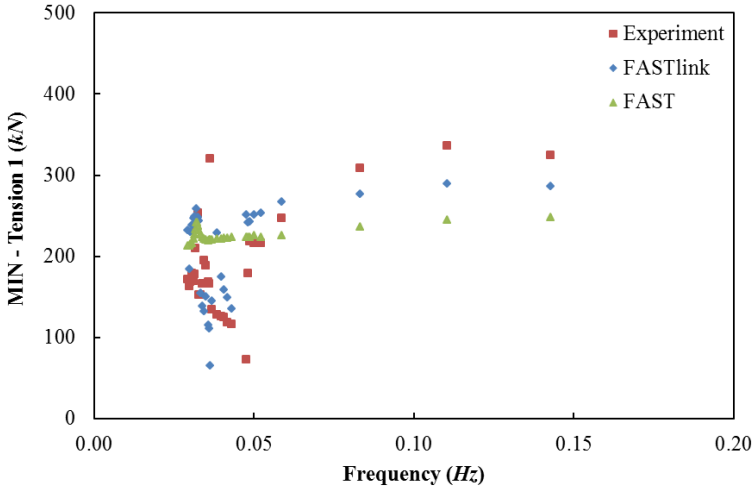

Figure 6. 41 Minimum value for Mooring Tension 1 (full scale)

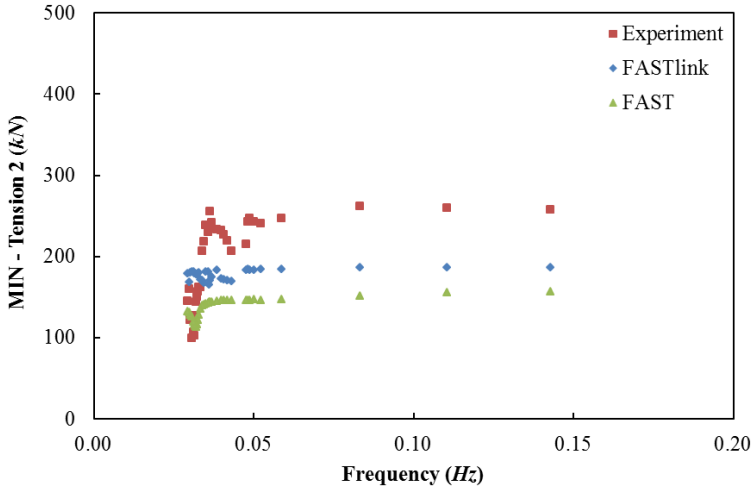

Figure 6. 42 Minimum value for Mooring Tension 2 (full scale)

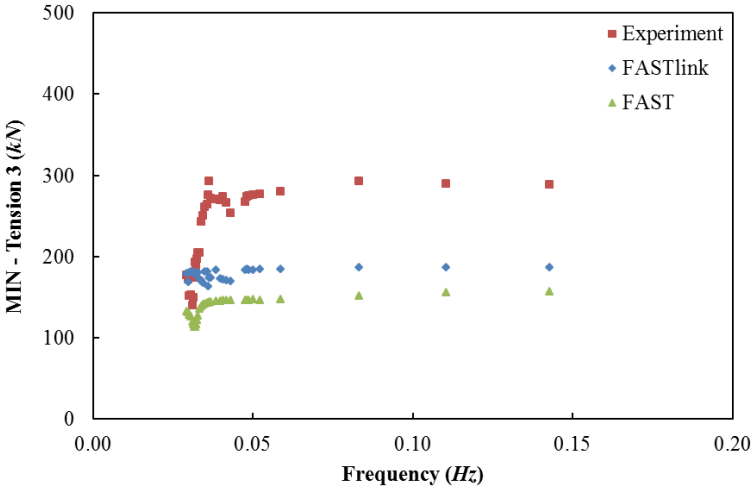

Figure 6. 43 Minimum value for Mooring Tension 3 (full scale)

Figure 6. 38 to Figure 6. 43, present the maximum and the minimum values on each mooring line. For the three mooring minimum tensions, it is seen that when the snatching happens and the mooring line are close to becoming slack, the minimum tension could be as low as 100 kN for Mooring Line 2 and 3, and about 60 kN for Mooring Line 1. For the maximum mooring tensions, the largest differences occur at frequencies higher than 0.050 Hz, while the differences between FASTlink and experiment are much greater for wave frequencies smaller than about 0.032 Hz (the

heave natural frequency). This indicates that the snatching phenomena are much more significant at the lower wave frequencies. From the above figures, it can be seen that the predicted maximum mooring tensions could reach up to 10,000 kN from the experiment data, while FASTlink predicts only about 2,000 kN. This big difference between the experiment and the numerical simulations indicates that the assumptions in the FASTlink calculation are not sufficiently accurate and the approach cannot deal properly with the snatching motions.

The sudden sharp increase in mooring tensions during the snatching is clearly very dangerous for the structure and could cause the failure in the mooring lines, and hence the inability of the software to predict this behaviour is clearly a concern.

6.5 Sea States

The results for the spar with mooring model in the four irregular waves shown in Table 4. 8 will be presented in this part. As with the spar-only tank tests, each wave was run for 20 minutes in the experiment and 9999 seconds in the numerical simulations. The peak shape parameter – 3.3 was applied to set up the JONSWAP spectral wave in both experiment and the numerical simulations.

As with the spar-only tank tests, the wave spectrum for the four sea states are shown in Chapter 5.4 and Appendix 5. The results of the platform's motions, Mooring Line 1 motions and three mooring line tensions response spectrum will be presented in this part for Sea State 2. Some results in Sea State 3 will also be presented at here, while the remaining detailed results can be found in Appendix 11 and Appendix 12).

Spar Platform Motion - Sea State 2

The heave, pitch and surge motion's PDF and spectrum from Sea State 2 will be presented at this part, and will be compared with FAST and FASTlink generated results. The experimental measured data have been calculated into full scale before calculating its PDF and spectrum. An example time history in Spike is shown in Figure 6. 44, where the platform heave/pitch/surge, Mooring Tension 1 and the wave profile are presented.

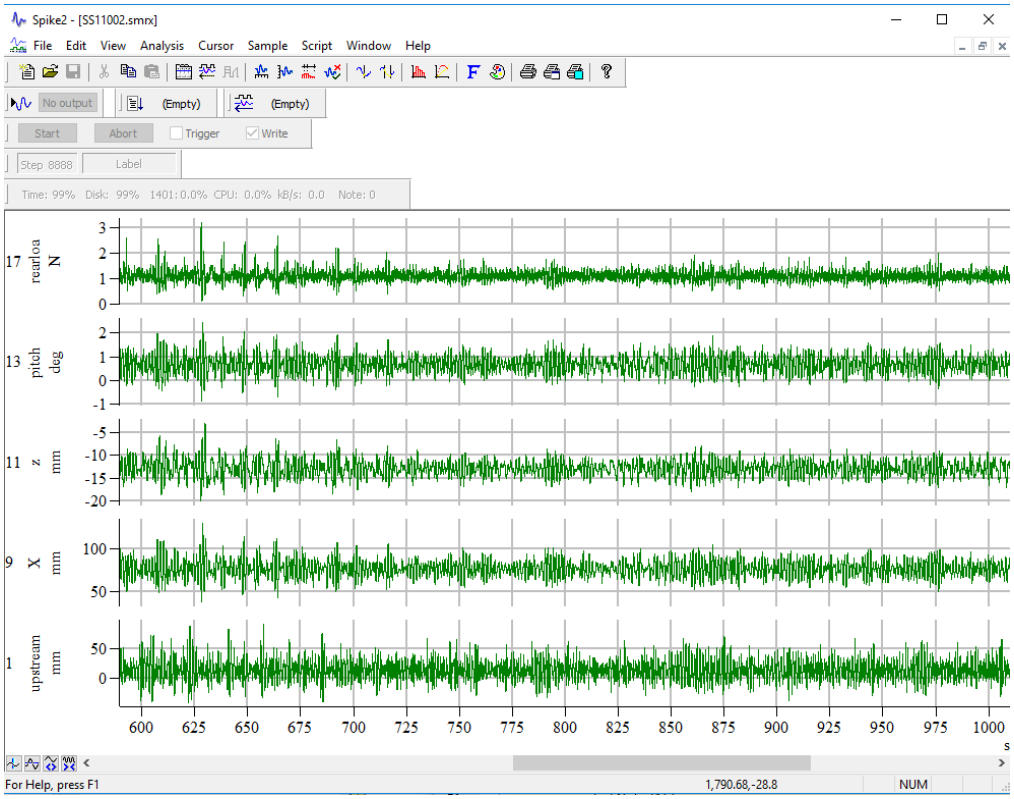

Figure 6. 44 Sea state 2 example time history in Spike (tank test)

In Figure 6. 45, it can be seen that the results for the heave motion amplitude probability density function (PDF) among the experiment, FAST and FASTlink are all mainly within 0.5 m; FASTlink results show somewhat wider motion range than the

experiment, while FAST shows similar results with the experiment. When looking at the heave motion spectrum, in Figure 6. 46, one peak has been found at the wave spectrum peak frequency (about 0.089 Hz) while another one is seen at the heave motion natural frequency (about 0.032 Hz) in both experiment and numerical simulations. FASTlink predicts a higher heave motion energy than both FAST and experiment; this is similar to the RMS results for the regular wave in which FASTlink shows a higher peak than FAST and experiment. Although the heave damping ratio found from free decay tests are almost the same between FASTlink and FAST, the heave motion predicted in FASTlink are higher than those from FAST. This can also be predicted from the linear test, as discussed in the Chapter 5.3 (see Figure 5. 10) and shown in the Appendix 9 (see Figure A9. 3), where the heave motion increasing higher and quicker in FASTlink than in FAST, which should be due to the different mooring models in the two software. As mentioned previously, the heave motions do not appear to be substantially affected by the presence of the mooring line, so the mooring system seems cannot affect the heave motion behaviour.

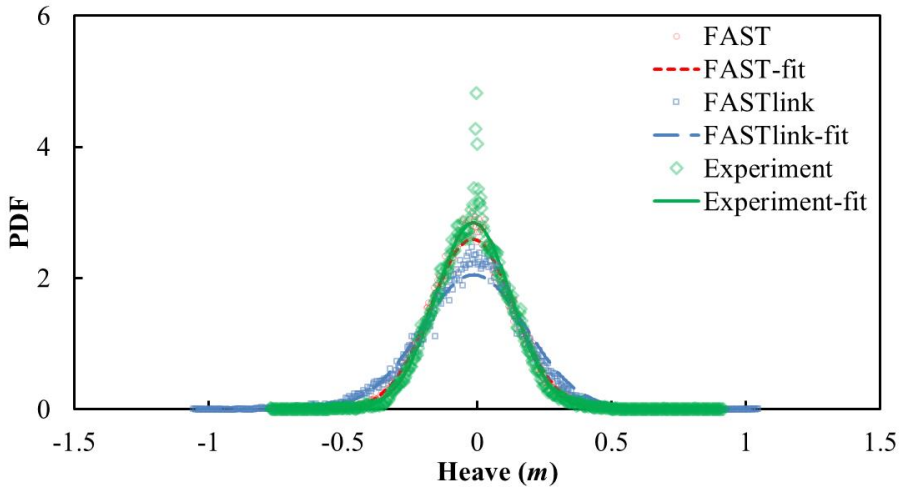

Figure 6. 45 Heave PDF for Sea State 2, spar with realistic mooring (full scale)

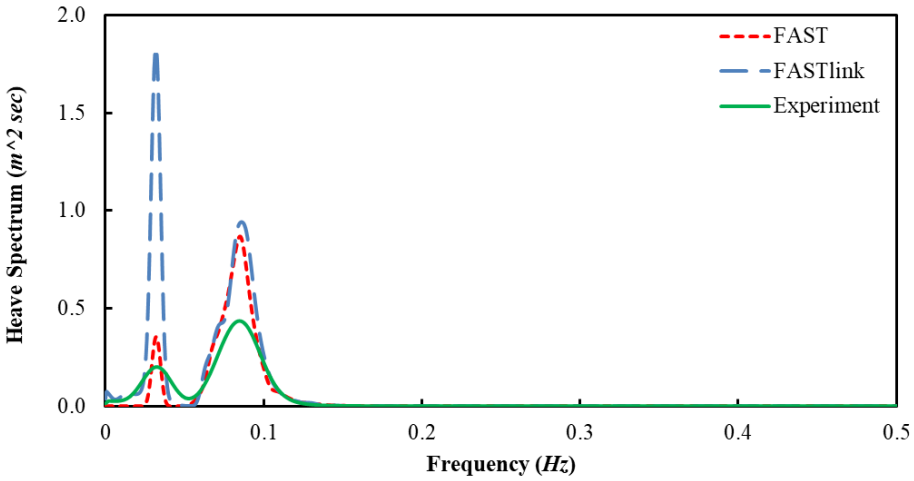

Figure 6. 46 Heave motion spectrum for Sea State 2, spar with realistic mooring (full scale)

When looking at the pitch motion PDF, as shown in Figure 6. 47, FASTlink still tends to predict the pitch motion range wider than FAST and experiment, while the FAST curve seems can match perfect with the experiment. In the experiment, the pitch amplitude mainly lies below 1° while the FASTlink predictions are shown to be up to around 1.5°. For the pitch motion spectrum, as shown in Figure 6. 47, the two peaks occur around the wave spectrum peak frequency, and the pitch natural frequency (around 0.034 Hz) – where FASTlink shows a much higher value than both experiment and FAST, this shows good agreement with the pitch RMS (and RAO) in the regular waves. Thus, it can be concluded that the pitch damping ratio in the experiment was calculated wrong and it should be similar with the FAST but smaller than in the FASTlink.

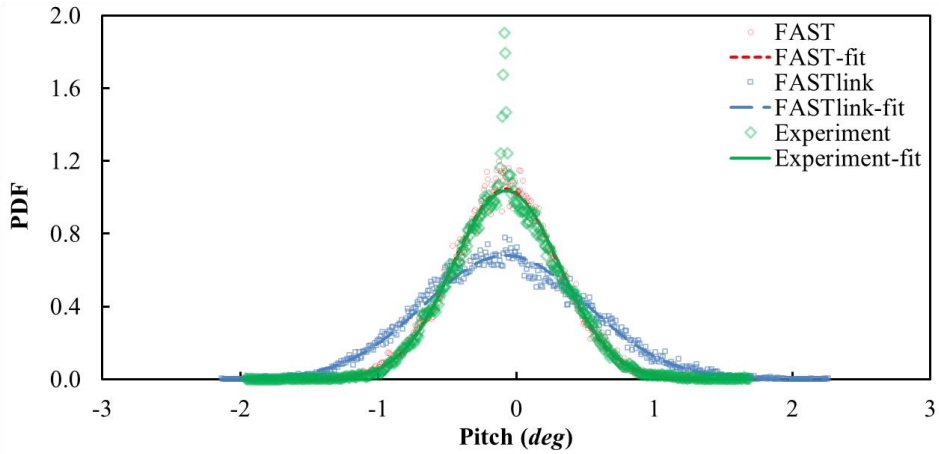

Figure 6. 47 Pitch PDF for Sea State 2, spar with realistic mooring (full scale)

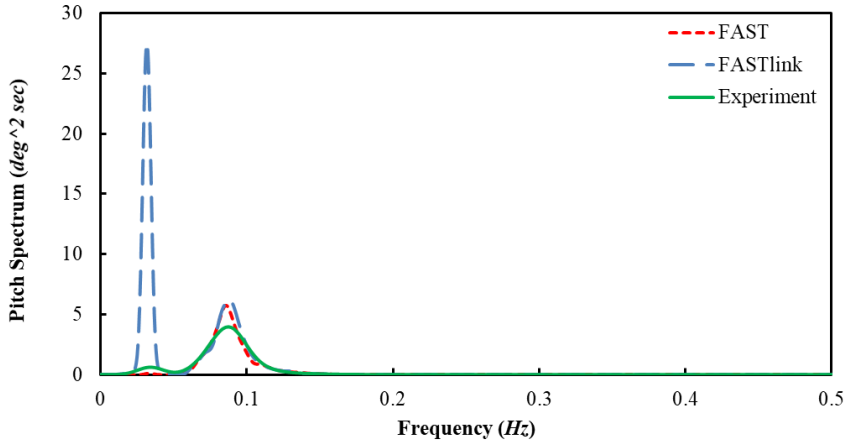

Figure 6. 48 Pitch motion spectrum for Sea State 2, spar with realistic mooring (full scale)

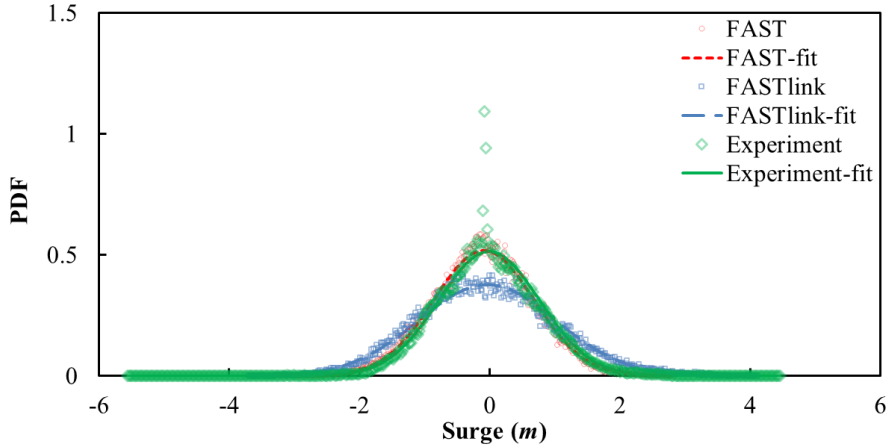

Figure 6. 49 Surge PDF for Sea State 2, spar with realistic mooring (full scale)

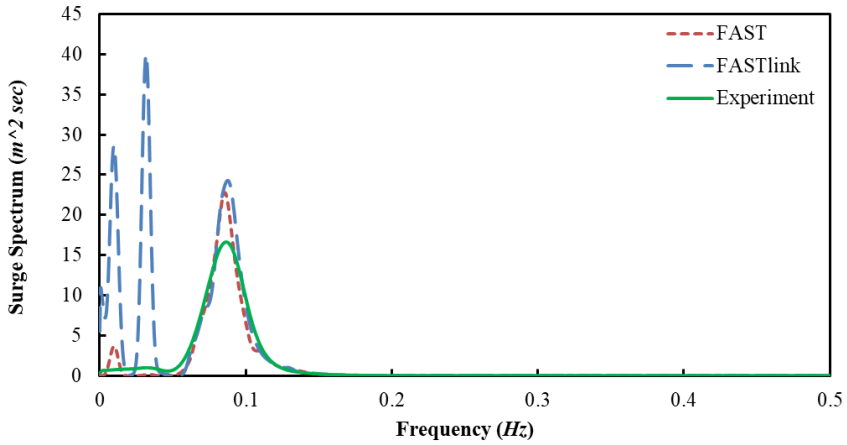

Figure 6. 50 Surge motion spectrum for Sea State 2, spar with realistic mooring (full scale)

In surge motion PDF, it is seen that the surge motion amplitude can range from 0 to 2 m and it is seen clearly in Figure 6. 49 that the FAST curve matches better with the experiment than FASTlink, as with the pitch motion PDF. For the surge motion spectrum, as shown in Figure 6. 50, the FASTlink data shows three clear peaks; two are similar in frequency to results with the other degrees of freedom at the peak wave spectrum frequency and the surge natural frequency (which is 0.008 Hz) while the middle one is around the pitch natural frequency (0.034 Hz), which shows the prediction of the coupling effect between the surge and pitch motion. In addition, as with the pitch spectrum, FASTlink predicts higher values than both the experiment and FAST results, which may due to the surge damping ratio in the FASTlink (around 0.014) is smaller than the other two methods (around 0.017).

Spar Platform Heave Motion - Sea State 3

A very low frequency behaviour – 0.002 Hz - has been discovered in the experimental data for platform heave motion spectrum in Sea State 3, as shown in Figure 6. 51. This

low frequency shows quite high energy. The spectrum of heave, pitch and surge motion in the heave free decay test were first checked to make sure that this small frequency is not related to any coupling effect, but no evidence of behaviour at this frequency was found.

The tank test time history (scaled into full scale) in Sea State 3 and the recorded video were then examined. The time history of the heave motion in Sea State 3 is shown in Figure 6.52. A few quite large motions can be seen from around 1500s to 4000s and from 5350s to 6100s; these large motions were also observed in the video, especially for the time from 5350s to 6100s (a picture and more details have been shown in Appendix 11). In particular, it can be seen that the mean vertical location of the platform is depressed for an extended period from 5350 to 6100s. At the same time, large values of tension can be seen in the tension time history, which suggests that the quite large heave energy is caused by a series of large waves. Large motions can be seen in sway and yaw at the same time. This suggests that this large slowly-varying vertical motion is not due to the model taking on water. A truncated time history has been produced to exclude these large motions, and the response spectrum recalculated as shown in Figure 6. 53. It can be seen that in this spectrum the large energy at 0.002 Hz has disappeared. Thus, it can be concluded that the large energy apparent at 0.002 Hz is caused by the slowly varying large vertical motion of the platform in the tank. The same small frequency (0.002 Hz) can also be seen in the mooring line motions along X-axis in Sea State 3 and it is assumed that this could be related to the large heave motion as well.

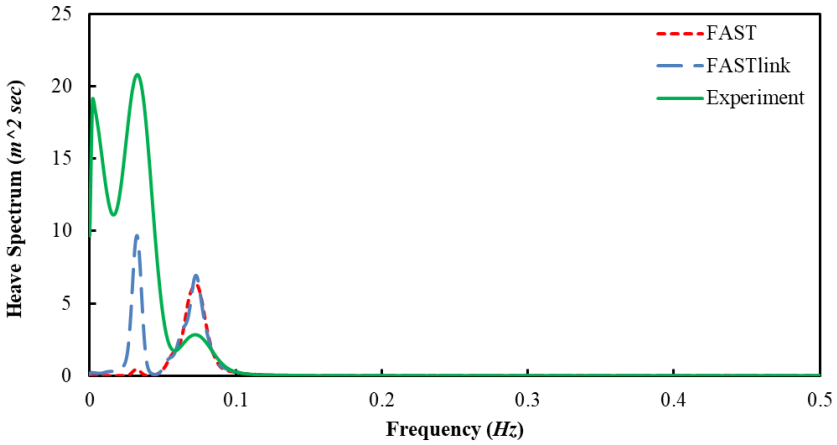

Figure 6. 51 Heave motion spectrum for Sea State 3, spar with realistic mooring (full scale)

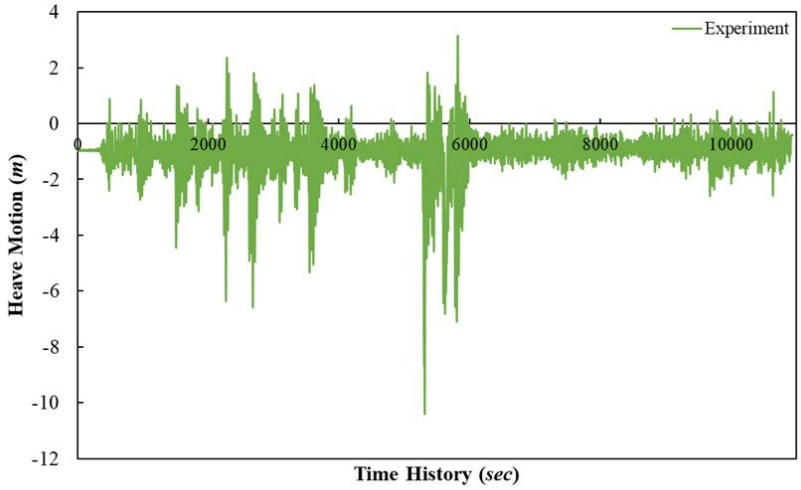

Figure 6. 52 Heave motion time history in experiment, Sea State 3, spar with realistic mooring (full scale)

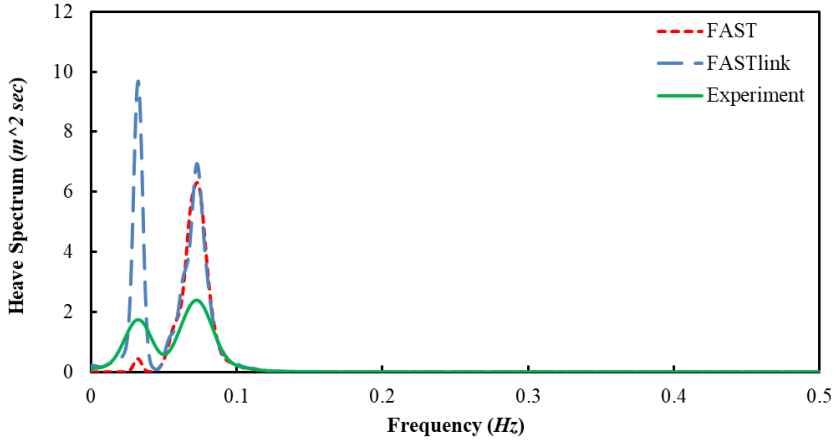

Figure 6. 53 Heave motion spectrum from truncated time history in experiment, Sea State 3, spar with realistic mooring (full scale)

Mooring Line 1 Motion - Sea State 2

In this part, the Mooring Line 1 motion recorded during the experiment, along both X-axis and Z-axis will be presented and compared with predictions from FASTlink. Only three points' data will be presented in this part and the data for the other three points will be presented in Appendix 12.

Figure 6. 54 to Figure 6. 59, show the motions of Point 1 (the point furthest from the spar platform apart from the anchor), Point 4 (point near the middle of the line) and the Fairlead position motion (as a reference point compared with the platform motion), along both X-axis and Z-axis. The detail of the arrangement of the five points is shown in Table 4. 5. For all of the motions of the three points in both directions, both experiment and FASTlink show an obvious peak in spectrum at the peak wave frequency (around 0.089 Hz). In FASTlink, for Point 1 and 4, both along the X-axis and Z-axis, another obvious peak is predicted at around 0.010 Hz, while in the experiment, the second peak occurs at about 0.025 Hz for motion along X-axis and 0.023 Hz in Z-axis. These peaks could indicate the mooring line motion natural frequencies along the two directions; similar peaks are also found in the other three sea states as shown in Appendix 12.

It seems that with the position changing from the anchor to the platform fairlead position, the mooring motions in both X-axis and Z-axis are increasing till the middle of the mooring line and then decreasing to the fairlead position in all of the four sea states. The experiment generally shows a higher peak spectrum at the peak wave frequency and a smaller peak spectrum at its natural frequencies. In Sea State 2, Point

1, its motion along X-axis from the experiment shows a higher energy than the FASTlink prediction, indicating that the mooring motion in experiment is more significant than in FASTlink. This is consistent with tests in regular waves where the RMS experiment results also shows more points with higher values than the FASTlink predictions. The predicted spectrum for motions of Point 4 along the X-axis in FASTlink shows about six peaks, which suggests a lot of snatching or other complex dynamic behaviour are predicted during the simulation. FASTlink tends to predict a higher energy for motion of Points 1 and 4 along Z-axis than that measured in the experiment. The difference is not large; and may be attributed to the mooring line damping in the experiment. Comparing all three points for motion along X-axis, reveals a tendency that the motion energy gets higher for the points near the platform, and weaker in the middle floating part of the mooring. Near the anchor position, the motion energy is still higher than the floating part but smaller than points near the platform, which could indicate the damping effect is the main factor in the middle parts. The motion along Z-axis shows an opposite behaviour than with the X-axis. At the fairlead position, it can be seen that the motion along the Z-axis matches perfectly with the platform heave spectrum which gives re-assurance that the underwater and above-water motion capture systems are working correctly. In contrast, the X-axis, motion at the fairlead position shows smaller energy than platform surge motion, but the curve shape is quite similar. This difference is believed to be due to the effect of platform pitch on the X-axis motion of the centre of gravity of the platform.

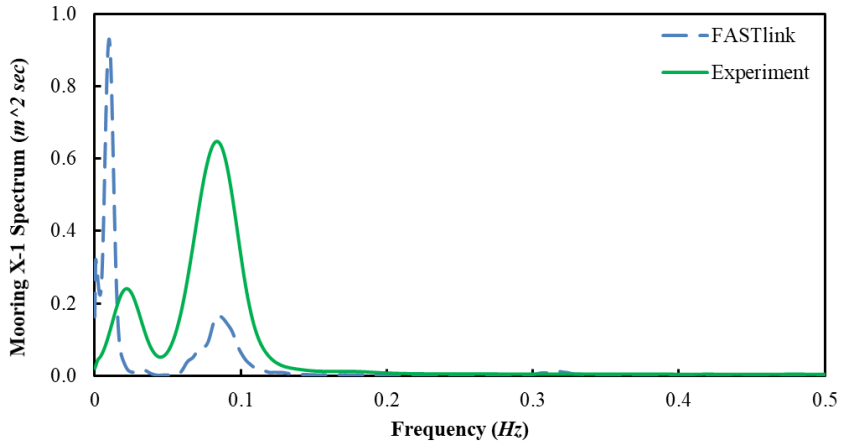

Figure 6. 54 Point-1 motion along X-axis, on Mooring Line 1 in Sea State 2 (full scale)

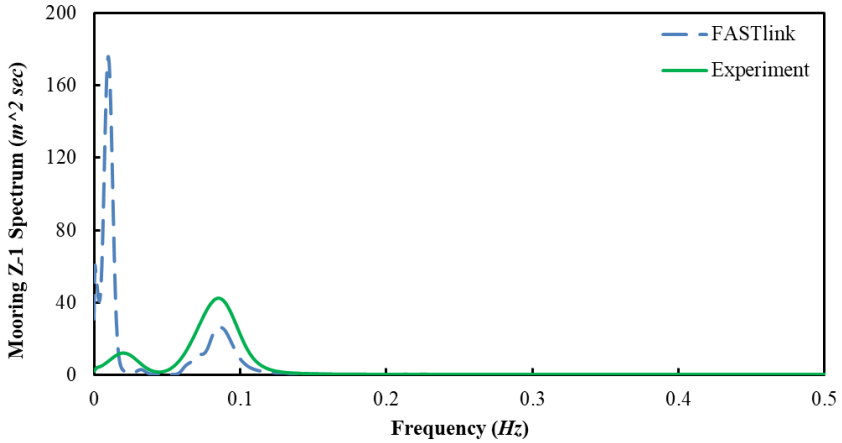

Figure 6. 55 Point-1 motion along Z-axis, on Mooring Line 1 in Sea State 2 (full scale)

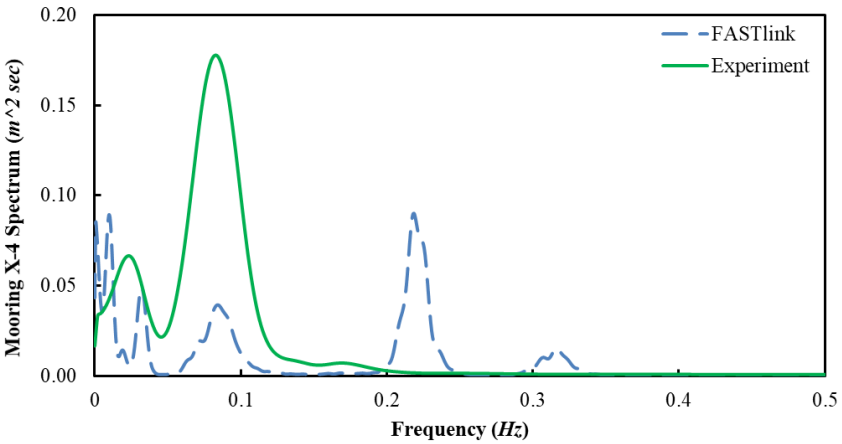

Figure 6. 56 Point-4 motion along X-axis, on Mooring Line 1 in Sea State 2 (full scale)

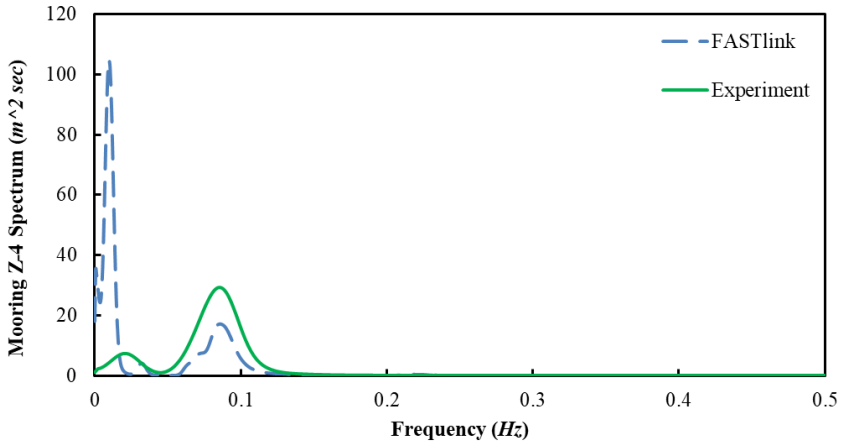

Figure 6. 57 Point-4 motion along Z-axis, on Mooring Line 1 in Sea State 2 (full scale)

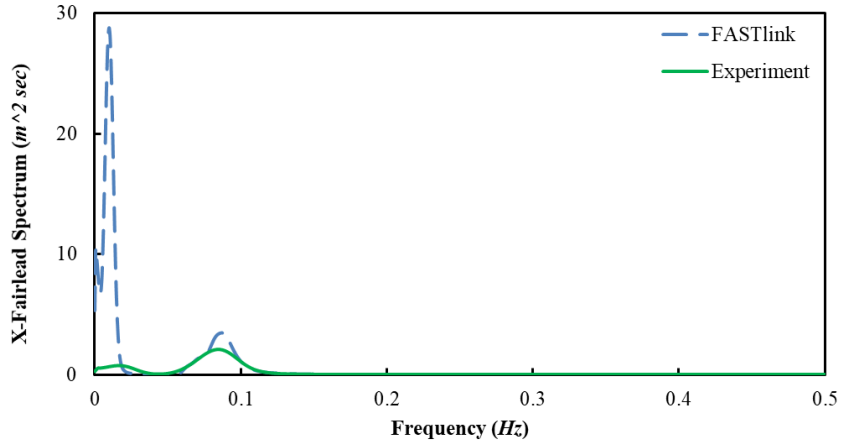

Figure 6. 58 Fairlead motion along X-axis, on Mooring Line 1 in Sea State 2 (full scale)

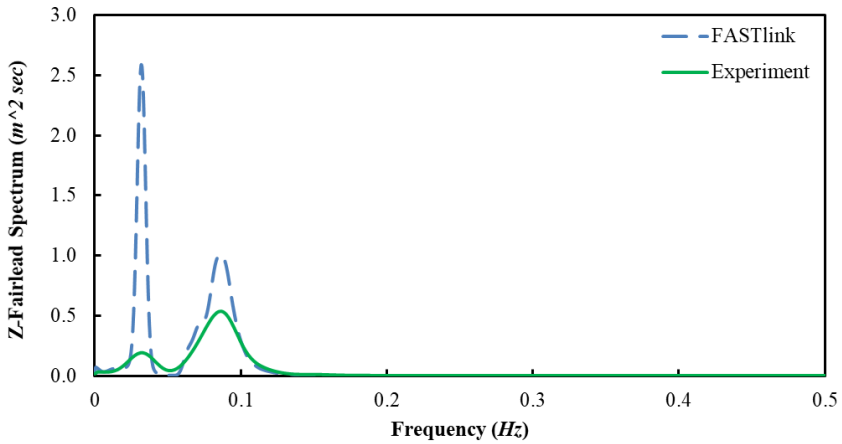

Figure 6. 59 Fairlead motion along Z-axis, on Mooring Line 1 in Sea State 2 (full scale)

Mooring Line Tensions - Sea State 2

The three mooring line tension spectrum from Sea State 2 have been presented in this part. As shown in Figure 6. 60, it can be seen that the Mooring Tension 1 spectrum shows much higher power in experiment than in the FASTlink results, while FAST shows only a tiny amount of energy compared to the other two approaches. This is similar with the tension RMS in regular waves, where experiment moorings show a much larger peak value than the numerical predictions due to the large loads which occur when the lines snatches in the experiment. In the experiment, tension spectrum of Mooring Line 1 shows two peaks – the main peak occurs at around 0.089 Hz, which is the peak wave frequency, while the other one occurs at around 0.025 Hz – which is similar to the mooring line motion spectrum along X-axis. In contrast, for the FASTlink data, the main peak is at around 0.010 Hz and only a small peak appears at the peak wave frequency. Both of the experiment and numerical results show a similar curve in the tension spectrum with the Mooring Line 1 motion spectrum, which indicates that the mooring line motion can indicate its tension behaviour.

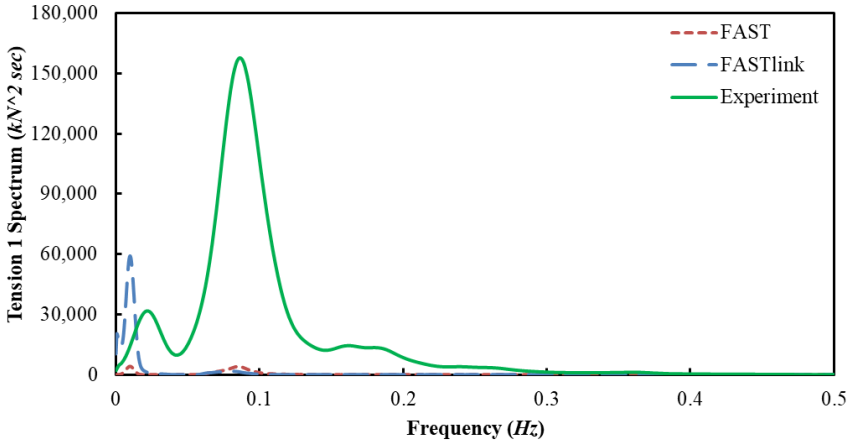

Figure 6. 60 Mooring Tension 1 in Sea State 2 (full scale)

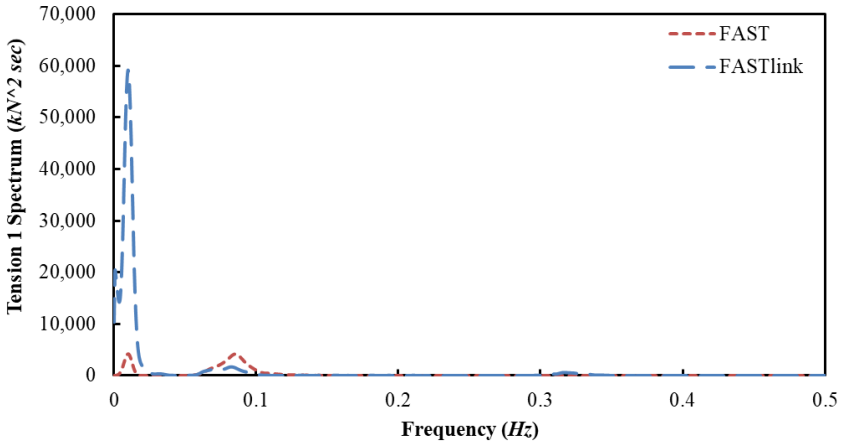

Figure 6. 61 Mooring Tension 1 in FAST and FASTlink, Sea State 2 (full scale)

For the mooring tension in Mooring Lines 2 and 3, as shown in the figures below, the experiment (and FAST) results show two clear peaks, but FASTlink shows a lot of noise (as seen clearly in Figure 6. 62). The time history of the three mooring line tensions in the FASTlink (OrcaFlex) has been checked, and it shows that the OrcaFlex cannot predict the mooring tension properly when under large sea states with this mooring design (when line snatching is happening), as shown in Figure 6. 64. This could be due to the mooring drag coefficient being set as 0 in this study (to make FASTlink show the snatching behaviour); when the mooring drag coefficient is set to 1.2 (as with the NREL published results), the mooring tension exhibit a plausible time history even in the largest Sea State 4. For the Sea State 1, FASTlink can still predict the tension correctly, but after Sea State 2, it obviously failed. The detailed time history of the mooring tensions in Sea State 1 and 2 are shown in Appendix 11. Compared with the Mooring Tension 1, the Mooring Tension 2 and 3 show quite smaller energy, which match with the results in regular waves.

As shown in Figure 6. 62 and Figure 6. 65, the experimental spectrum exhibits two peaks – one is still at the peak wave frequency, and the major one is at a quite low frequency, about 0.002 Hz, which corresponds to the frequency observed in the heave motion in Sea State 3. This indicates there should exist some non-linear dynamic behaviour at this small frequency which could usefully be investigated with further studies.

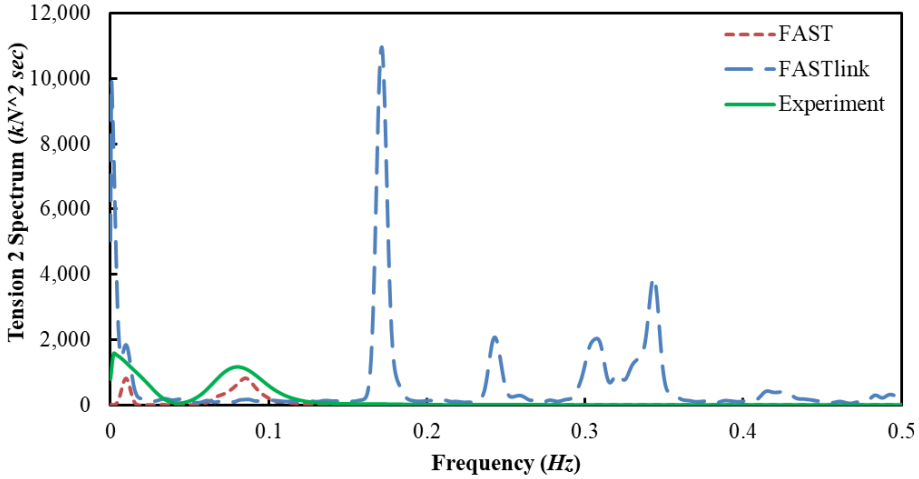

Figure 6. 62 Mooring Tension 2 in Sea State 2 (full scale)

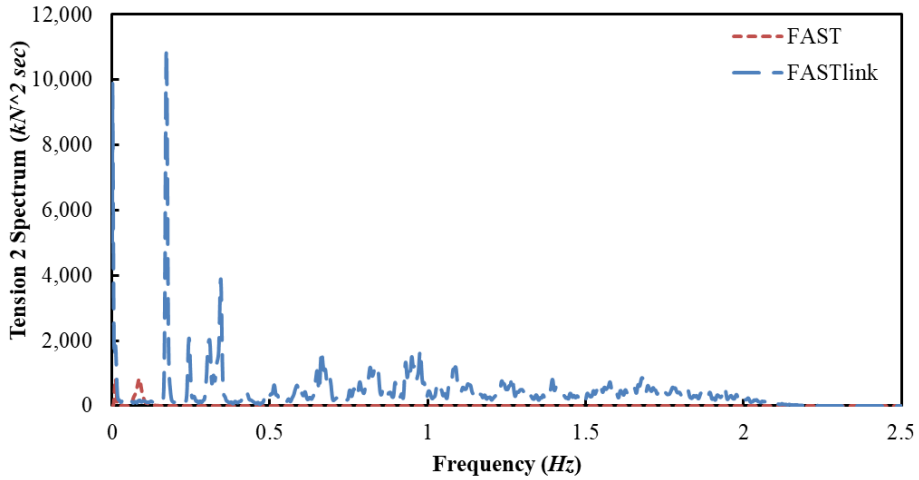

Figure 6. 63 Mooring Tension 2 (and 3) in FAST and FASTlink, Sea State 2 (full scale)

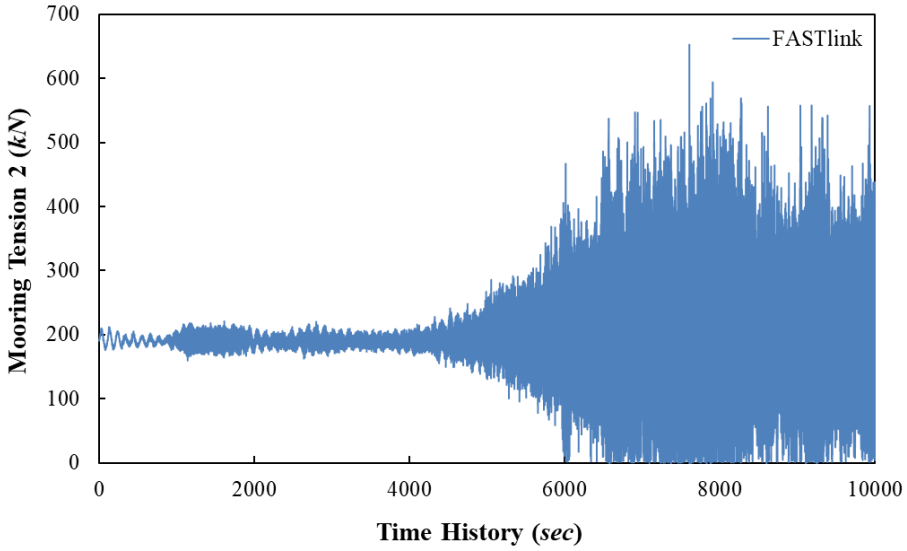

Figure 6. 64 Mooring Tension 2 time history in FASTlink, Sea State 2 (full scale)

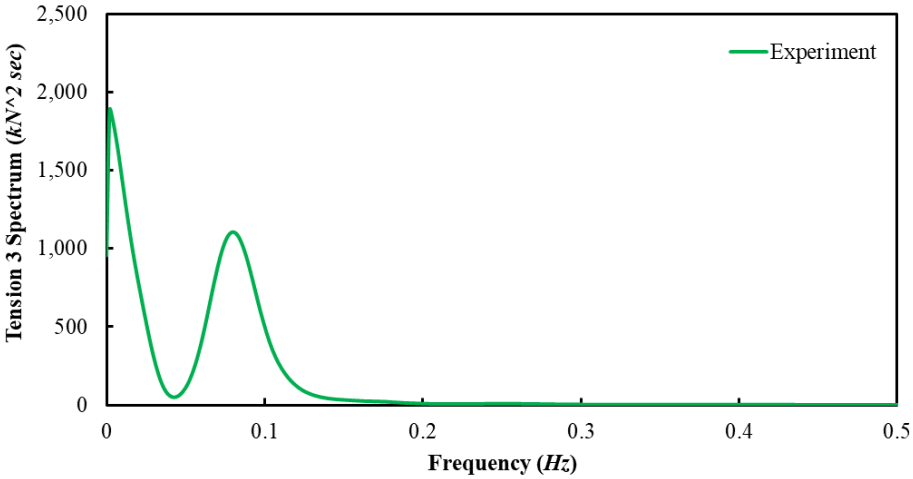

Figure 6. 65 Mooring Tension 3 time history in experiment, Sea State 2 (full scale)

Since the tension in mooring line cannot be calculated properly in FASTlink in Sea State 2 when Cd is set to zero, a comparison with the predicted line tension when Cd is 1.2 is shown in Figure 6. 66. This shows that the peak spectrum frequency of the tension in Mooring Line 1 is not substantially affected by the Cd but that the energy is reduces due to the existence of the mooring drag. Thus, as shown in Figure 6. 67, it is

seen that a peak spectrum in both experiment and FASTlink (when Cd=1.2), for tension in Mooring Lines 2/3 show a spectral peak at the peak wave frequency. In FASTlink (when Cd=1.2), a major peak is at the 0.010 Hz, which is same with Mooring Tension 1 and mooring line motions.

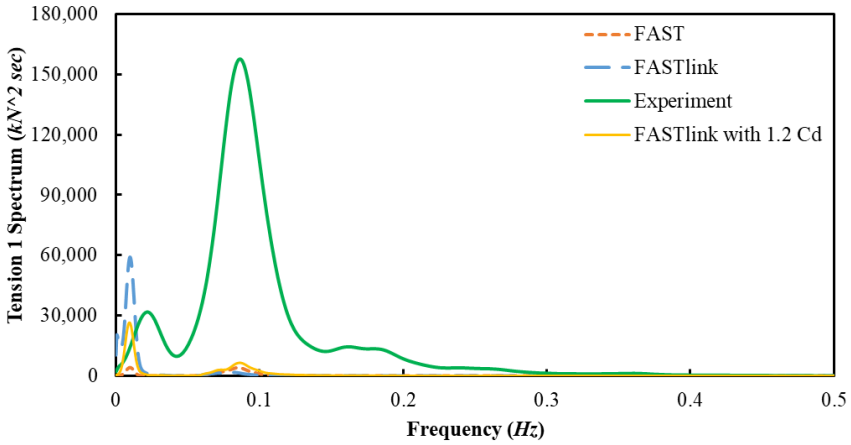

Figure 6. 66 Mooring Tension 1, comparing when Cd=1.2, Sea State 2 (full scale)

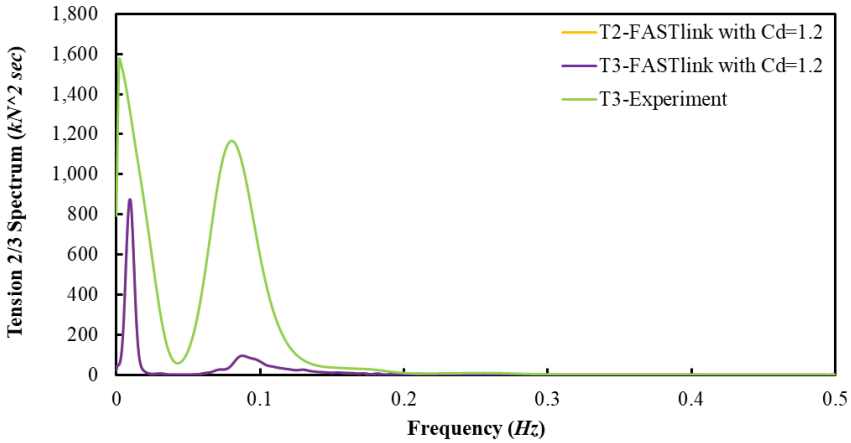

Figure 6. 67 Mooring Tension 2/3 in FASTlink when Cd=1.2, Sea State 2 (full scale)

6.6 Summary

This chapter presented both the experimental results and the numerical results for the spar with realistic mooring lines. In all of the cases, the platform heave, pitch and surge, three mooring line tensions and the Mooring Line 1 motions are being analyzed.

A free decay test has been conducted first in the tank to get the platform 6 DOF motion's natural frequencies and the results are matching quite well with the NREL paper. The damping matrix is being calculated and added into the numerical models. Although the pitch damping ratio from the decay tests are much smaller than the numerical model (after the damping matrix been modified), it is seen from both RMS figures from the regular waves and pitch motion spectrum in irregular waves that the differences are not that much and there could be some calculation error with the Fit Function when dealing with the tank test data.

A range of regular waves has been generated by the wave maker in the tank to investigate the response of the spar platform, along with mooring tensions and motions and the results are being shown with both RAO and RMS values. A snatching phenomenon has been observed in some of the wave frequencies in the experiment and FASTlink, which can cause the line tension to reach high values very suddenly. One of the waves has been repeated three times at the tank test to make sure that the results from the experiment are reliable. The linearity tests have been conducted to examine the variation of both heave and pitch motions at their natural frequency with a range of wave heights. The peak RMS frequencies for both heave and pitch are found to match well between the experiment and numerical simulations, but the peak RAO

amplitude shows that the numerical simulations tend to overestimate the results compared to experiment. This is assumed to be due to the different damping ratio and some weakness in the software calculation of the dynamic viscous damping. While for the mooring tensions, the results from the experiment are much higher than the numerical models due to the limitations for the software in calculating the loads during snatching. FASTlink can predict a curve with similar tendency but poor agreement in magnitude for both the mooring tensions and motions with the experiment.

Four sea states, i.e., irregular waves, have been run for the spar platform. The results from Sea State 2 are been mainly discussed in this part, the details of the other three sea states are shown in the appendices. For the platform heave, pitch and surge, the spectra show clear peaks at both the peak wave frequency and the natural frequencies of motion, and a coupling between pitch and surge has been identified. A very low frequency (0.002 Hz) with quite high energy in the heave motion in Sea State 3 (in experiment), which was found due to the large slowly-varying vertical motion in a certain times and it disappears when these part of the time history been removed. Some mooring tensions/motions have also been discovered with this small frequency (with quite high energy) are getting more obvious when increasing the wave energy, which indicates the existence of some non-linear dynamic behaviour at this small frequency and could usefully be investigated with further studies.

Chapter 7 Summary, Conclusion and Recommendations

This chapter will give a summary of the main results presented in this thesis and recommendations for future research are given.

7.1 Summary of Key Findings

Wind energy is a very promising sustainable and environmental-friendly resources and the onshore installed wind energy capacity has already reached up to 540,000 MW by the end of 2017. Apart from the greater availability of wind resources on sea surface than in land, with the development of wind turbine technology and the increasing volume of the wind turbines, harvesting the offshore wind energy, i.e. building offshore floating wind turbines can be seen as a necessary action. Both the fixed offshore platforms and floating platforms for the wind turbines were been introduced in Chapter 1. As discussed, when the water depth is beyond 50m or 60m, it would be more economic to use the floating platforms than the fixed ones. The spar platform was chosen as the research model in this study due to its simplicity in shape and ease of modelling in numerical codes.

The technical background relative with the fluid dynamic and flow passing through a spar platform was given in Chapter 2. The research methods in both experiment and numerical about OFWT had been reviewed. A brief introduction about the NREL 5MW baseline wind turbine properties and working principles were given. The OC3-Hywind is a very popular design for research of spar type OFWT which is also the basic model in this study. Most of the research about the OC3-Hywind are focusing on the dynamic analysis of floating platforms and mooring tensions. The research gap had

been found in the experiment validation of the FASTlink software and the lack of research about mooring line motion behaviours.

The FAST code, which is an sophisticated software to model the wind turbines has been introduced and its combination with another hydrodynamic analysis software-OrcaFlex, known as FASTlink has also been introduced. The limitations of the numerical modelling have been discussed. Prior to the start of the simulations, these numerical codes have been verified with available published results as shown in Chapter 3.

Conducting the experiment campaign is one of the most important parts in this thesis, thus, the calibrations and the set-up procedures were described in detail in Chapter 4 to show the fidelity of the experiment results. The limitations of the experiment have also been discussed and they are all felt to be acceptable in this study scope. The platform 6 DOF motions and the mooring line motions were captured by the Qualysis camera both above the tank and under the water line of the tank. The captured motion spectrums are then transferred into the Spike software. Two wave probes are being set up and calibrated before the experiment and the wave spectrum are also being recorded by the Spike system. To record the three mooring line tensions, the load cells are being calibrated first and then put into their adjusted anchor position and the time history are also being recorded by the Spike. The detailed model parameters in both tank test scale and full scale were given. For the irregular waves, the wave maker had also been calibrated without the model in the tank. These procedures are necessary to ensure the tank test results are reliable.

The spar-only properties had been checked firstly without realistic mooring restrictions. From the free decay tests, the tank test model shows good agreement in its natural frequencies with the numerical model. The damping ratio had been adjusted in the numerical simulations to match with the tank test model. In this part, only the heave and pitch motion were analysed due to the single wave direction and the absence of realistic mooring lines. In both heave and pitch motion, experiment results show smaller responses than the two numerical software, it shows the limited ability somehow in the numerical predictions. The soft elastic moorings are necessary in the tank tests to prevent the model drifting away and the restriction effect is assumed to be ignored as the natural frequencies and damping ratios show no difference with and without the moorings in place. One wave frequency has been chosen randomly and been repeated three times to make sure that the results are reliable. The linearity of the system has been checked by increasing the wave height with wave frequency at heave/pitch natural frequencies. It is seen that with the increasing of the wave height, the heave/pitch RAO curve is decreasing in experiment and FAST. But for heave motion in FASTlink, the curve is increasing quite linearly. For the irregular waves, the platform motions can show two peaks in the response spectra which are at the heave/pitch natural frequencies and the peak wave frequencies. When at the platform natural frequencies, the FASTlink tend to over predict the results than the experiment while the FAST can show good agreement at the peak wave frequency but can hardly show the spectrum peak at their natural frequencies.

In Chapter 6, the platform properties have been investigated with realistic mooring systems in both numerical and experimental studies. The three mooring line tensions

and one of the mooring line motions have been recorded and compared with numerical results. In the free decay tests, apart from the yaw motion, other DOFs can agree well with the NREL models; discrepancies in yaw are assumed to be because of the lack of the delta mooring configurations in these tank tests. The damping properties have been checked in the experiment and the numerical damping matrix have been adjusted to match with the tank test model. A series of regular waves have been applied to the model in the tank and the non-linear responses including snatching phenomena have been observed in some wave frequencies. This is not a good sign, as the sudden stretching and slackening of the lines can result in mooring line failures. This snatching phenomenon can be affected by many factors. For example, initially, when the mooring line drag coefficient was set as 1.2 (which is same with the NREL model,), this behaviour does not happen in FASTlink, and FAST cannot show any snatching, which could probably due to the quasi-static mooring models in the code. When the mooring drag coefficient is set to zero in FASTlink, the snatching in the mooring line happens at the same wave frequencies as in the experiment, while the platform responses were not affected by the change of the mooring drag coefficient. It suggests that the occurrence of snatching in the physical system can be predicted using the FASTlink software if the mooring drag coefficient is set to zero. But as the mooring drag coefficient should not be zero in reality, it is likely that other reasons caused the snatching.

For the snatching phenomenon, perhaps surprisingly, it is found that when the wave frequency is near the heave/pitch natural frequencies, the snatching disappears, while for other wave frequencies it shows quite strong effect, which can indicate that the

mooring line motions are mainly driven by the platform motions when at the platform natural frequencies. In addition, other factors which can cause this snatching motion could be the mooring system configurations, the mooring line weight/length or the platform shapes, etc., which can be figured out by further studies. For the mooring line motions along X-axis, in full scale, the experiment results show its natural frequencies is 0.023 Hz and FASTlink predict it at about 0.010 Hz, through all the sea states. For the mooring tensions, in this thesis, FASTlink can only show proper results in Sea State 1 for all the three mooring lines; for Sea State 2 and above, it shows the limitations and the results cannot convergence.

A very low frequency component (0.002 Hz in full scale) was found in the Mooring Tension spectra for moorings 2 and 3 for all the four sea states and also in heave motion in Sea State 3 and 4 in the experiment. This was found to be due to a large slowly-varying vertical motion occurring at certain times; the platform was observed to undergo a vertical displacement downwards (but did not touch the tank bottom) and stayed down for an extended period before returning back up to its mean vertical position. The spectral component disappears when these sections of the time history are removed. The mooring tensions/motions spectra also exhibit this low frequency component (with quite high energy); the component is more obvious when increasing the wave energy, which could be due to the increasing for the non-linear snatching effect under extreme sea states.

Conclusions

In this study, the hydrodynamic properties of a spar platform with a certain design of mooring systems under various wave loads are been investigated via both experimental and numerical approaches. The main contribution of the thesis is to show the ability and limitations of the numerical software, especially when predicting the mooring line motion characteristics.

In this study, all the platform motions, mooring tensions and motions have responded obviously at the wave frequencies (or peak wave frequencies), which means the first order wave is dominant.

The platform motion responses, for spar only and with the designed mooring system, in both regular and irregular waves have been investigated. The platform heave/pitch/surge natural frequencies and damping ratios have been checked in both numerical simulations and tank tests. The damping characters has been adjusted in the software to match with the experiment. The overall natural frequencies match extremely well between the two approaches – with the differences below 2%. Although the numerical predictions tend to overestimate the amplitude of the platform motion responses in regular waves when compared with tank tests – in most of the case, the differences are less than 1% but can go up to 25%, especially when the nonlinear snatching happens. In spar only tests, in irregular waves, FASTlink shows a much higher peak value of the heave response spectrum than that found from the experiment; however, when the energy around the peak is calculated it is found that the total energy associated with the spectral peak in prediction and experiment are

almost the same – the difference is less than 0.6%, which suggests that FASTlink can predict the platform response in heave quite accurately.

For the mooring line motions, FASTlink can capture some of the features (the nonlinear snatching) after adjusting the mooring drag coefficient, but the natural frequency and motion amplitude cannot match with the experiment results; FAST cannot predict the snatching phenomenon at all. The mechanisms for the nonlinear snatching during the tank tests and how to predict it in numerical studies are still unclear, and it is recommended as a topic for future work.

For the mooring line tensions, the two numerical approaches are matching well at its natural or peak wave frequencies. But when the sea states are larger, FASTlink cannot correctly calculate the mooring line tensions, due to the complicated non-linear snatching effect and also the setup of the mooring drag coefficient.

Overall, the FAST and FASTlink can predict platform dynamic responses well with tank tests results, but they cannot capture the non-linear snatching behaviour properly in the mooring line motions and show the limitations when calculating mooring line tensions in extreme sea states.

7.2 Recommendations for Future Research

The recommendations for future research based on the results of this thesis are pointed out briefly below:

- As the snatching phenomenon have been observed, the detailed factors which can cause it should be investigated. Also, whether the non-linear motion associated with snatching can affect the turbine behaviour should be examined.

- In this study, the environmental loads are only in one direction, a combination of different wave/wind direction and turbulent wind flow should be applied to see the effect on the snatching phenomenon.

- The different spar platform design and mooring line configurations can also be studied to understand better the snatching phenomenon.

- It is important to develop tools/methods to predict the snatching behaviour so that it can be avoided in real design.

References

Ahn, H.J. and Shin, H., 2017. Model test & numerical simulation of OC3 spar type floating offshore wind turbine. International Journal of Naval Architecture and Ocean Engineering.

Barahona, B., Jonkman, J.M., Damiani, R., Robertson, A. and Hayman, G., 2015. Verification of the new FAST v8 capabilities for the modeling of fixed-bottom offshore wind turbines. In 33rd wind energy symposium (p. 1205).

Blevins, R. D. (1990), Flow Induced Vibration, 2nd Edn., Van Nostrand Reinhold Co.

Brommundt, M., Krause, L., Merz, K. and Muskulus, M. (2012). Mooring system optimization for floating wind turbines using frequency domain analysis. Energy Procedia, 24, pp.289-296.

Burton, T., Sharpe, D., Jenkins, N. and Bossanyi, E. (2011). Wind energy handbook. John Wiley & Sons

Caballero, R., Vega, A., Berbey, A. and Armada, M., 2014. Six Degree of Freedom Underwater Vehicle for Culvert Inspection. In CLAWAR 2014 – Proceedings of the Seventeenth International Conference on Climbing and Walking Robots and the Support Technologies for Mobile Machines, Poznan, Poland.

Chakrabarti, S.K. (1994). Offshore structure modeling (Vol. 9). World Scientific.

Clancy, L.J., 1975. Aerodynamics. Halsted Press.

Stansberg, C.T., Contento, G., Hong, S.W., Irani, M., Ishida, S., Mercier, R., Wang, Y., Wolfram, J., Chaplin, J. and Kriebel, D., 2002. The specialist committee on waves final report and recommendations to the 23rd ITTC. *Proceedings of the 23rd ITTC, 2*, pp.505-551.

Czyzewski, A. (2012). Wind energy gets serial. The Engineer.

de Ridder, E.J., Otto, W., Zondervan, G.J., Huijs, F. and Vaz, G. (2014). Development of a scaled-down floating wind turbine for offshore basin testing. In ASME 2014 33rd International Conference on Ocean, Offshore and Arctic Engineering (pp. V09AT09A027-V09AT09A027). American Society of Mechanical Engineers.

Dinh, V.N. and Basu, B. (2013). On the modeling of spar-type floating offshore wind turbines. In Key Engineering Materials (Vol. 569, pp. 636-643). Trans Tech Publications.

Driscoll, F., Jonkman, J., Robertson, A., Sirnivas, S., Skaare, B. and Nielsen, F.G., 2016. Validation of a FAST model of the statoil-hywind demo floating wind turbine. Energy Procedia, 94, pp.3-19.

Duan, L. and Kajiwara, H. (2014). A coupled aero-hydrodynamic simulator for offshore floating wind turbines. In ASME 2014 33rd International Conference on Ocean, Offshore and Arctic Engineering. American Society of Mechanical Engineers.

Duan, F., Hu, Z. and Wang, J. (2015). Model tests of a spar-type floating wind turbine under wind/wave loads. In ASME 2015 34th International Conference on Ocean, Offshore and Arctic Engineering (pp. V009T09A044-V009T09A044). American Society of Mechanical Engineers.

Duan, F., Hu, Z., Liu, G. and Wang, J. (2016 a). Experimental comparisons of dynamic properties of floating wind turbine systems based on two different rotor concepts. Applied Ocean Research, 58, pp.266-280

Duan, F., Hu, Z. and Niedzwecki, J.M. (2016 b). Model test investigation of a spar floating wind turbine. Marine Structures, 49, pp.76-96.

EOWDC (The European Offshore Wind Deployment Centre) (2018) (Aberdeen Offshore Wind Farm – European Offshore Wind Deployment Centre). Available at: <https://www.aberdeenrenewables.com/portfolio/eowdc/j>

EWEA, E. (2016). The European offshore wind industry - key trends and statistics 2015. European Wind Energy Association (EWEA)

Fitzpatrick R. (2012) Fluid Mechanics. Available at <http://farside.ph.utexas.edu/teaching/336L/Fluidhtml/Fluidhtml.html>

Global Wind Energy Council (2018), "GLOBAL WIND STATISTICS 2017".

Goupee, A.J., Koo, B., Lambrakos, K. and Kimball, R. (2012). Model tests for three floating wind turbine concepts. In Offshore technology conference. Offshore Technology Conference.

Hall, M., Buckham, B., Crawford, C. and Nicoll, R.S. (2011). The importance of mooring line model fidelity in floating wind turbine simulations. In OCEANS 2011 (pp. 1-8). IEEE.

Hill, J.S. (2018). New Global Offshore Wind Capacity In 2017 Hits 3.3 Gigawatts. Available from: <https://cleantechnica.com/2018/02/07/new-global-offshore-wind-capacity-2017-hits-3-3-gw/>

Hong, S., Lee, I., Park, S.H., Lee, C. and Chun, H.H. (2013). Scale Model Experiments of the SPAR-Type Floating Offshore Platform. In The Twenty-third International Offshore and Polar Engineering Conference. International Society of Offshore and Polar Engineers.

How Hywind works. (2019). Available at <https://www.equinor.com/en/what-we-do/hywind-where-the-wind-takes-us/hywind-up-close-and-personal.html>

Hsu, W.T., Thiagarajan, K.P., MacNicoll, M. and Akers, R. (2015). Prediction of extreme tensions in mooring lines of a floating offshore wind turbine in a 100-year storm. In ASME 2015 34th International Conference on Ocean, Offshore and Arctic Engineering (pp. V009T09A050-V009T09A050). American Society of Mechanical Engineers.

IAPWS, 2008. Viscosity of water. Available at <https://wiki.anton-paar.com/en/water/>

Ideol, (2018), France's first offshore wind turbine and Ideol's first demonstrator. Availabe from: < https://www.ideol-offshore.com/en/floatgen-demonstrator>

Ishida, S., Kokubun, K., Nimura, T., Utsunomiya, T., Sato, I. and Yoshida, S., 2013, June. At-sea experiment of a hybrid spar type offshore wind turbine. In ASME 2013 32nd International Conference on Ocean, Offshore and Arctic Engineering (pp. V008T09A035-V008T09A035). American Society of Mechanical Engineers.

ITTC (2014), ITTC Quality System Manual Recommended Procedures and Guidelines Procedure Uncertainty Analysis, Instrument Calibration (7.5-01-03-01)

Jeon, S.H., Cho, Y.U., Seo, M.W., Cho, J.R. and Jeong, W.B. (2013). Dynamic response of floating substructure of spar-type offshore wind turbine with catenary mooring cables. Ocean Engineering, 72, pp.356-364.

Jonkman, J. and Buhl, M.J. (2007 a). Loads analysis of a floating offshore wind turbine using fully coupled simulation. Reprint Conference Paper NREL. CP-500-41714.

Jonkman, J.M. (2007 b). Dynamics modelling and loads analysis of an offshore floating wind turbine (No. NREL/TP-500-41958). National Renewable Energy Lab.(NREL), Golden, CO (United States).

Jonkman, J., Butterfield, S., Musial, W. and Scott, G. (2009). Definition of a 5-MW reference wind turbine for offshore system development. National Renewable Energy Laboratory, Golden, CO, Technical Report No. NREL/TP-500-38060.

Jonkman, J. (2010 a). Definition of the Floating System for Phase IV of OC3 (No. NREL/TP-500-47535). National Renewable Energy Laboratory (NREL), Golden, CO.

Jonkman, J., Larsen, T., Hansen, A., Nygaard, T., Maus, K., Karimirad, M., Gao, Z., Moan, T. and Fylling, I. (2010 b). Offshore Code Comparison Collaboration within IEA Wind Task 23: Phase IV Results Regarding Floating Wind Turbine Modeling; Preprint (No. NREL/CP-500-47534). National Renewable Energy Laboratory (NREL), Golden, CO.

Jonkman, J. and Matha, D. (2010 c). Quantitative comparison of the responses of three floating platforms (No. NREL/CP-500-46726). National Renewable Energy Lab.(NREL), Golden, CO (United States).

Jonkman, B. and Jonkman, J., 2016. FAST v8. 16.00 a–bjj. National Renewable Energy Laboratory.

Karimirad, M. and Moan, T. (2011). Wave-and wind-induced dynamic response of a spar-type offshore wind turbine. Journal of waterway, port, coastal, and ocean engineering, 138(1), pp.9-20.

Karimirad, M. and Moan, T. (2012). Feasibility of the application of a spar-type wind turbine at a moderate water depth. Energy Procedia, 24, pp.340-350.

Karimirad, M. (2013). Modelling aspects of a floating wind turbine for coupled wave–wind-induced dynamic analyses. Renewable Energy, 53, pp.299-305.

Kimball, R., Goupee, A.J., Fowler, M.J., de Ridder, E.J. and Helder, J. (2014). Wind/wave basin verification of a performance-matched scale-model wind turbine on a floating offshore wind turbine platform. In ASME 2014 33rd International Conference on Ocean, Offshore and Arctic Engineering (pp. V09BT09A025-V09BT09A025). American Society of Mechanical Engineers.

Koo, B., Goupee, A.J., Lambrakos, K. and Lim, H.J. (2014). Model test data correlations with fully coupled hull/mooring analysis for a floating wind turbine on a semi-submersible platform. In ASME 2014 33rd International Conference on Ocean, Offshore and Arctic Engineering (pp. V09BT09A034-V09BT09A034). American Society of Mechanical Engineers.

Ledru, R., Le Cunff, C., Heurtier, J.M., Perdrizet, T. and Poirette, Y. (2014). Influence of Hydrodynamic Modeling Assumptions on Floating Wind Turbine Behaviour. In ASME 2014 33rd International Conference on Ocean, Offshore and Arctic Engineering (pp. V09BT09A042-V09BT09A042). American Society of Mechanical Engineers.

Lee, H.T., Chen, S.H. and Kang, H.Y. (2004). A study of generalized reduced gradient method with different search directions. Journal of Quantitative Management, 1(1), pp.25-38.

Lefebvre, S. and Collu, M. (2012). Preliminary design of a floating support structure for a 5 MW offshore wind turbine. Ocean Engineering, 40, pp.15-26.

Lin, Z. and Sayer, P. (2015). Influence of water depth variation on the hydrodynamics of deep-water mooring characteristics. Ocean Engineering, 109, pp.553-566.

Lupton, R.C. and Langley, R.S. (2014). Assessing the Importance of the Slow Drift Motion of Floating Wind Turbine Platforms. In ASME 2014 33rd International Conference on Ocean, Offshore and Arctic Engineering (pp. V09AT09A051-V09AT09A051). American Society of Mechanical Engineers.

Masciola, M., Robertson, A., Jonkman, J. and Driscoll, F. (2011). Investigation of a FAST-OrcaFlex Coupling Module for Integrating Turbine and Mooring Dynamics of

Offshore Floating Wind Turbines: Preprint (No. NREL/CP-5000-52896). National Renewable Energy Laboratory (NREL), Golden, CO.

Masciola, M., Robertson, A., Jonkman, J., Coulling, A. and Goupee, A. (2013). Assessment of the importance of mooring dynamics on the global response of the DeepCwind floating semisubmersible offshore wind turbine. In The Twenty-third International Offshore and Polar Engineering Conference. International Society of Offshore and Polar Engineers.

Matha, D. (2010). Model development and loads analysis of an offshore wind turbine on a tension leg platform with a comparison to other floating turbine concepts: April 2009 (No. NREL/SR-500-45891). National Renewable Energy Laboratory (NREL), Golden, CO.

Matzat, G. (2014). Top 10 Things You Didn't Know About Offshore Wind Energy. Available from: <http://www.energy.gov/articles/top-10-things-you-didn-t-know-about-offshore-wind-energy>

Molina, M.G. and Alvarez, J.G. (2011). Technical and regulatory exigencies for grid connection of wind generation. INTECH Open Access Publisher.

Musial, W., Butterfield, S. and Boone, A. (2004). Feasibility of floating platform systems for wind turbines. In 42nd AIAA aerospace sciences meeting and exhibit (p. 1007).

Mustto, A.A. and Bodstein, G.C., 2011. Subgrid-scale modeling of turbulent flow around circular cylinder by mesh-free vortex method. Engineering applications of computational fluid mechanics, 5(2), pp.259-275.

Myhr, A., Maus, K.J. and Nygaard, T.A. (2011). Experimental and computational comparisons of the OC3-Hywind and tension-leg-buoy (TLB) floating wind turbine conceptual designs. In The Twenty-first International Offshore and Polar Engineering Conference. International Society of Offshore and Polar Engineers.

Oswald, J., Raine, M. and Ashraf-Ball, H. (2008). Will British weather provide reliable electricity?. Energy Policy, 36(8), pp.3212-3225.

Peng, C., Yan, F. and Zhang, J. (2014). Coupled dynamic response of a spar type floating offshore wind turbine. In ASME 2014 33rd International Conference on Ocean, Offshore and Arctic Engineering (pp. V09AT09A035-V09AT09A035). American Society of Mechanical Engineers.

Philippe, M., Babarit, A. and Ferrant, P. (2013). Modes of response of an offshore wind turbine with directional wind and waves. Renewable energy, 49, pp.151-155.

Proskovics, R. (2015). Dynamic response of spar-type offshore floating wind turbines (Doctoral dissertation, University of Strathclyde).

Ramachandran, G.K.V., Robertson, A., Jonkman, J.M. and Masciola, M.D. (2013). Investigation of Response Amplitude Operators for Floating Offshore Wind Turbines: Preprint (No. NREL/CP-5000-58098). National Renewable Energy Laboratory (NREL), Golden, CO.

Robertson, A.N. and Jonkman, J.M. (2011). Loads analysis of several offshore floating wind turbine concepts. In The Twenty-first International Offshore and Polar Engineering Conference. International Society of Offshore and Polar Engineers.

Robertson, A.N., Jonkman, J., Masciola, M., Song, H., Goupee, A., Coulling, A. and Luan, C. (2012). Definition of the semisubmersible floating system for phase II of OC4. Offshore Code Comparison Collaboration Continuation (OC4) for IEA Task, 30.

Rolo, L. (2014). Design, testing and validation of a scale model semisubmersible offshore wind turbine under regular/irregular waves and wind loads, MSc Thesis: University of Strathclyde.

Ruzzo, C., Fiamma, V., Collu, M., Failla, G., Nava, V. and Arena, F., 2018. On intermediate-scale open-sea experiments on floating offshore structures: Feasibility and application on a spar support for offshore wind turbines. Marine Structures, 61, pp.220-237.

SANTOSSantos-HERRÁNHerrán, M. (2016). Model Design, Testing and Validation of Three Scaled Spar Type Offshore Floating Wind Turbines under Wave Loads, MSc Thesis: University of Strathclyde.

Savenije, L.B., Ashuri, T., Bussel, G.J. and Staerdahl, J.W. (2010). Dynamic modeling of a spar-type floating offshore wind turbine. In Scientific Proceedings European Wind Energy Conference & Exhibition.

Seebai, T. and Sundaravadivelu, R. (2009). Effect of Taut And Catenary Mooring On Spar Platform With 5MW Wind Turbine. In Eighth ISOPE Ocean Mining Symposium. International Society of Offshore and Polar Engineers.

Sethuraman, L. and Venugopal, V. (2013). Hydrodynamic response of a stepped-spar floating wind turbine: Numerical modelling and tank testing. Renewable Energy, 52, pp.160-174.

Shin, H., 2011, January. Model test of the OC3-Hywind floating offshore wind turbine. In The Twenty-first International Offshore and Polar Engineering Conference. International Society of Offshore and Polar Engineers.

Shin, H., Dam, P.T., Jung, K.J., Rim, C. and Chung, T., 2013. Model test of new floating offshore wind turbine platforms. International Journal of Naval Architecture and Ocean Engineering, 5(2), pp.199-209.

Skaare, B., Hanson, T.D., Nielsen, F.G., Yttervik, R., Hansen, A.M., Thomsen, K. and Larsen, T.J., 2007, May. Integrated dynamic analysis of floating offshore wind turbines. In European Wind Energy Conference, Milan, Italy (pp. 7-10).

Statoil UK Ltd (2015) Statoil to build the world's first floating wind farm: Hywind Scotland. Available at: <https://www.agcc.co.uk/news-article/statoil-to-build-the-worlds-first-floating-wind-farm-hywind-scotland>

Sumer, B.M., 2006. Hydrodynamics around cylindrical strucures (Vol. 26). World scientific.

Tomasicchio, G.R., D'Alessandro, F., Avossa, A.M., Riefolo, L., Musci, E., Ricciardelli, F. and Vicinanza, D., 2018. Experimental modelling of the dynamic behaviour of a spar buoy wind turbine. Renewable energy, 127, pp.412-432.

Utsunomiya, T., Sato, T., Matsukuma, H. and Yago, K. (2009). Experimental validation for motion of a spar-type floating offshore wind turbine using 1/22.5 scale model. In ASME 2009 28th International Conference on Ocean, Offshore and Arctic Engineering (pp. 951-959). American Society of Mechanical Engineers.

Utsunomiya, T., Matsukuma, H., Minoura, S., Ko, K., Hamamura, H., Kobayashi, O., Sato, I., Nomoto, Y. and Yasui, K., 2013 a. At sea experiment of a hybrid spar for floating offshore wind turbine using 1/10-scale model. Journal of Offshore Mechanics and Arctic Engineering, 135(3), p.034503.

Utsunomiya, T., Sato, I., Yoshida, S., Ookubo, H. and Ishida, S., 2013 b, June. Dynamic response analysis of a floating offshore wind turbine during severe typhoon event. In ASME 2013 32nd International Conference on Ocean, Offshore and Arctic Engineering (pp. V008T09A032-V008T09A032). American Society of Mechanical Engineers.

Utsunomiya, T., Yoshida, S., Kiyoki, S., Sato, I. and Ishida, S., 2014 a, October. Dynamic response of a spar-type floating wind turbine at power generation. In ASME 2014 33rd International Conference on Ocean, Offshore and Arctic Engineering. American Society of Mechanical Engineers Digital Collection.

Utsunomiya, T., Yoshida, S., Ookubo, H., Sato, I. and Ishida, S. (2014 b). Dynamic analysis of a floating offshore wind turbine under extreme environmental conditions. Journal of Offshore Mechanics and Arctic Engineering, 136(2), p.020904.

Utsunomiya, T., Sato, I., Kobayashi, O., Shiraishi, T. and Harada, T., 2015, October. Design and installation of a hybrid-spar floating wind turbine platform. In ASME 2015 34th International Conference on Ocean, Offshore and Arctic Engineering. American Society of Mechanical Engineers Digital Collection.

Utsunomiya, T., Sato, I., Kobayashi, O., Shiraishi, T. and Harada, T., 2019. Numerical modeling and analysis of a hybrid-spar floating wind turbine. Journal of Offshore Mechanics and Arctic Engineering, 141(3), p.031903.

Vijfhuizen, W.J.M. (2006). Design of a wind and wave power barge. Universities of Glasgow and Strathclyde, Glasgow, Scotland.

Viré, A., Xiang, J., Piggott, M., Cotter, C. and Pain, C. (2013). Towards the fully-coupled numerical modelling of floating wind turbines. Energy Procedia, 35, pp.43-51.

Wang, C.M., Utsunomiya, T., Wee, S.C. and Choo, Y.S. (2010). Research on floating wind turbines: a literature survey. The IES Journal Part A: Civil & Structural Engineering, 3(4), pp.267-277.

Wayman, E.N., Sclavounos, P.D., Butterfield, S., Jonkman, J. and Musial, W. (2006). Coupled Dynamic Modeling of Floating Wind Turbine Systems: Preprint (No. NREL/CP-500-39481). National Renewable Energy Lab.(NREL), Golden, CO (United States).

Xu, X. and Srinil, N. (2015). Dynamic response analysis of spar-type floating wind turbines and mooring lines with uncoupled vs coupled models. In 34th ASME International Conference on Ocean, Offshore and Arctic Engineering. St. John's, Newfoundland, Canada

Yu, M., Hu, Z.Q. and Xiao, L.F. (2015). Wind-wave induced dynamic response analysis for motions and mooring loads of a spar-type offshore floating wind turbine. Journal of Hydrodynamics, Ser. B, 26(6), pp.865-874.

Zhang, R., Tang, Y., Hu, J., Ruan, S. and Chen, C. (2013). Dynamic response in frequency and time domains of a floating foundation for offshore wind turbines. Ocean Engineering, 60, pp.115-123.

Zhao, J., Zhang, L. and Wu, H. (2012). Motion performance and mooring system of a floating offshore wind turbine. Journal of Marine Science and Application, 11(3), pp.328-334.

Zürcher, K., 2016. Waterjet testing techniques for powering performance estimation using a single catamaran demihull (Doctoral dissertation, University of Tasmania).

Appendix 1 Calculation of the Equivalent Mooring Line Extensional Stiffness

The wire been used in the experiment is the code number 603.000.018 from the TecniCable company (the detailed information can be found in: <http://www.tecni-cable.co.uk/Products/US-Mil-Spec-Cable-7x7-Stainless-Mil-DTL-83420-Composition-B>)

The

$$E = 116{,}739\ N/mm^2 = 1.16739*10^{-5}\ N/m^2$$

The diameter is 1.8mm.

$$Equivalent\ mooring\ line\ extensional\ stiffness = E*a$$

Where *a* is the equivalent cross sectional area is about 55% of the whole area.

Figure A1. 1 Schematic plot of the mooring line's cross sectional area

i.e.

$$a = 55\%*\pi*(1.8/2)^2 = 1.4\ mm^2$$

Thus,

$$the\ equivalent\ mooring\ line\ extensional\ stiffness = 163{,}268\ N/m$$

Appendix 2 the Qualysis Underwater Ball Density

Due to these Qualysis underwater reflections balls are quite light, thus, the weight for each of them can hardly be measured. Thus, the detailed calculation is shown below. According to the measurement, the diameter of the Qualysis ball is 19 mm and the 3 mooring lines plus the 6 Qualysis balls is 160g

*the total mooring line weight = 3*3.555(m)*0.013 (kg/m) = 0.139 kg*

Thus,

*the weight of 1 Qualysis ball = 160-(0.1386*1000)/6 = 3.560g*

Thus,

the density of the Qualysis ball = 991.267 kg/m3,

which is quite near the fresh water density and the buoyancy effect can be ignored.

Appendix 3 Calculation for the Calibration Residuals for Wave Probe 1

This part gives the details for the calculation of the calibration residuals for Wave Probe 1. To get the 95% confidence level uncertainty, the Standard Error of Estimate (SEE) will be calculated first by using the STEYX function in Excel (to calculate the standard error of "Measured voltage" with the given "Displacement"). According to the ITTC recommendation, according to the calibration theory, when the SEE is used for uncertainty estimate purpose, the 95% confidence level uncertainty should use 3*SEE (ITTC, 2014). The detail of the residuals are shown in Table A3.1, which shows that the residuals are all within the 95% confidence level uncertainty.

SEE = STEYX (displacement, measured voltage) = 0.531 mm

95% confidence level uncertainty= 3 SEE = $\pm$ 1.594 mm*

Residual = calculated displacement – displacement

Table A3. 1 the Residual details

Displacement (*mm*)	Measured voltage (*N*)	Calculated displacement (*mm*)	Residuals (*mm*)
60	0.333	61.081	1.081
40	0.220	40.136	0.136
20	0.109	19.806	-0.194
12	0.066	11.782	-0.218
8	0.044	7.769	-0.231
4	0.021	3.524	-0.476
0	0.000	-0.384	-0.384
-4	-0.021	-4.288	-0.288
-8	-0.044	-8.467	-0.467
-12	-0.064	-12.202	-0.202
-20	-0.107	-20.060	-0.060
-40	-0.213	-39.670	0.330
-60	-0.318	-59.025	0.975

Appendix 4 Load Cell Re-measured Mass Compared with Measured Mass

As introduced in Chapter 4, to make sure that the calibration of the load cells is working correctly, the added mass has been put on again and the measured output data (in *N*) have been compared with the actual weight. The following three tables show the detailed data and it can be seen that the difference between the output number (Re-measured weight) are all less than 1% with the original number (Added weight). Thus, it can be confirmed that the measured tensions for the three mooring lines are trustable.

Table A4. 1 Rear Load Cell (Load Cell 1)

Added mass (kg)	Added weight (N)	Re-measured weight (N)	error (%)
0	0	0	0
0.1	0.981	0.972	-0.916
0.2	1.961	1.947	-0.740
0.3	2.942	2.923	-0.624
0.4	3.922	3.900	-0.575
0.5	4.903	4.878	-0.517
0.6	5.884	5.864	-0.340
0.7	6.864	6.845	-0.286
0.8	7.845	7.823	-0.273
0.9	8.825	8.804	-0.241
1	9.806	9.783	-0.232
1.1	10.787	10.769	-0.168
1.2	11.767	11.751	-0.140
1.3	12.748	12.730	-0.139
1.4	13.729	13.709	-0.146
1.5	14.709	14.689	-0.137
1.6	15.690	15.676	-0.088
1.7	16.670	16.654	-0.099
1.8	17.651	17.633	-0.101
1.9	18.632	18.612	-0.103
2	19.612	19.594	-0.090

Table A4. 2 Left Load Cell (Loade Cell 2)

Added mass (kg)	Added weight (N)	Re-measured weight (N)	error (%)
0	0	0	0
0.1	0.981	0.984	0.322
0.2	1.961	1.967	0.275
0.3	2.942	2.952	0.331
0.4	3.922	3.943	0.519
0.5	4.903	4.928	0.514
0.6	5.884	5.920	0.618
0.7	6.864	6.907	0.621
0.8	7.845	7.889	0.563
0.9	8.825	8.874	0.544
1	9.806	9.856	0.506
1.1	10.787	10.845	0.540
1.2	11.767	11.829	0.523
1.3	12.748	12.815	0.525
1.4	13.729	13.800	0.518
1.5	14.709	14.786	0.524
1.6	15.690	15.773	0.528
1.7	16.670	16.762	0.549
1.8	17.651	17.744	0.529
1.9	18.632	18.730	0.530
2	19.612	19.709	0.496

Table A4. 3 Right Load Cell (Load Cell 3)

Added mass (kg)	Added weight (N)	Re-measured weight (N)	error (%)
0	0	0	0
0.1	0.981	0.983	0.279
0.2	1.961	1.970	0.448
0.3	2.942	2.960	0.602
0.4	3.922	3.950	0.711
0.5	4.903	4.938	0.705
0.6	5.884	5.939	0.945
0.7	6.864	6.927	0.921
0.8	7.845	7.914	0.884

0.9	8.825	8.900	0.842
1	9.806	9.882	0.775
1.1	10.787	10.887	0.934
1.2	11.767	11.869	0.861
1.3	12.748	12.853	0.827
1.4	13.729	13.840	0.814
1.5	14.709	14.826	0.792
1.6	15.690	15.820	0.830
1.7	16.670	16.800	0.779
1.8	17.651	17.780	0.733
1.9	18.632	18.763	0.703
2	19.612	19.745	0.676

Appendix 5 Irregular wave Spectrum and wave amplitude distribution

This part will present the tank test irregular wave amplitude distribution first and then present the wave spectrum compared between the Wave Probe 1 calibrated results with the target calculated wave spectrum. In addition, the numerical wave elevation PDF and the wave spectrum comparisons between tank tests and numerical simulations will be presented.

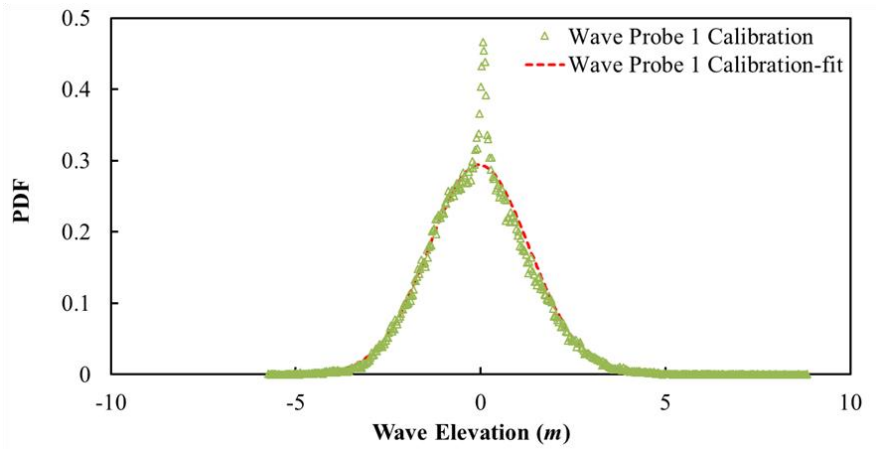

Figure A5. 1 Wave amplitude distribution, measured by Wave Probe 1 for Sea State 2 (full scale)

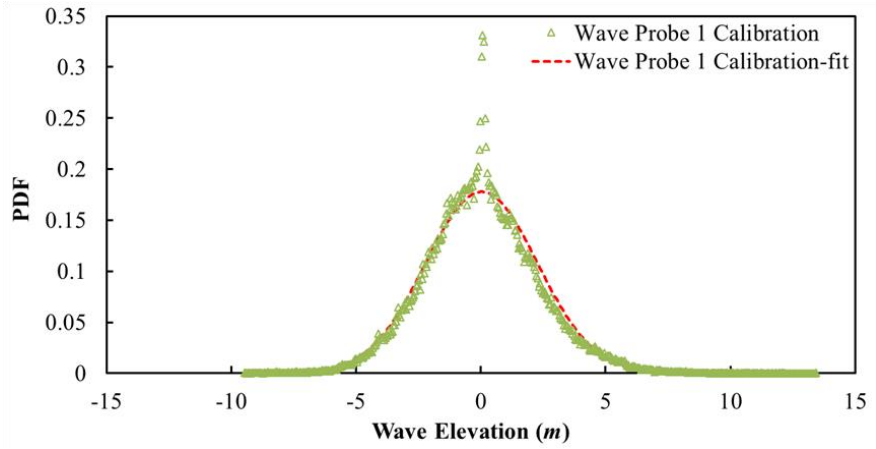

Figure A5. 2 Wave amplitude distribution, measured by Wave Probe 1 for Sea State 3 (full scale)

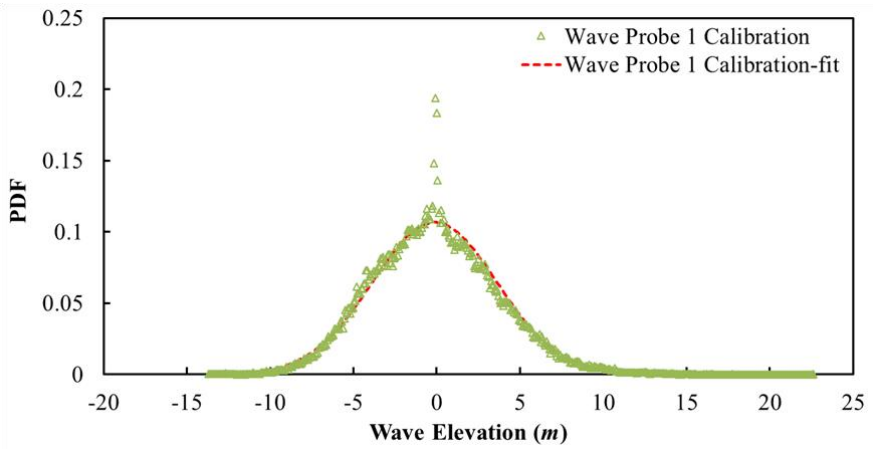

Figure A5. 3 Wave amplitude distribution, measured by Wave Probe 1 for Sea State 4 (full scale)

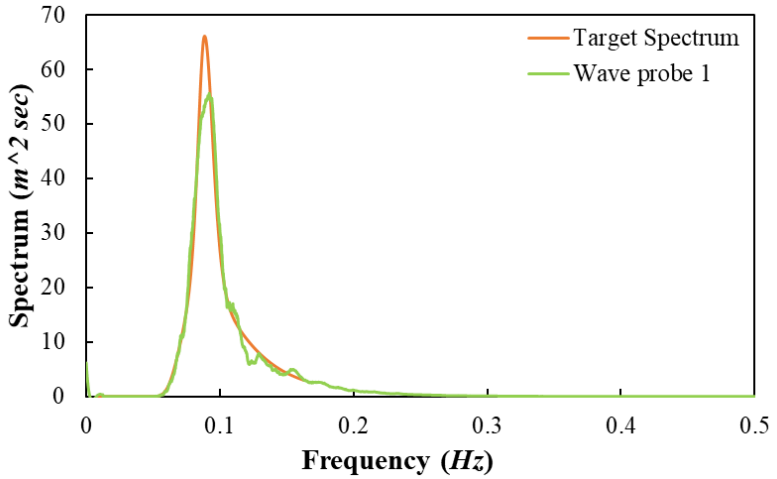

Figure A5. 4 Wave spectrum, measured by Wave Probe 1 compared with the target wave spectrum, for Sea State 2 (full scale)

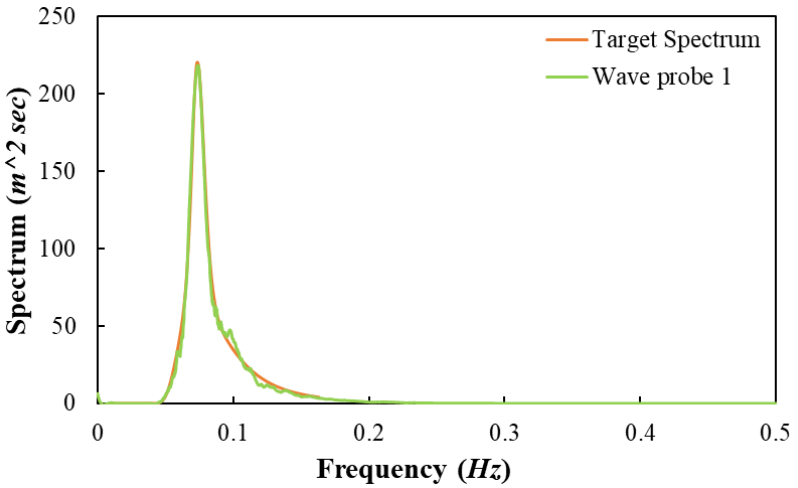

Figure A5. 5 Wave spectrum, measured by Wave Probe 1 compared with the target wave spectrum, for Sea State 3 (full scale)

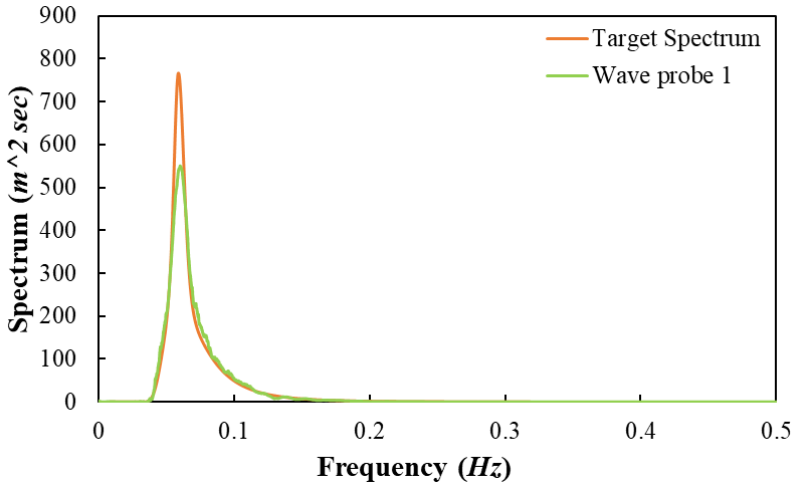

Figure A5. 6 Wave spectrum, measured by Wave Probe 1 compared with the target wave spectrum, for Sea State 4 (full scale)

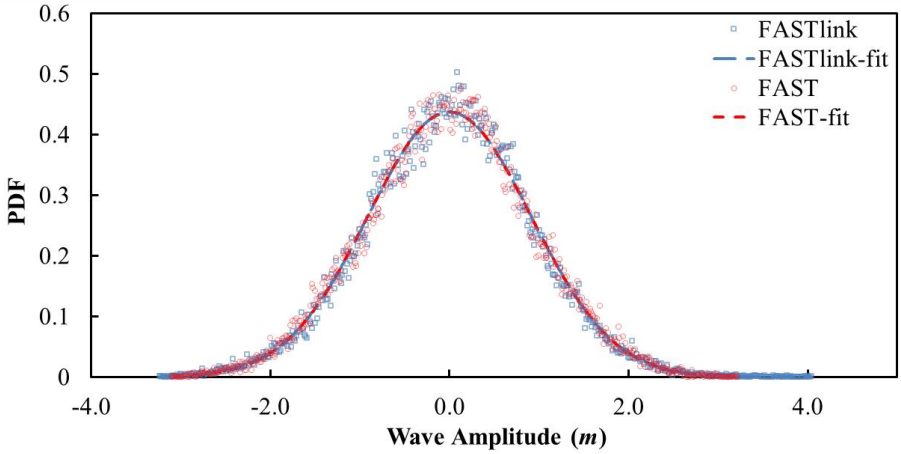

Figure A5. 7 Wave amplitude PDF for Sea State 1 (full scale)

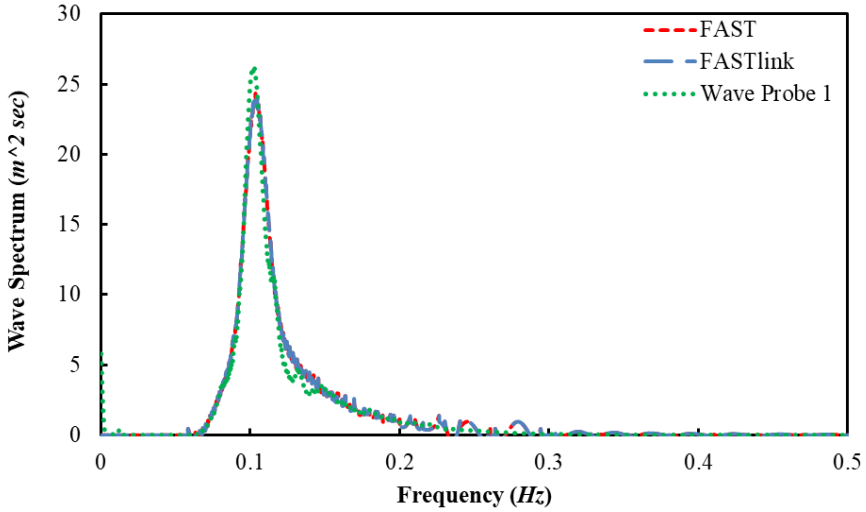

Figure A5. 8 Wave Spectrum of both numerical and experimental for Sea State 1 (full scale)

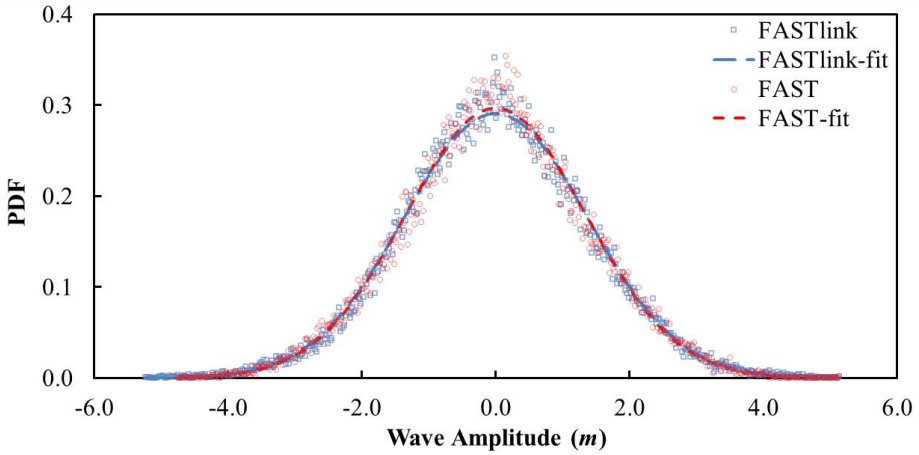

Figure A5. 9 Wave amplitude PDF for Sea State 2 (full scale)

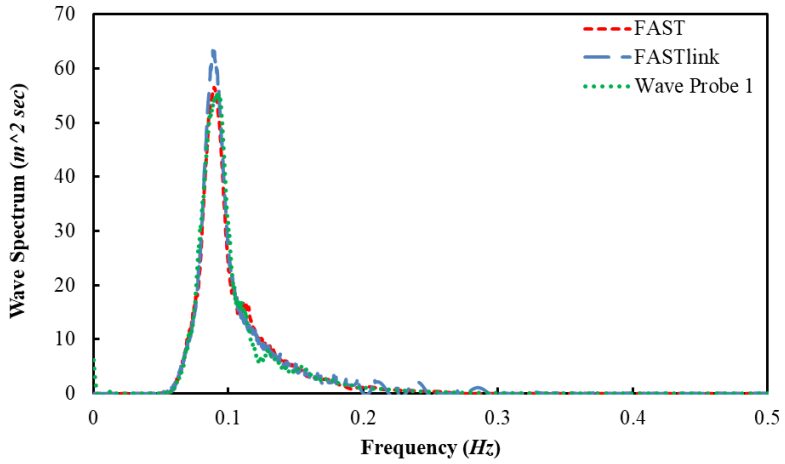

Figure A5. 10 Wave Spectrum of both numerical and experimental for Sea State 2 (full scale)

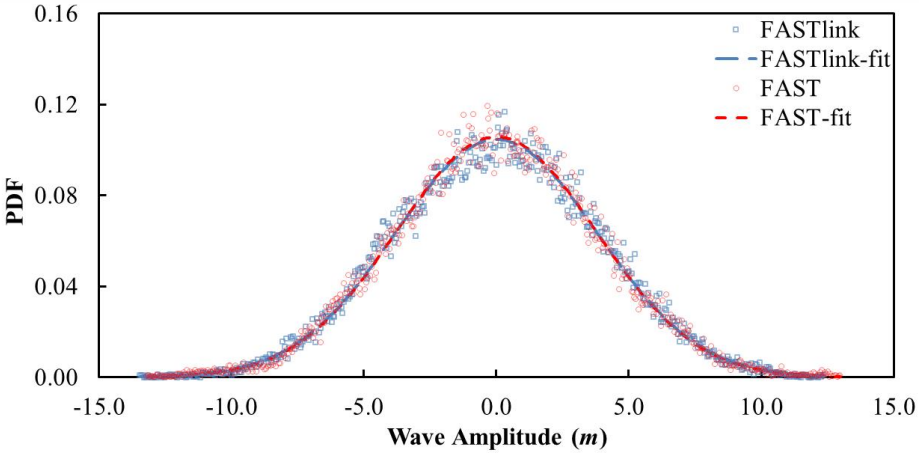

Figure A5. 11 Wave amplitude PDF for Sea State 4 (full scale)

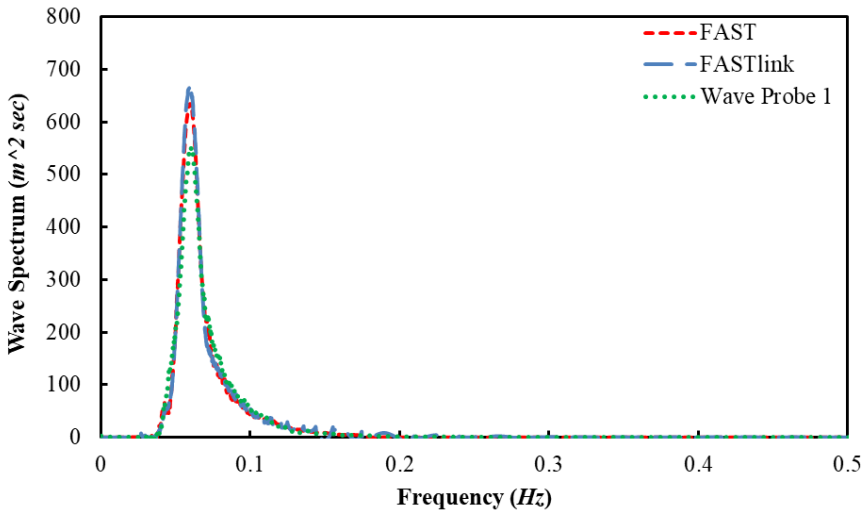

Figure A5. 12 Wave Spectrum of both numerical and experimental for Sea State 4 (full scale)

Appendix 6 Spar-Only Platform Motions in Sea States 1, 2 and 4

Sea State 1

Figure A6. 1 and Figure A6. 2 present the heave PDF and the motion spectrum from FAST, FASTlink and experiment measurement. It can be seen that for both the numerical simulations and experimental results, the heave motion amplitude is mainly around 0.0 m to 0.3 m. In both the numerical simulations and the experiment, there have two major peaks of the heave spectrum at the frequency about 0.032 Hz and 0.1 Hz. The higher peak is at 0.032 Hz which is due to the natural frequency of the spar platform. The smaller peak is at 0.1 Hz which should due to the peak wave frequency of Sea State 1, as shown in Figure A6. 2.

In Figure A6. 3, the experimental pitch has a very similar degree range with the numerical simulations – the amplitude is about 0.6°. FAST shows a better match curve with the experiment results than FASTlink. For pitch motion spectrum, there are still two peaks, as shown in Figure A6. 4, the first peak is about 0.033 Hz for FAST and FASTlink and 0.035 Hz for experiment, which match with its natural frequency as shown in the RAO results in Figure A6. 7. The other peak is approximately at 0.1 Hz, which is due to the same reason with the heave motion spectrum – the peak wave frequency of the Sea State 1.

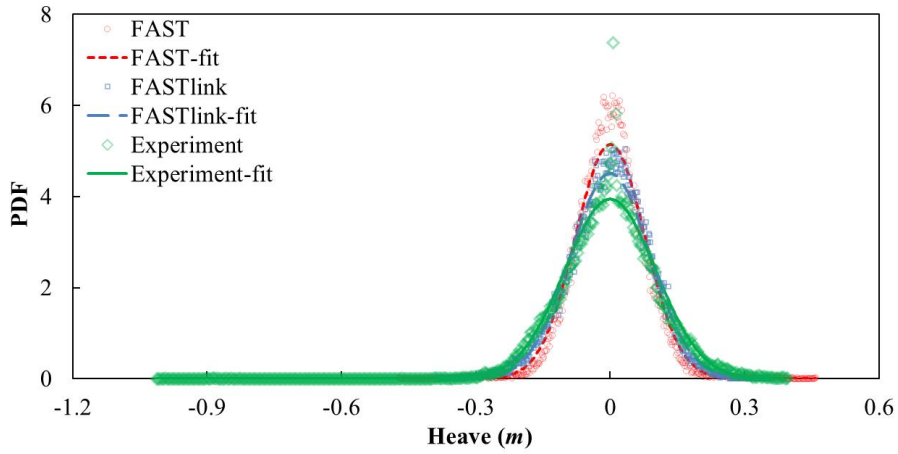

Figure A6. 1 Heave PDF for Sea State 1, spar-only (full scale)

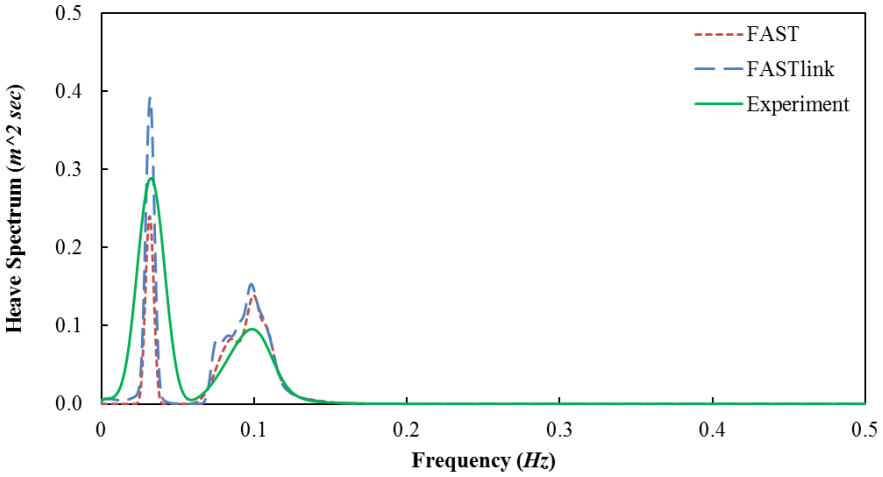

Figure A6. 2 Heave motion spectrum for Sea State 1, spar-only (full scale)

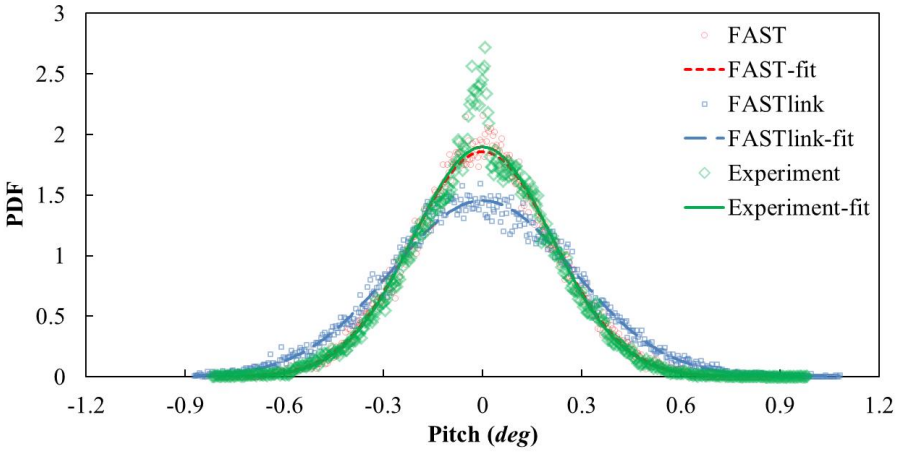

Figure A6. 3 Pitch PDF for Sea State 1, spar-only (full scale)

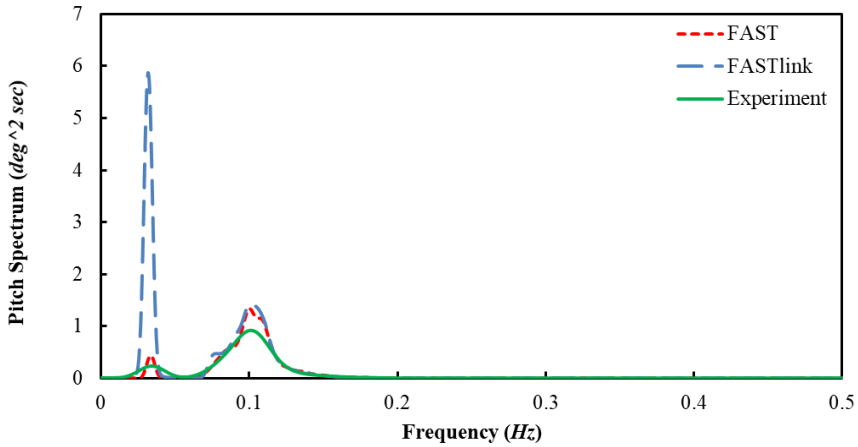

Figure A6. 4 Pitch motion spectrum for Sea State 1, spar-only (full scale)

Sea State 2

Similar with the Sea State 1, the heave amplitude in both numerical simulation and experiment have the amplitude up to about 0.5 m, and the pitch PDF matching perfectly between the FAST results and the experiment and the OrcaFlex shows a wider pitch motion range. Figure A6. 6 shows that the higher peak spectrum of heave motion from experiment is still happening at its natural frequency – 0.032 Hz, and the other peak is at the wave peak frequency – around 0.088 Hz. The FASTlink result shows such properties more obvious than FAST, as the higher peak spectrum in FAST is at the wave peak frequency instead of the pitch natural frequency. The numerical result (in FASTlink) shows higher spectrum than experiment. While for pitch motion spectrum, the major peak for FAST and experimental results happened at the peak wave frequency and only the FASTlink presented quite significant pitch motion spectrum at its natural frequency – 0.035 Hz, although FASTlink still shows a larger response at 0.880 Hz than experiment, as shown in Figure A6. 8.

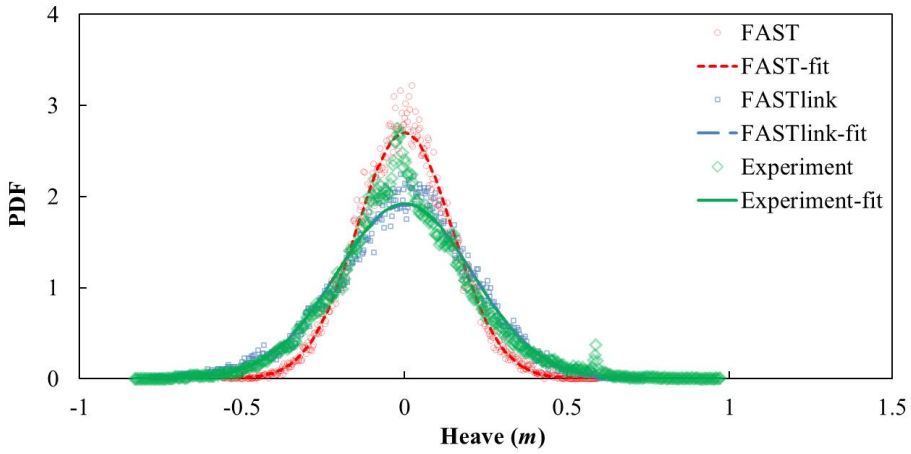

Figure A6. 5 Heave PDF for Sea State 2, spar-only (full scale)

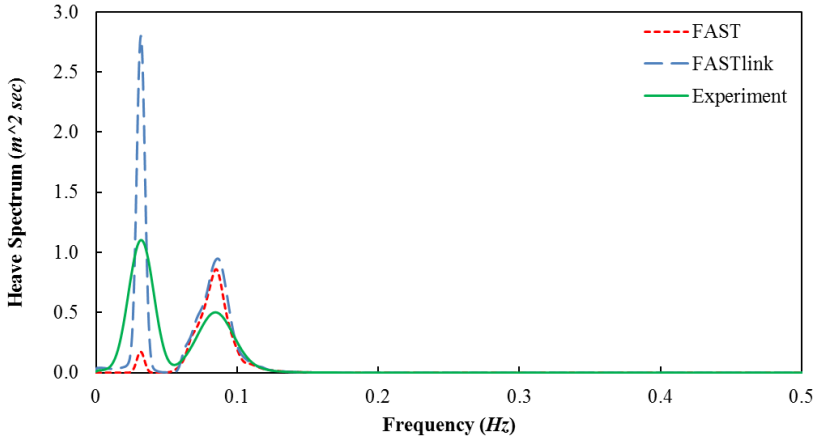

Figure A6. 6 Heave motion spectrum for Sea State 2, spar-only (full scale)

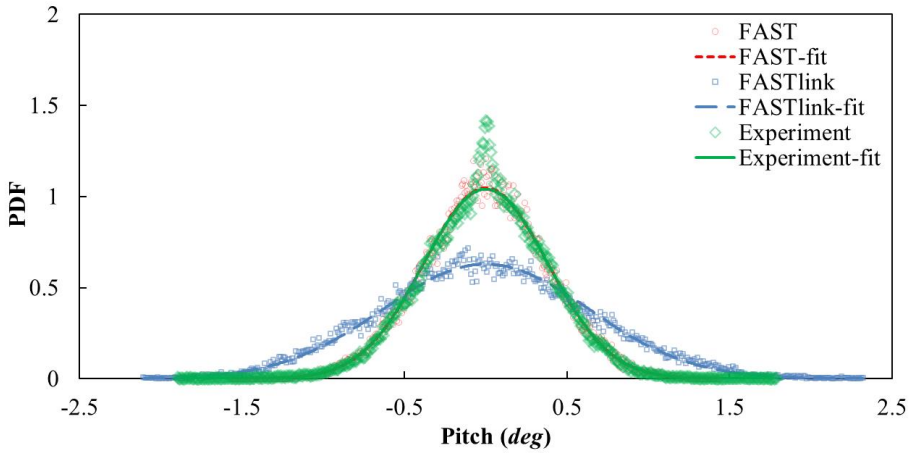

Figure A6. 7 Pitch PDF for Sea State 2, spar-only (full scale)

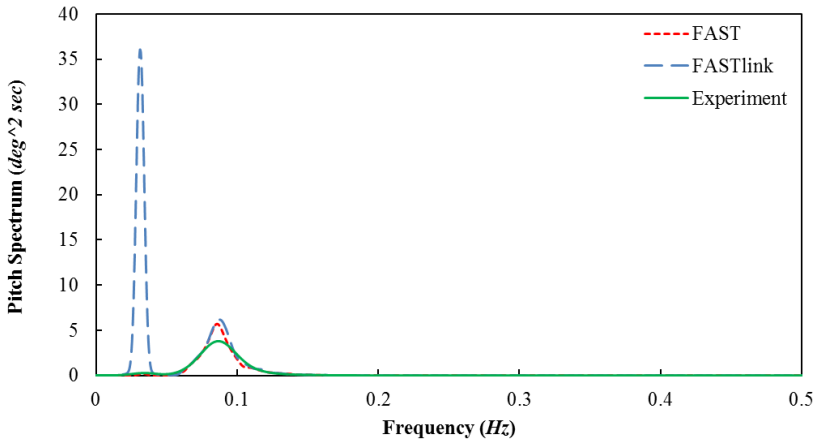

Figure A6. 8 Pitch motion spectrum for Sea State 2, spar-only (full scale)

Sea State 4

Due to the very significant waves, the simulations in both FAST and FASTlink cannot reach a convergence but it does not fail in the experiment. Thus, only the experiment results will be shown in this part to give a general idea about the floating systems behaviour under extreme sea state.

The motion of the heave PDF, in this extreme sea state, its amplitude can reach up to 2.4 m, and when compare with the previous three sea states, it can be seen that this range is keep increasing when the wave condition getting significant, which can also be seen in the pitch PDF figures.

In Figure A6. 10, it shows two quite large peaks - the major peak is at the heave natural frequency and the smaller one is at the wave peak frequency – around 0.06 Hz, which is similar with the previous three sea states. While for pitch motion, it seems that the major peak only happens at the peak wave frequency, as shown in Figure A6. 12.

When comparing with all the four sea states, it can be seen that the major peak pitch spectrum are all happening at the wave peak frequency and the peak at pitch natural frequency are getting smaller and smaller and disappears at the most extreme sea state.

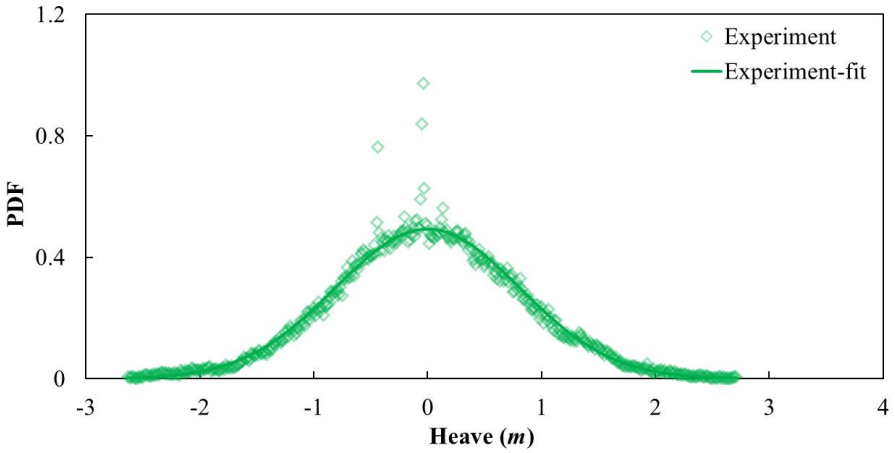

Figure A6. 9 Heave PDF for Sea State 4, spar-only (full scale)

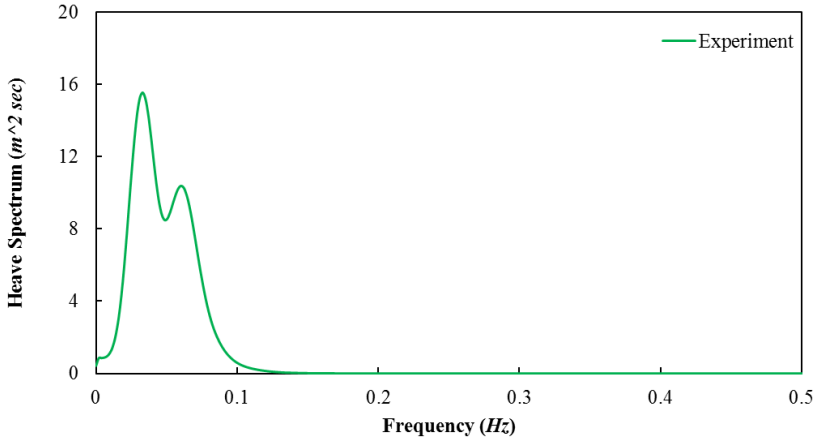

Figure A6. 10 Heave motion spectrum for Sea State 4, spar-only (full scale)

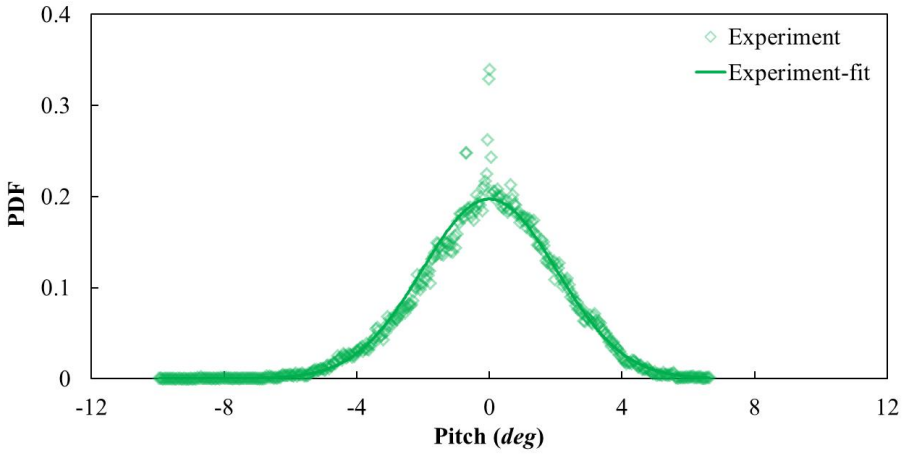

Figure A6. 11 Pitch PDF for Sea State 4, spar-only (full scale)

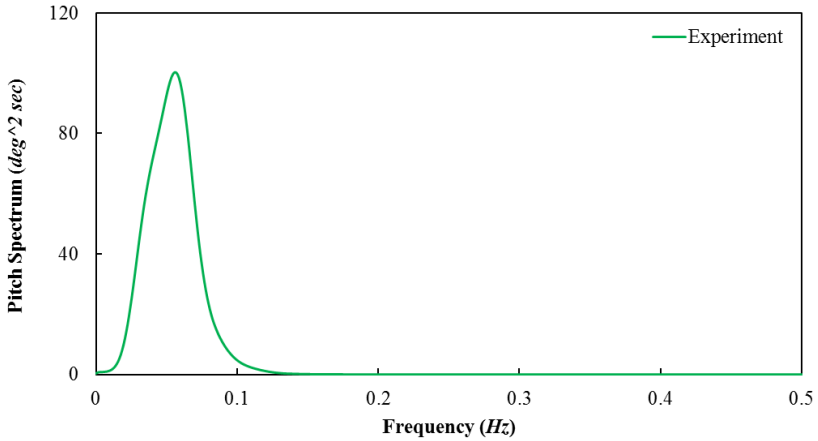

Figure A6. 12 Pitch motion spectrum for Sea State 4, spar-only (full scale)

Appendix 7 Spar Platform RAO with Cd

This part shows the platform RAO when the mooring drag is set to 1.2 in FASTlink. It is seen from the following figures that the platform peak RAO frequencies still at the platform each DOF natural frequencies, but the peak amplitude is getting smaller in FASTlink due to the add-in of the mooring drag.

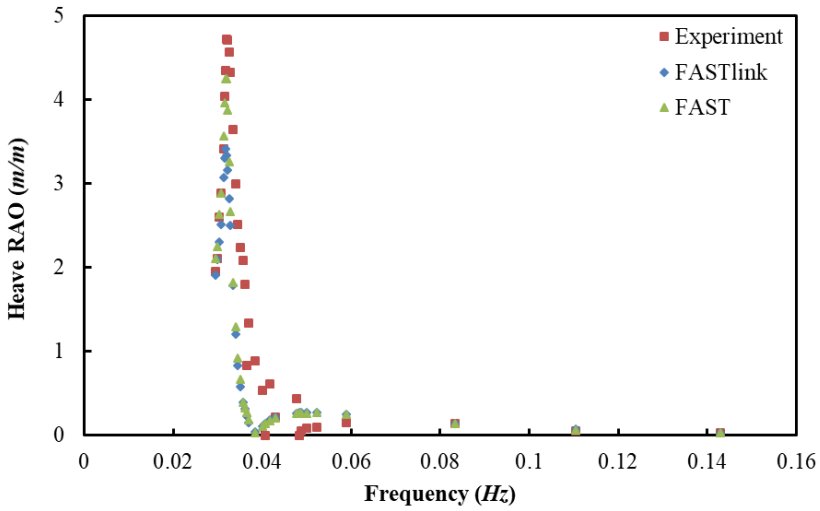

Figure A7. 1 Heave RAO, Cd=1.2 in FASTlink, spar with realistic mooring (full scale)

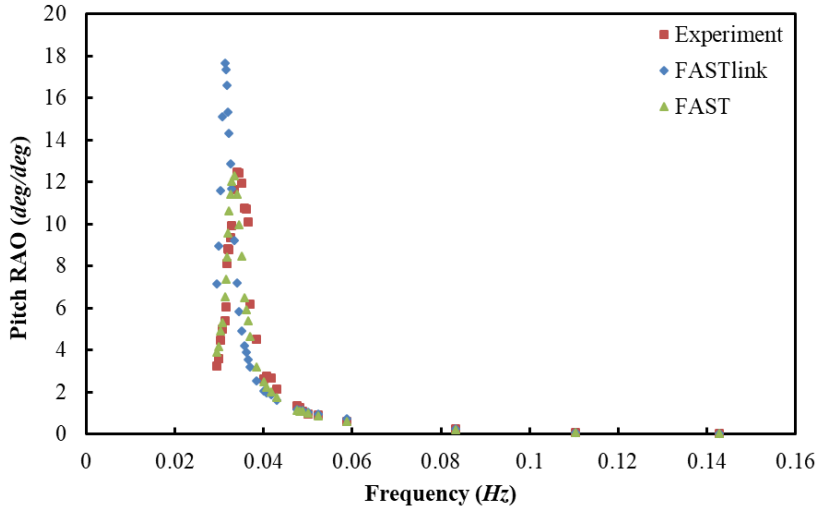

Figure A7. 2 Pitch RAO, Cd=1.2 in FASTlink, spar with realistic mooring (full scale)

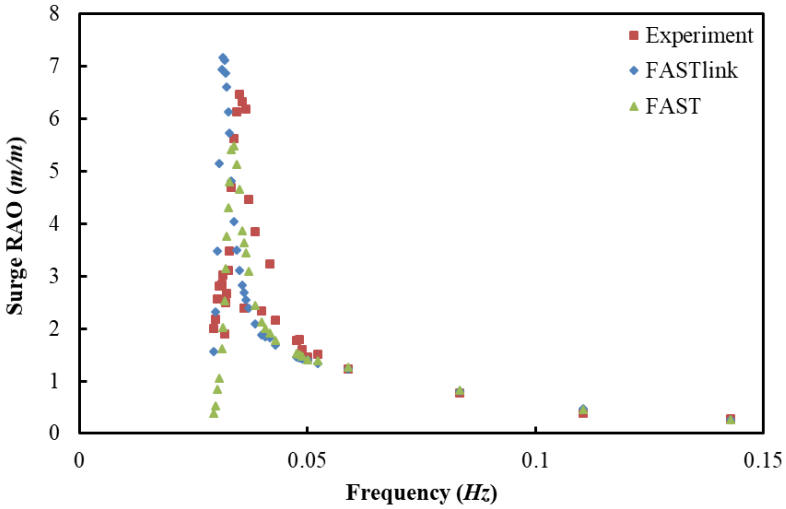

Figure A7. 3 Surge RAO, Cd=1.2 in FASTlink, spar with realistic mooring (full scale)

Appendix 8 The Snatching Phenomenon in Different Wave Frequencies

As discussed in Chapter 6, the surge motion has already been presented when the wave period is 23.25 s in full scale, so the heave/ pitch motion time history and one of the mooring line tension and one point of mooring motions on Mooring Line 1 will be presented in this part. It can be seen from the below figures, apart from the pitch motion, the strong snatching phenomenon can be observed from the experiment. In addition, these time histories from FASTlink simulation results will also be presented. From these figures, it is seen that the platform responses, mooring motion/ tension show no snatching curves when the wave frequency at its natural frequencies and strong snatching phenomenon for other wave frequencies.

For heave motion, in both FASTlink simulations and experiment results, the heave motion's natural period is at 31.20 s, and all the motion or tension curves show good regularity without the snatching.

When the wave period is 29.46 s, the pitch motion in the experiment reached its natural frequency. The regular sinusoidal motion curves appear again with no snatching. Similar with the experiment, the pitch reaches its natural period at 32.00 s in FASTlink and the snatching motion disappears.

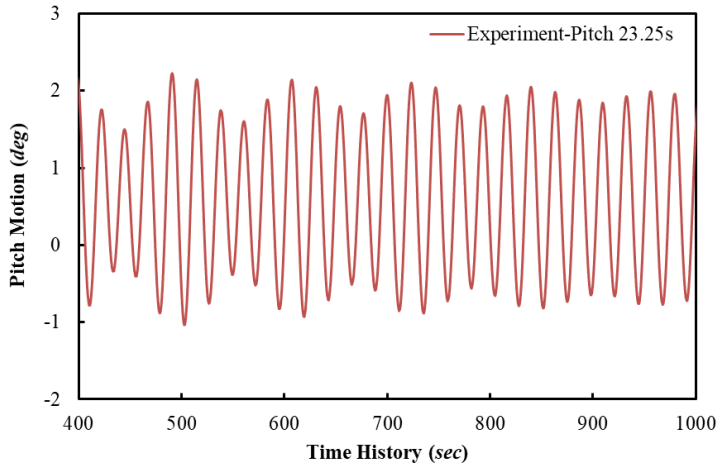

Figure A8. 1 Pitch motion time history in experiment at 23.25 s (full scale)

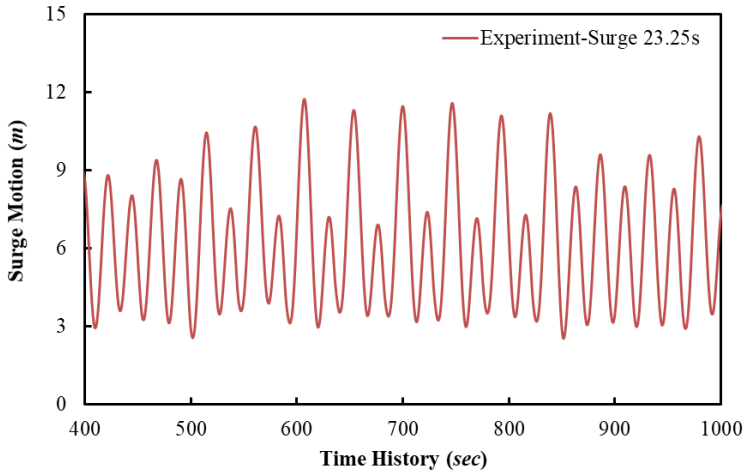

Figure A8. 2 Surge motion time history in experiment at 23.25 s (full scale)

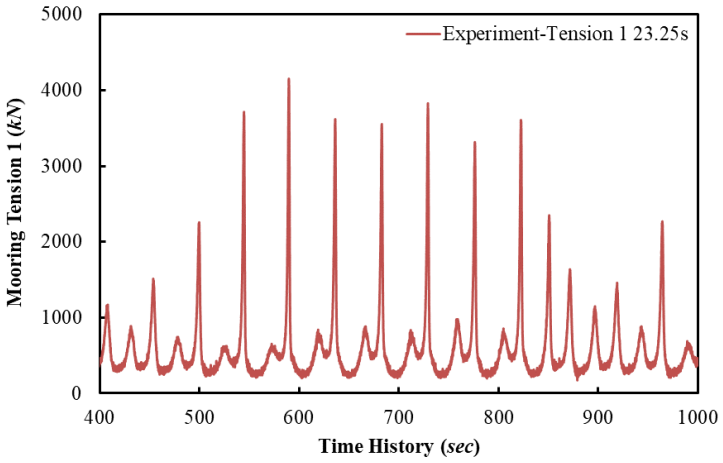

Figure A8. 3 Mooring Tension 1 in experiment at 23.25 s (full scale)

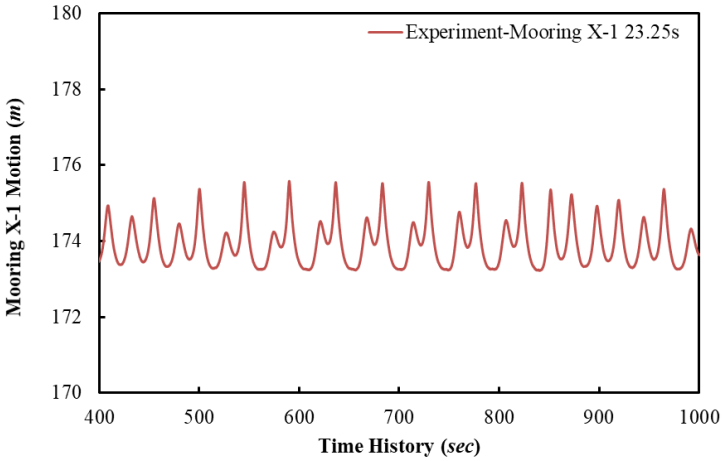

Figure A8. 4 Mooring motion Point X-1 in experiment at 23.25 s (full scale)

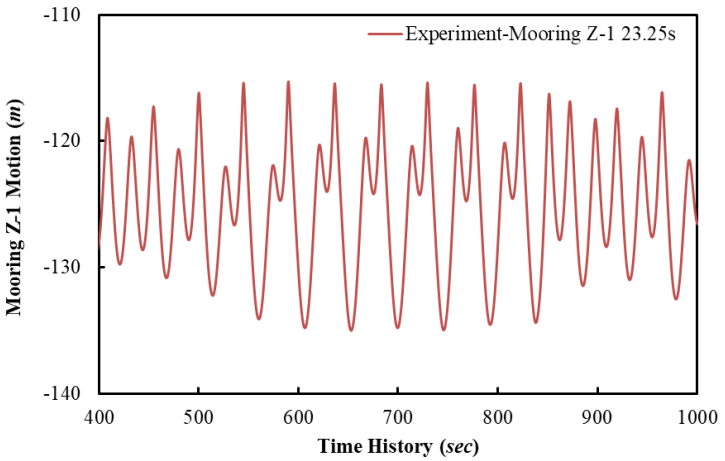

Figure A8. 5 Mooring motion Point Z-1 in experiment at 23.25 s (full scale)

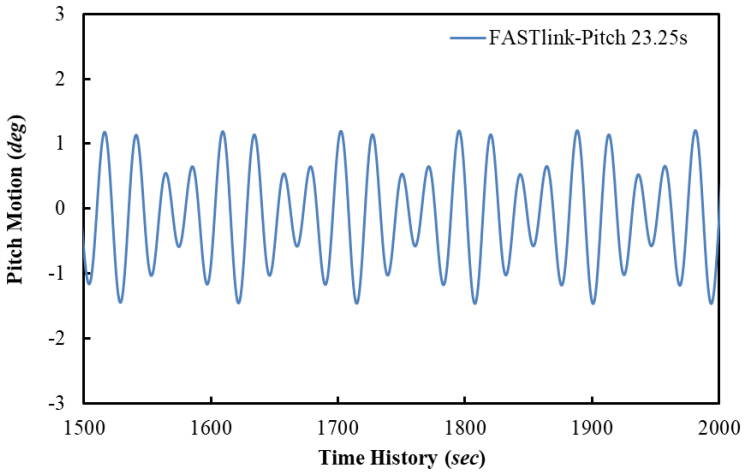

Figure A8. 6 Pitch motion time history in FASTlink at 23.25 s (full scale)

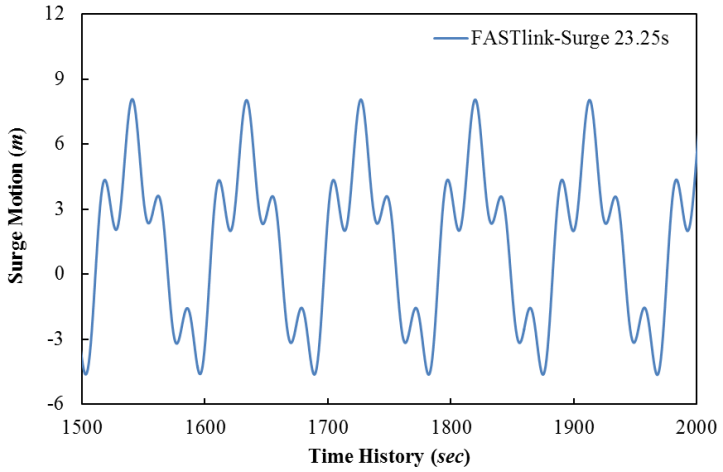

Figure A8. 7 Surge motion time history in FASTlink at 23.25 s (full scale)

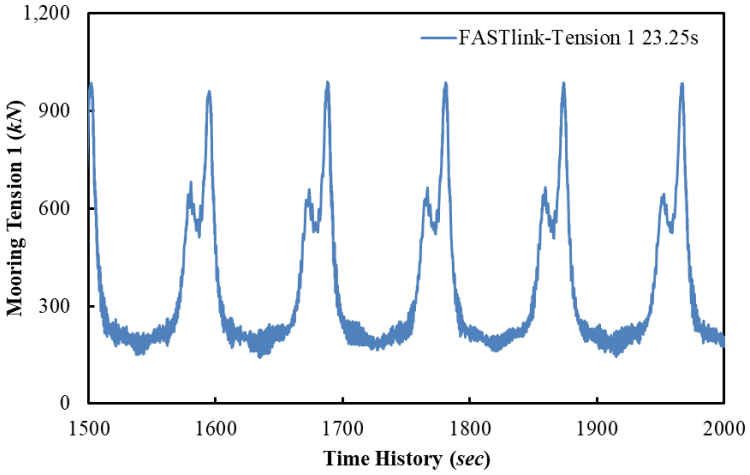

Figure A8. 8 Mooring Tension 1 time history in FASTlink at 23.25 s (full scale)

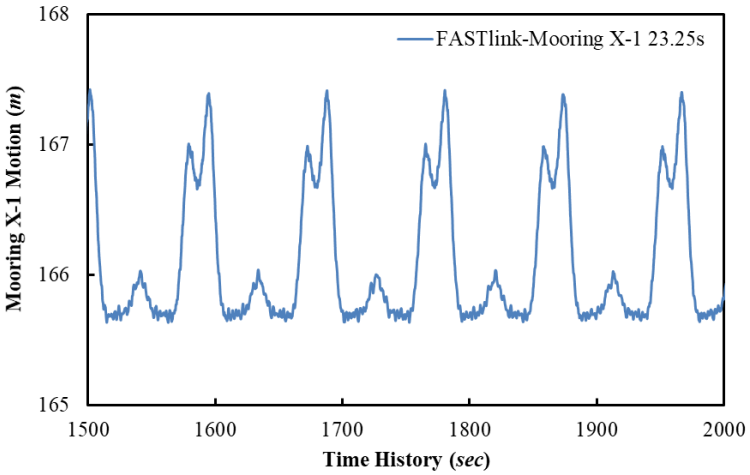

Figure A8. 9 Mooring motion X-1 time history in FASTlink at 23.25 s (full scale)

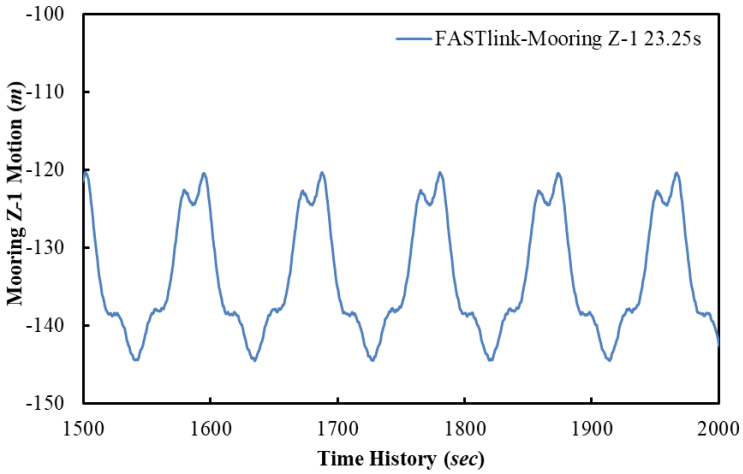

Figure A8. 10 Mooring motion Z-1 time history in FASTlink at 23.25 s (full scale)

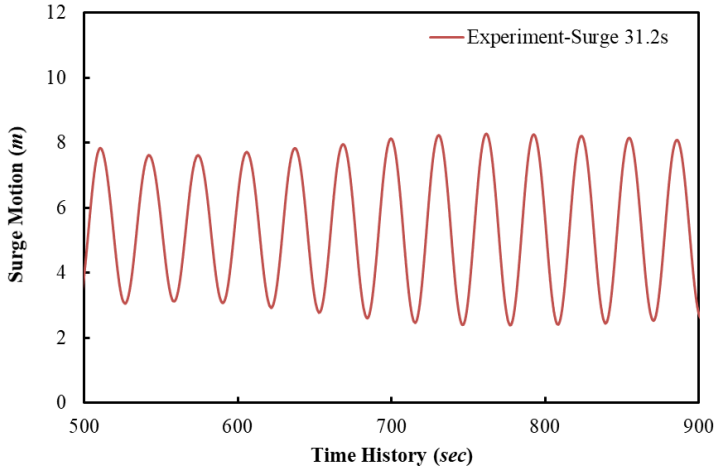

Figure A8. 11 Surge motion time history in experiment at heave natural period (full scale)

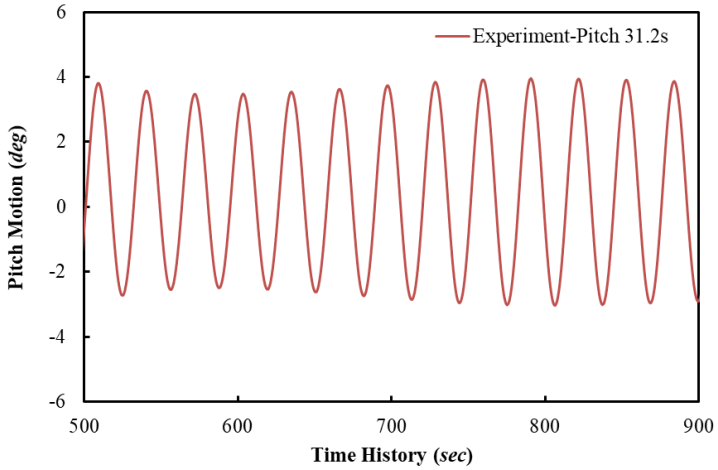

Figure A8. 12 Pitch motion time history in experiment at heave natural period (full scale)

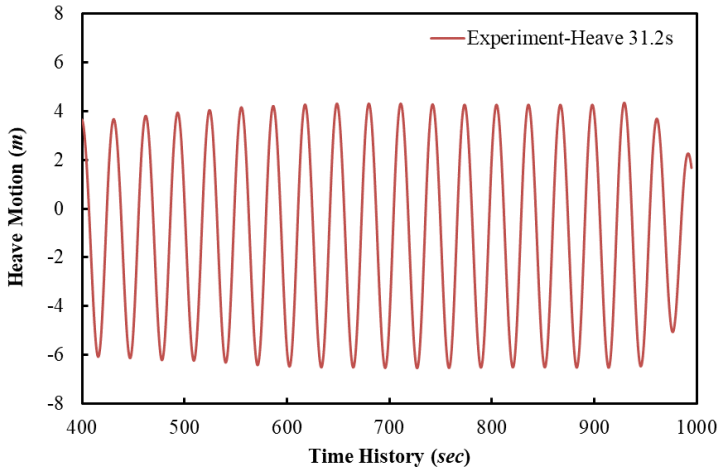

Figure A8. 13 Heave motion time history in experiment at heave natural period (full scale)

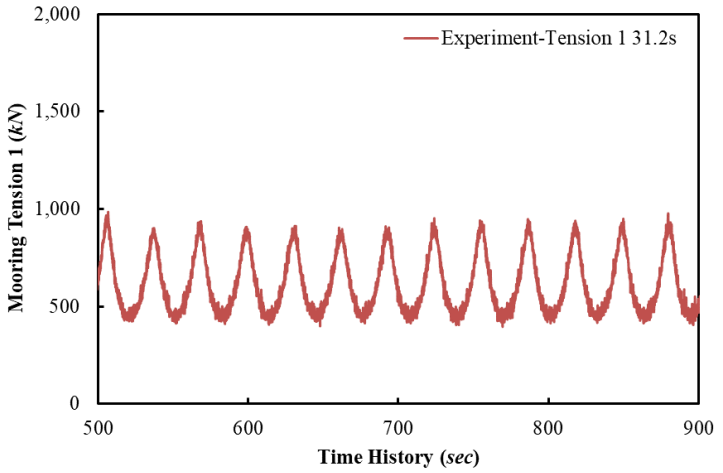

Figure A8. 14 Mooring Tension 1 time history in experiment at heave natural period (full scale)

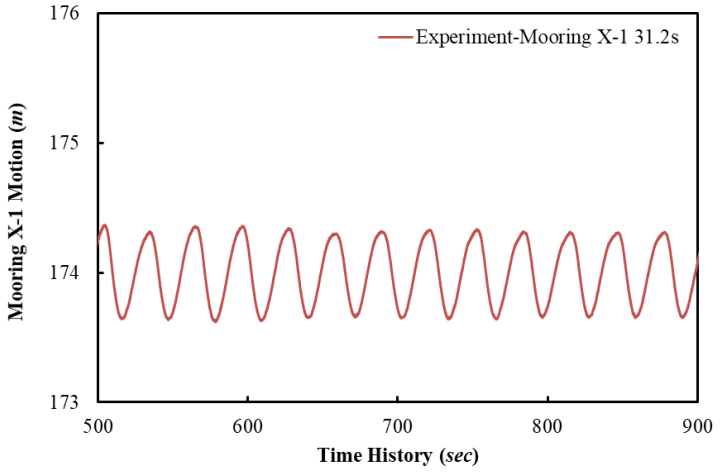

Figure A8. 15 Mooring motion X-1 time history in experiment at heave natural period (full scale)

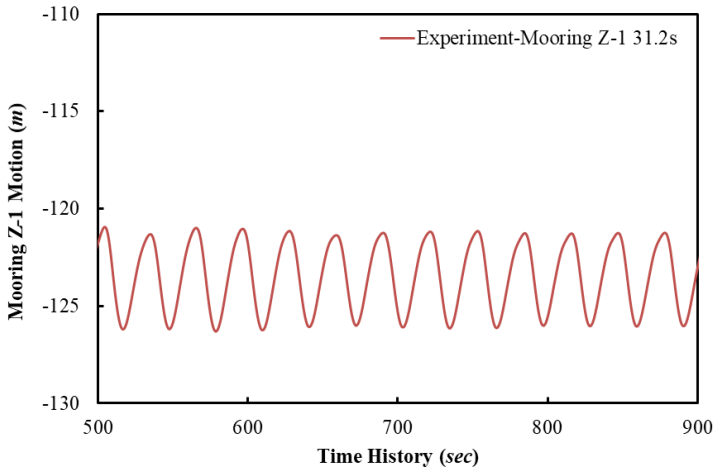

Figure A8. 16 Mooring motion Z-1 time history in experiment at heave natural period (full scale)

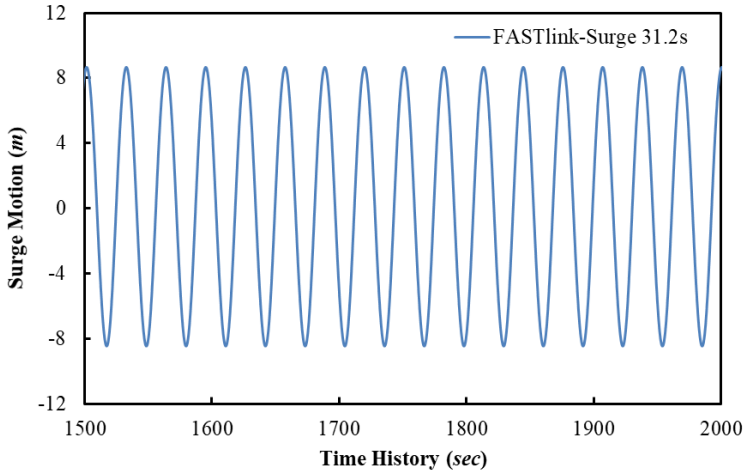

Figure A8. 17 Surge motion time history in FASTlink at heave natural period (full scale)

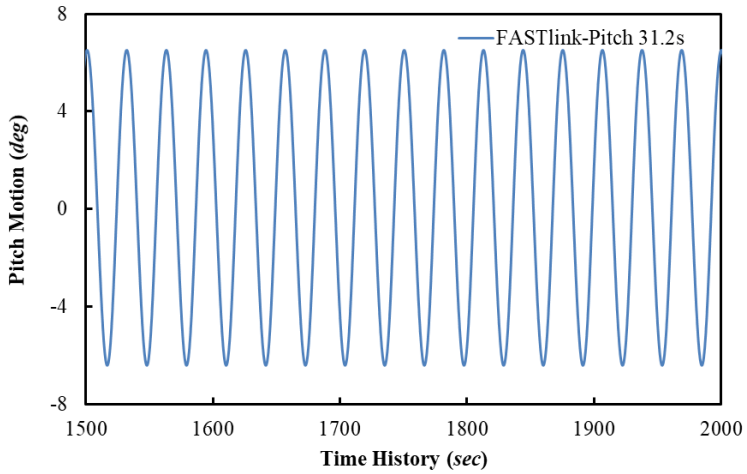

Figure A8. 18 Pitch motion time history in FASTlink at heave natural period (full scale)

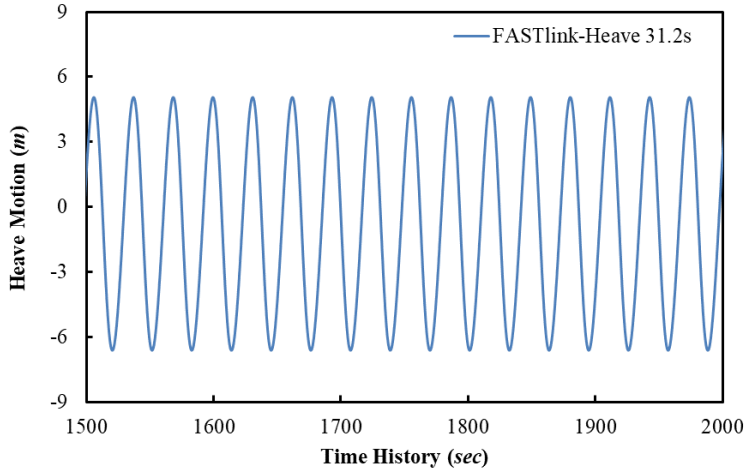

Figure A8. 19 Heave motion time history in FASTlink at heave natural period (full scale)

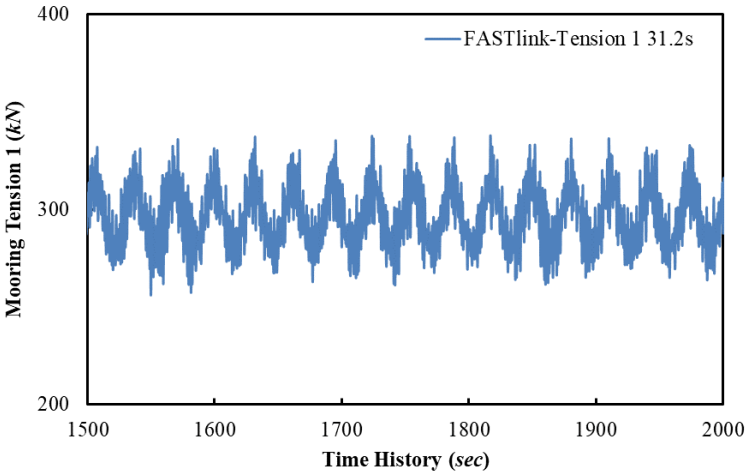

Figure A8. 20 Mooring Tension 1 time history in FASTlink at heave natural period (full scale)

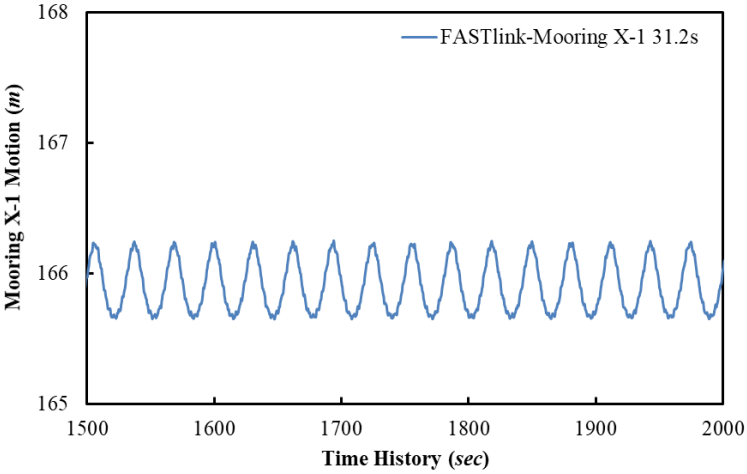

Figure A8. 21 Mooring motion X-1 time history in FASTlink at heave natural period (full scale)

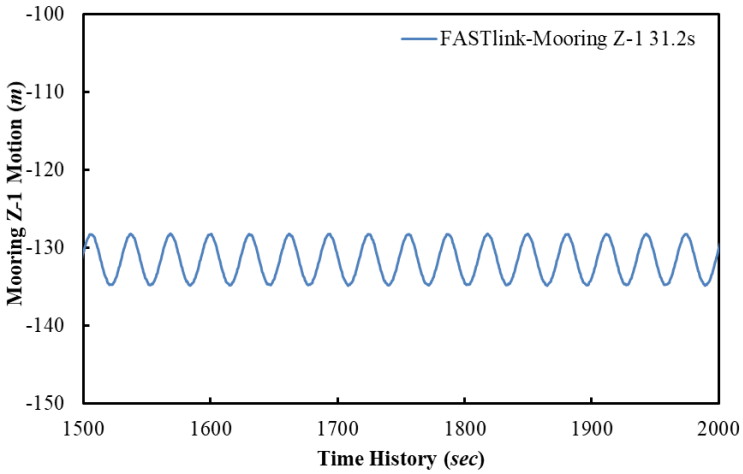

Figure A8. 22 Mooring motion Z-1 time history in FASTlink at heave natural period (full scale)

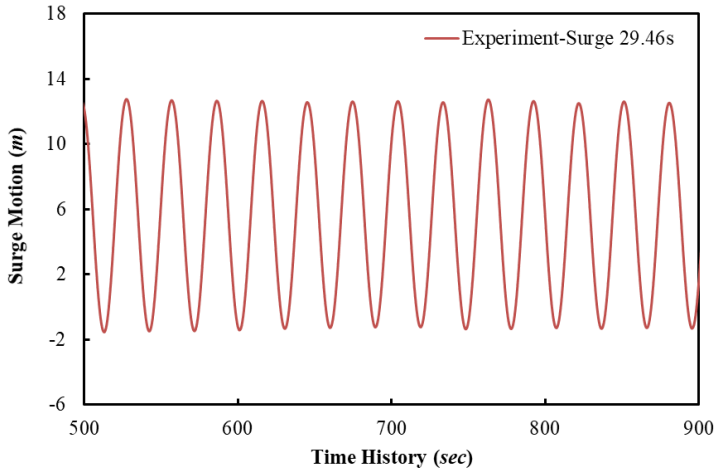

Figure A8. 23 Surge motion time history in experiment at pitch natural period (full scale)

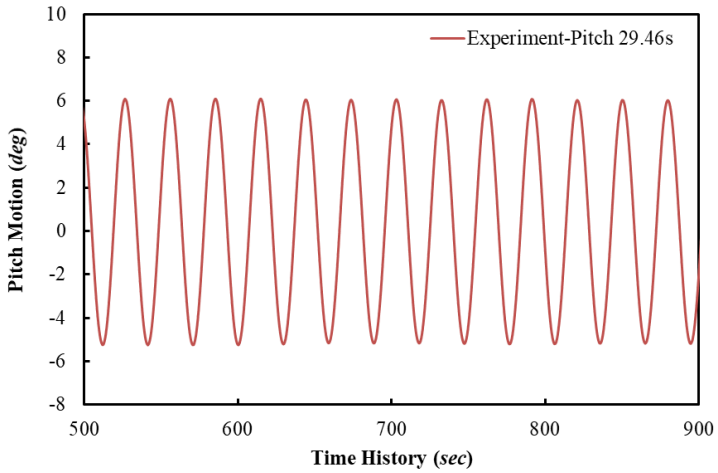

Figure A8. 24 Pitch motion time history in experiment at pitch natural period (full scale)

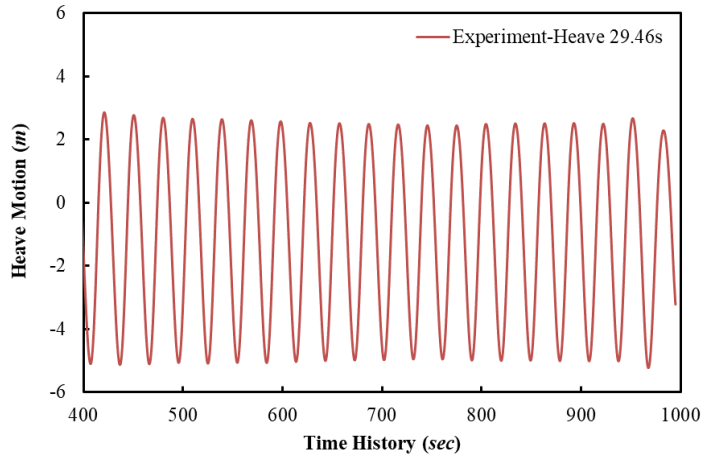

Figure A8. 25 Heave motion time history in experiment at pitch natural period (full scale)

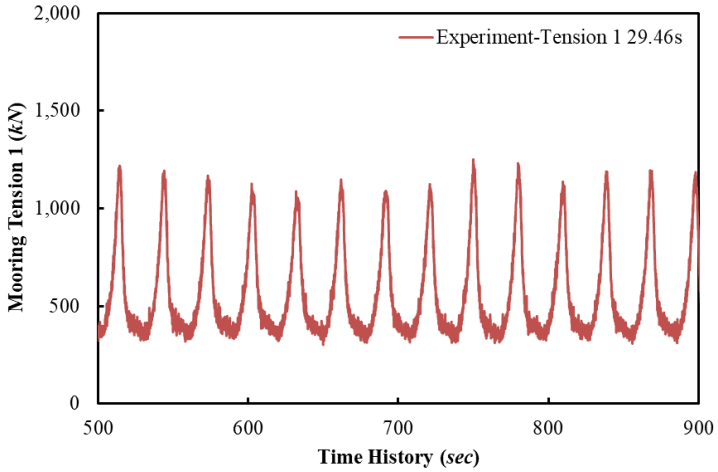

Figure A8. 26 Mooring Tension 1 time history in experiment at pitch natural period (full scale)

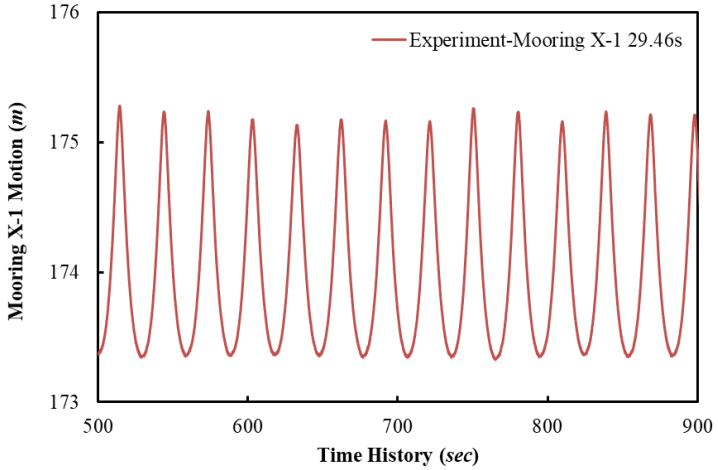

Figure A8. 27 Mooring motion X-1 time history in experiment at pitch natural period (full scale)

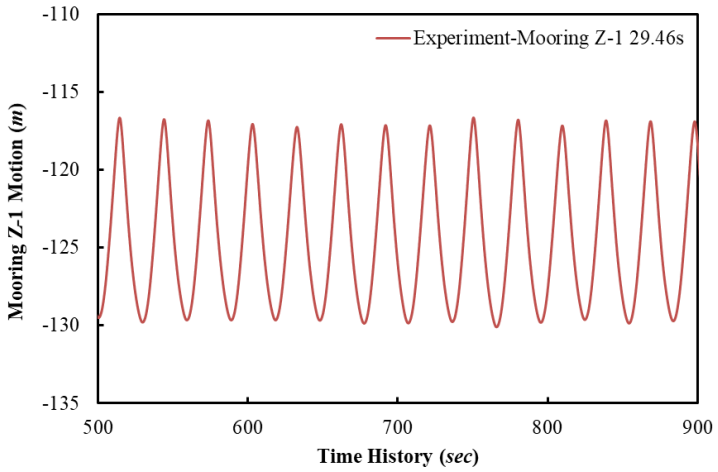

Figure A8. 28 Mooring motion Z-1 time history in experiment at pitch natural period (full scale)

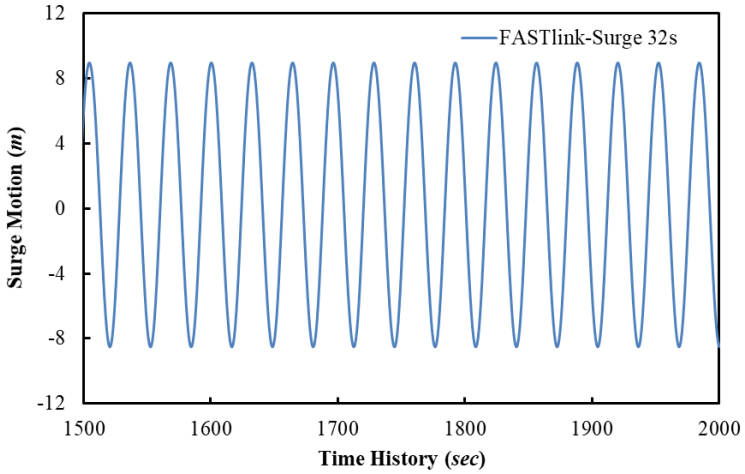

Figure A8. 29 Surge motion time history in FASTlink at pitch natural period (full scale)

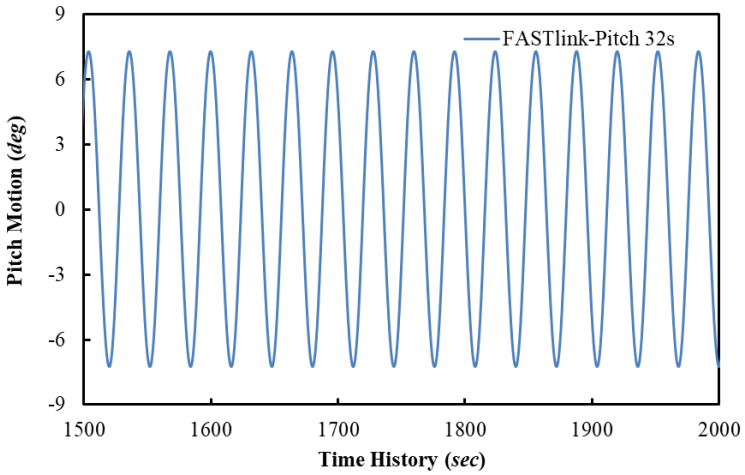

Figure A8. 30 Pitch motion time history in FASTlink at pitch natural period (full scale)

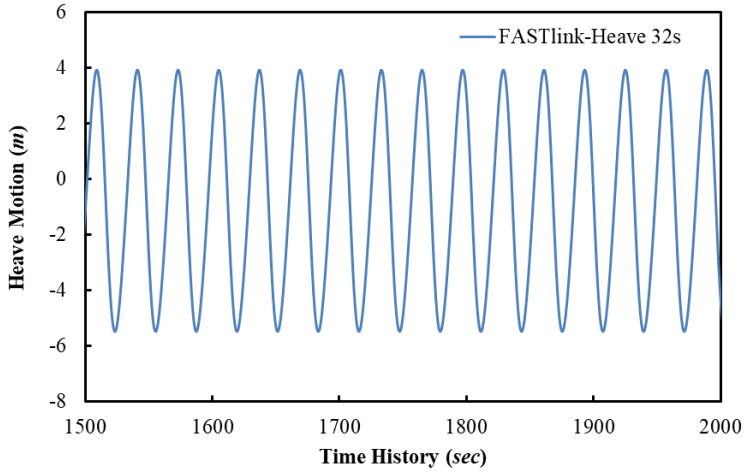

Figure A8. 31 Heave motion time history in FASTlink at pitch natural period (full scale)

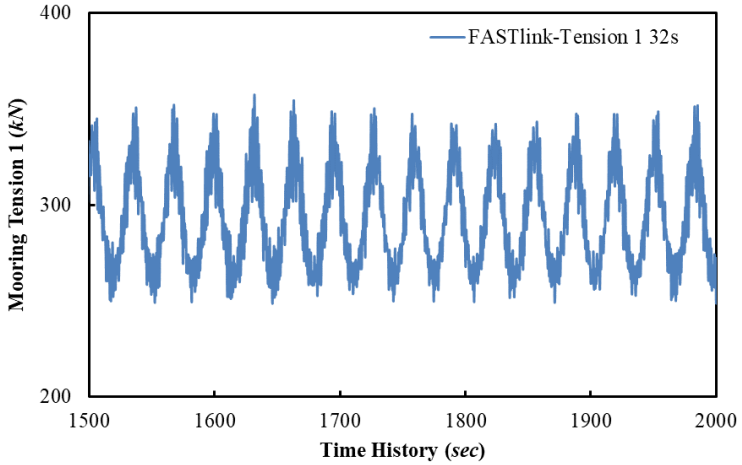

Figure A8. 32 Mooring Tension 1 time history in FASTlink at pitch natural period (full scale)

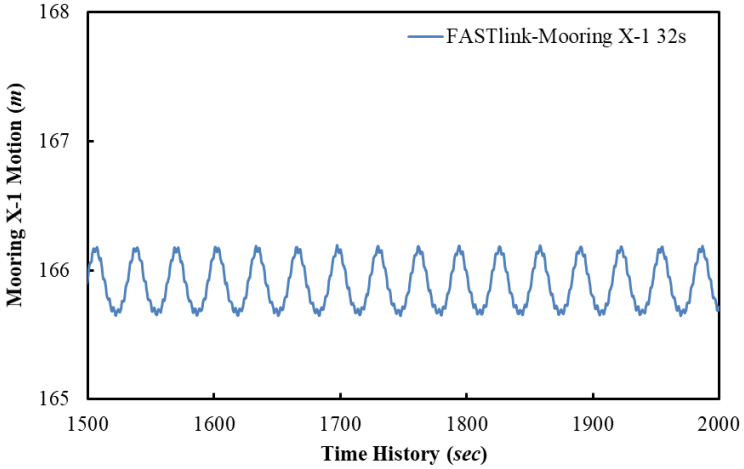

Figure A8. 33 Mooring motion X-1 time history in FASTlink at pitch natural period (full scale)

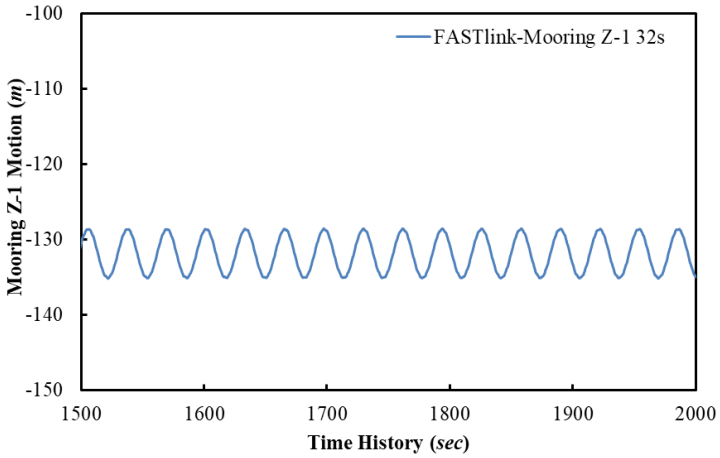

Figure A8. 34 Mooring motion Z-1 time history in FASTlink at pitch natural period (full scale)

Appendix 9 Linearity Tests for Spar with Mooring

Table A9. 1 and Table A9. 2 present the wave data for the linearity tests. Since the experimental and numerical results have different peak RAO frequencies for pitch motion, thus, the pitch linearity tests in FASTlink and FAST will be calculated with different wave frequencies with the experiment. For pitch linearity tests:

- In FAST, the wave frequency is 0.033 Hz and its wave length is 1016.319 m.
- In FASTlink, the wave frequency is 0.032 Hz and the wave length is 1089.501 m.

Figure A9. 1 and Figure A9. 2 present the linearity tests results for heave, pitch, which show perfect linear curves from experiment and FAST. In FASTlink, the pitch RAO decreases linearly with the increasing of wave heights, while in heave it increases with the wave heights increasing. As shown clearly in Figure A9. 3, same with the spar-only tests, the heave motion in FASTlink is growing quicker than in FAST with the increasing of wave heights.

Table A9. 1 Heave Linearity Test Wave Data for spar with mooring lines

Tank Test Scale			Full Scale (FAST & FASTlink)	
Wave Frequency (*Hz*)	Input Wave Amplitude of Wave Maker (*m*)	Measured Wave Amplitude (*m*)	Wave Frequency (*Hz*)	Wave Amplitude (*m*)
0.276	0.004	0.004	0.032	0.296
0.276	0.006	0.005	0.032	0.444
0.276	0.008	0.007	0.032	0.592
0.276	0.010	0.009	0.032	0.740
0.276	0.012	0.011	0.032	0.888
0.276	0.014	0.013	0.032	1.036

0.276	0.016	0.015	0.032	1.184
0.276	0.017	0.006	0.032	1.260
0.276	0.018	0.017	0.032	1.332

Table A9. 2 Pitch and Surge Linearity Test Wave Data for spar with mooring lines

Tank Test Scale				Full Scale
Wave Frequency (*Hz*)	Input Wave Amplitude of Wave Maker (*m*)	Measured Wave Amplitude (*m*)	Wave Length (*m*)	Wave Amplitude (*m*)
0.297	0.004	0.004	13.138	0.296
0.297	0.006	0.006	13.138	0.444
0.297	0.008	0.008	13.138	0.592
0.297	0.010	0.010	13.138	0.740
0.297	0.012	0.012	13.138	0.888
0.297	0.014	0.014	13.138	1.036
0.297	0.016	0.016	13.138	1.184
0.297	0.017	0.017	13.138	1.260
0.297	0.018	0.018	13.138	1.332

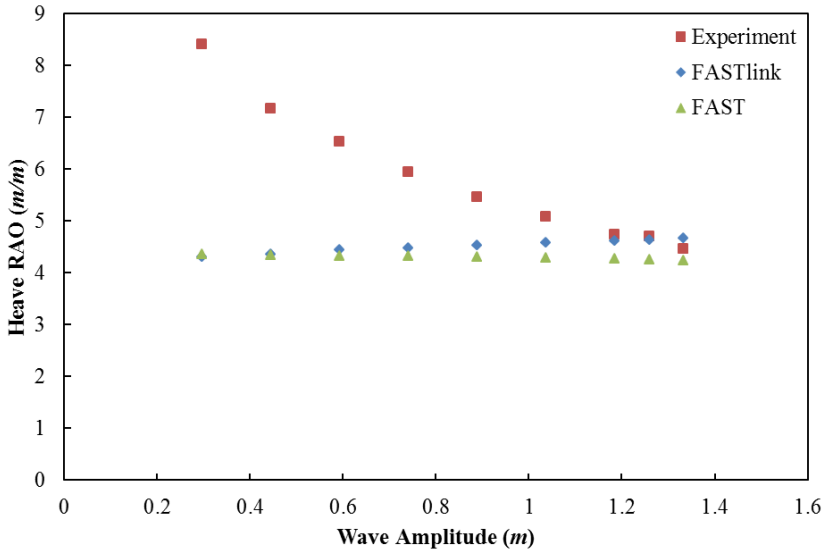

Figure A9. 1 Heave linearity check for spar with realistic mooring lines, at the platform heave motion natural frequency (full scale)

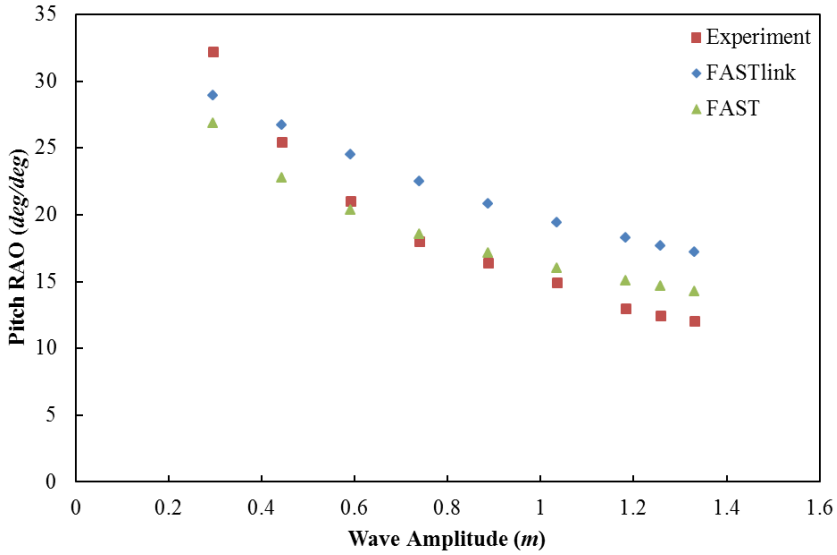

Figure A9. 2 Pitch linearity check, spar with realistic mooring lines, at the platform heave motion natural frequency (full scale)

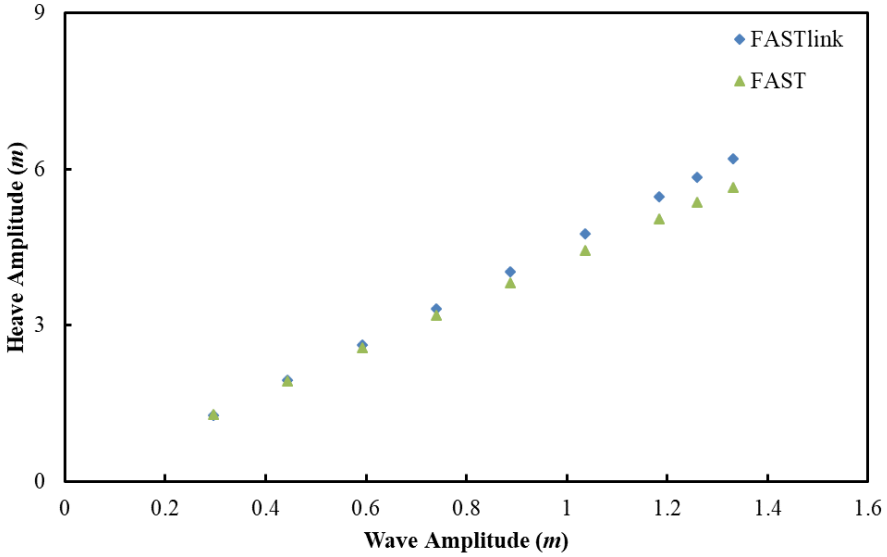

Figure A9. 3 Heave linearity check, spar realistic with mooring lines, FASTlink and FAST, at the platform heave motion natural frequency (full scale)

Appendix 10 Mooring Motion RMS in Regular Waves

This part shows the motion RMS of Point 2, 3 and 5 on Mooring Line 1.

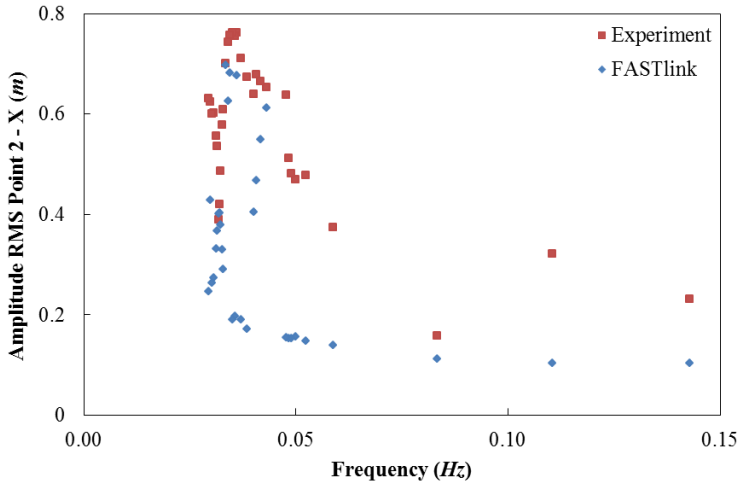

Figure A10. 1 Amplitude RMS for Point 2 along X-axis (full scale)

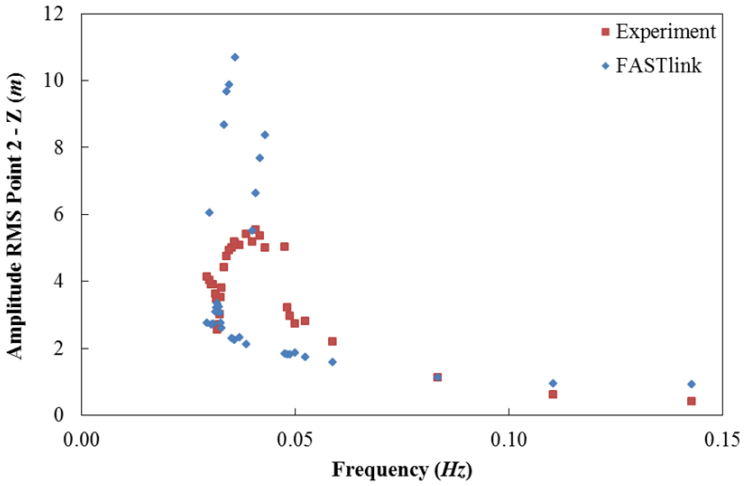

Figure A10. 2 Amplitude RMS for Point 2 along Z-axis (full scale)

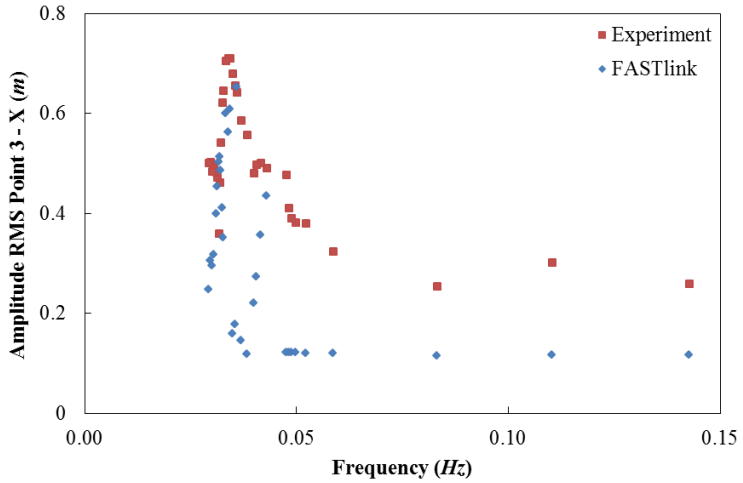

Figure A10. 3 Amplitude RMS for Point 3 along X-axis (full scale)

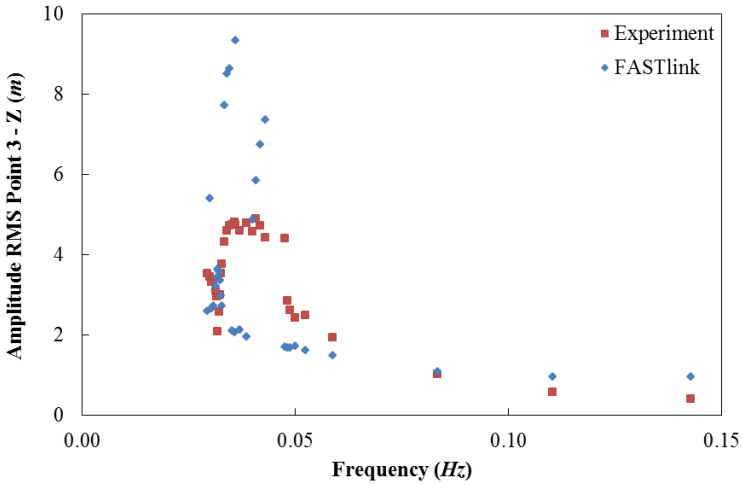

Figure A10. 4 Amplitude RMS for Point 3 along Z-axis (full scale)

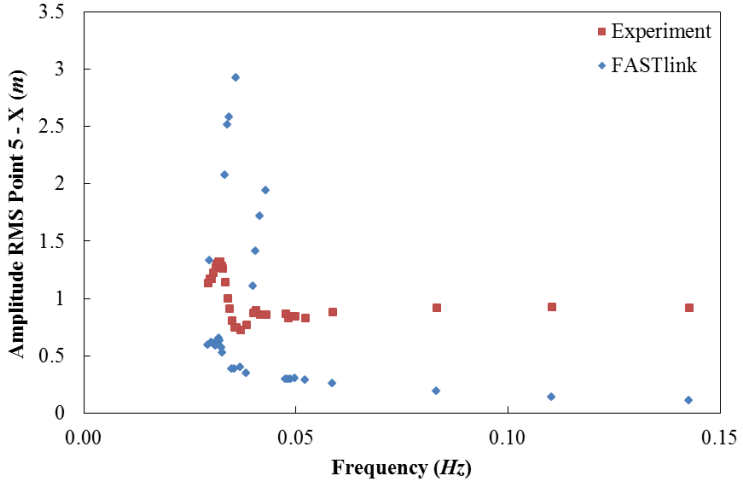

Figure A10. 5 Amplitude RMS for Point 5 along X-axis (full scale)

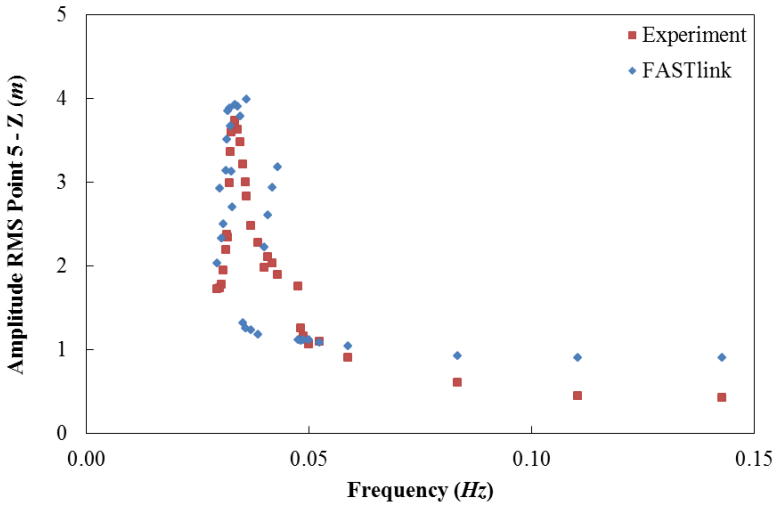

Figure A10. 6 Amplitude RMS for Point 5 along Z-axis (full scale)

Appendix 11 Platform (spar with moorings) Motion Responses and Mooring Tensions in Sea States

As been discussed in Chapter 6, for the spar with real mooring lines, the tank tests result in the Sea State 1, 3 and 4 will be shown here, and the numerical simulation results under Sea State 1 and 3 will be presented. Since the detailed information have already been discussed in Chapter 6, thus only the figures for the platform responses and three mooring tensions, their spectrum and the PDF, along with the comparison with the numerical simulation results will be presented in this part and with some discussions about the Sea State 3. The mooring motion spectrums in the irregular waves will be shown in the Appendix 12.

Sea State 1

For the platform surge, heave and pitch motions, they can all show two peak spectrums and the major one is at the peak wave frequency - 0.103 Hz, and the other one is at their only natural frequencies (the detailed can be find in Chapter 6.3).

For the mooring tension, as shown in Figure A11. 9, Figure A11. 12 and Figure A11. 15, the FASTlink can calculate the tension properly when under small sea state. The experiment shows higher tension values than in the numerical model, as shown in the PDF figures, which is match with the pre-tensions, as shown in Table 6. 1. For Mooring Tension 1, it shows a major peak at the peak wave frequency, and a smaller peak at 0.023 Hz, which is same with the peak motion spectrum of the Mooring Line 1 along X-axis, as discussed in Chapter 6.5. The quite small frequency – 0.002 Hz has

been discovered in Mooring Tension 2 and 3, which have also been discovered in the Sea State 2, and it could be due to the snatching effect.

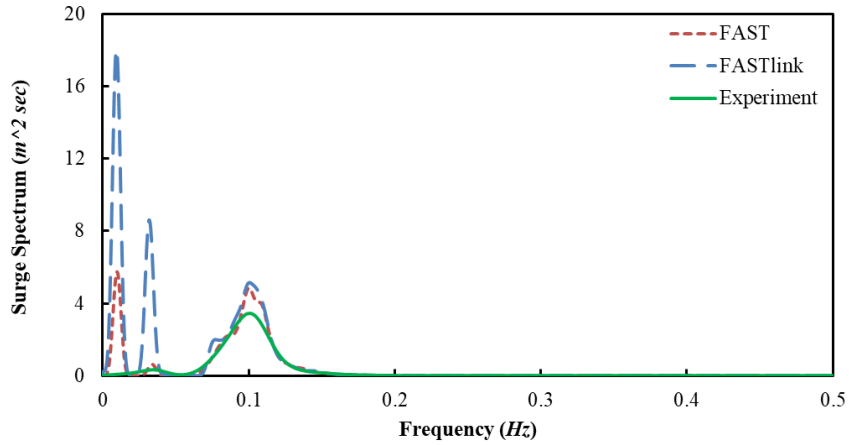

Figure A11. 1 Surge motion spectrum in spar with realistic mooring lines, Sea State 1 (full scale)

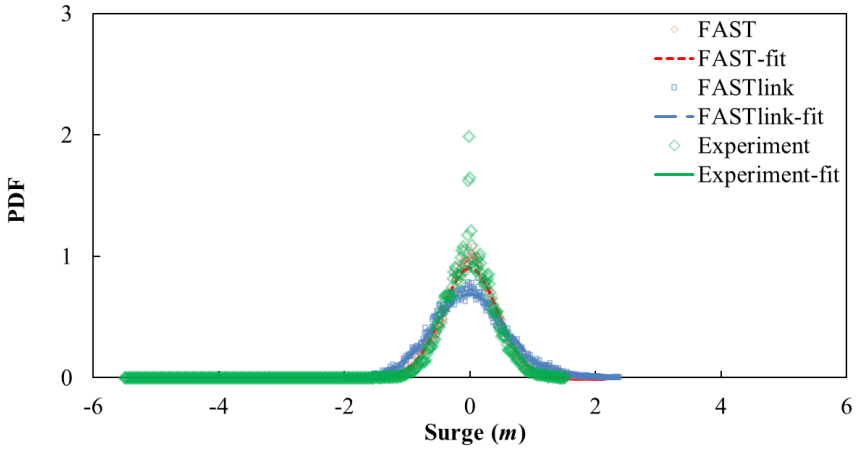

Figure A11. 2 Surge motion PDF in spar with realistic mooring lines, Sea State 1 (full scale)

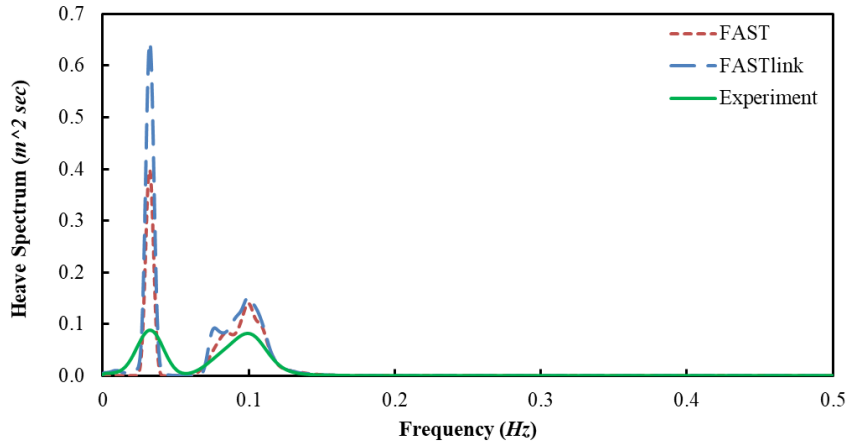

Figure A11. 3 Heave motion spectrum in spar with realistic mooring lines, Sea State 1 (full scale)

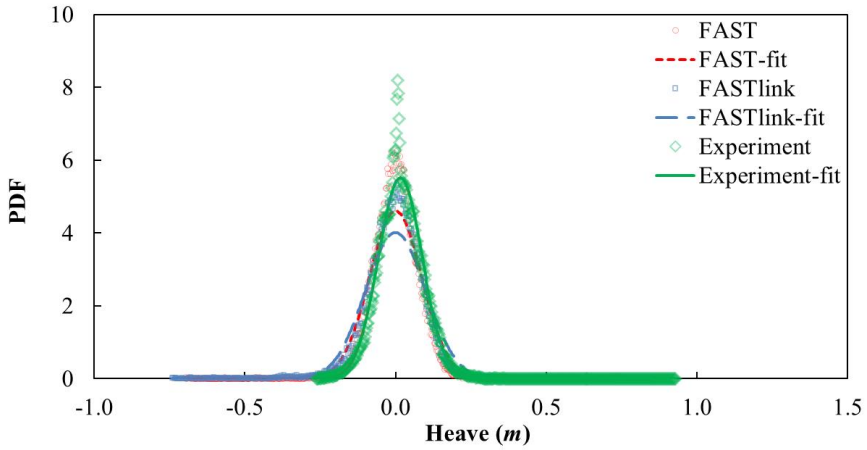

Figure A11. 4 Heave motion PDF in spar with realistic mooring lines, Sea State 1 (full scale)

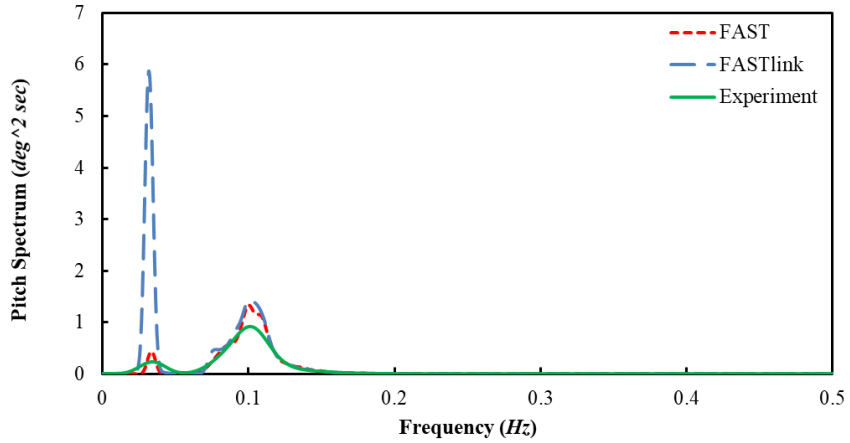

Figure A11. 5 Pitch motion spectrum in spar with realistic mooring lines, Sea State 1 (full scale)

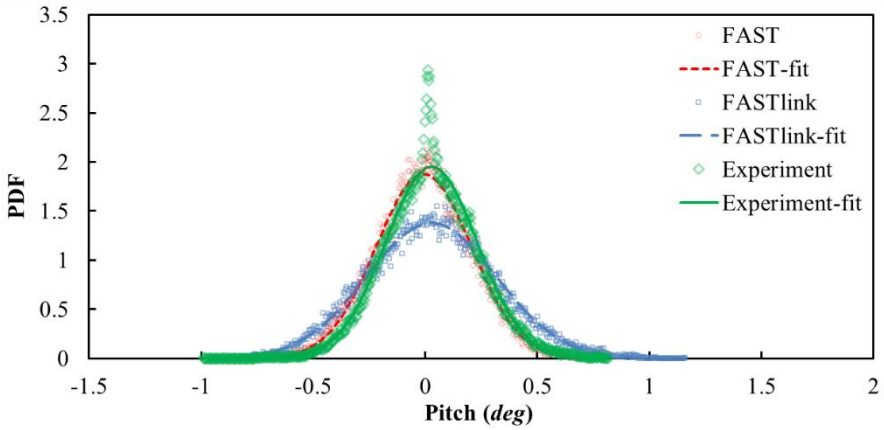

Figure A11. 6 Pitch motion PDF in spar with realistic mooring lines, Sea State 1 (full scale)

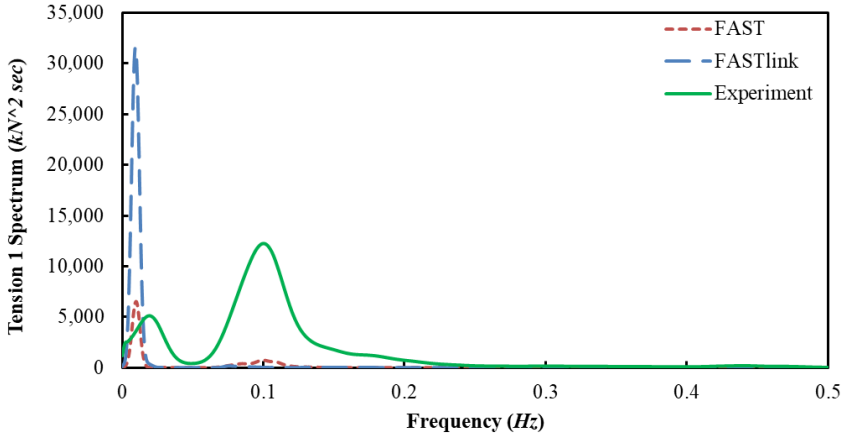

Figure A11. 7 Mooring Tension 1 spectrum in spar with realistic mooring lines, Sea State 1 (full scale)

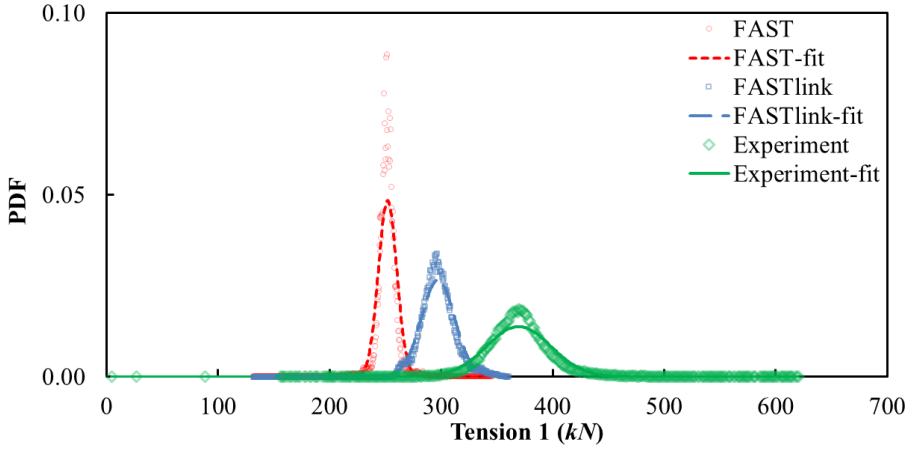

Figure A11. 8 Mooring Tension 1 PDF in spar with realistic mooring lines, Sea State 1 (full scale)

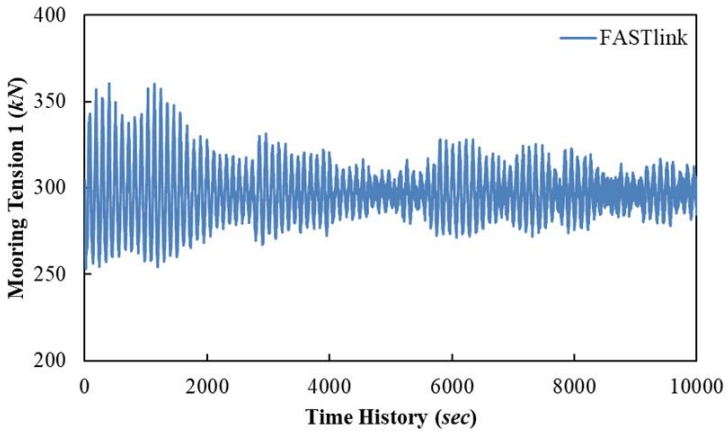

Figure A11. 9 Mooring Tension 1 time history, Sea State 1 (full scale)

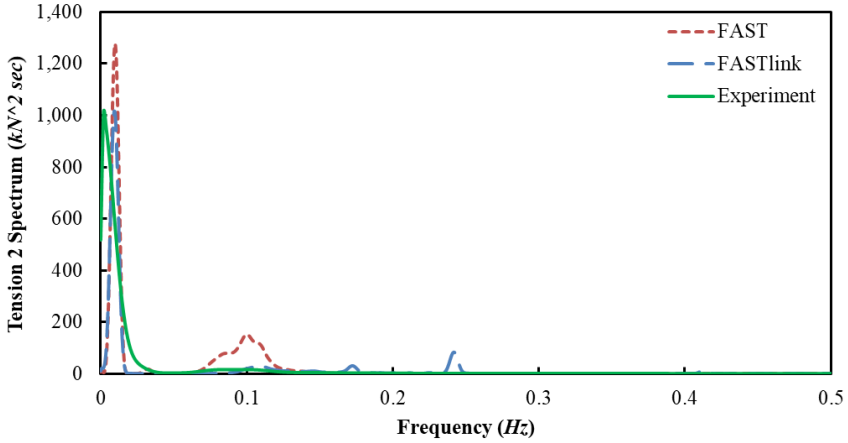

Figure A11. 10 Mooring Tension 2 spectrum in spar with realistic mooring lines, Sea State 1 (full scale)

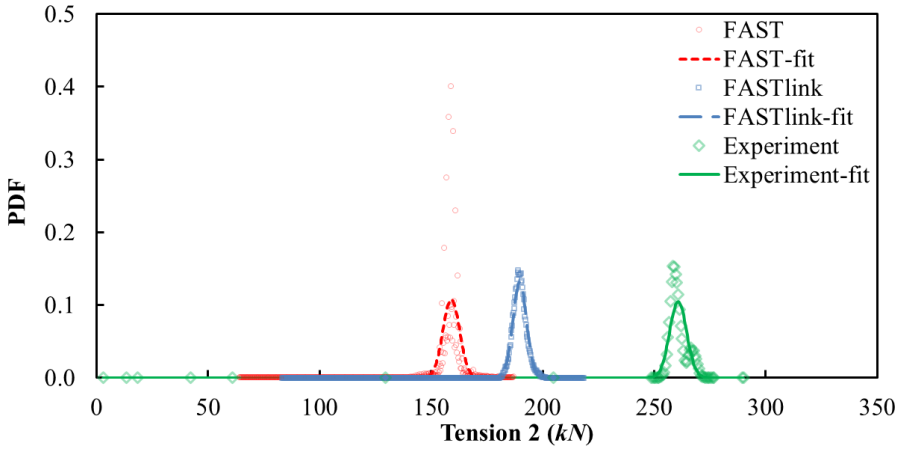

Figure A11. 11 Mooring Tension 2 PDF in spar with realistic mooring lines, Sea State 1 (full scale)

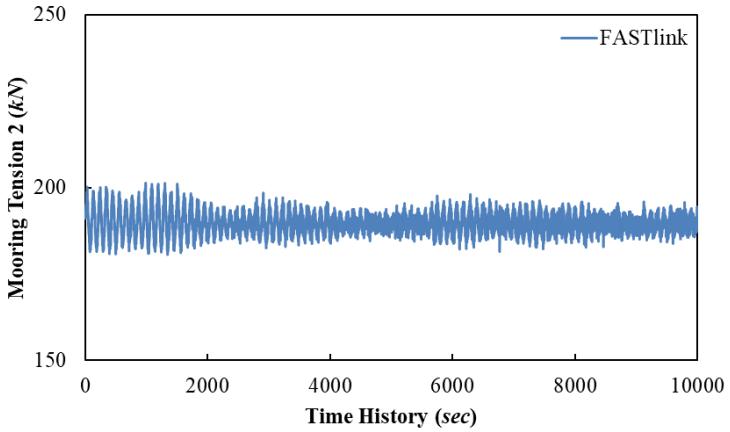

Figure A11. 12 Mooring Tension 2 time history, Sea State 1 (full scale)

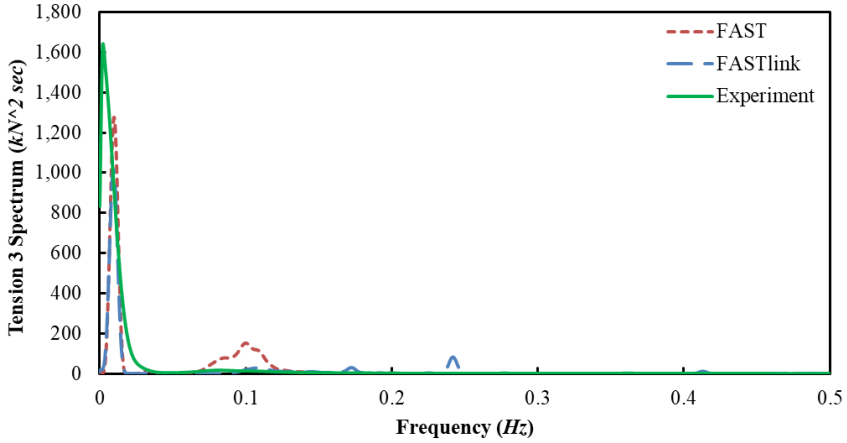

Figure A11. 13 Mooring Tension 3 spectrum in spar with realistic mooring lines, Sea State 1 (full scale)

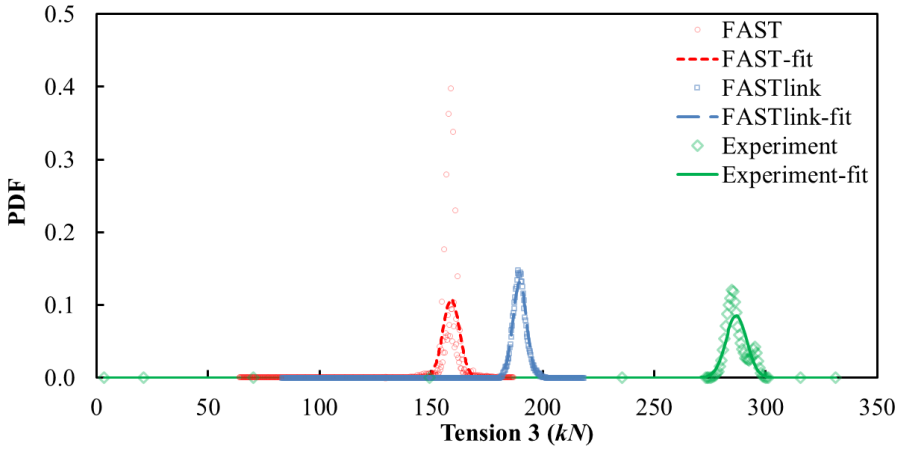

Figure A11. 14 Mooring Tension 3 PDF in spar with realistic mooring lines, Sea State 1 (full scale)

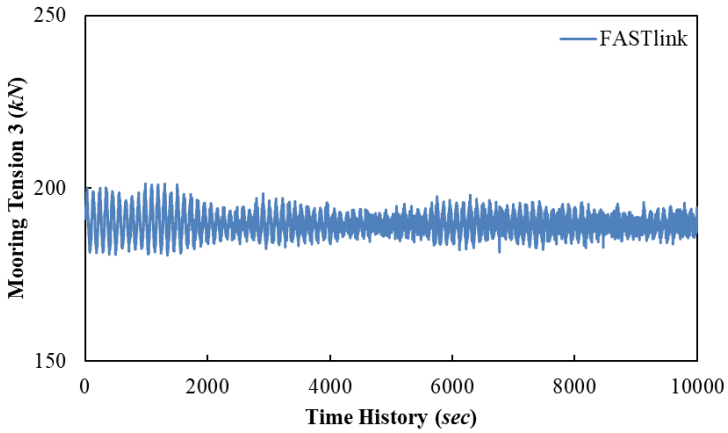

Figure A11. 15 Mooring Tension 3 time history, Sea State 1 (full scale)

Sea State 2

As shown in Figure A11. 17 and Figure A11. 20, FASTlink can still show good results for Mooring Tension 1 but obviously calculated the Mooring Tension 3 wrong. Thus, it means that FASTlink cannot predict the mooring tensions when the sea state is getting large and when the snatching is happening.

In addition, due to the mooring drag coefficient has been set as 0, which could be the main reason causing the failure of the OrcaFlex calculations. As when adding the mooring drag 1.2 into the OrcaFlex, the tension time history is appear as in Figure A11. 21, which shows the simulation are running correctly. However, since the mooring drag can hardly be measured in this experiment and also the snatching phenomenon can disappear with the setup of the mooring drag coefficient, and this study will still use the 0 mooring drag coefficient-also, it works good in both the free decay and regular waves.

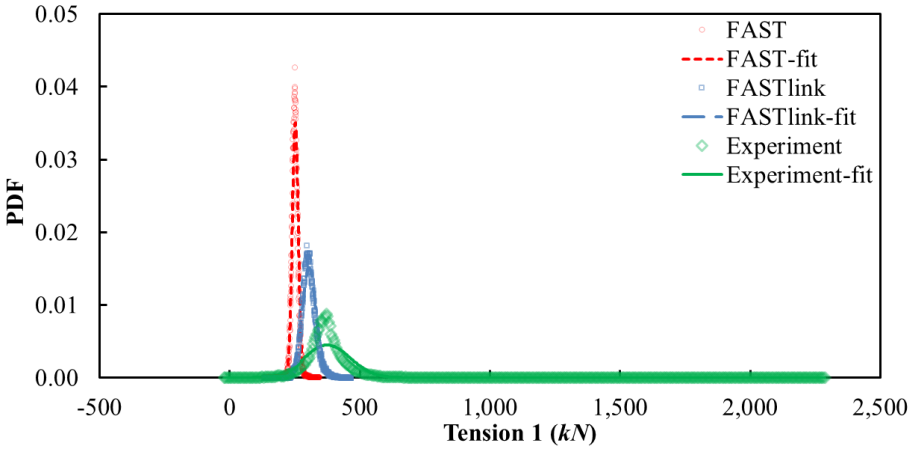

Figure A11. 16 Mooring Tension 1 PDF in spar with realistic mooring lines, Sea State 2 (full scale)

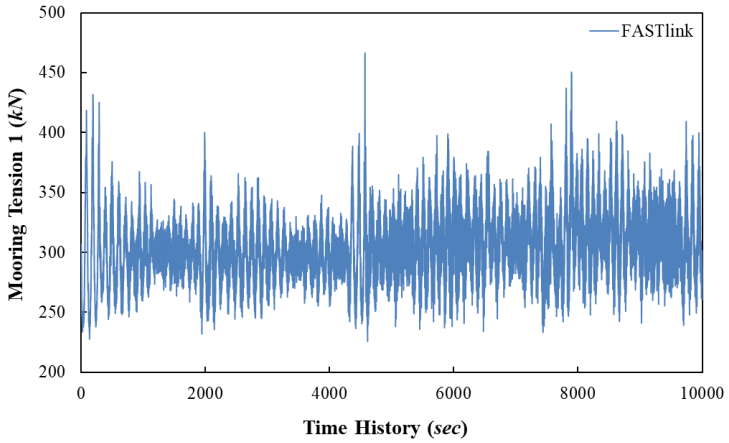

Figure A11. 17 Mooring Tension 1 time history, Sea State 2 (full scale)

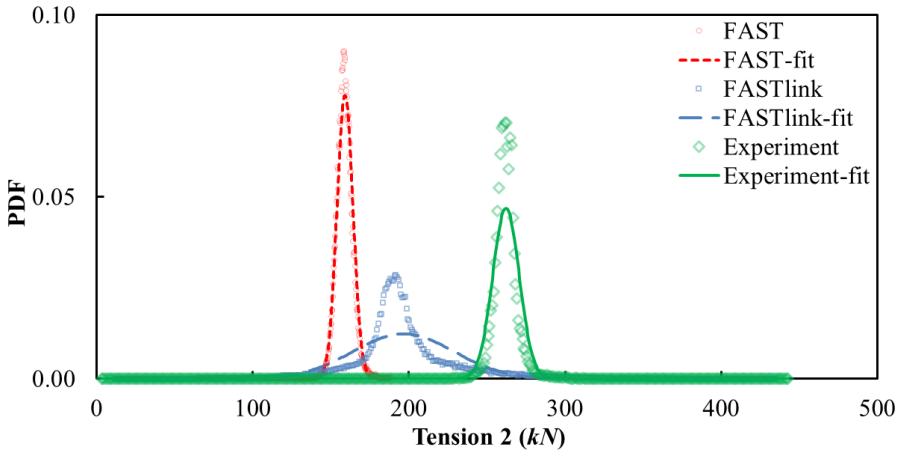

Figure A11. 18 Mooring Tension 2 PDF in spar with realistic mooring lines, Sea State 2 (full scale)

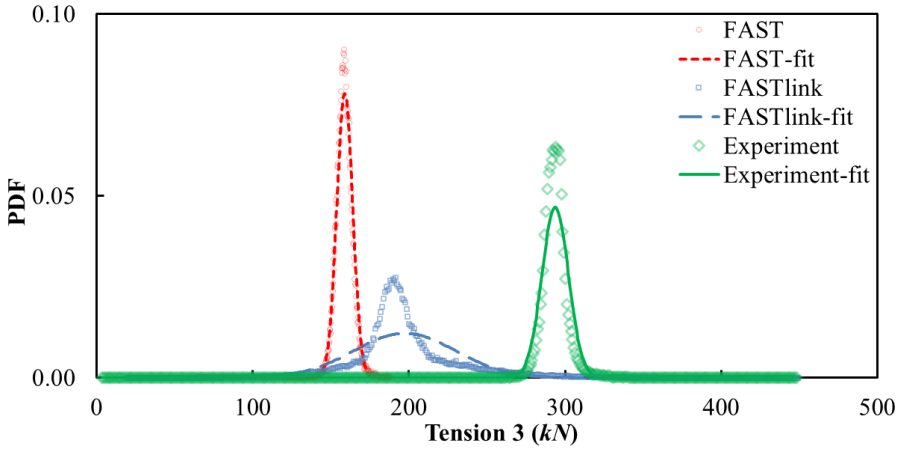

Figure A11. 19 Mooring Tension 3 PDF in spar with realistic mooring lines, Sea State 2 (full scale)

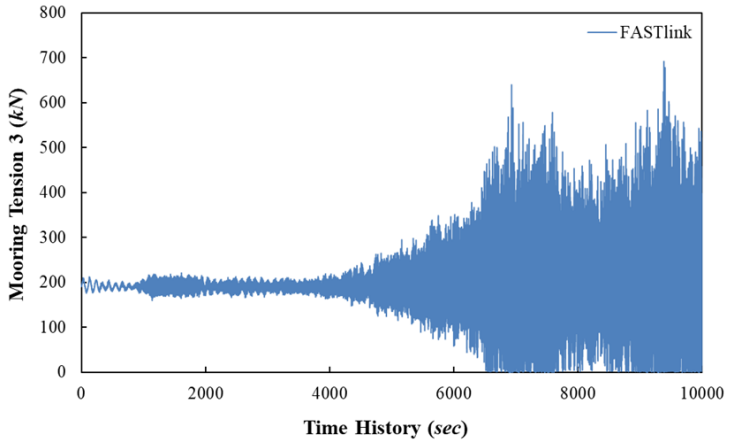

Figure A11. 20 Mooring Tension 3 time history, Sea State 2 (full scale)

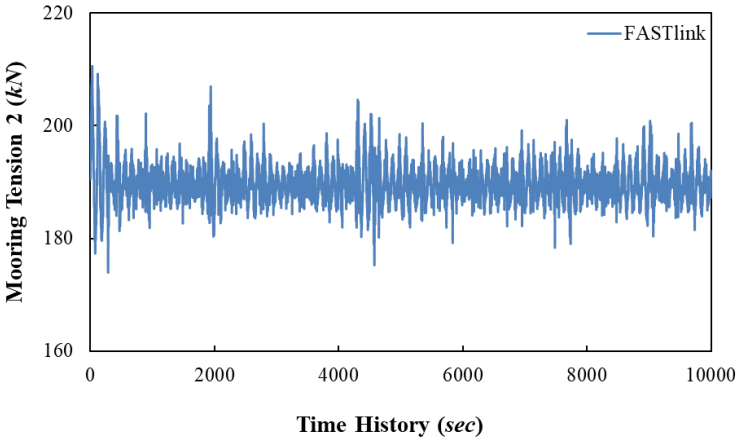

Figure A11. 21 Mooring Tension 2, with mooring drag (Cd=1.2), in Sea State 2 (full scale)

Sea State 3

As mentioned in Chapter 6.5, a quite small peak frequency with quite high energy have been found in the heave motion spectrum. The video has been checked, as shown in Figure A11. 26, a quite large wave have been generated from the wave maker at around 10 min 10 seconds at the tank test scale. The resulted large heave motion, snatching related mooring tensions are all shown the same results, which caused the higher heave motion spectrum energy than the numerical simulations. For the mooring tensions, the small peak frequency 0.002 Hz are still happening and due to the large amount of snatching are happening, the experiment results do not show clear peak frequencies.

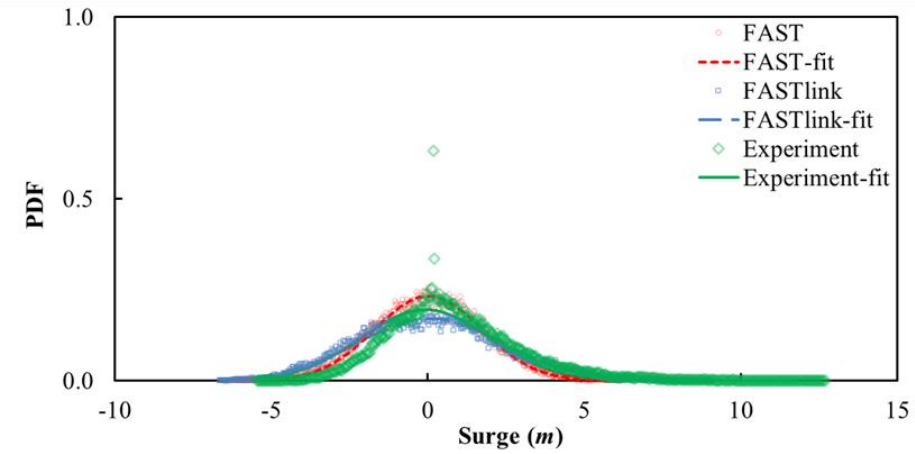

Figure A11. 22 Surge motion PDF in spar with realistic mooring lines, Sea State 3 (full scale)

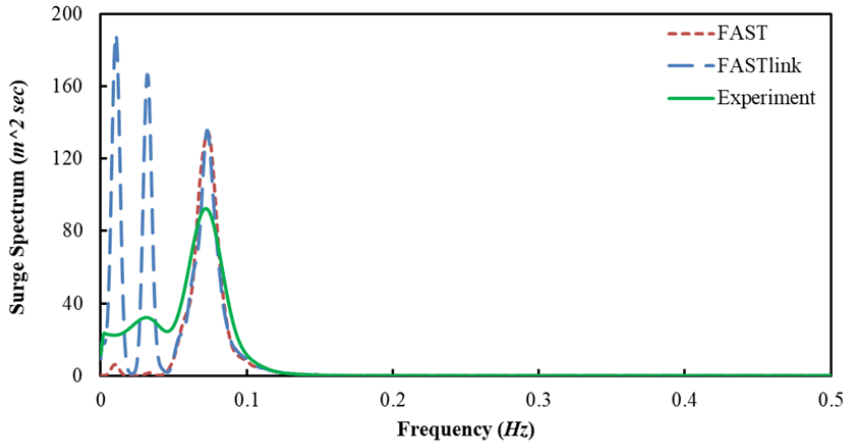

Figure A11. 23 Surge motion spectrum in spar with realistic mooring lines, Sea State 3 (full scale)

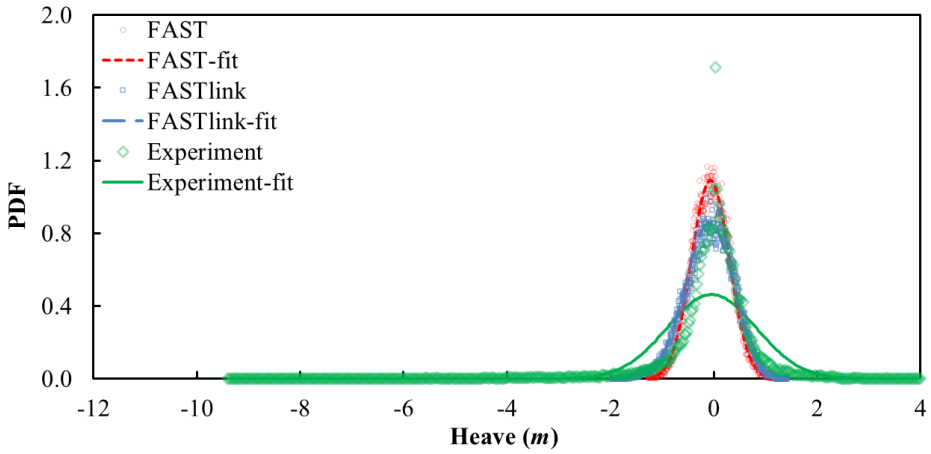

Figure A11. 24 Heave motion PDF in spar with realistic mooring lines, Sea State 3 (full scale)

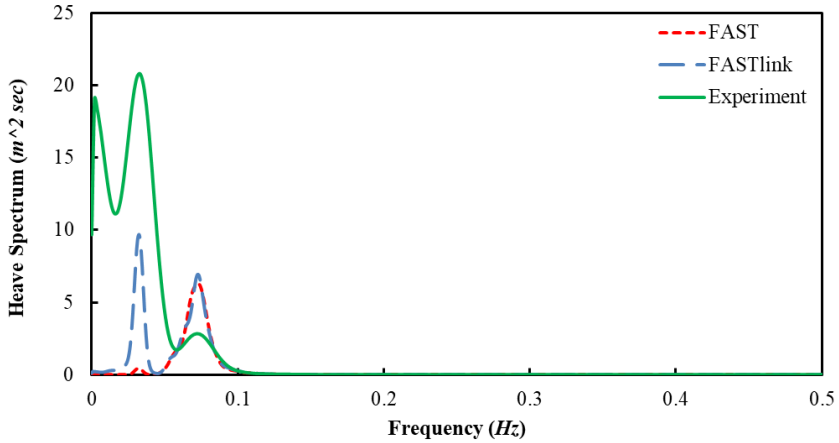

Figure A11. 25 Heave motion spectrum in spar with realistic mooring lines, Sea State 3 (full scale)

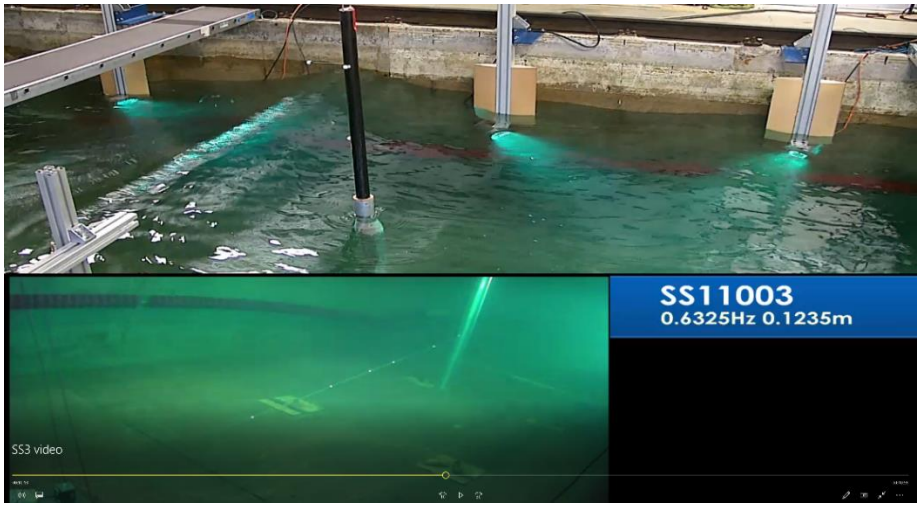

Figure A11. 26 Screen-cut from the video in the tank at around 10 mins10 secs (tank scale, and 5350 seconds in full scale), in Sea State 3

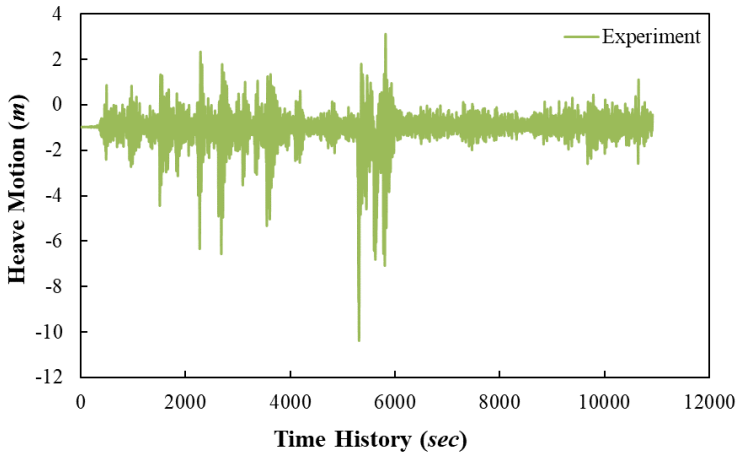

Figure A11. 27 Heave motion time history from the tank tests, in spar with realistic mooring lines, Sea State 3 (full scale)

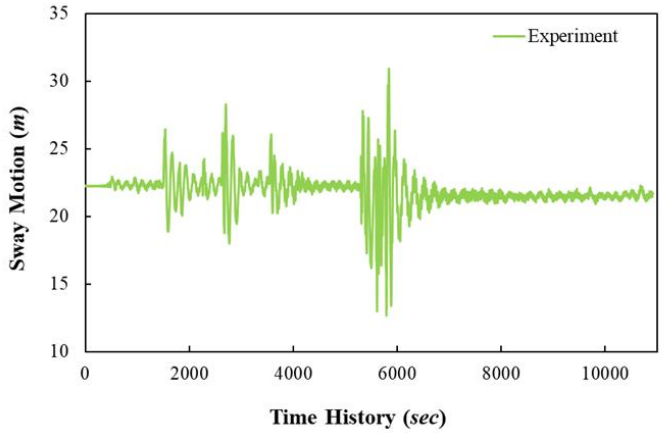

Figure A11. 28 Sway motion time history from the tank tests, in spar with realistic mooring lines, Sea State 3 (full scale)

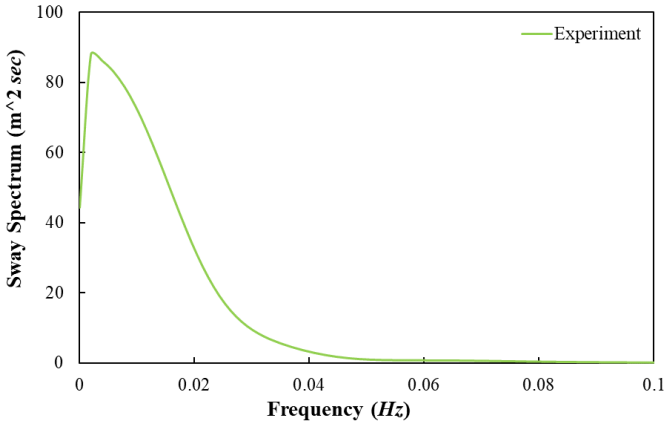

Figure A11. 29 Sway motion spectrum in spar with realistic mooring lines from tank tests, Sea State 3 (full scale)

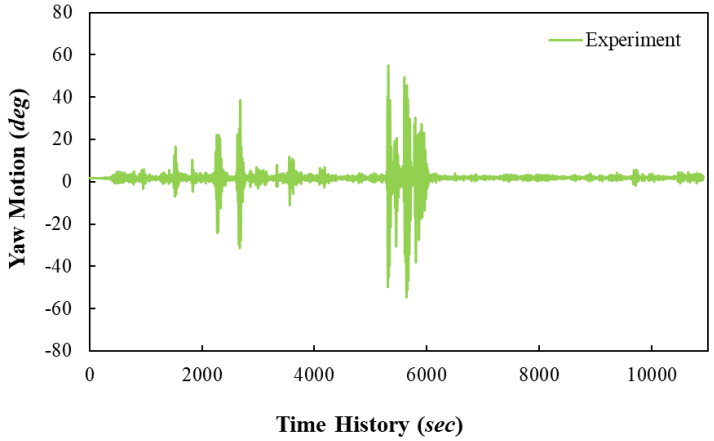

Figure A11. 30 Yaw motion time history from the tank tests, in spar with realistic mooring lines, Sea State 3 (full scale)

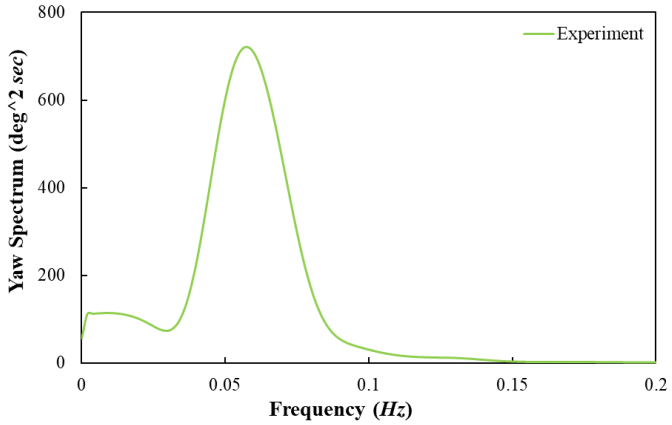

Figure A11. 31 Yaw motion spectrum in spar with realistic mooring lines from tank tests, Sea State 3 (full scale)

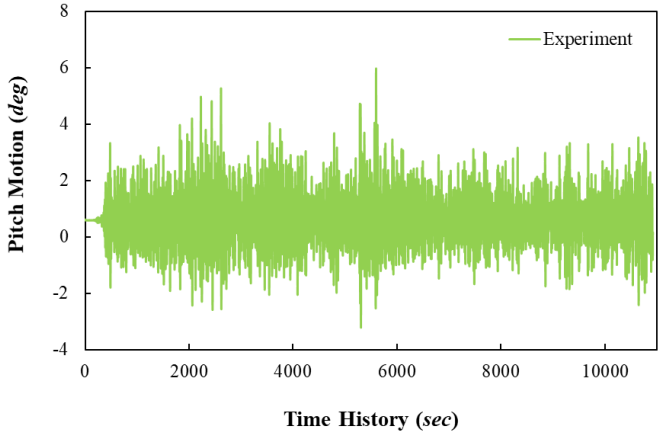

Figure A11. 32 Pitch motion time history from the tank tests, in spar with realistic mooring lines, Sea State 3 (full scale)

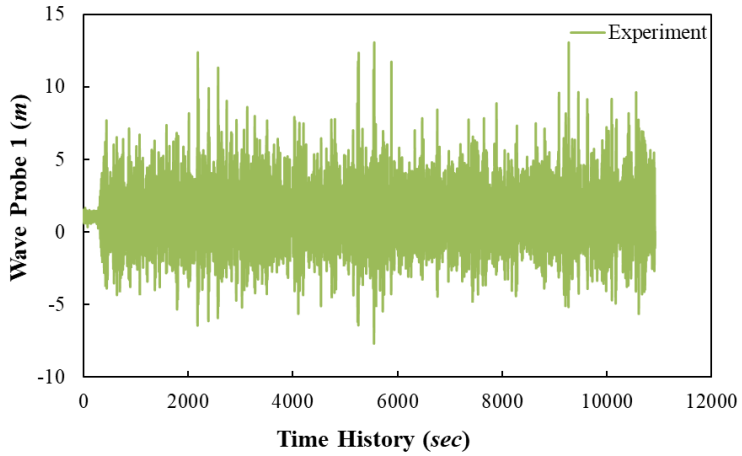

Figure A11. 33 Wave amplitude time history from the tank tests, in spar with realistic mooring lines, Sea State 3 (full scale)

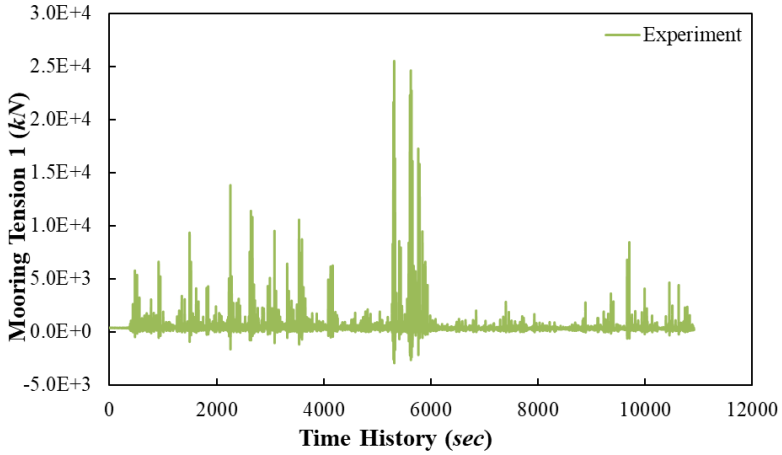

Figure A11. 34 Mooring Tension 1 time history from the tank tests, in spar with realistic mooring lines, Sea State 3 (full scale)

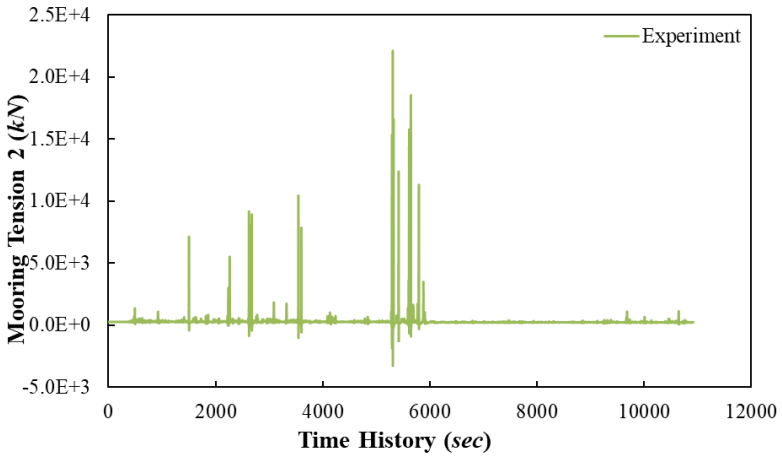

Figure A11. 35 Mooring Tension 2 time history from the tank tests, in spar with realistic mooring lines, Sea State 3 (full scale)

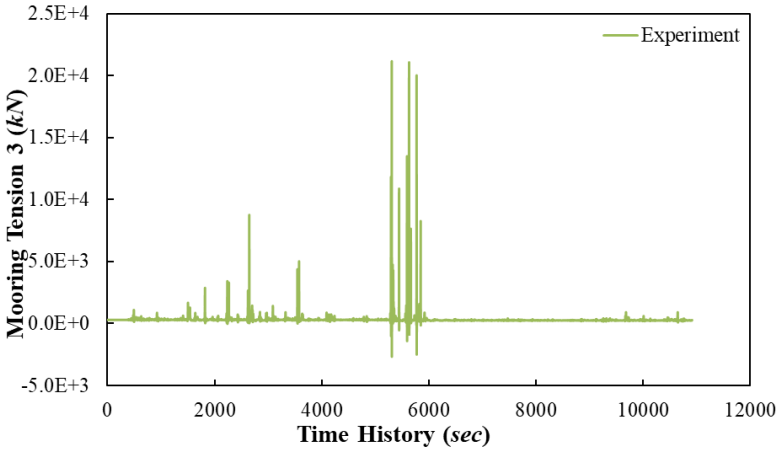

Figure A11. 36 Mooring Tension 3 time history from the tank tests, in spar with realistic mooring lines, Sea State 3 (full scale)

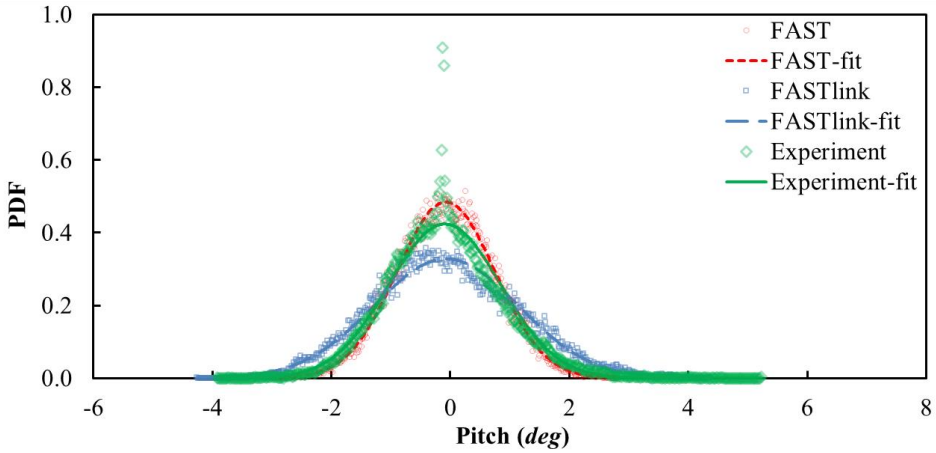

Figure A11. 37 Pitch motion PDF in spar with in spar with realistic mooring lines, Sea State 3 (full scale)

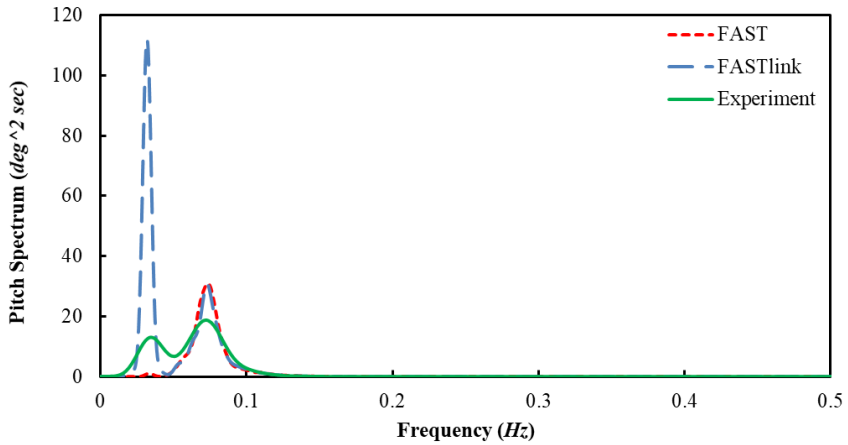

Figure A11. 38 Pitch motion spectrum in spar with in spar with realistic mooring lines, Sea State 3 (full scale)

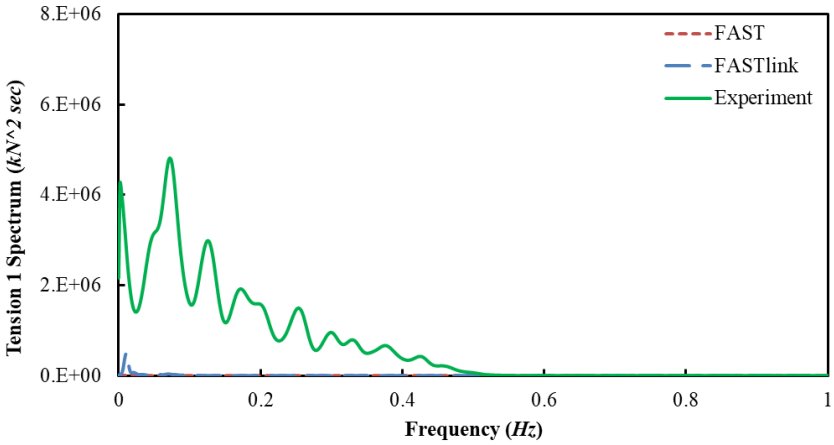

Figure A11. 39 Mooring Tension 1 spectrum in spar with in spar with realistic mooring lines, Sea State 3 (full scale)

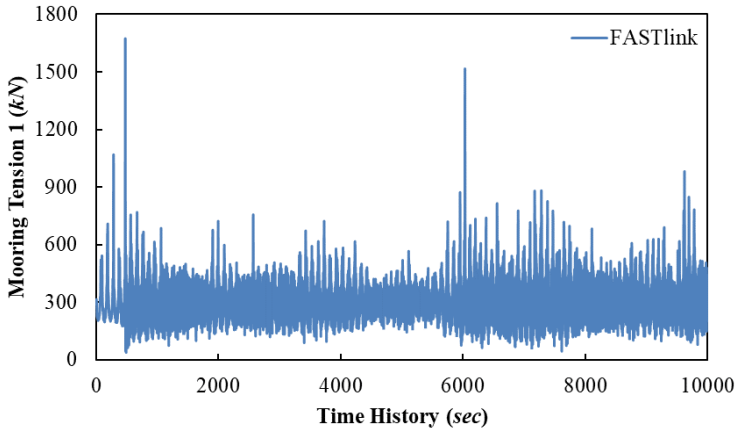

Figure A11. 40 Mooring Tension 1 time history in spar with in spar with realistic mooring lines, Sea State 3 (full scale)

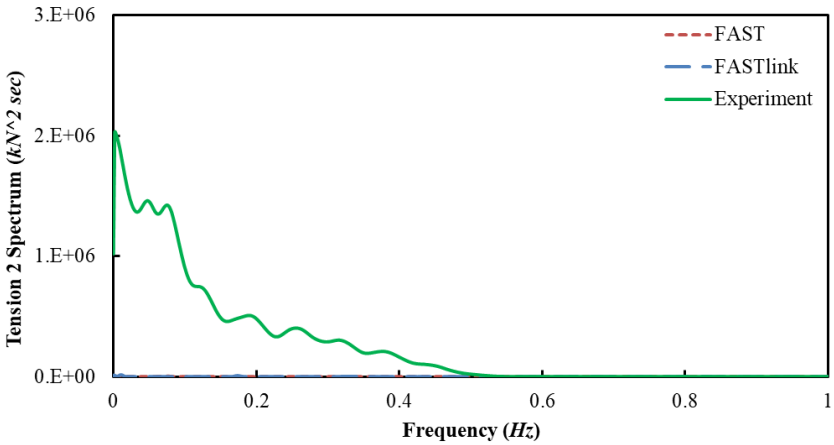

Figure A11. 41 Mooring Tension 2 spectrum in spar with in spar with realistic mooring lines, Sea State 3 (full scale)

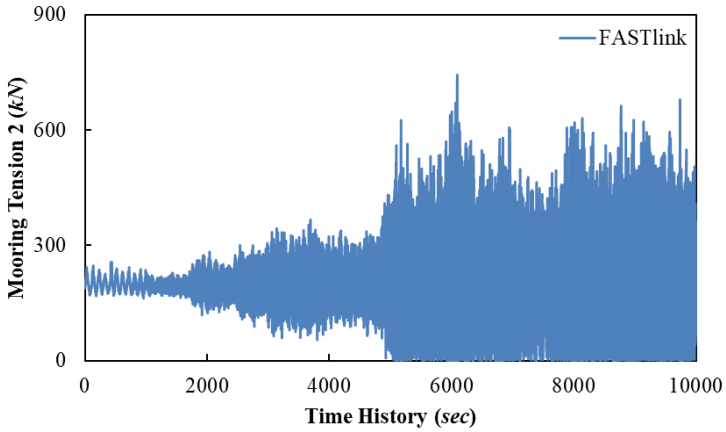

Figure A11. 42 Mooring Tension 2 time history in spar with in spar with realistic mooring lines, Sea State 3 (full scale)

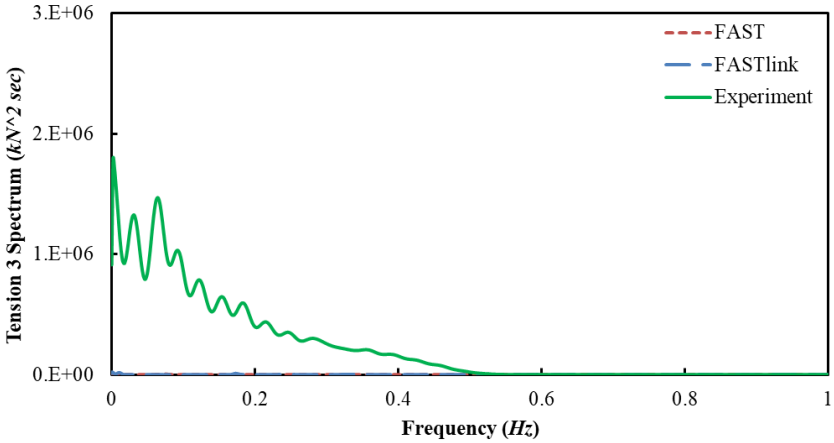

Figure A11. 43 Mooring Tension 3 spectrum in spar with in spar with realistic mooring lines, Sea State 3 (full scale)

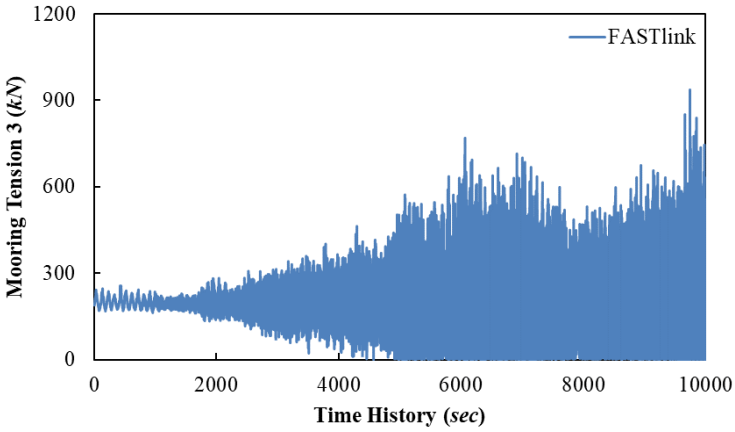

Figure A11. 44 Mooring Tension 3 time history in spar with in spar with realistic mooring lines, Sea State 3 (full scale)

Sea State 4

The numerical approaches have failed when running this extreme sea states, which could be due to the setup of the 0 mooring drag coefficient, as it can run successfully when adding the 1.2 mooring drag coefficient in. In addition, as mentioned in Chapter 6.2, the anchor position of Mooring Line 1 has changed for about 50 mm (3.7 m in full scale) during this sea states, which indicates a possible failure in real condition. Thus, this part is just presented for your information. Apart from the pitch motion, for all the other spectrums, the 0.002 Hz peak frequency can be seen.

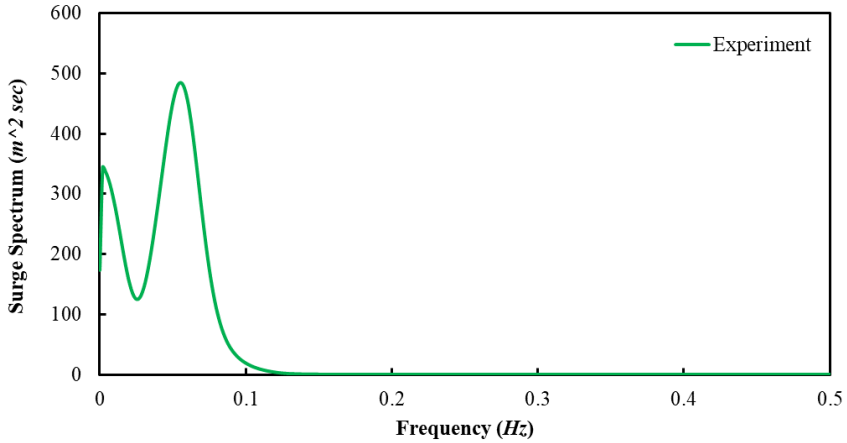

Figure A11. 45 Mooring Tension 3 time history in spar with in spar with realistic mooring lines, Sea State 4 (full scale)

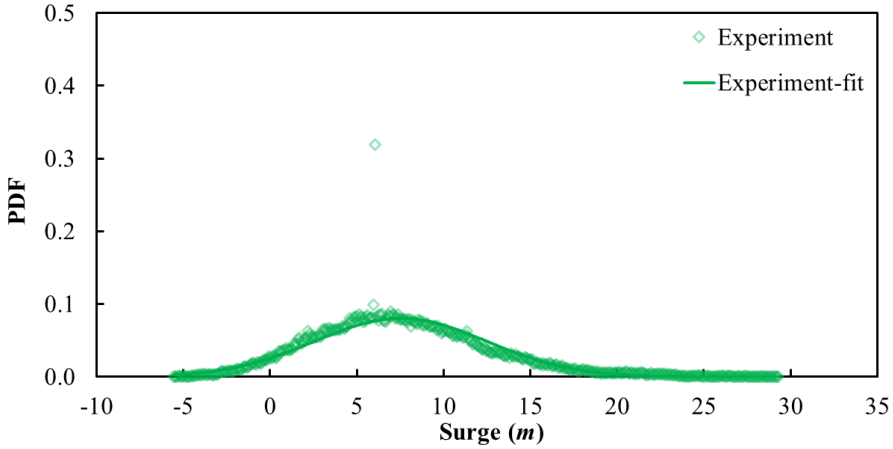

Figure A11. 46 Surge motion PDF in spar with realistic mooring lines, Sea State 4 (full scale)

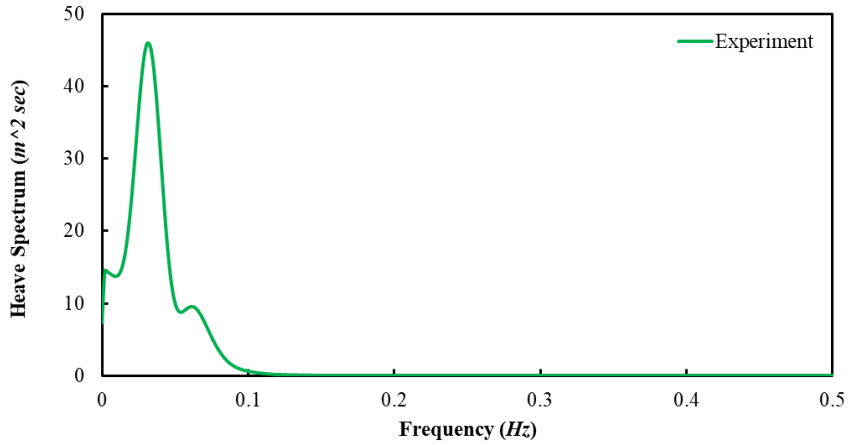

Figure A11. 47 Heave motion spectrum in spar with realistic mooring lines, Sea State 4 (full scale)

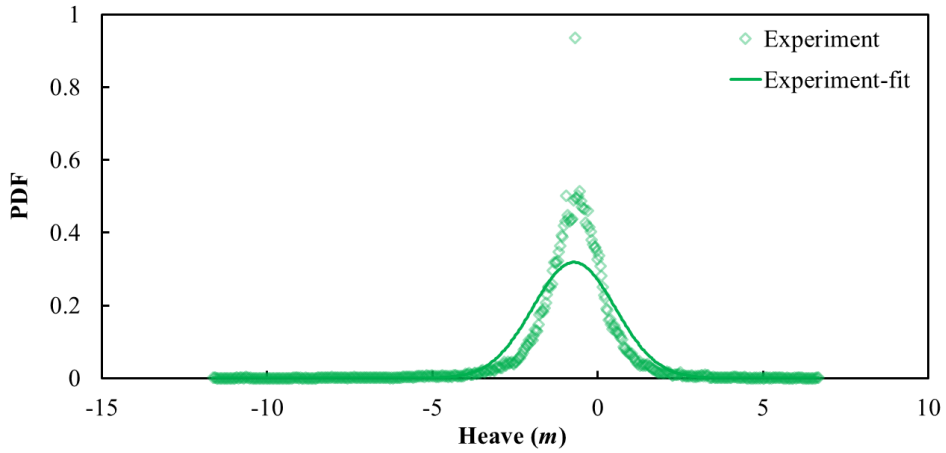

Figure A11. 48 Heave motion PDF in spar with realistic mooring lines, Sea State 4 (full scale)

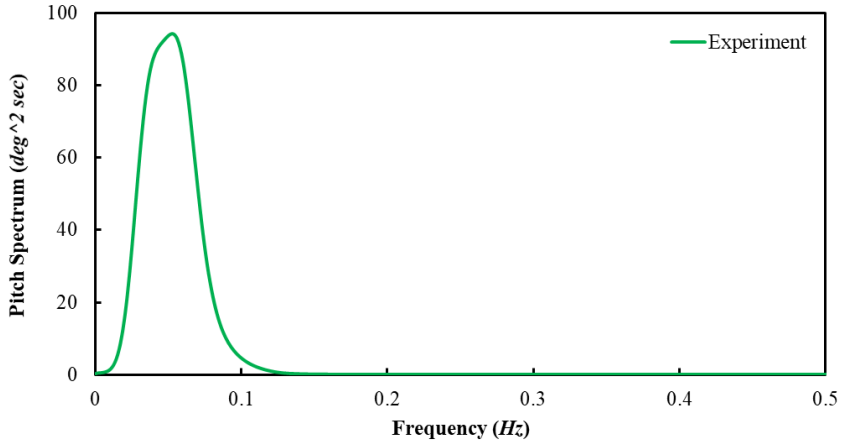

Figure A11. 49 Pitch motion spectrum in spar with realistic mooring lines, Sea State 4 (full scale)

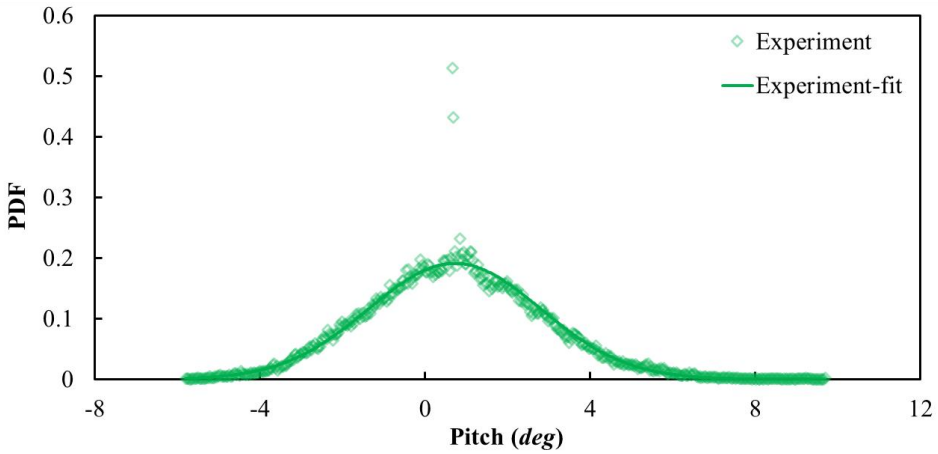

Figure A11. 50 Pitch motion PDF in spar with realistic mooring lines, Sea State 4 (full scale)

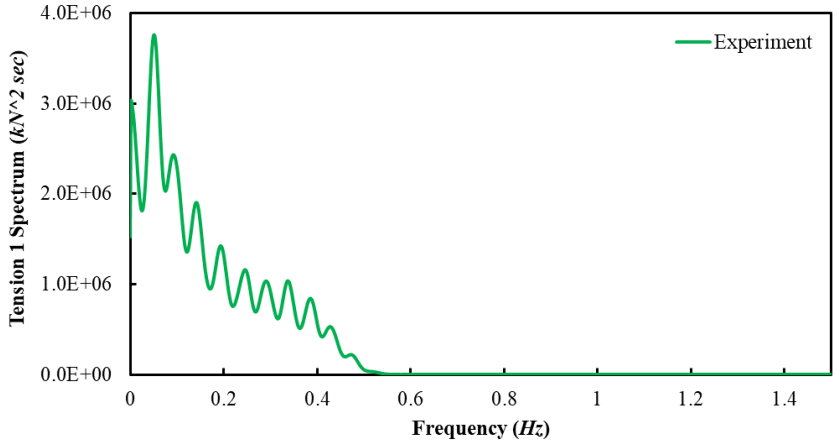

Figure A11. 51 Mooring Tension 1 spectrum in spar with realistic mooring lines, Sea State 4 (full scale)

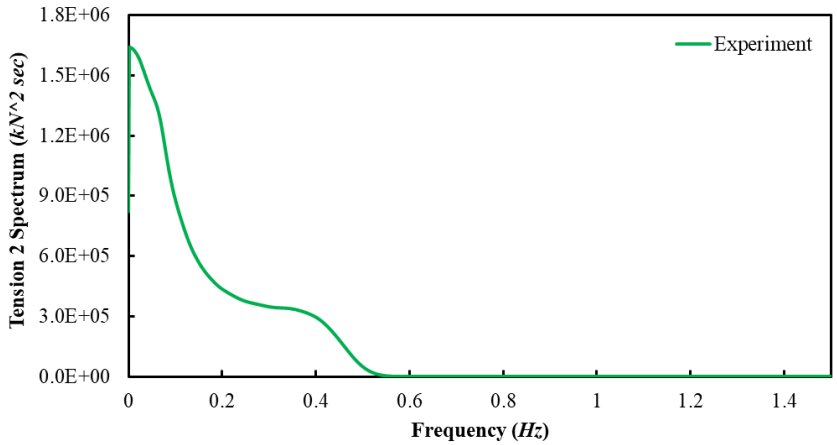

Figure A11. 52 Mooring Tension 2 spectrum in spar with realistic mooring lines, Sea State 4 (full scale)

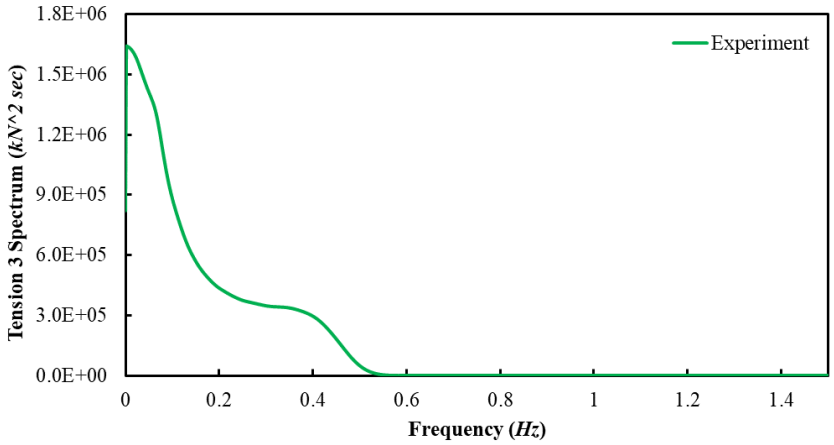

Figure A11. 53 Mooring Tension 3 spectrum in spar with realistic mooring lines, Sea State 4 (full scale)

Appendix 12 Mooring Motion Spectrum (spar with moorings) in the Four Sea States

For all the five points and fairlead motion on Mooring Line 1, their spectrum, along both X-axis and Z-axis are been presented in this part. They overall can show a peak at the peak wave frequency in each sea state, along both X-axis and Z-axis. As discussed in Chapter 6.4, it seems that the mooring line motion along X-axis natural frequency in FASTlink is around 0.01 Hz while it is around 0.023 Hz in the experiment. In addition, with the increasing of the sea states, the 0.002 Hz frequency appear as well, which is matching with the mooring tension spectrums, etc.

Sea State 1

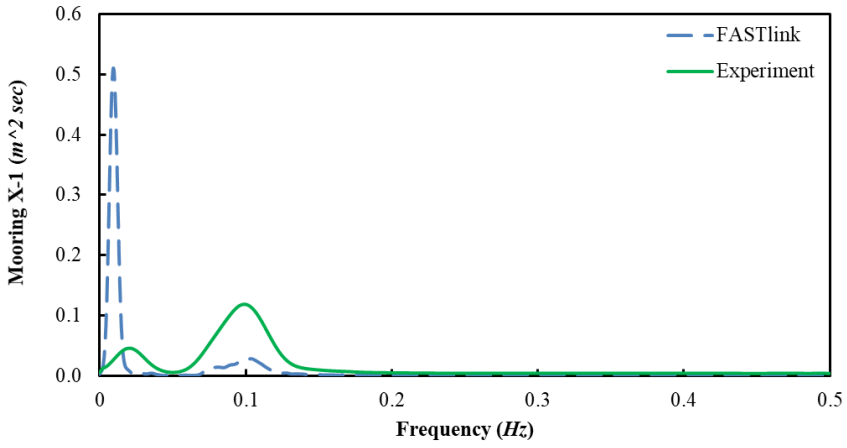

Figure A12. 1 Point-1 motion along X-axis, on Mooring Line 1, Sea State 1 (full scale)

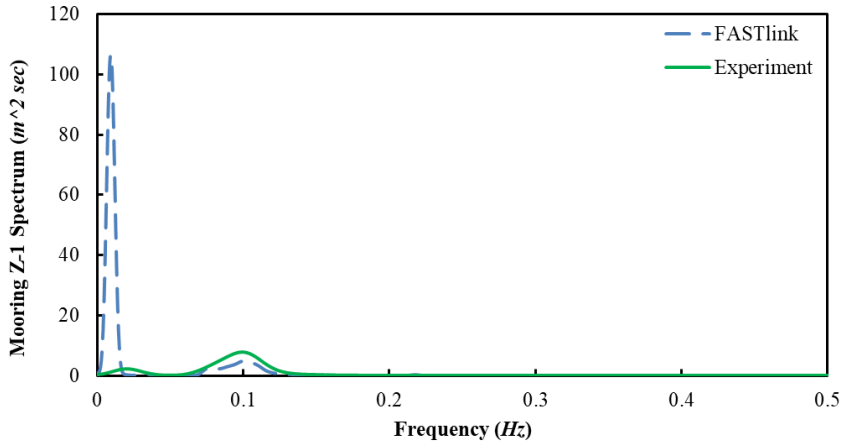

Figure A12. 2 Point-1 motion along Z-axis, on Mooring Line 1, Sea State 1 (full scale)

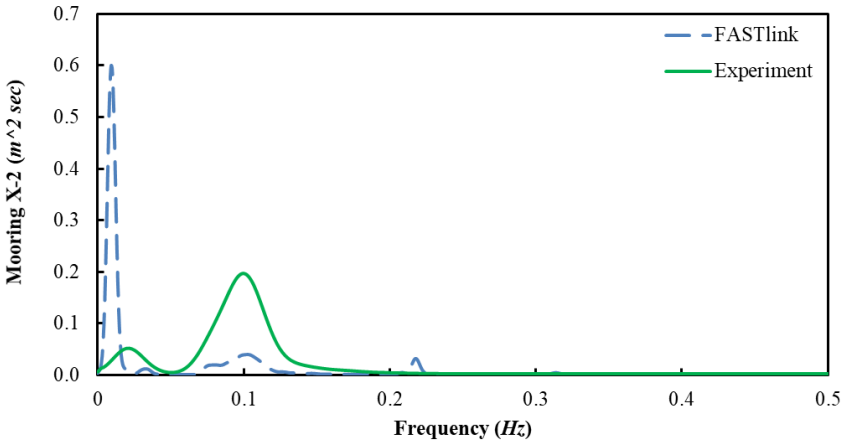

Figure A12. 3 Point-2 motion along X-axis, on Mooring Line 1, Sea State 1 (full scale)

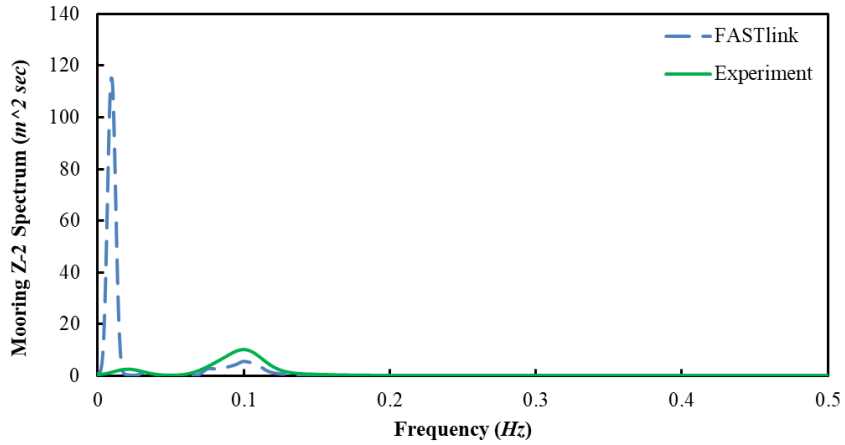

Figure A12. 4 Point-2 motion along Z-axis, on Mooring Line 1, Sea State 1 (full scale)

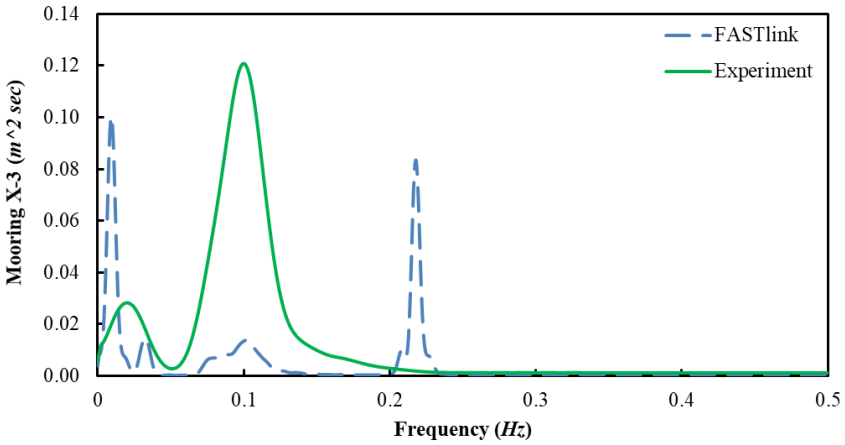

Figure A12. 5 Point-3 motion along X-axis, on Mooring Line 1, Sea State 1 (full scale)

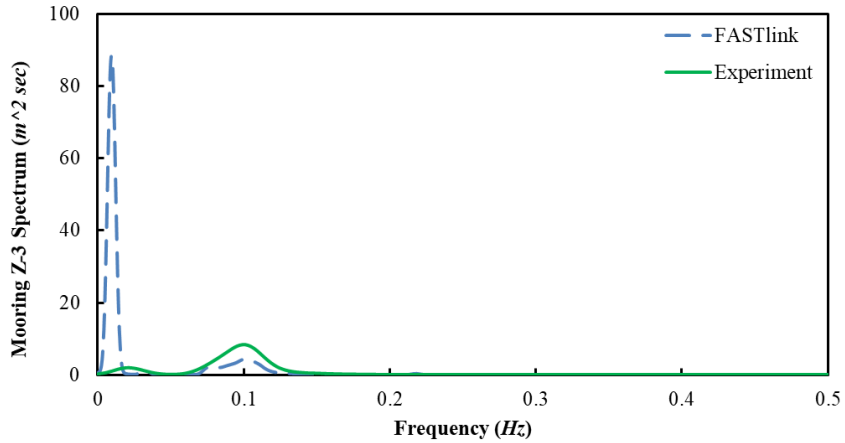

Figure A12. 6 Point-3 motion along Z-axis, on Mooring Line 1, Sea State 1 (full scale)

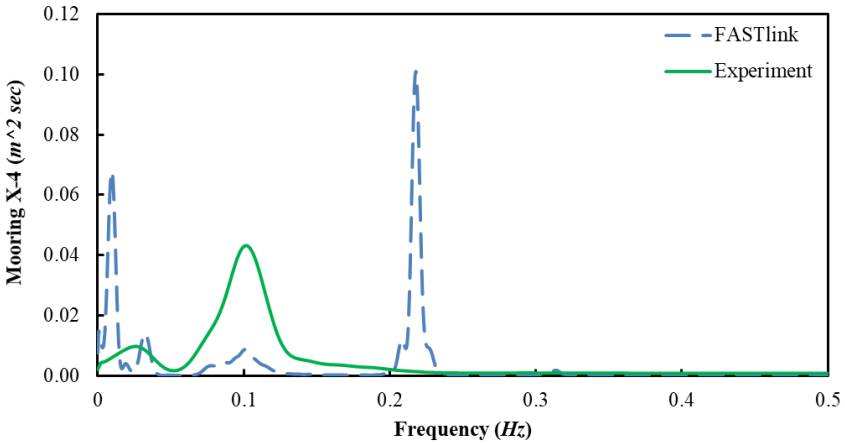

Figure A12. 7 Point-4 motion along X-axis, on Mooring Line 1, Sea State 1 (full scale)

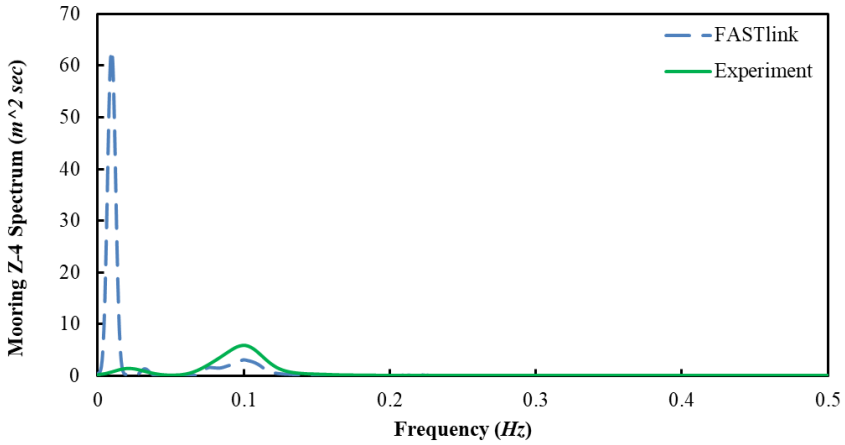

Figure A12. 8 Point-4 motion along Z-axis, on Mooring Line 1, Sea State 1 (full scale)

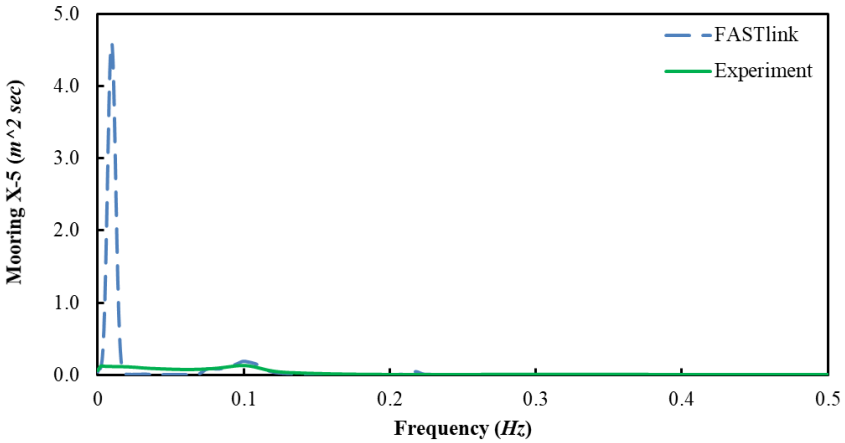

Figure A12. 9 Point-5 motion along X-axis, on Mooring Line 1, Sea State 1 (full scale)

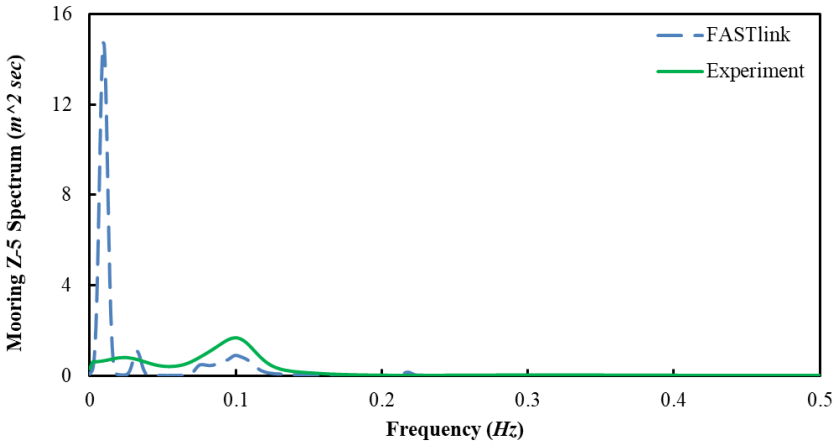

Figure A12. 10 Point-5 motion along Z-axis, on Mooring Line 1, Sea State 1 (full scale)

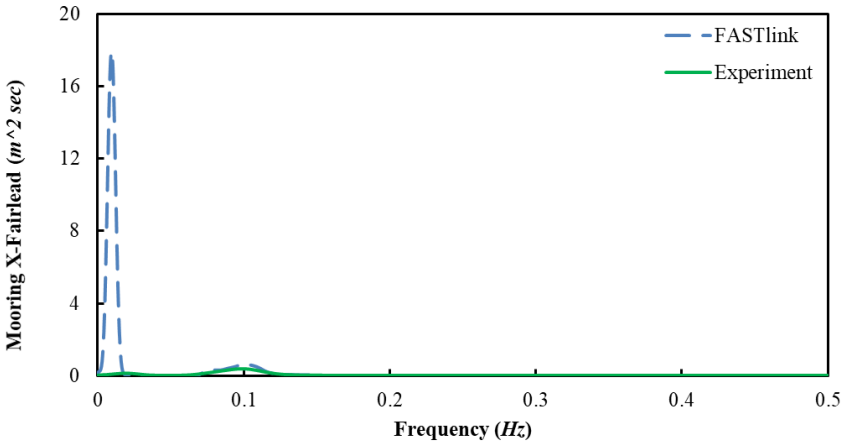

Figure A12. 11 Point-Fairlead motion along X-axis, on Mooring Line 1, Sea State 1 (full scale)

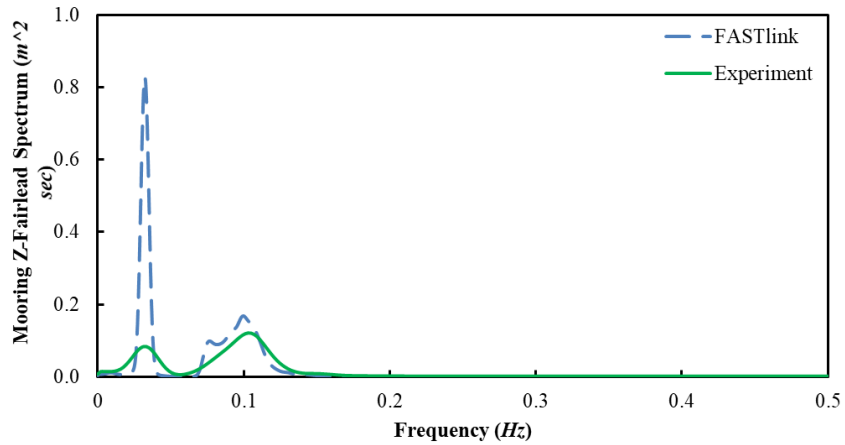

Figure A12. 12 Point-Fairlead motion along Z-axis, on Mooring Line 1, Sea State 1 (full scale)

Sea State 2

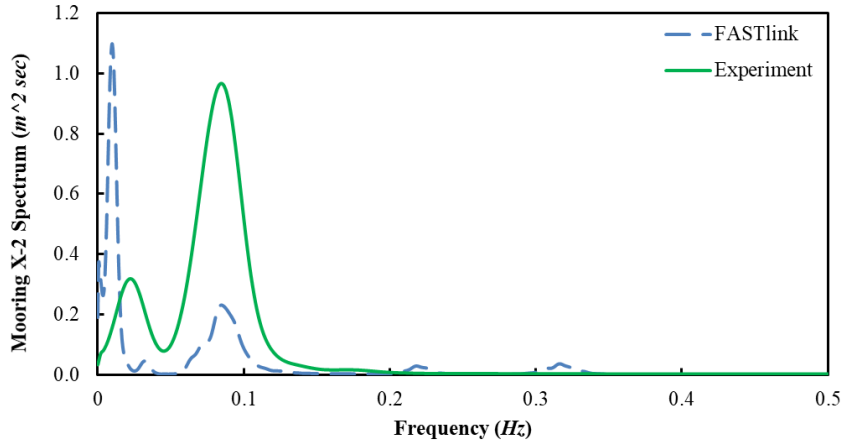

Figure A12. 13 Point-2 motion along X-axis, on Mooring Line 1, Sea State 2 (full scale)

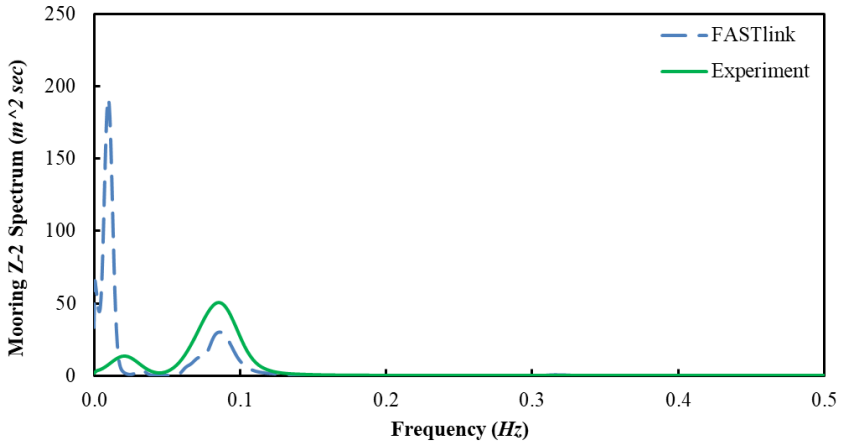

Figure A12. 14 Point-2 motion along Z-axis, on Mooring Line 1, Sea State 2 (full scale)

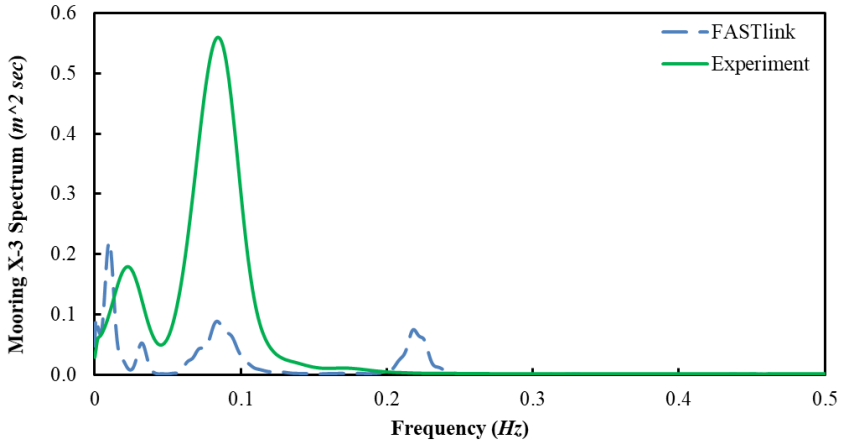

Figure A12. 15 Point-3 motion along X-axis, on Mooring Line 1, Sea State 2 (full scale)

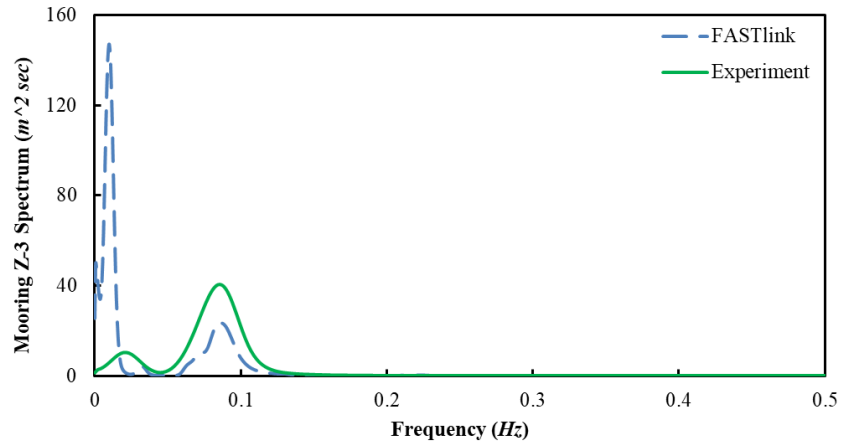

Figure A12. 16 Point-3 motion along Z-axis, on Mooring Line 1, Sea State 2 (full scale)

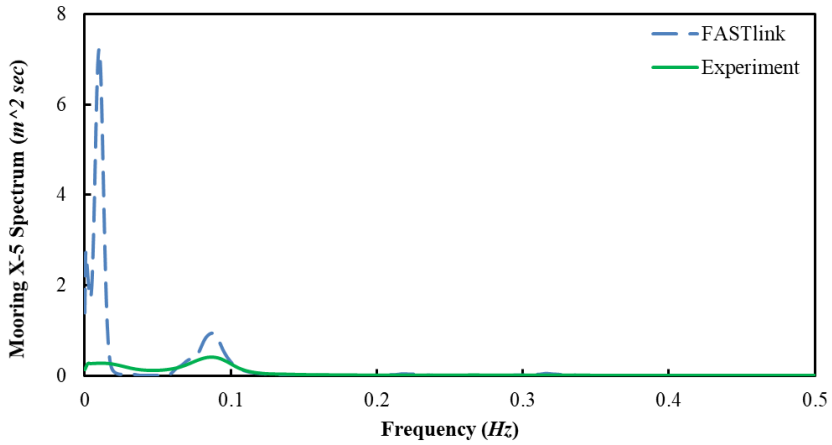

Figure A12. 17 Point-5 motion along X-axis, on Mooring Line 1, Sea State 2 (full scale)

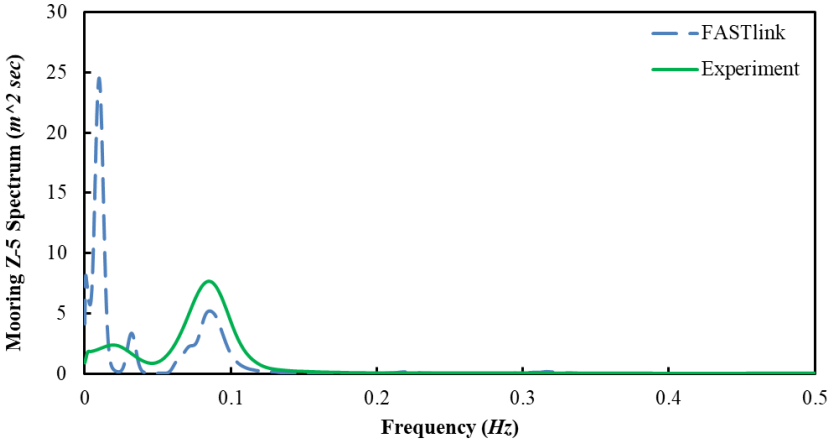

Figure A12. 18 Point-5 motion along Z-axis, on Mooring Line 1, Sea State 2 (full scale)

Sea State 3

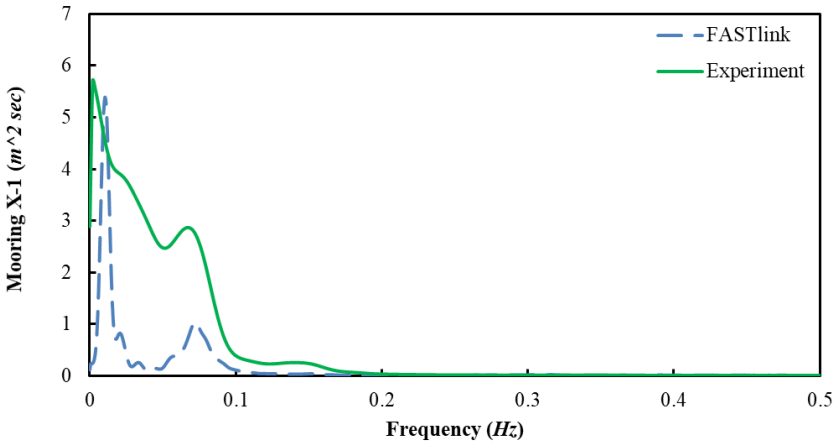

Figure A12. 19 Point-1 motion along X-axis, on Mooring Line 1, Sea State 3 (full scale)

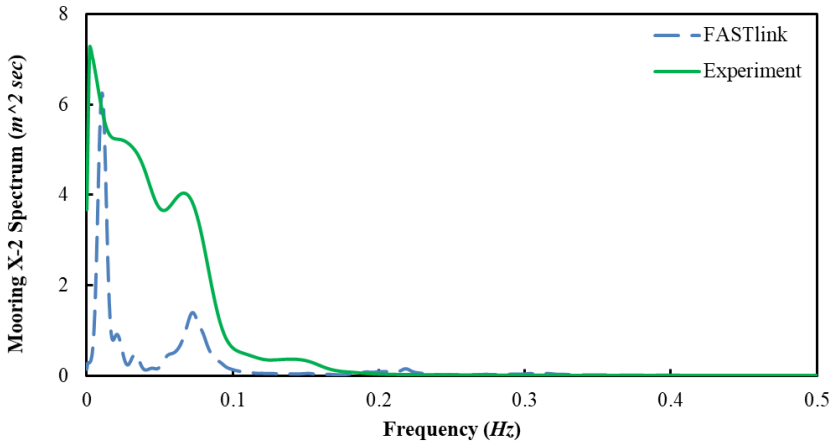

Figure A12. 20 Point-2 motion along X-axis, on Mooring Line 1, Sea State 3 (full scale)

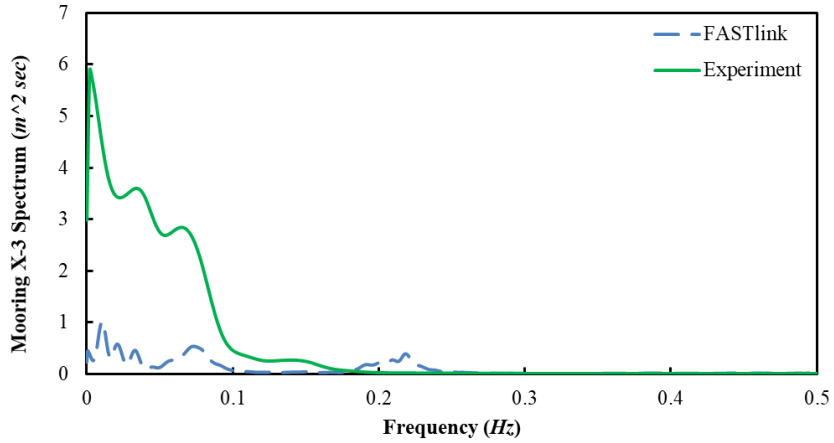

Figure A12. 21 Point-3 motion along X-axis, on Mooring Line 1, Sea State 3 (full scale)

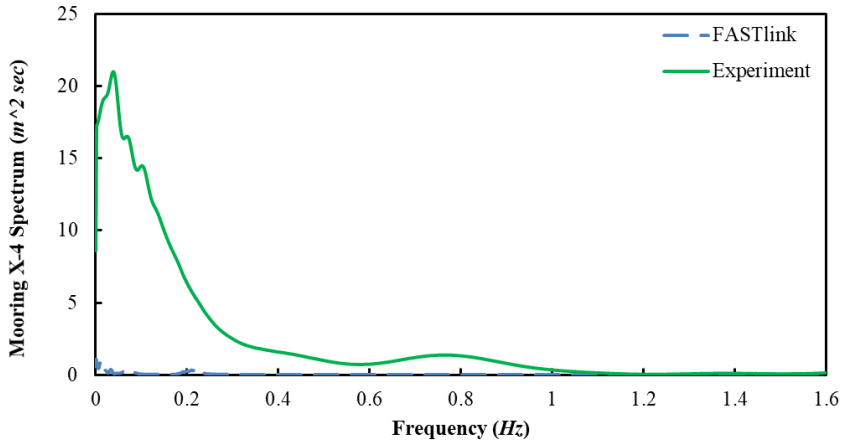

Figure A12. 22 Point-4 motion along X-axis, on Mooring Line 1, Sea State 3 (full scale)

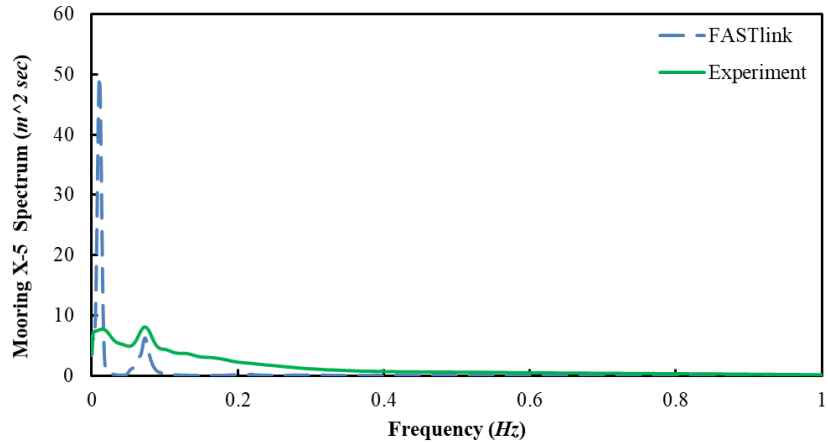

Figure A12. 23 Point-5 motion along X-axis, on Mooring Line 1, Sea State 3 (full scale)

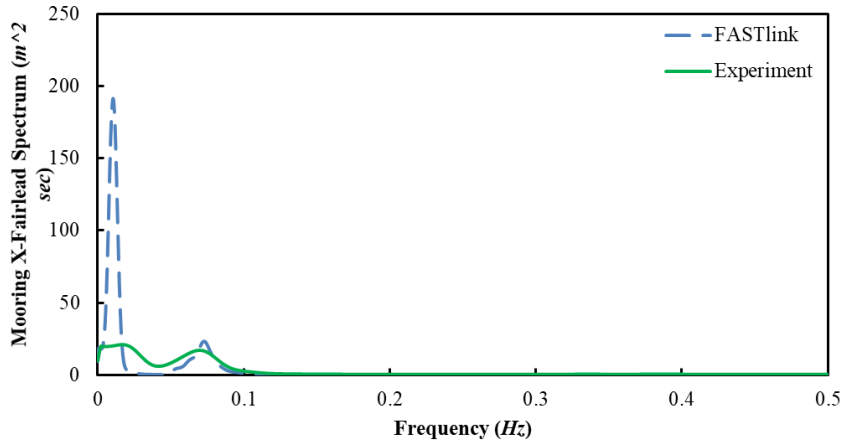

Figure A12. 24 Point-Fairlead motion along X-axis, on Mooring Line 1, Sea State 3 (full scale)

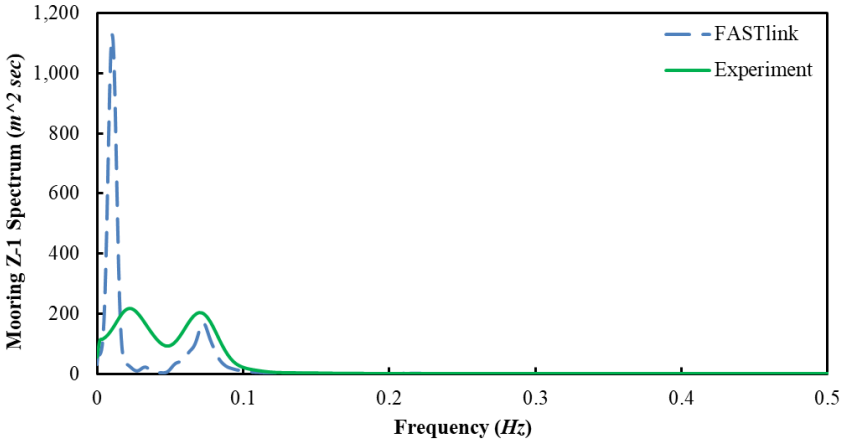

Figure A12. 25 Point-1 motion along Z-axis, on Mooring Line 1, Sea State 3 (full scale)

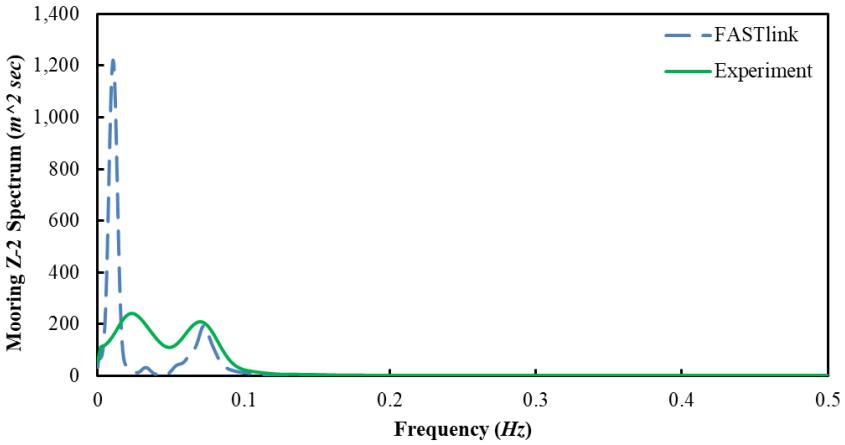

Figure A12. 26 Point-2 motion along Z-axis, on Mooring Line 1, Sea State 3 (full scale)

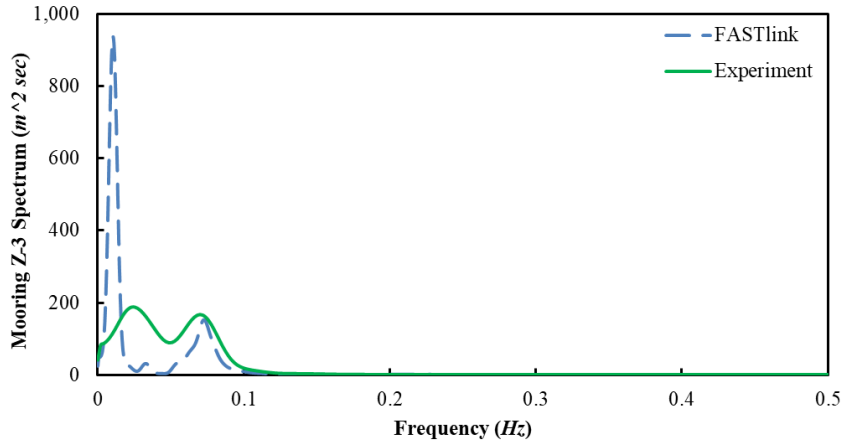

Figure A12. 27 Point-3 motion along Z-axis, on Mooring Line 1, Sea State 3 (full scale)

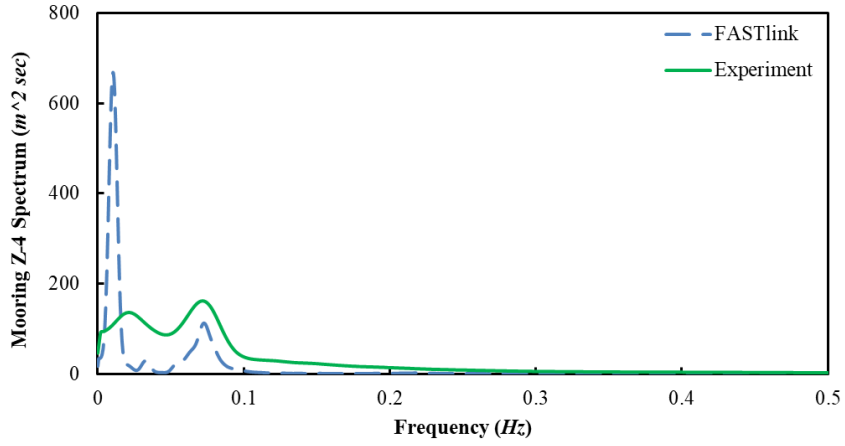

Figure A12. 28 Point-4 motion along Z-axis, on Mooring Line 1, Sea State 3 (full scale)

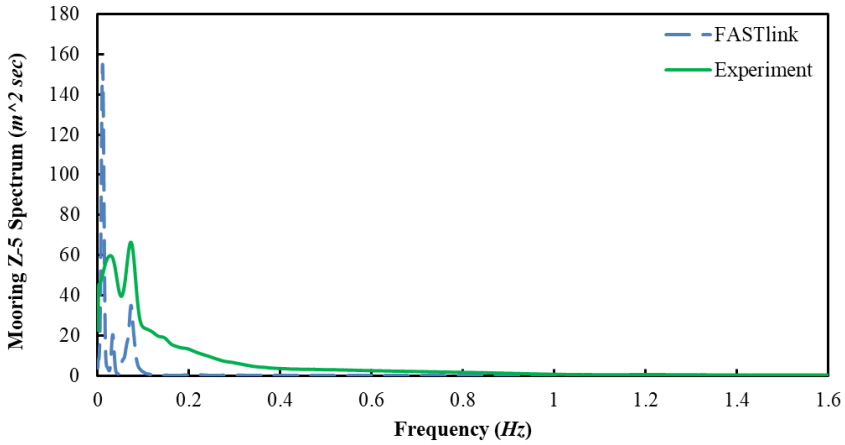

Figure A12. 29 Point-5 motion along Z-axis, on Mooring Line 1, Sea State 3 (full scale)

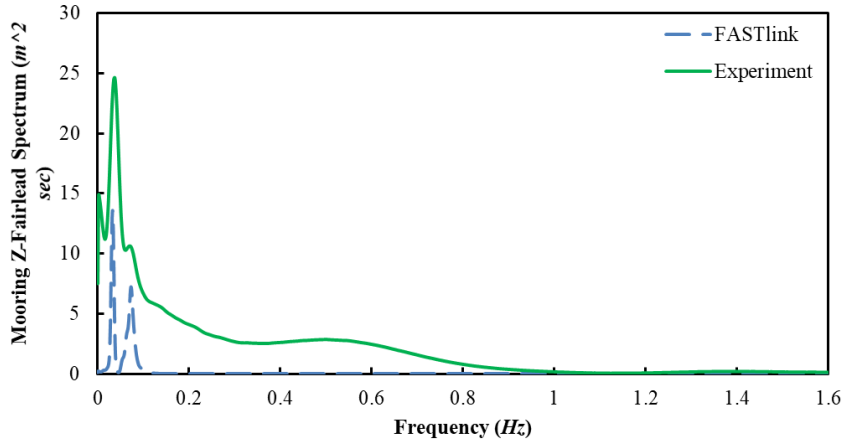

Figure A12. 30 Point-Fairlead motion along Z-axis, on Mooring Line 1, Sea State 3 (full scale)

Sea State 4

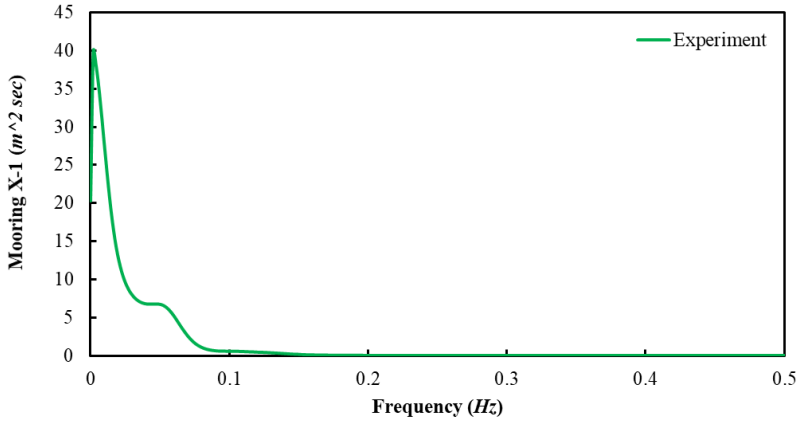

Figure A12. 31 Point-1 motion along X-axis, on Mooring Line 1, Sea State 4 (full scale)

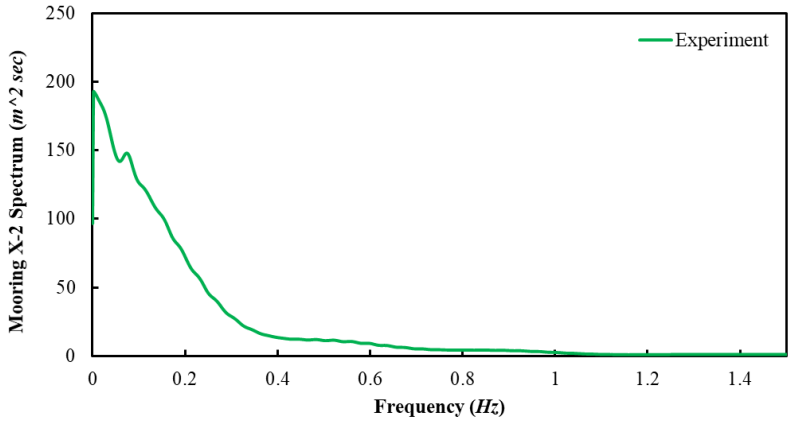

Figure A12. 32 Point-2 motion along X-axis, on Mooring Line 1, Sea State 4 (full scale)

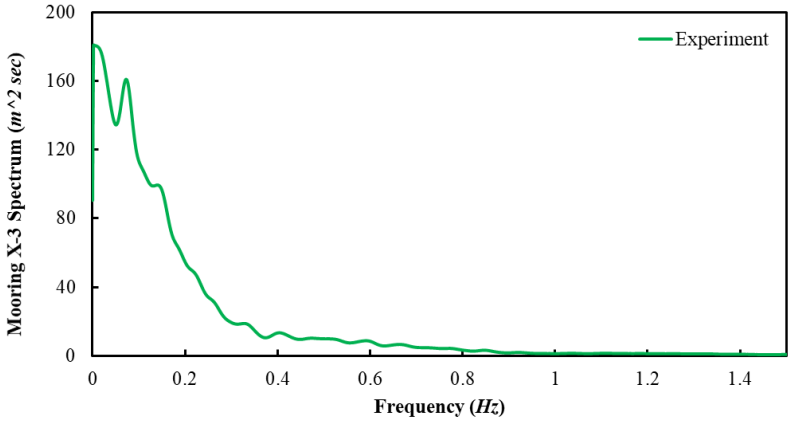

Figure A12. 33 Point-3 motion along X-axis, on Mooring Line 1, Sea State 4(full scale)

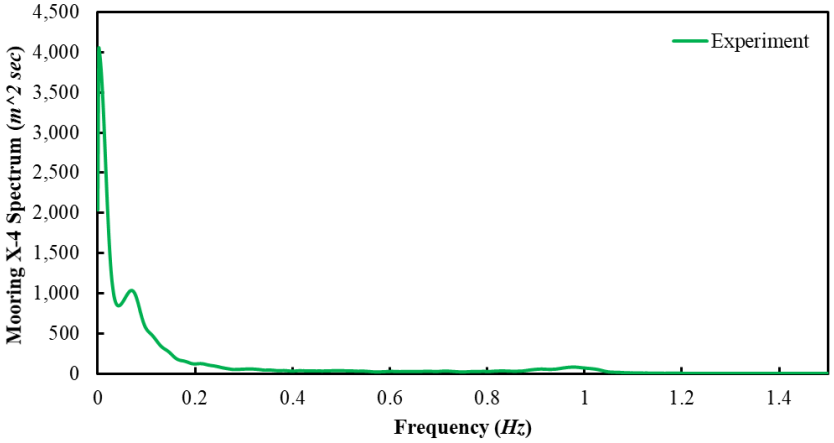

Figure A12. 34 Point-4 motion along X-axis, on Mooring Line 1, Sea State 4 (full scale)

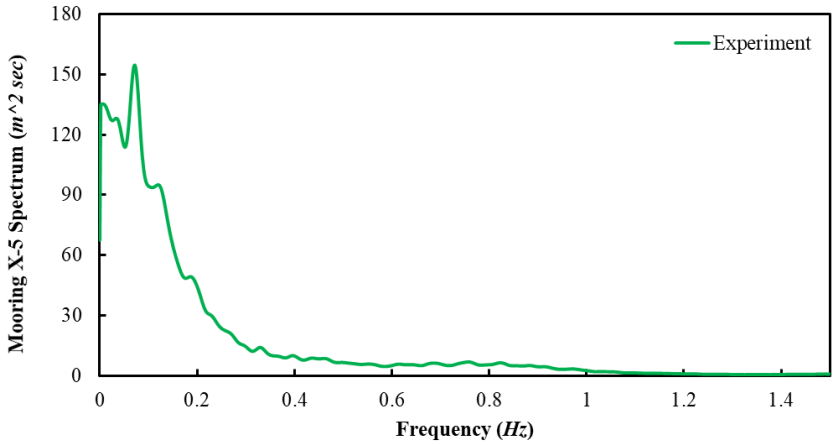

Figure A12. 35 Point-5 motion along X-axis, on Mooring Line 1, Sea State 4 (full scale)

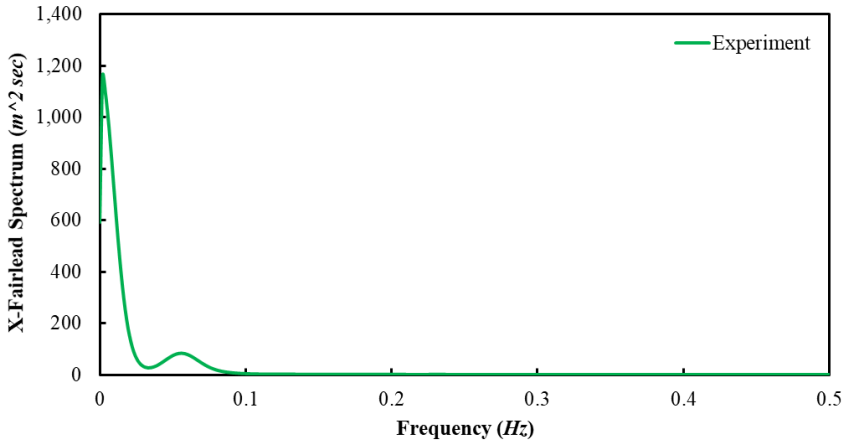

Figure A12. 36 Point-Fairlead motion along X-axis, on Mooring Line 1, Sea State 4 (full scale)

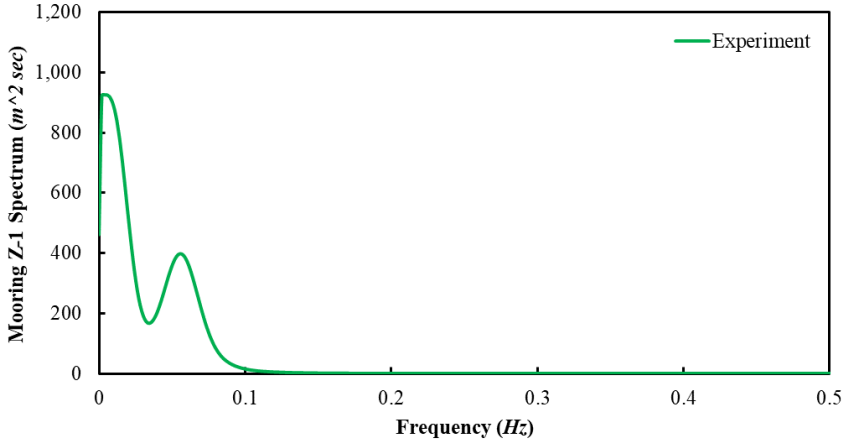

Figure A12. 37 Point-1 motion along Z-axis, on Mooring Line 1, Sea State 4 (full scale)

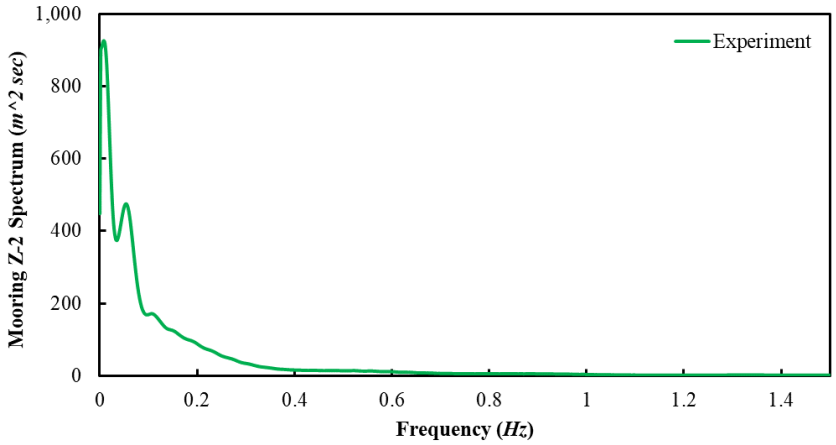

Figure A12. 38 Point-2 motion along Z-axis, on Mooring Line 1, Sea State 4 (full scale)

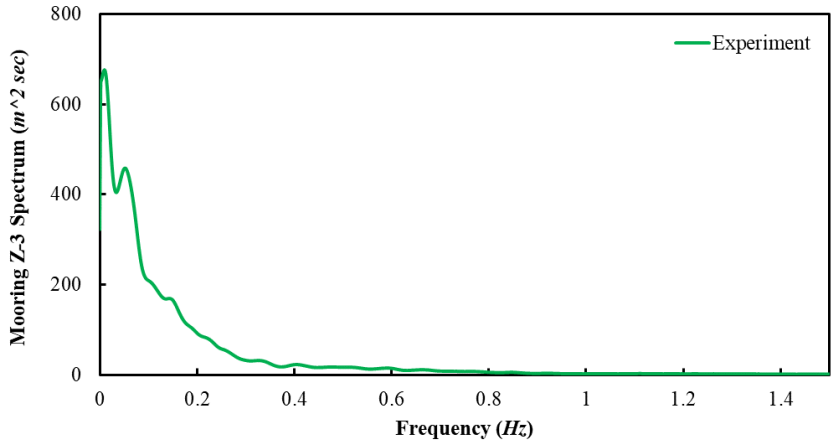

Figure A12. 39 Point-3 motion along Z-axis, on Mooring Line 1, Sea State 4 (full scale)

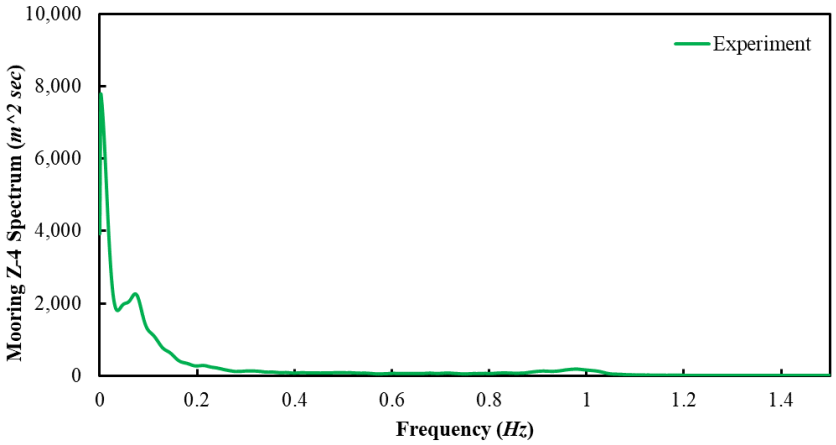

Figure A12. 40 Point-4 motion along Z-axis, on Mooring Line 1, Sea State 4 (full scale)

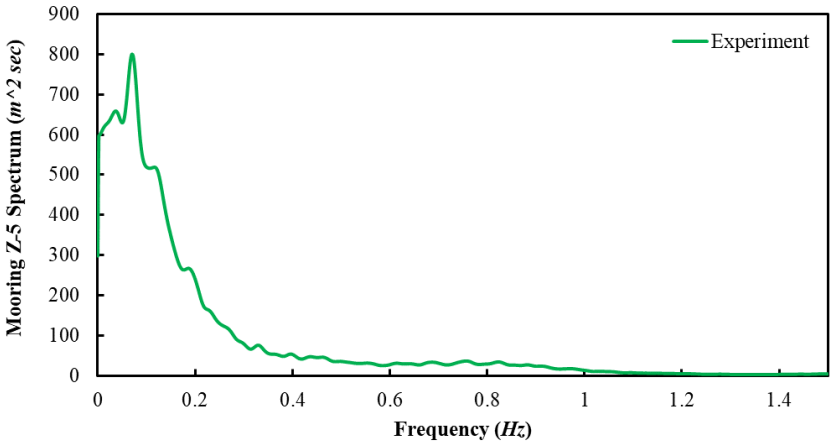

Figure A12. 41 Point-5 motion along Z-axis, on Mooring Line 1, Sea State 4 (full scale)

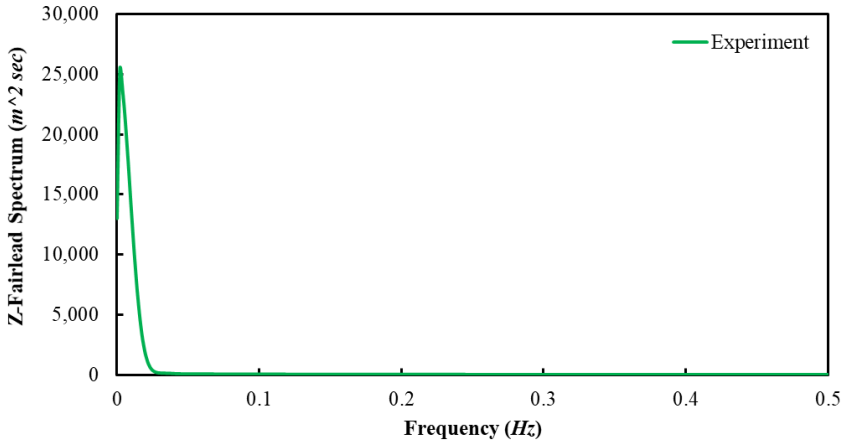

Figure A12. 42 Point-Fairlead motion along Z-axis, on Mooring Line 1, Sea State 4 (full scale)

Appendix 13 Matlab Code for PDF and Spectrum Calculation

An example for the PDF calculation:

```
function [pd1 x y xfit yfit] = createFit(dataset)

[y,x]=hist(dataset,50);

y=y./trapz(x,y);

pd1 = fitdist(dataset, 'rayleigh');

yfit = pdf(pd1,x);

xfit=x;
```

2. An example for the spectrum calculation:

```
T=load('t3 and 2 exp.txt');

time=T(54802:173919,1);

fast=T(54802:173919,2);

fastlink=T(54802:173919,3);

delta_t=time(2)-time(1);

fs=1/delta_t;

plot(time,fast,time,fastlink);

legend('Fast', 'Fastlink');

grid;

%for spectral analysis

%Design a Butterworth low pass filter

nyquist = fs/2;

filter_order = 4;

cutoff_freq_hz = 2;

cutoff = cutoff_freq_hz/nyquist;
```

```
[b,a] = butter(filter_order,cutoff);

%filter the data

fast=filter(b,a,fast);

fastlink=filter(b,a,fastlink);

[pfast,ffs]=pwelch(fast_s,1024,0,8192,fs);

[pfastlink,ffs]=pwelch(fastlink_s,1024,0,8192,fs);

figure;

plot(time,fast_s,time,fastlink_s);

legend('Fast_s', 'Fastlink_s');

grid;

ffsize1=size(ffs);

plot(ffs(1:ffsize1),pfast(1:ffsize1),ffs(1:ffsize1),pfastlink(1:ffsize1));

xlabel('Frequency [Hz]')

ylabel('spectrum [m^2 sec]')

legend('FAST','FASTLINK');

grid
```

Appendix 14 Matlab Code for Target Wave Spectrum Calculation

An example for the target wave spectrum calculation:

```
Hs=15.24;
Tp=17;
garma=3.3;
w=linspace(0.05,2,10000);
[S_w,w]=Jonswapspectrum(Hs,Tp,w,garma)
figure
plot(w,S_w)
xlabel('omega rad/s');
ylabel('PSD')
legend(['Hs=' num2str(Hs) '  ' 'Tp=' num2str(Tp)])
function [S_w,w]=Jonswapspectrum(Hs,Tp,w,garma)
frac1=5/(32*pi)*Hs^2*Tp;
wp=2*pi/Tp;
wratio=(wp./w);
sigma=(w<=wp)*0.07+(w>=wp)*0.09;
frac2=wratio.^5;
frac3=exp(-5/4*wratio.^4);
frac4=1-0.287*log(garma);
alpha=exp(-0.5*((w-wp)./(sigma*wp)).^2);
frac5=garma.^alpha;
S_w=frac1.*frac2.*frac3.*frac4.*frac5;
end
```